MICROCHARACTERISATION OF HALOGENATED COPPER PHTHALOCYANINES USING TRANSMISSION ELECTRON MICROSCOPY

Jacqueline Margaret Smith

Submitted for the degree of Doctor of Philosophy at the Department of Physics and Astronomy, University of Glasgow.

September, 1997

ProQuest LLC.
789 East Eisenhower Parkway
P.O. Box 1346
Ann Arbor, MI 48106 – 1346

ACKNOWLEDGEMENTS

I owe particular thanks to Dr Alan Craven and Prof. John Chapman for their help, support and guidance throughout this project. I would also like to thank Prof. Chapman for providing the facilities within the Solid State Physics group. I am also grateful to my industrial supervisor Dr Peter Bloyce of Zeneca Colours PLC for his useful discussions and suggestions during this project, as well as arranging for my samples to be made.

My thanks also go to EPSRC and Dr. Vass of Zeneca for providing the funding for this CASE award.

For technical support I am grateful to the late Mr. James Simms and Miss Margaret Howe for maintenance of the 1200EX and Mr. Alan Howie for maintenance of the HB5.

I would also like to thank everyone in the solid state physics group who have always been willing to give their time to help me.

Finally, I would like to thank my family and friends who have also given me the support and encouragement I have needed, particularly while writing this thesis.

For my husband Lee, my mother and father and Robert.

Synopsis

Halogenated copper phthalocyanines are widely used in the pigmentary form to colour paints, plastics, dyes and printing inks. Their colouring properties are strongly dependent on the size, shape and chemical composition of the individual pigment particles which have dimensions of typically 50nm. Batches of pigments, produced using nominally the same industrial process, can exhibit differences in their colouring properties. Electron microscopy can provide the high spatial resolution required to analyse both the physical and chemical properties of the pigment particles and thus help to determine the reasons for their differing colouring properties. Various techniques, available in electron microscopy, were used in an attempt to characterise as fully as possible samples of highly chlorinated CPC's. Low magnification images revealed differences in the particle size, shape and particle size distribution, between pigment samples, which would explain differences in their performance. These images also showed that the pigments consisted mainly of small aggregates with dimensions of the order of several pigment particles. Diffraction studies of these aggregates suggested that most of them were pieces of pigmentary material which had not been broken down by the pigmentation process. Further diffraction studies also suggested that the particles were faceted and that these facets coincided with preferred crystallographic planes. Lattice images showed that many particles deviated considerably from perfect crystallinity. The modified differential phase contrast imaging technique allowed simultaneous topographic and lattice images to be recorded from the same area, distinguishing aggregates which had not been broken down by the pigmentation process. The chemical composition of highly chlorinated CPC material was obtained using electron energy loss spectroscopy. An accuracy of ±0.7Cl atoms per molecule could be obtained from a diameter of ~35nm on epitaxially grown thin films. However, the actual value obtained had a small dependence on thickness.

With individual pigment particles, other effects were apparent, preventing a precise determination of the composition. The technique showed that with further refinements, it might be possible to analyse accurately single pigment particles.

TABLE OF CONTENTS

Chapter 1

INTRODUCTION TO THE PHTHALOCYANINES AND ELECTRON MICROSCOPY

1.1 Introduction

The phthalocyanines are a range of organic materials which are widely used in industry as colouring pigments. The most important class of pigments are those based on copper phthalocyanine (CPC). Copper phthalocyanine is blue in colour, however, its shade can be altered by substitution of peripheral hydrogen atoms with halogen atoms. A highly chlorinated CPC pigment has a strong blue green shade, whilst substitution of the majority of the hydrogen atoms with bromine gives a strong yellow green shade. The structure and bonding in the phthalocyanines and its halogenated derivatives are described in section 1.2. Whilst the shade of the pigment is highly dependent on the chemical composition, other properties of the pigments affect their performance in the application medium. A description of the physical characteristics of the CPC pigments and their affect on their colouring properties is given in section 1.3. Variations in the colouring properties are often observed between batches of pigments produced under nominally identical conditions. A description of the industrial preparation

process, together with the associated problems, is given in section 1.4. Colouring properties, such as colour strength and dispersibility, are strongly dependent on the size, shape and chemical composition of the pigment particles. There is therefore considerable incentive for investigating these properties on a microscopic scale to characterise the materials and determine how variations arise. Individual pigment particles have typical dimensions of 50nm, thus investigating their structure and composition requires imaging and analytical techniques capable of high spatial resolution. Information on the pigment structure and composition, on the required scale, can be achieved using electron microscopy. The techniques used to obtain information regarding the physical structure of the pigments, and the problems associated with these techniques, are described in section 1.5. Analytical techniques used to acquire compositional information about the pigmentary particles are described in section 1.6. One of the main problems using electron microscopy to exam these pigments is that they are subject to damage by the electron beam. The effects of radiation damage on chlorinated CPC pigments is discussed in section 1.7. The preparation techniques, used to provide specimens suitable for investigation in the electron microscope, are described in section 1.8.

1.2 The Phthalocyanines

As mentioned in the introduction the phthalocyanines are widely used as pigments. Organic pigments are intensely coloured, particulate organic solids that are essentially insoluble in, and physically or chemically unaffected by, the vehicle or substrate into which they are incorporated. They are mainly used as colourants in paints, plastics, printing inks, coatings and other polymeric materials. Throughout the colouration process, the pigments retain their

crystalline structure. A comprehensive review of the phthalocyanines is found in Moser & Thomas, 1983.

The molecular structure of the phthalocyanines is shown in figure 1.1. The central position can be occupied by a single metal atom or two hydrogen atoms. The most frequently used metal is copper but platinum, silicon, nickel and aluminium have been coordinated in this position. Five membered porphyrin rings are connected to the inner four nitrogen atoms. The outer four nitrogens have lone pairs of electrons which have a considerable influence on substitutional reactions, as occurs in the halogenation process. There are then four benzene type rings which influence the stability of the material during electron irradiation, as will be discussed in section 1.7. Finally there are sixteen peripheral sites which can be occupied by hydrogen atoms as is the case for the crude blue copper phthalocyanine. The hydrogen atoms can be substituted by halogen atoms, most commonly chlorine and bromine, to change the shade of the pigment. The phthalocyanine molecules are apt to pile up in a direction almost perpendicular to the molecular plane because the anisotropic intermolecular forces act more strongly through the π electronic interactions between two adjacent molecules. (Kobayashi et al., 1982). This gives rise to long needle shaped molecular columns which are then attracted to each other by weak Van der Waals forces. A consequence of the weak bonding in molecular crystals is the existence of many different crystal phases of comparable lattice energies (Hom & Honigman, 1974; Fryer, 1977).

1.3 Physical characteristics of CPC pigments and their effects on application properties

The physical characteristics of the pigment particles have a considerable effect on their application properties. The properties which are of major

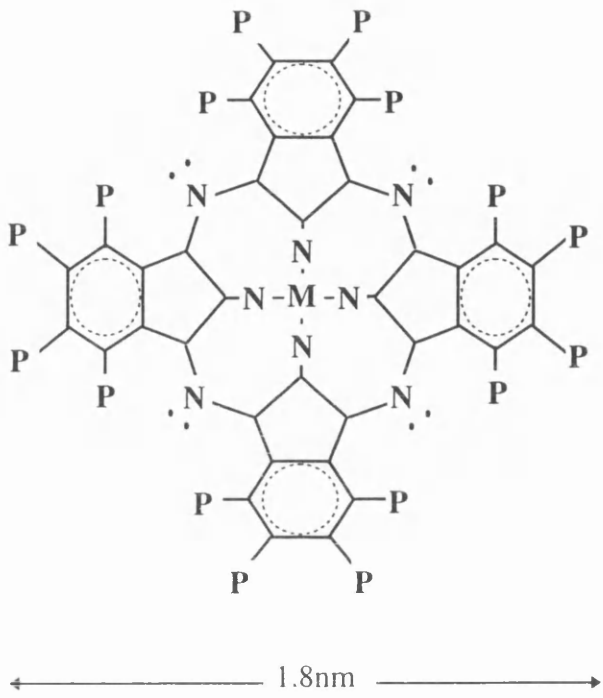

: = lone pair of electrons

M = a metal atom or two hydrogen atoms

P = a peripheral atom site, occupied either by a halogen or hydrogen atom

Figure 1.1: A schematic diagram showing the structure of a phthalocyanine.

importance are the shade, colour strength, dispersibility, flocculation and brightness. This section gives a brief review of these properties and includes the definition of terms which will be used throughout this work.

Whilst the characteristic colour of a pigment is determined primarily by the chemical composition of its molecules, the way in which the molecules are arranged in the crystal lattice can have important secondary effects. As mentioned in the previous section the phthalocyanines can exist in several lattice arrangements (Fryer et al., 1981). These forms are sufficiently different in hue to represent commercially distinct types of pigment.

The colour strength of a pigment is a measure of the intensity of colour per unit weight of pigment. It has been demonstrated experimentally, in paint systems, that colour strength increases with decreasing particle size. Optimum colour strength requires a mean particle size of the order of 0.1 micron or less. However, colour development is not continuous and the colour strength passes through a maximum.

The pigment particles are insoluble in their application medium and therefore they have to be dispersed by mechanical means. The effectiveness of a pigment in imparting colour is dependent upon how finely it can be dispersed in the application medium (Mackay, 1988). Factors affecting the dispersibility of a pigment are the size and shape of the pigmentary particles, and the strength of attraction between the crystals. The pigment is not only dispersed in the form of single isolated primary particles but also as aggregates and agglomerates. These terms are defined below :

primary particle : single crystals or crystals composed of crystallites

aggregates : consist of primary particles attached at their surfaces. The surface area of such an

aggregate is smaller than that of the sum of the surface areas of the primary particles.

agglomerates : is a loose arrangement of primary particles or aggregates or a mixture of the two, attached for instance, at the corners and edges. The total surface is identical to the sum of the surfaces of the individual particles.

The dispersibility of a pigment can be measured in various ways including: (1) the colour strength developed at various dispersion stages; (2) the actual colour strength developed; (3) the size of the largest particles remaining incompletely dispersed. As mentioned earlier, optimum colour strength is achieved with a mean particle size of the order of 0.1mm or less. The pigment particles are of various shapes, most commonly brick, rod or plate, with the minor dimension usually in the range 0.02 to 0.05 micron. The particle shape should be such that area of contact between particles is minimised. This requires an open aggregate structure with predominant edge-to-edge or edge-to-face contact of crystals, so that the area of contact is minimised (Mackay, 1988).

Good dispersibility can also be achieved by using additives which reduce aggregation/agglomeration of the pigment crystals during pigment manufacture. There are two stabilising methods which are known to prevent particles in a dispersion from reaggregating. One depends on the lowering of the polarity of crystal surfaces thereby reducing the strength of interaction at the areas of contact. The other depends on the adsorption of long chain molecules of a surfactant onto the surface of the particles to give an opposing force (Carr, 1978).

A flocculate can be distinguished from an agglomerate as a comparatively unstable association of particles in the dispersion medium that can be broken up into individual components by intensive stirring. Flocculation impairs the stability

of dispersions and is responsible for many undesirable changes, such as shift in hue. Flocculation phenomena are related to particle size. The smaller the particles, the larger their specific surface area and thus the greater the tendency to flocculate.

Brightness or gloss is the visual impression of reflected light. A review of the various factors affecting and the methods used to measure this phenomenon are presented in Lewis, (1982). As a general rule, pigment particles with dimensions greater than 0.3μm may cause a substantial reduction in brightness regardless of whether they are crystals, agglomerates or flocculates.

Other properties of the pigments which are affected by the physical characteristics of the pigmentary particles include the fastness to light and weathering and rheology.

1.4 Industrial preparation of halogenated copper phthalocyanine pigments and their properties

There are several processes involved in the production of copper phthalocyanine on an industrial scale. This section describes the major processes involved. However, due to the commercial importance of this product precise details of the processes have been omitted. The first stage is the production of the initial 'crude' copper phthalocyanine. Many variations of processes for manufacturing CPC have been developed (Moser & Thomas, 1983). The pigments analysed in this work were produced from a crude CPC manufactured using the "Phthalic Anhydride - Urea Process". Details of this process can be found in Moser & Thomas, 1983. The second stage is halogenation in which some or all of the outer 16 hydrogen atoms of the CPC molecules are substituted with halogen atoms. As discussed in section 1.2, the shade of pigment depends on the number and type of halogens used. In the blue and green colour areas no other

class of pigment can compete in terms of cost, tinctorial strength, brightness of shade and fastness properties. The crude copper phthalocyanine is added to an aluminium chloride - sodium chloride melt to which chlorine and or bromine is added. The melt is heated further, poured into water and filtered to remove the $AlCl_3$ and NaCl. This forms an intermediate paste consisting of large particles in the range 0.5μm to 50μm, with mean dimension ~5μm. Since the optimum dimensions for a pigment particle are ~50nm (Brockes, 1964), the strength of the intermediate is low. In an attempt to alter the pigment size to a value closer to the minimum, the intermediate is subjected to a pigmentation process. Again, there are various methods which can be used to convert the halogenated CPC to the pigment form. One pigmentation method used, and the one used in the manufacture of the pigments analysed in this work, involves the intermediate being reslurried with various solvents in the presence of surfactants. This leads to lattice expansion and internal disruption of the intermediate material, resulting in the larger particles being split at weaker areas where defects are present. The process yields a large number of pigmentary particles of roughly the optimum particle size. The final stage involves washing the pigments in water and dilute sulphuric acid to remove any impurities which may have been introduced. The surfactant reduces agglomeration on drying and increases dispersion in the application medium. By varying the amounts of solvent and surfactant, pigments for use in different application media are produced. Another method of pigmentation involves milling the intermediate with some form of salt. This is thought to produce a better pigment, however, the process is much more costly.

Since the production of CPC pigments is a batch process, the object for manufacturers is to be able to reproduce the properties for each batch of nominally the same pigment. Unfortunately industrial preparation does not always meet this requirement, with variations in both the strength and shade of the final pigment arising from nominally identical conditions. Manufacturers are also aware that different drying conditions can affect the properties of the pigments

but are unaware of how this occurs. Thus, there is considerable incentive for investigating the factors which determine the size, shape and composition of the pigmentary particles, in an attempt to explain how the observed variations can arise.

1.5 Introduction to electron microscopy

It was mentioned in the introduction that the spatial resolution required to investigate the internal structure of CPC pigments can be provided by the electron microscope. The aim of this section is to give a brief introduction to the diffraction and imaging techniques available in both the conventional transmission electron microscope (CTEM) and the scanning transmission electron microscope (STEM).

As its name implies, the transmission electron microscope is used to obtain information from samples which are thin enough to transmit electrons. The transmitted electrons are generally used to form either an image or a diffraction pattern of the specimen. The diffraction pattern is formed in the back focal plane of the objective lens. A magnified version of this can be transferred to the final viewing screen by subsequent lenses. There are two methods which can be used to define the area of the specimen from which the diffraction pattern originates. The electron beam can be altered to the required dimension or an area defining aperture can be inserted in a plane conjugate to the specimen. The probe or aperture position can then be adjusted to select the area of interest. Both techniques are described in greater detail in chapter 2. The diffraction pattern from a single crystal structure consists of a simple array of bright spots. The information available in the diffraction patterns can be used to determine the crystal system and lattice type, the orientation of the atomic array and any defects from the perfect crystal structure. Further details of the information available

from the diffraction patterns is given in chapter 2. The results of diffraction studies of halogenated CPC materials are presented in chapter 3.

There are two fundamentally different ways of obtaining images of samples in the electron microscope. The first involves the use of an aperture in the back focal plane which allows only one electron beam to contribute to the image. Contrast in the images arises from diffraction contrast i.e. scattering of electrons outside the aperture. The second method involves the use of an aperture which allows the direct beam and a number of diffracted beams to contribute to the image. In this way periodic information such as lattice images can be obtained. Lattice images provide information on the crystalline structure of the pigmentary particles. The theory of imaging in the CTEM and STEM is described in chapter 3. The major disadvantage of STEM lattice imaging is the inefficient use of electrons. More specifically, the larger dose to which the specimen must be subjected, to achieve images comparable with those in the CTEM, is problematic when investigating beam sensitive materials. For this reason novel detector systems have been developed which allow lattice images to be recorded. A new technique based on the differential phase contrast (DPC) mode of microscopy, is one which is particularly well suited to recording lattice images from CPC materials. The theory of the technique is described in chapter 4. The advantages of this technique are not only its efficient use of electrons but also it allows both lattice and topographic images to be recorded simultaneously. Lattice images recorded using the CTEM are presented in chapter 3 and those obtained using DPC are presented in chapter 4. One of the main difficulties in recording lattice images is that of radiation damage. This process is discussed further in section 1.7.

1.6 Elemental analysis in the electron microscope

It has been emphasised throughout this chapter that the colour of a pigment is highly dependent on its chemical composition. In particular, the shade of the pigment depends on the halogen content of the molecules. There are various techniques which can be used to determine the halogen content. A technique which has been used by McColgan et al. (1990) is energy dispersive X-ray (EDX) analysis. When electrons interact with a specimen, X-rays will be generated. If the energy of the incident electrons is high enough to eject inner-shell electrons, electrons with a characteristic energy loss will be generated and characteristic X-rays will be emitted from the ionised atom as an outer shell electron falls into the inner shell vacancy. Another technique which measures the energy lost by the electrons transmitted through the specimen is electron energy loss spectroscopy (EELS). The characteristic energy losses give rise to edges which lie on a background. These edges can be measured to determine the chemical composition of the specimen. In this project EELS analysis of CPC pigments was performed using a parallel detection system. The theory of parallel electron energy loss spectroscopy (PEELS) is presented in more detail in chapter 5. The advantages of this technique over EDX are the much higher spatial resolution and the ability to measure the signal from low atomic number elements. Indeed, initial estimates suggest that it should be possible to analyse a single pigment particle with dimensions ~50nm. Thus it may be possible to measure compositional variations from particle to particle.

The interaction of the electron beam with the CPC pigments results in the breaking of chemical bonds, leading to loss of the peripheral halogen atoms as a result of diffusion. To obtain accurate analysis, from areas as small as a single pigment particle, requires reducing the rate of halogen loss from the specimen. The technique used to record PEELS spectra, including additional hardware designed to reduce radiation damage during experimental set-up, are described in

chapter 5. The results of the PEELS analysis of highly chlorinated CPC pigments are also presented in chapter 5.

1.7 Radiation damage in CPC pigments

The application of electron microscopy to the study of organic materials is severely limited by the damage induced in the specimen by the electron beam. This is particularly true for high resolution electron microscopy. In this section the mechanisms for radiation damage in CPC pigments is discussed. This is not intended to be an exhaustive discussion and further details of the processes involved and the measurements made of radiation damage can be found in numerous publications including : Reimer, 1960; Murata et al., 1977; Murata, 1978; Fryer, 1984.

There are two distinct ways in which an electron can interact with a specimen, these being elastically and inelastically (Isaacson, 1977). In the first process the electron interacts with the atomic nuclei. In this case no, or virtually no, energy is lost by the electron and it provides structural information without damage to the specimen. In inelastic scattering the electron interacts, primarily but not exclusively, with the orbital electrons. Due to their identical masses the process involves large energy transfers which result in molecular excitation and, in certain cases, ionisation. A consequence of this process, particularly in organic materials, is damage induced in the specimen by the electron beam. The results of this damage are destruction of crystallinity and mass loss which become more pronounced as irradiation continues.

Various methods have been used to investigate radiation damage in organic materials. These methods fall into two categories; those which are in-situ measurements and methods applied after an electron pre-irradiation. The dose value most commonly used to quantify the damage is $D_{1/e}$, which corresponds to

a reduction in the signal intensity to 1/e of its initial value. This is often referred to as the critical dose. In-situ methods which have been used to investigate radiation damage in CPC pigments include measuring the fading of electron diffraction patterns. Measuring dose values for disappearance of the high and low order diffraction spots provides information on the dose sustainable by the specimen before structural disorder occurs (Clark et al., 1980). These investigations found the critical dose for a fully chlorinated CPC pigment to be ~60Ccm^{-2}. Another method used to investigate the damage mechanism in CPC involves observing the fading of contrast in lattice images (Smith et al., 1986; Murata et al., 1977). In both methods the radiation damage mechanism was strongly dependent on the specimen environment and could be explained in terms of an encapsulation or "cage" effect. This suggested that a molecule could only be damaged if its nearest neighbours were damaged, thus allowing diffusion of the large chlorine atoms. Other in-situ methods which have been used to measure radiation damage in organic materials are EDX analysis and EELS. Clark (1979) used EDX to measure the rate of chlorine loss from specimens of highly chlorinated CPC pigments. In a fully chlorinated sample of CPC pigment ~20% of chlorine was lost after a dose of ~100Ccm^{-2}. Whilst for a material with an average of ~14.5 Cl atoms/molecule ~40% of chlorine was lost after an equivalent dose. Investigations by Kobayashi et al. (1982) using EELS found that at the stage of damage where the diffraction spots from the crystal disappeared, ~75% of the chlorine still remained. With further irradiation all the chlorine disappeared after a total dose of ~100Ccm^{-2}. The critical dose for a variety of organic specimens is presented in table 1.1. Methods used to measure radiation damage, after electron pre-irradiation, including electron spin resonance and nuclear magnetic resonance are described in Reimer, 1985.

It is clear that if reliable information on specimen structure or composition is to be obtained, it is necessary to reduce the electron dose to a value less than a certain value which is determined by the amount of damage that can be tolerated

Material	$D_{1/e}$ (Ccm^{-2})	E (keV)	Method	Reference
Amino Acids				
Glycine	$1.5x10^{-3}$	60	ED	Reimer (1960)
l-Valine	$1.5x10^{-3}$	80	ED	Glaeser (1971)
Aliphatic hydrocarbons				
Paraffin	$3\text{-}5\ x10^{-3}$	60	ED	Reimer (1960)
Polyvinylformal	10^{-2}	100	ED	Bahr et al. (1965)
Bases of nucleic acids				
Adenosine	10^{-2}	80	ED	Reimer (1978)
Cytosine	$4x10^{-2}$	20	EELS	Crewe et al. (1970)
Aromatic compounds				
Anthracene	$6\text{-}8\ x10^{-2}$	60	ED	Reimer (1960)
Coronene	$5x10^{-2}$	100	ED	Siegal (1972)
Phthalocyanine	10^{-1}	100	ED	Reimer (1960)
Cu Pc	0.8	100	EELS (N_2 loss)	Egerton (1979)
Cu Pc	1-2	100	ED	Reimer (1960)
Cl_{16}Cu Pc*	25-35	100	ED	Uyeda et al. (1972)
Cl_{16}Cu Pc*	60	100	ED	Clark (1979)

Table 1.1 Characteristic doses for several organic materials and experimental techniques

NOTES ED electron diffraction; EELS electron energy loss spectroscopy
*complete fading of diffraction pattern

without affecting the accuracy of results required. A consequence of the dose constraints is that to obtain information pertaining to the undamaged material the smallest possible electron dose should be used. This requires that exposure outwith image acquisition or data accumulation should be kept to a minimum. Experimental techniques have been employed in this work in an attempt to meet these requirements. These include scanning the material at low magnifications to select suitable areas to be investigated, performing focusing and astigmatism corrections on areas nearby and only switching to the area of interest when the image or data are to be acquired.

1.8 Specimen Preparation

There were two methods of sample preparation of highly chlorinated CPC's used in this project. The first of these forms epitaxial films of the pigments by vacuum evaporation onto an alkali halide substrate. The CPC powder was evaporated from a molybdenum boat which had a top cover made from a folded over piece of molybdenum, with holes pierced along its centre. The holes in the top cover prevent the powder from jumping out of the boat on initial heating. Firstly the boat was placed in an evacuation chamber, evacuated to ~$2x10^{-1}$Torr, and heated till white hot in order to clean it. The chamber was then let up to air and a small amount of the CPC powder was placed in the boat. A single crystal of KBr was cleaved in air and immediately placed in the evacuation chamber, about 4 inches above the boat. The evacuation chamber was then evacuated to ~10^{-5}Torr. The substrate crystal was baked out at ~350^{o}C for one hour. The substrate was then allowed to cool to ~220^{o}C, at which point the chlorinated CPC was evaporated from the boat onto the substrate. The temperature of the substrate is such that the molecules of CPC are relatively mobile and have a strong tendency to form an ordered base layer. Subsequent layers build up a perfect

crystal extensive in the a-b plane or molecular plane, and thin in the c-direction, corresponding to the column axis. From the small amount of powder placed in the molybdenum boat, films of thicknesses ~50nm were produced. Initially the films were floated off on distilled water and picked up on uncoated grids. However, these grids did not provide enough support for the films which would often break apart. Investigations of the elemental composition of the material required areas of films, which were unsupported, to be analysed. In order to provide enough support for the films and be able to analyse areas containing the films alone, lacey carbon films supported on 300 mesh nickel grids were used. Large areas of CPC film lay over large holes on the lacey carbon film and it was these areas which could be used for analysis.

In order to examine the physical properties of the pigment which affect its performance, it is necessary to use a preparation technique which presents the pigments as they would appear in their application medium. Fortunately chlorinated CPC's are insoluble in almost all solvents, apart from concentrated sulphuric acid. Thus the pigments may be dispersed in a liquid without it affecting its structure. The technique used was similar to that used by Drummond (1985) and McColgan (1990). A small amount of the CPC powder was mixed with a few drops of a dispersing agent, dispersol T, a sodium based dispersing agent supplied by Zeneca PLC. This mixture was then rubbed out several hundred times on a glass plate, using a flexible palette knife. During this process several drops of a 35% ethanol/water mixture were added periodically to prevent the mixture from drying out. The mixture was then further diluted in the ethanol/water mixture until a bright green transparent dispersion was obtained. The experimental apparatus used to produce specimens suitable for use in the electron microscope is presented in figure 1.2. The bright green dispersion was placed in a test tube and sealed with a rubber stopper. Spray tubes were prepared by extruding fine bore glass tubes. Nitrogen gas fed from a standard gas cylinder created a region of low pressure above the capillary tube, causing liquid to be drawn up the tube and

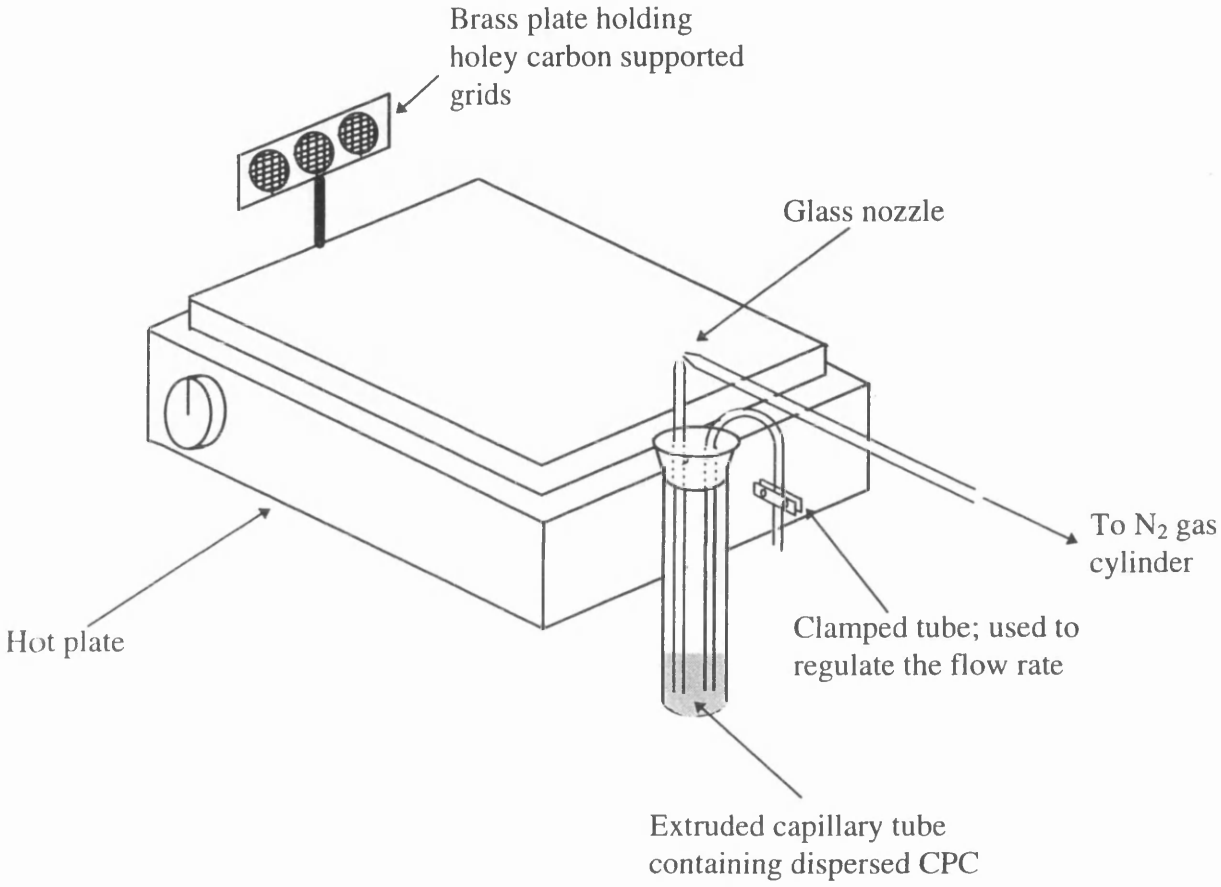

Figure 1.2: A schematic diagram showing the apparatus used to prepare the CPC specimens. During operation, the equipment was encased within a metal framed box with transparent walls and enclosed in a fume cupboard.

forming a spray. The emergent spray was directed across an electrical hot plate. The speed of the spray was adjusted to be as low as possible to allow the ethanol/water mixture to evaporate such that the dry dispersed powder impinged on the suitable prepared grids. A suitable particle density was achieved by placing filter paper behind the grids and continuing to spray until the filter paper achieved a light green shade. The grids used were 300 mesh copper grids covered by a layer of holey carbon. These are useful at low magnification for focusing and correcting astigmatism. Whilst, at high magnifications, the contrast of the carbon film itself provides a more accurate test.

Chapter 2

INSTRUMENTATION AND THE THEORY OF DIFFRACTION AND IMAGE FORMATION IN THE ELECTRON MICROSCOPE

2.1 Introduction

The effects of the interaction of a high energy electron beam with a thin specimen were described in the previous chapter. There are two main scattering processes, elastic scattering and inelastic scattering which can result in damage to the specimen. The information obtained from electron microscopical techniques is derived from these scattering processes. This chapter gives a review of the major features and basic principles of the operation of the CTEM and STEM used in this project.

A brief description of the essential components of the CTEM is presented in section 2.2 and includes the instrumentation which allows the CTEM to be operated in scanning transmission mode. The formation of an electron diffraction pattern in the CTEM and the information available from the diffraction patterns are described in sections 2.3 and 2.4, respectively.

The formation of an image in the CTEM is detailed in section 2.5. It is shown that the propagation of an electron beam from the exit surface of the

specimen through the imaging system can be described by a linear transfer theory. The transfer function includes the effects of lens aberrations and defocus and can be extended to include the effects of energy spread and finite source size.

The major components of the STEM are described in section 2.6. In section 2.7 it is shown that, under certain restrictions, based on the reciprocity principle, STEM images will be the same as images in CTEM. However, to record STEM lattice images with comparable contrast and signal to noise as CTEM lattice images requires a considerably greater electron dose. This is a problem when the specimen is radiation sensitive.

2.2 The Conventional Transmission Electron Microscope

A schematic diagram of the JEOL JEM 1200EX conventional transmission electron microscope (CTEM) is shown in figure 2.1. At the top of the microscope is the electron gun which uses a tungsten hairpin cathode. This is a wire filament 0.1 - 0.2mm in diameter bent like a hairpin with a V-shaped tip that is ~ 100μm in diameter. The electrons are emitted thermionically by passing a current directly through the filament wire. At the filament operating temperature electrons leave the filament tip and are accelerated to ground by a large negative potential between the cathode and anode. Surrounding the filament is a Wehnelt cylinder with a circular aperture centred at the filament tip. The Wehnelt cylinder is biased negatively with respect to the cathode. The effect of the electric field formed in such a gun configuration, causes the emitted electrons to converge to a crossover. To avoid the formation of tungsten oxides the filament and its surrounding Wehnelt are kept under vacuum. A more detailed explanation of the behaviour of the gun assembly can be found in Haine (1961).

The next component is the condenser lens system, the purpose of which is to control the area of irradiation and the divergence of the electron beam.

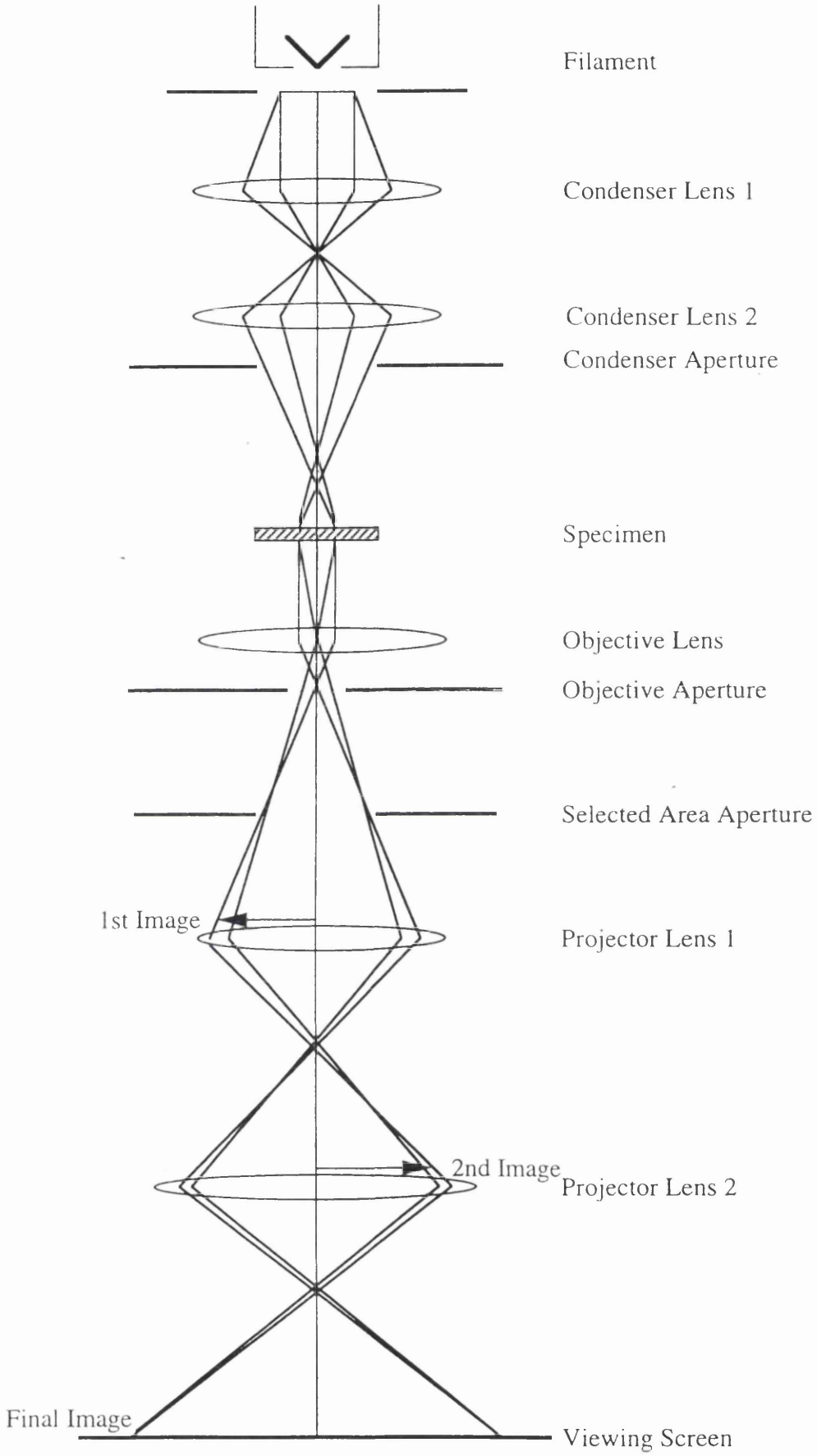

Figure 2.1 : Schematic diagram of a CTEM

The condenser lens C1 forms a demagnified image of the gun crossover . C2 then forms a demagnified image of the crossover at, above or below the specimen plane, depending on the illumination required. The demagnifying factor of the combined lenses produces submicrometer probes at the specimen. The variable condenser aperture ensures highly parallel coherent illumination is incident on the specimen.

The objective lens forms the diffraction pattern in its back focal plane and the first intermediate image. The design and aberrations of this lens determine the resolution and contrast in the final image. The effect of aberrations on the image transfer are considered in section 2.5.

The objective aperture, situated in the back focal plane of the objective lens, defines the angular range of scattered electrons reaching the image plane. In this way, the contrast in the final image is controlled. The size and position of the aperture determines the nature of the contrast. The contrast is increased by reducing the size of the aperture. If the aperture is centred about the optic axis electrons scattered through an angle greater than α, as shown in figure 2.1 do not contribute to the final image. This is referred to as diffraction contrast. Regions of the specimen which are thicker, scatter more strongly and appear darker in the image. For a fuller explanation of diffraction contrast the reader is referred to Hirsch et al., 1965. For high resolution imaging, the aperture should be as large as possible to allow high spatial frequencies to pass through and contribute to the image. Alternatively, the aperture may be positioned to exclude all beams except a particular diffracted beam of interest.

The three remaining lenses are the projector lenses. The first projector lens, also known as the intermediate lens, can usually be switched between two settings. In the image mode it is focused on the image plane of the objective lens. The remaining two projector lenses control the magnification of the image on the viewing screen. In the diffraction mode the intermediate lens is focused on the back focal plane of the objective lens and the diffraction pattern is projected on to

the viewing screen. The magnification of the diffraction pattern is controlled by the projector lenses and is described in terms of an the effective camera length of the system.

The final component of the microscope is the recording device. In the CTEM this is usually a photographic plate but increasingly low light level cameras are being used to display the image. The image can then be transferred to a computer for real time or subsequent image processing.

The JEOL 1200EX can also be operated in scanning transmission mode. In this mode very small electron probes, ~2-5nm in diameter, can be formed by means of a three-stage condenser lens system, the last lens of which is the objective pre-field in front of the specimen. A schematic ray diagram of this mode in the CTEM is presented in figure 2.2. The electron probe can be scanned across the specimen plane by means of pairs of scanning coils which rock the incident electron beam. If the pivot of this beam rocking is at the front focal plane (FFP), the pivot point of the rays behind the specimen will be at the back focal plane (BFP) because these planes are conjugate. Thus the position of the first diffraction pattern in the BFP is stationary and the diffraction pattern can be imaged on the detector plane. The generator that produces the saw tooth currents for the deflection coils simultaneously deflects, in synchronisation, the electron beam of a cathode ray tube (CRT). The intensity of the CRT beam can be modulated by any of the signals that can be obtained from the electron-specimen interactions. In the 1200EX, these include transmitted electrons, back-scattered electrons and secondary electrons. The main advantage of the STEM attachment, in this project, is the formation of a very small electron probe with which microdiffraction can be performed on very small areas.

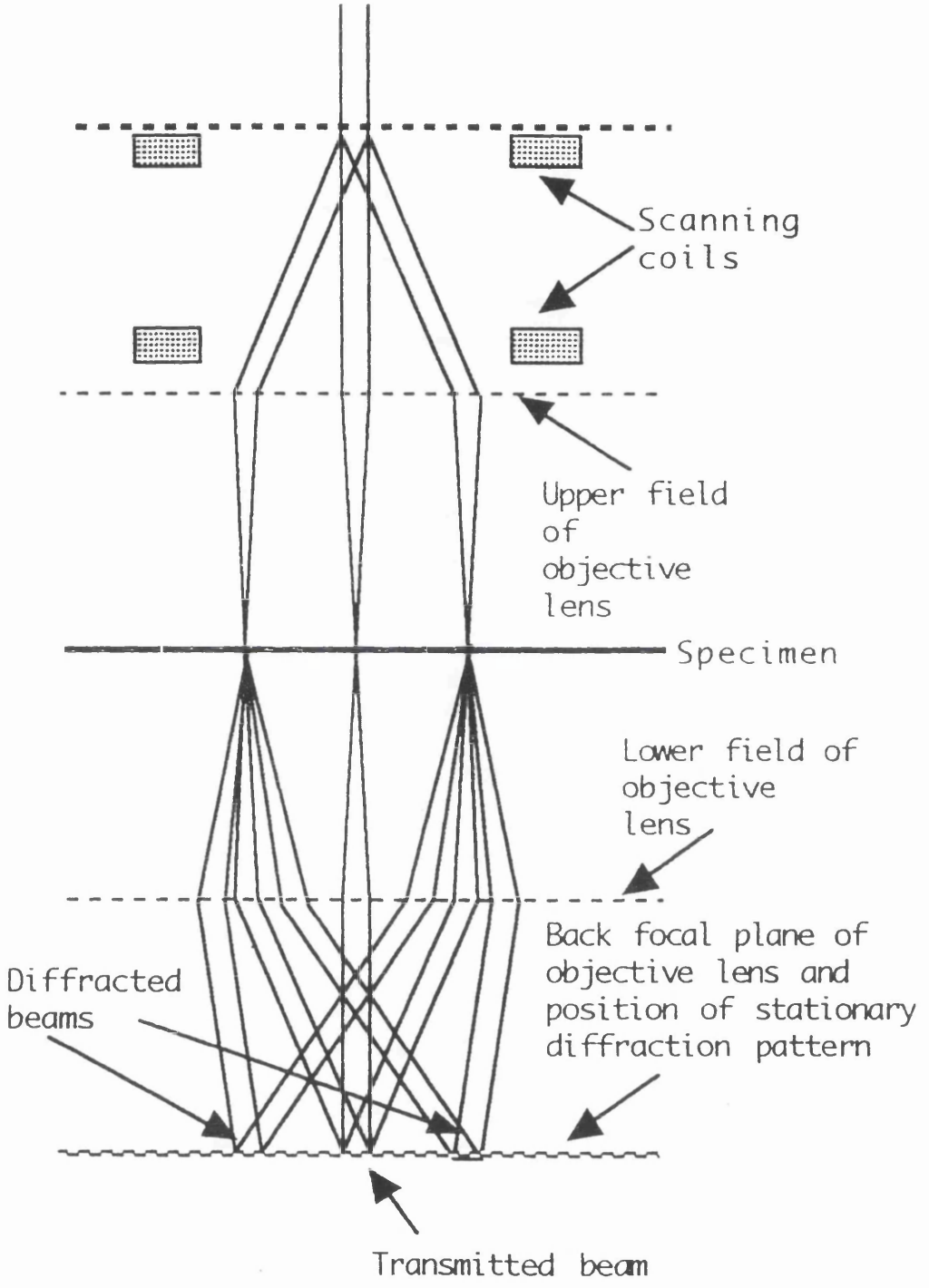

Figure 2.2: Schematic diagram of the principles of STEM image formation in the CTEM.

2.3 Diffraction in the electron microscope

A beam of electrons incident on a crystalline specimen is scattered by a set of suitably oriented lattice planes according to Bragg's Law. The scattered and unscattered beams are then focused by the objective lens to form a diffraction pattern in its back focal plane. The intermediate and projector lens system can be used to project either the image or the diffraction pattern on the viewing screen. Ray diagrams showing the formation of an image and a diffraction pattern are presented in figure 2.3.

It is possible to limit the size of the area from which the diffraction pattern is obtained. This is achieved by inserting the intermediate selected area diffraction (SAD) aperture at the first intermediate image plane. Figure 2.4 shows a schematic ray diagram of the SAD mode. A diffraction pattern from the total illuminated area is formed in plane C and the first intermediate image of the area is produced at D. An aperture is inserted in this plane thus limiting the rays which pass further down the column. The diffraction pattern at F is formed using only electrons from the selected area. The typical sizes of the SAD aperture range from 10-50μm giving a minimum selected diameter at the specimen of ~0.2μm. However, the electron lenses are not perfect and the main source of error in SAD is a result of spherical aberration of the objective lens (Agar 1960, Phillips, 1960 and Reicke, 1961). Spherical aberration has the effect of reducing the focal length of the electron beam passing through the outer regions of the lens. Thus if the image of the specimen formed using the unscattered beam is brought to focus in the plane of the SAD aperture, the image formed using the diffracted beam is brought to a focus in a plane some distance above this aperture. Thus the same points on the aperture plane are formed by transmitted and diffracted electrons from slightly different areas of the specimen and the value of the displacement is given by

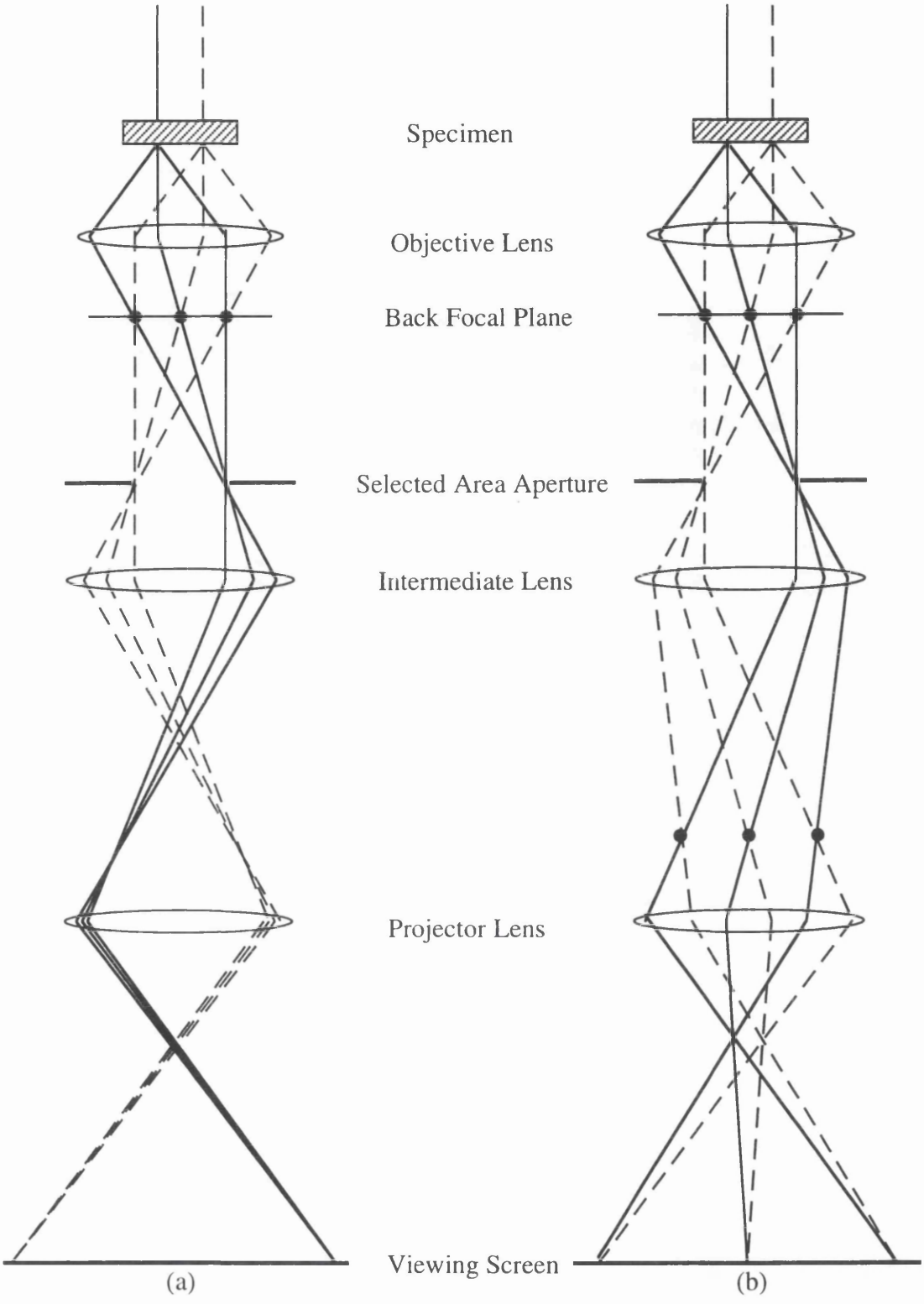

Figure 2.3 : Schematic ray diagram for a CTEM operated (a) for imaging and (b) for selected area diffraction.

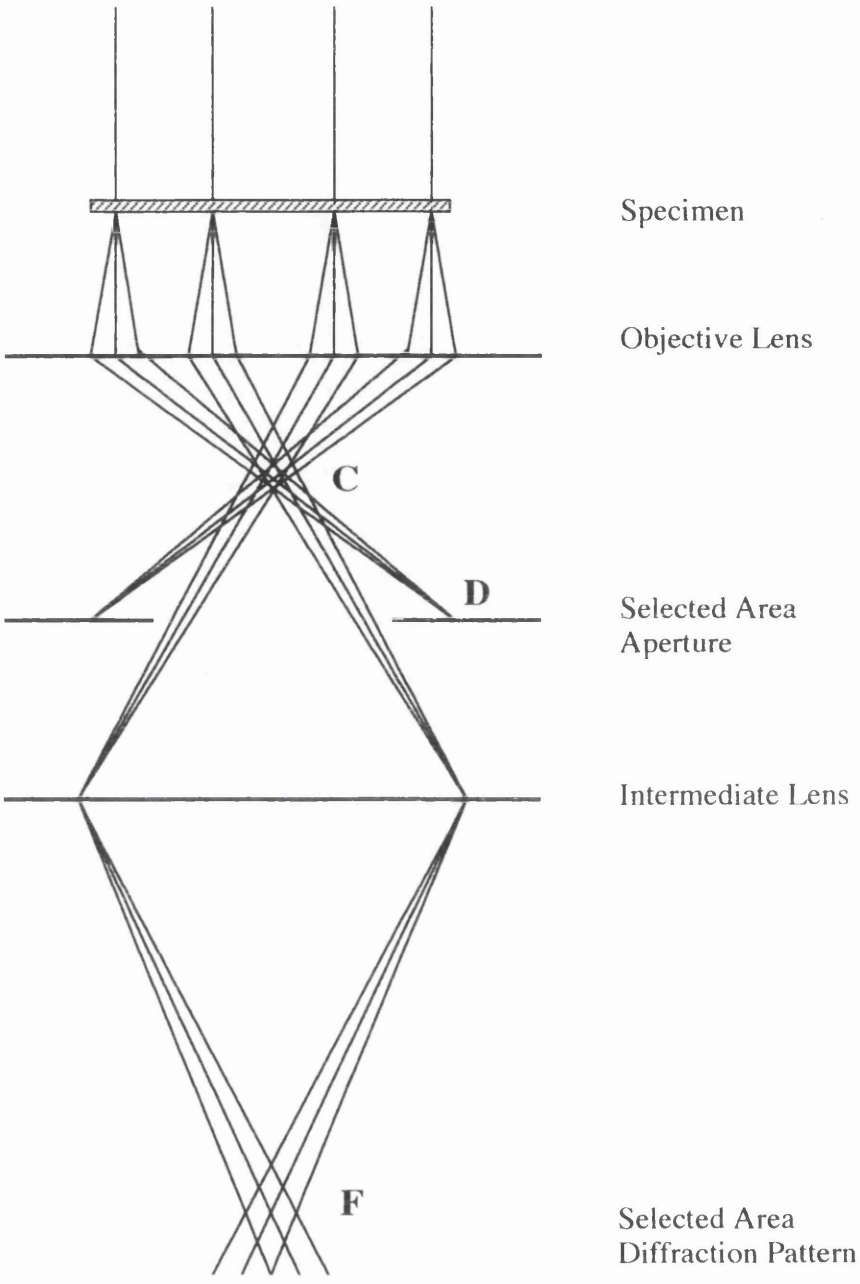

Figure 2.4 : Ray diagram for selected area electron diffraction.

$$d = MC_s \theta^3 \tag{2.1}$$

where M is the magnification , C_s the spherical aberration coefficient and θ the scattering angle.

A schematic diagram showing diffraction from a crystalline specimen is shown in figure 2.5. The incident beam is scattered through an angle $2\theta_B$ and a diffraction spot is formed a distance D from the optic axis. From simple geometry

$$tan(2\theta_B) = \frac{D}{L} \tag{2.2}$$

where L is the camera length. Braggs law states that

$$2dsin\theta_B = \lambda \tag{2.3}$$

Since the Bragg angle is small both $sin\theta_B$ and $tan\theta_B$ can be approximated by θ_B giving

$$2\theta_B = \frac{D}{L} \quad \text{and} \quad 2d\theta_B = \lambda$$

$$\Rightarrow \frac{\lambda}{d} = \frac{D}{L}$$

$$\Rightarrow Dd = \lambda L \tag{2.4}$$

If the values of D, λ and L for a particular diffraction pattern can be measured the d-spacing of the set of lattice planes can be determined.

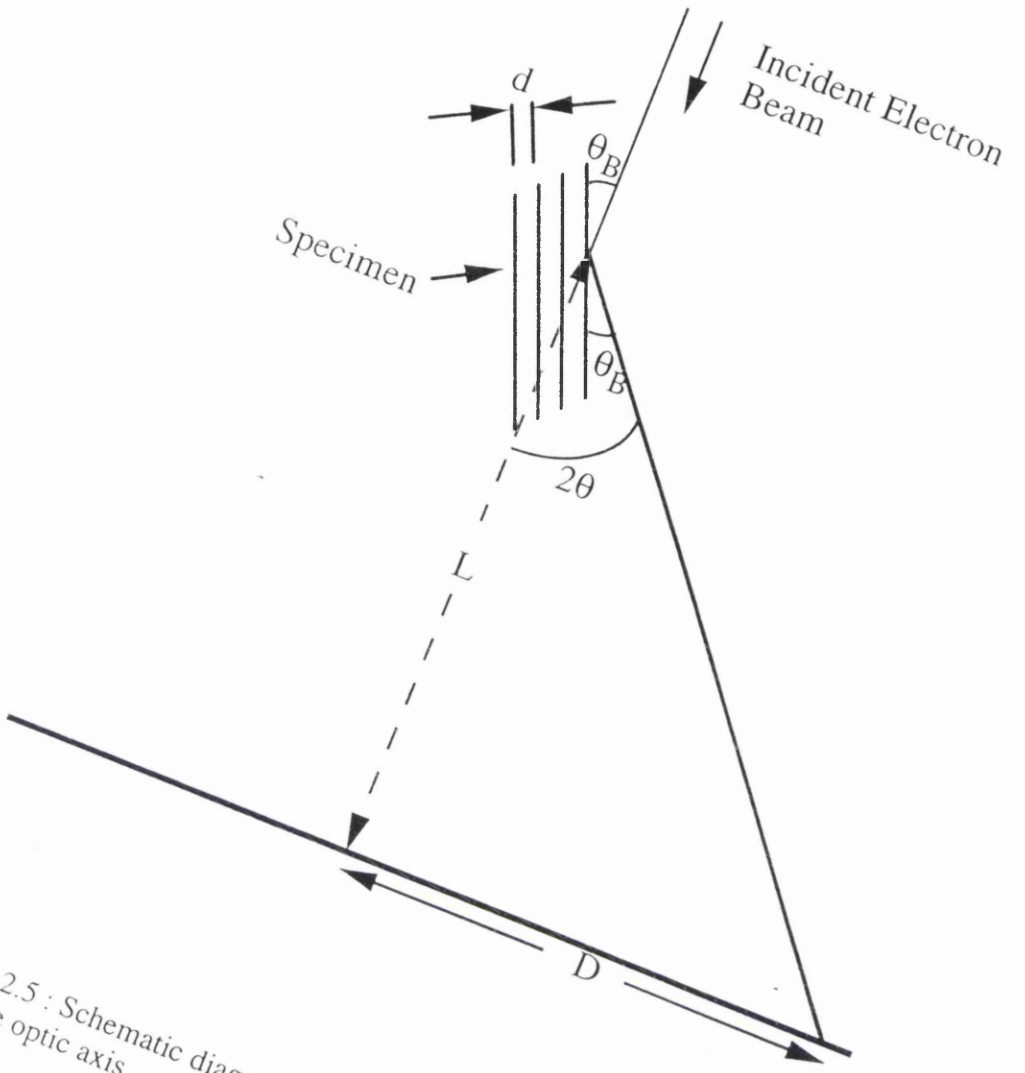

Figure 2.5 : Schematic diagram showing distance of a diffraction spot from the optic axis

2.4 Information from electron diffraction patterns

For a thin perfect crystal the electron diffraction pattern is directly related to the crystal structure. For a single crystal specimen the position of the diffraction spots are a function only of the crystal lattice. Indexing of the spot patterns allows the various lattice plane spacings and the orientation of the crystal to be determined. The structure factor provides a useful guide to the intensity of the spots, although exact intensities will depend on crystal geometries and dynamical, rather than kinematic, effects. The structure factor is obtained by adding together the amplitudes of waves scattered by atoms at different points in the unit cell and finding the resultant (Andrews et al., 1971). The atomic separations and hence the extent to which waves are scattered by any two atoms are out of phase with each other, must be taken into account. The structure factor determines that certain reciprocal lattices have systematic absences, that is, zero intensity. These systematic absences must be determined to characterise the structure of the lattice.

Changes in the position, shape and intensity of the diffraction spots provide information on deviations from perfect crystallinity. For example, if the crystal is distorted or bent, the spots will be spread into arcs or the intensities will be changed. If the atoms are disordered on the lattice sites, there will be diffuse scattering in the background between the spots. Extra spots or streaked patterns can indicate stacking faults or a twinned structure.

2.5 Image Formation in the CTEM

In the case of thin weakly scattering specimens the kinematic or single scattering theory of image formation can be applied. The formation of an image can be thought of as a two stage process based on the Abbe theory in light optics.

The first stage is the formation of a diffraction pattern in the back focal plane of the lens by a Fourier transform operation. The second stage is a further Fourier transform operation in which the diffracted beams are recombined to form the image.

For a thin weakly scattering specimen, the effect of the specimen on an incident electron wave $\psi_o(xy)$ is represented by a transmission function $q(xy)$. The diffraction pattern amplitude at the back focal plane of an ideal lens is given by

$$\Psi_e(\mathbf{uv}) = Q(\mathbf{uv})^* \Psi_O(\mathbf{uv}) \tag{2.5}$$

where $(\mathbf{uv})$ are coordinates in reciprocal space and Q and Ψ_O are the Fourier transforms of q and ψ_O, respectively. For a thin specimen the transmission function represents a change of phase of the incident wave by an amount proportional to the potential distribution in the beam direction

$$q(xy) = exp\left[-i\sigma\phi(xy)\right] \tag{2.6}$$

where $\phi(xy) = \int \phi(\mathbf{r})\, dz$ the projection of the Coulomb potential distribution in the beam direction and σ is the interaction constant given by $\sigma = \pi/\lambda V$ where V is the accelerating voltage. For a weak phase object the assumption $\sigma\phi(xy) << 1$ gives the single scattering approximation and the transmission function can be written as

$$q(xy) = 1 - i\sigma\phi(xy) \tag{2.7}$$

However, in a real lens not all the diffracted beams are brought back in the image plane with the exact phase relationships and the wave function in the back focal plane is given by

$$\Phi(\mathbf{uv}) = \Im q(\mathrm{xy}) \cdot T(\mathbf{uv}) \tag{2.8}$$

The transfer function, $T(\mathbf{uv})$, modifies the amplitude of the diffraction pattern in the back focal plane and is given by

$$T(\mathbf{uv}) = A(\mathbf{uv}) \exp[i\chi(\mathbf{uv})] \tag{2.9}$$

where, $A(\mathbf{uv})$,the aperture function, is zero outside the aperture and unity within it. The phase factor, $\chi(\mathbf{uv})$ includes the effects of defocus and spherical aberration and is given by

$$\chi(\mathbf{uv}) = \pi\Delta f\lambda(\mathbf{u}^2 + \mathbf{v}^2) + \frac{1}{2}\pi C_S \lambda^3(\mathbf{u}^2 + \mathbf{v}^2)^2 \tag{2.10}$$

The wave function given in equation 2.8 can thus be written as

$$\Phi(\mathbf{uv}) = [\delta(\mathbf{uv}) - i\sigma\Phi(\mathbf{uv})] \times A(\mathbf{uv}) \exp[i\chi(\mathbf{uv})] \tag{2.11}$$

where $\delta(\mathbf{uv})$ represents the transmitted unscattered beam and the remaining terms represent the real and imaginary parts of the scattered amplitude. The disturbance in the image plane is then given by

$$\psi(\mathrm{xy}) = [1 - i\sigma\phi(\mathrm{xy})] * \Im[A(\mathbf{uv})\cos\chi(\mathbf{uv}) + i\sin\chi(\mathbf{uv})] \tag{2.12}$$

Neglecting terms of second order in $\sigma\phi$ the intensity in the image plane given by

$$\begin{aligned} I(xy) &= \psi^{*}\psi \\ &= 1 + 2\sigma\phi(\mathrm{xy}) * \Im[A(\sin\chi(\mathbf{uv})] \end{aligned} \tag{2.13}$$

where φ^* is a complex conjugate and * denotes a convolution. Thus the image contrast, given by the deviation of the intensity from unity, is described directly as the projected potential smeared out by a spread function which describes the effects of defocus and lens aberrations.

Sinχ (**uv**) is known as the phase contrast transfer function (PCTF) and determines the transfer of information to the image plane. Maximum contrast over the widest range of spatial frequencies is achieved for sinχ (**u**)~1. The widest range is achieved by balancing the effects of spherical aberration and defocus. The value of optimum defocus is known as the Scherzer defocus (Scherzer, 1949) and is given by,

$$\Delta f = \left(C_s \lambda\right)^{1/2} \tag{2.14}$$

At the Scherzer defocus the optimum resolution attainable is given by (Eisenhandler & Siegal, 1966),

$$d_{min} = 0.66\left(C_s \lambda^3\right)^{1/4} \tag{2.15}$$

Figure 2.6 shows the PCTF for a range of defocus values applied to the JEOL 1200EX where C_s=1.8mm and λ=3.46pm. From equation 2.14 the optimum defocus is 900Å. In this case sinχ(**u**)~1 for a wide range of frequencies out to a maximum value $\mathbf{u}_{max}$ ~0.27. Above this frequency the PCTF passes through zero at certain points and for the corresponding value of **u**, no specimen information reaches the image. Negative values of the PCTF are also obtained in which case the maxima and minima in the image of a periodic structure are interchanged compared to those seen with positive phase contrast. At frequencies above $\mathbf{u}_{max}$ the PCTF is strongly modulated and the image is difficult to interpret, thus an objective aperture is used to cut-off higher spatial frequencies.

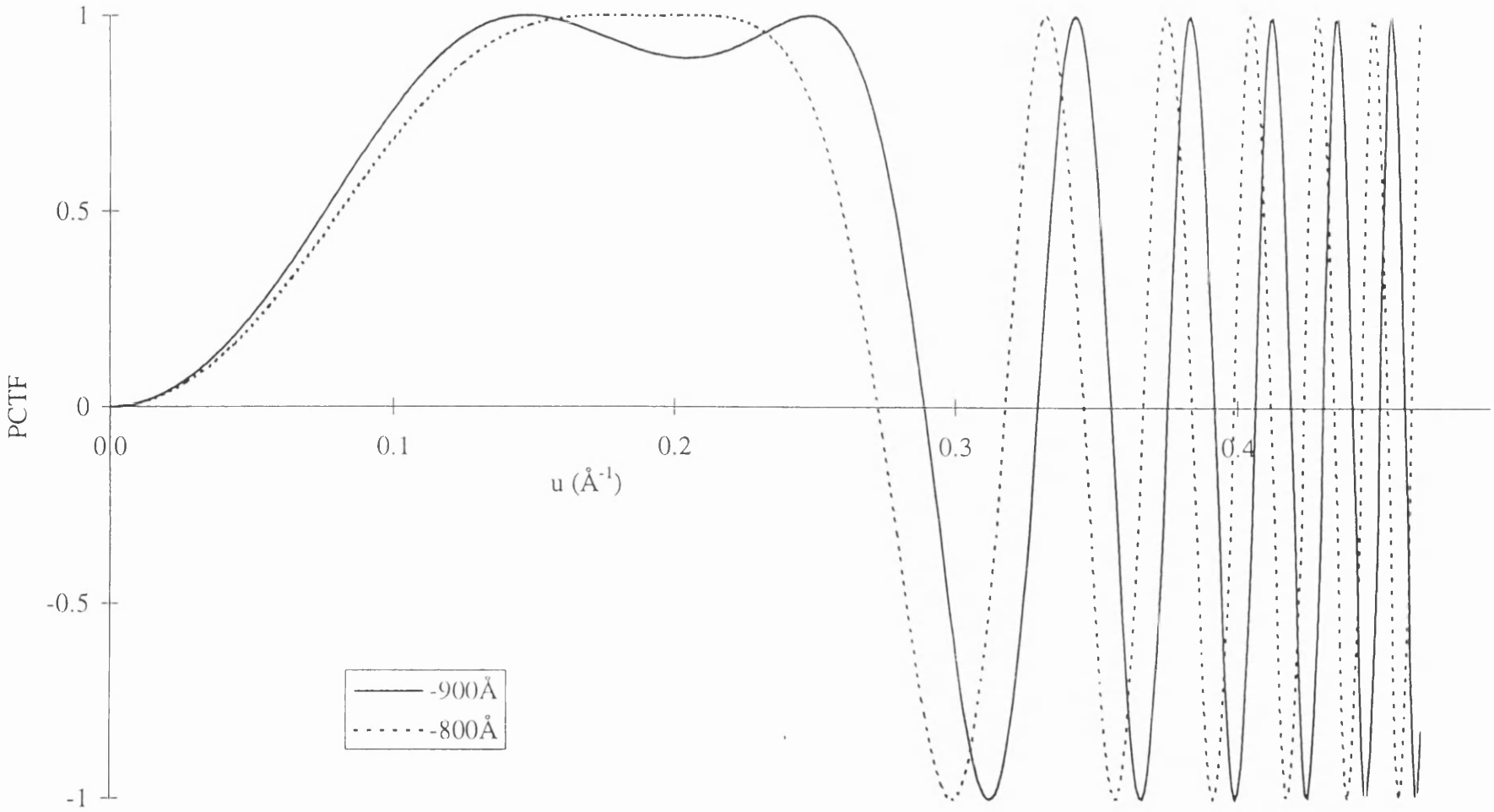

Figure 2.6 : Calculated phase contrast transfer functions for the JEOL 1200EX CTEM, with Cs=1.8mm, λ=3.46pm and defocus values of -800Å and -900Å.

It has been assumed that the electron beam is monochromatic and a point source i.e. perfect temporal and spatial coherence. However, in reality, the electrons are emitted with an energy spread ΔE and the electron source has a finite size. The variation of the electron energy ΔE and the variations of the accelerating voltage ΔV and lens currents ΔI result in variations Δf of the defocusing. The effects of electrons with different values of Δf on the transfer function can be included by multiplying the PCTF by an envelope function (Frank, 1973; Krivanek, 1976; Saxton, 1977). Humphreys and Spence (1980) showed that the damping due to chromatic aberration effects could be expressed as:

$$E_c = \exp\left(-\frac{\pi}{2}\lambda^2 C_c^2 Q^2 \mathbf{u}^4\right) \tag{2.16}$$

where

$$Q^2 = \left(\frac{\Delta(E)}{E}\right)^2 + \left(\frac{\Delta(V)}{V}\right)^2 + \left(\frac{2\Delta(I)}{I}\right)^2 \tag{2.17}$$

and C_c is the chromatic aberration coefficient. The effect of the envelope function is to damp the PCTF oscillation for increasing $\mathbf{u}$. Using typical values of $\Delta V/V = 2\text{x}10^{-6}$ and $\Delta I/I = 1\text{x}10^{-6}$ the envelope function for the JEOL 1200EX where C_c=2mm is shown in figure 2.7. The energy spread values of 1 and 2eV are typical for a thermionic cathode.

The effect of a finite electron source size and thus an illumination angle α_i is included by multiplying the PCTF by another envelope function given by

$$E_a = exp\left(-\pi^2 \alpha_i^2 \left(C_s \lambda^2 \mathbf{u}^3 + \Delta f\ \mathbf{u}\right)^2\right) \tag{2.18}$$

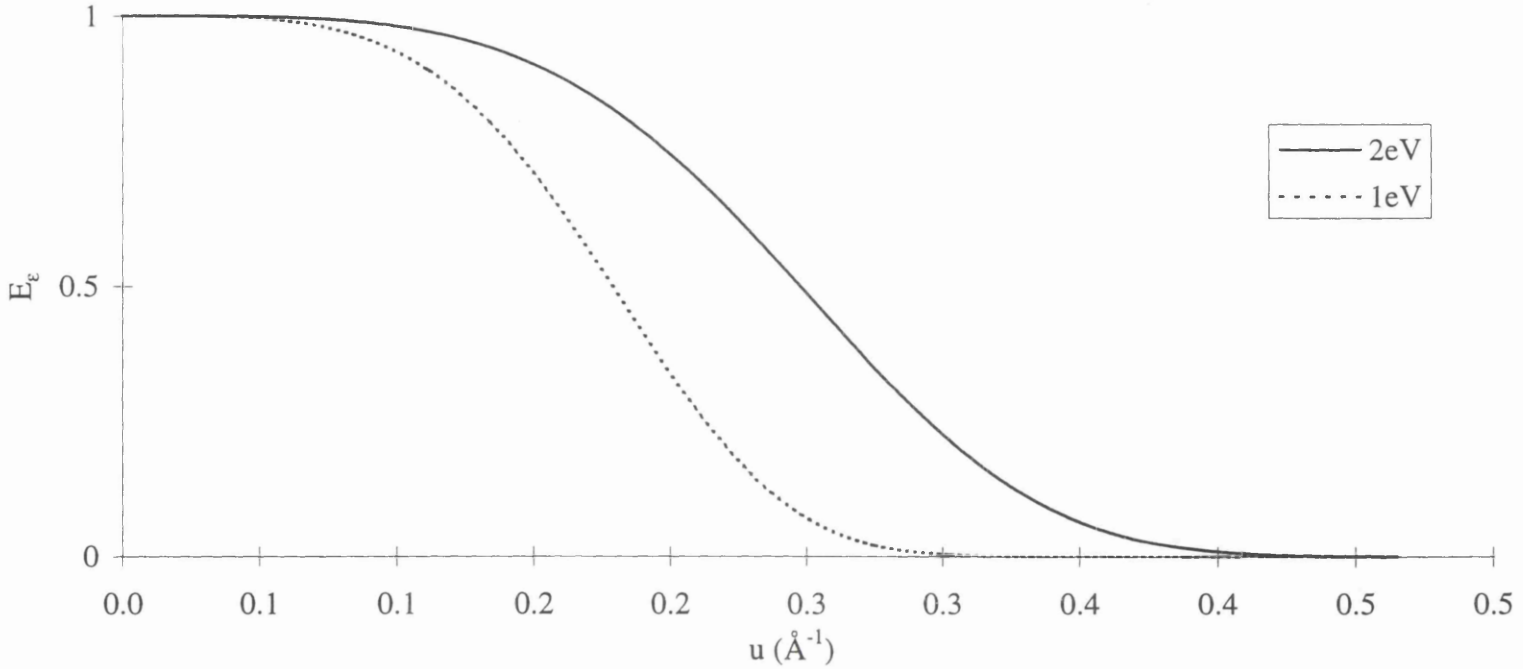

Figure 2.7 : Calculated chromatic envelope function with Cc=2mm for Δ=1eV and 2eV.

The envelope functions for the JEOL 1200 EX with α_i =1 and 2mrad are shown in figure 2.8. Again the PCTF is damped by the envelope function. Under the usual conditions in TEM of both a finite source and an energy spread the effective envelope function is a product of the envelope functions E_α and E_C, thus the modified transfer function is given by

$$T = \sin \chi E_\alpha E_C \tag{2.19}$$

Figure 2.9 shows the modified PCTF for the optimum defocus of ~900Å, α_i =1mrad and ΔE=1eV together with the unmodified function.

This description of image formation has used the simple phase-object approximation which has been shown to give significant errors for crystal thicknesses of ~20Å for 100keV electrons. A more reliable calculation of image formation must involve the use of a three-dimensional, many beam diffraction theory. The multislice formulation of Cowley and Moodie's (1957) dynamical theory divides the crystal into a number of very thin slices perpendicular to the beam. Each thin slice then acts as a thin phase object through which the beam is propagated in order to calculate the wave function at the exit face of the specimen. The resulting wave function is then propagated through the imaging system to determine the image intensities at the detector plane.

2.6 The Scanning Transmission Electron Microscope

The operation of the STEM can be considered to be the reverse of the CTEM instrument. In the STEM the objective lens forms a reduced image of the electron source at the specimen. Deflector coils scan the probe across the specimen thus the image is formed sequentially. The various signals resulting

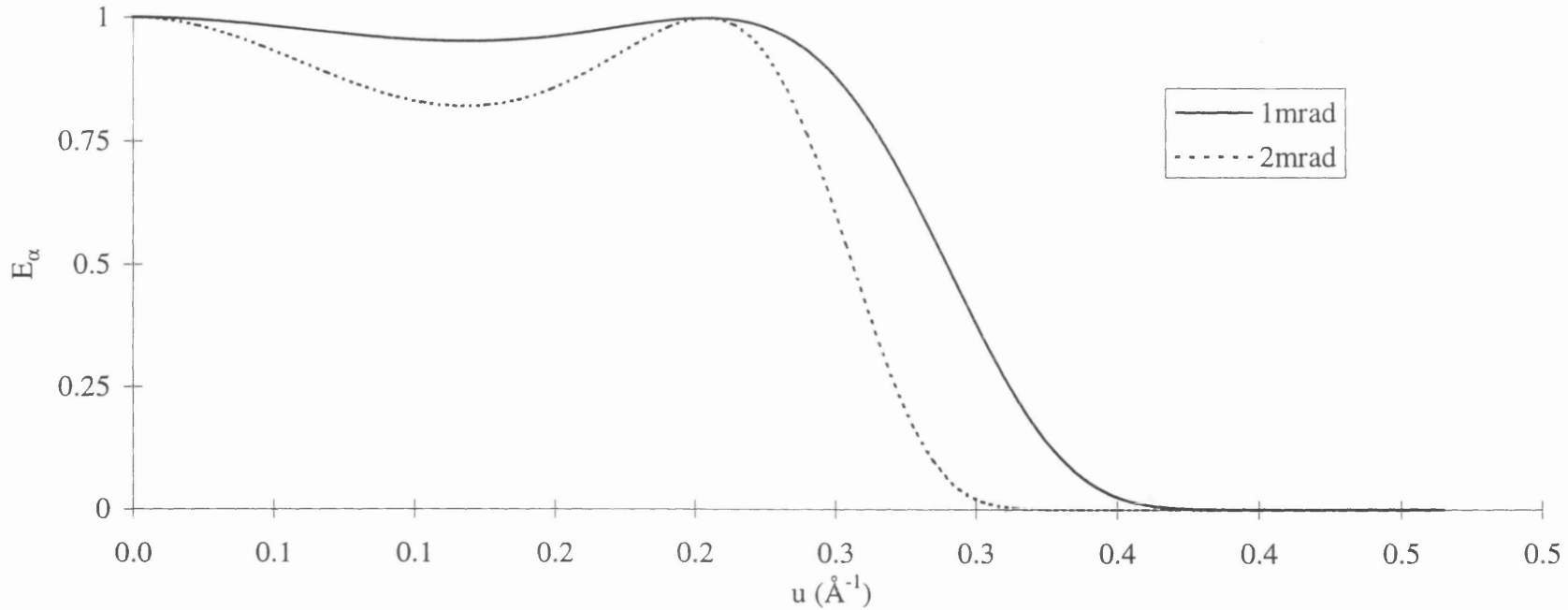

Figure 2.8: Partial coherence envelope function with Cs=2mm, Df=-900Å for specimen illumination angles α_c of 1mrad and 2mrad.

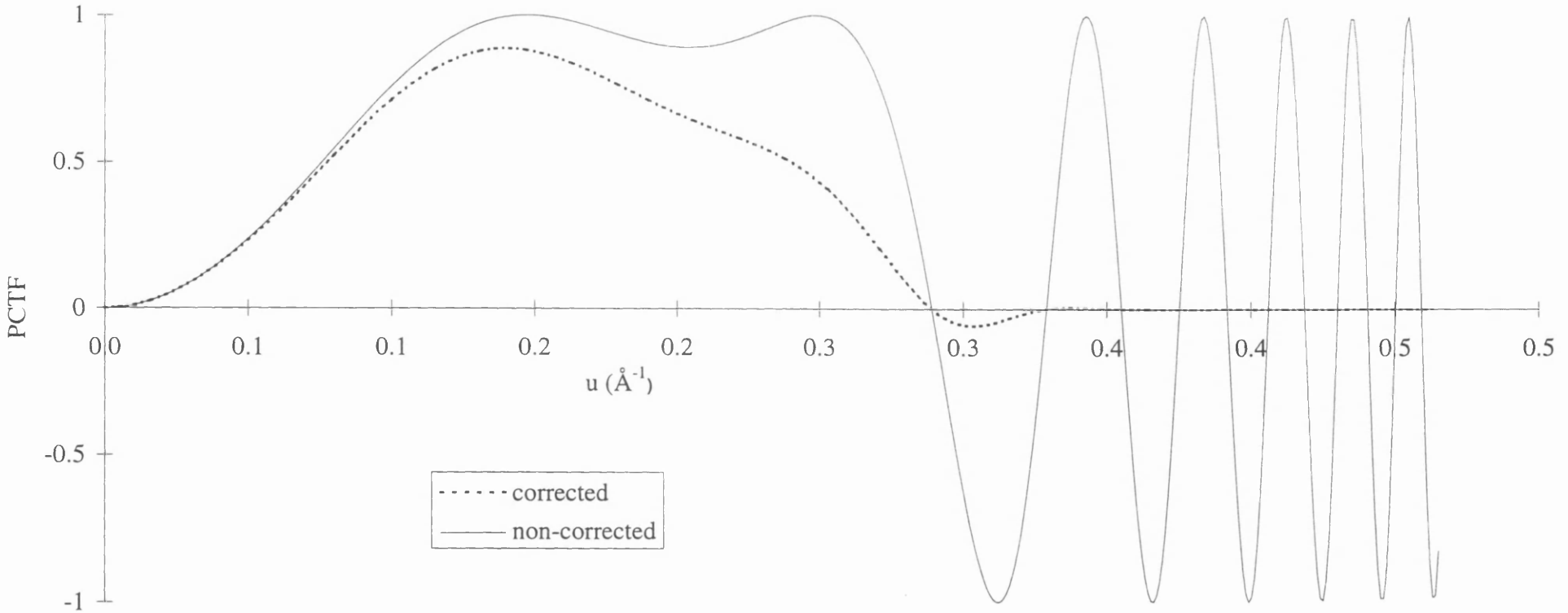

Figure 2.9: Optimum defocus PCTF, with and without corrections for the effects of chromatic aberrations and partial coherence (Δf=-900Å, ΔE=1eV, α_c=1mrad)

from the interaction of the primary beam of electrons with the specimen are collected and measured with suitable detectors.

Schematic diagrams of both the CTEM and STEM are presented in figure 2.10. The relationship between the imaging modes of both instruments can be described by the reciprocity principle (Cowley, 1969). Under identical conditions the signal recorded at B due to the point source at A in the STEM is the same signal which would be produced at A by a point source at B in the CTEM. Although the principle relates to ideal point sources and point detectors Cowley (1969) has shown that it can be extended, within limits, to describe actual situations and has been demonstrated experimentally by Crewe and Wall (1970) and by Colliex et al. (1977).

The main differences between the CTEM and STEM are in the methods of detecting and recording the images. The standard recording medium in the CTEM is the photoplate on which the intensity distribution of a 2-dimensional image is recorded simultaneously. In the STEM the image is detected one image point at a time. The sequential electrical signal from a photomultiplier detector can be used to display the image on a CRT or be recorded in any analogue or digital form. The CTEM can also be interfaced to a digital computer by arrangements such as a TV camera and frame store system. However, recording an electron image simultaneously requires a converter which is capable of resolving a number of image elements. The sequential signal in the STEM allows a more direct connection. The more important advantage of the STEM is that a variety of detectors can be used to obtain several different image signals simultaneously.

The work described in chapters 4 and 5 of this thesis was performed using an extended Vacuum Generators HB5 STEM equipped with a series of post specimen lenses. A schematic diagram of the microscope is given in figure 2.11. The HB5 uses a field emission source (Crewe, 1971) which has a cathode made of monocrystalline tungsten wire welded onto a tungsten filament. The radius of

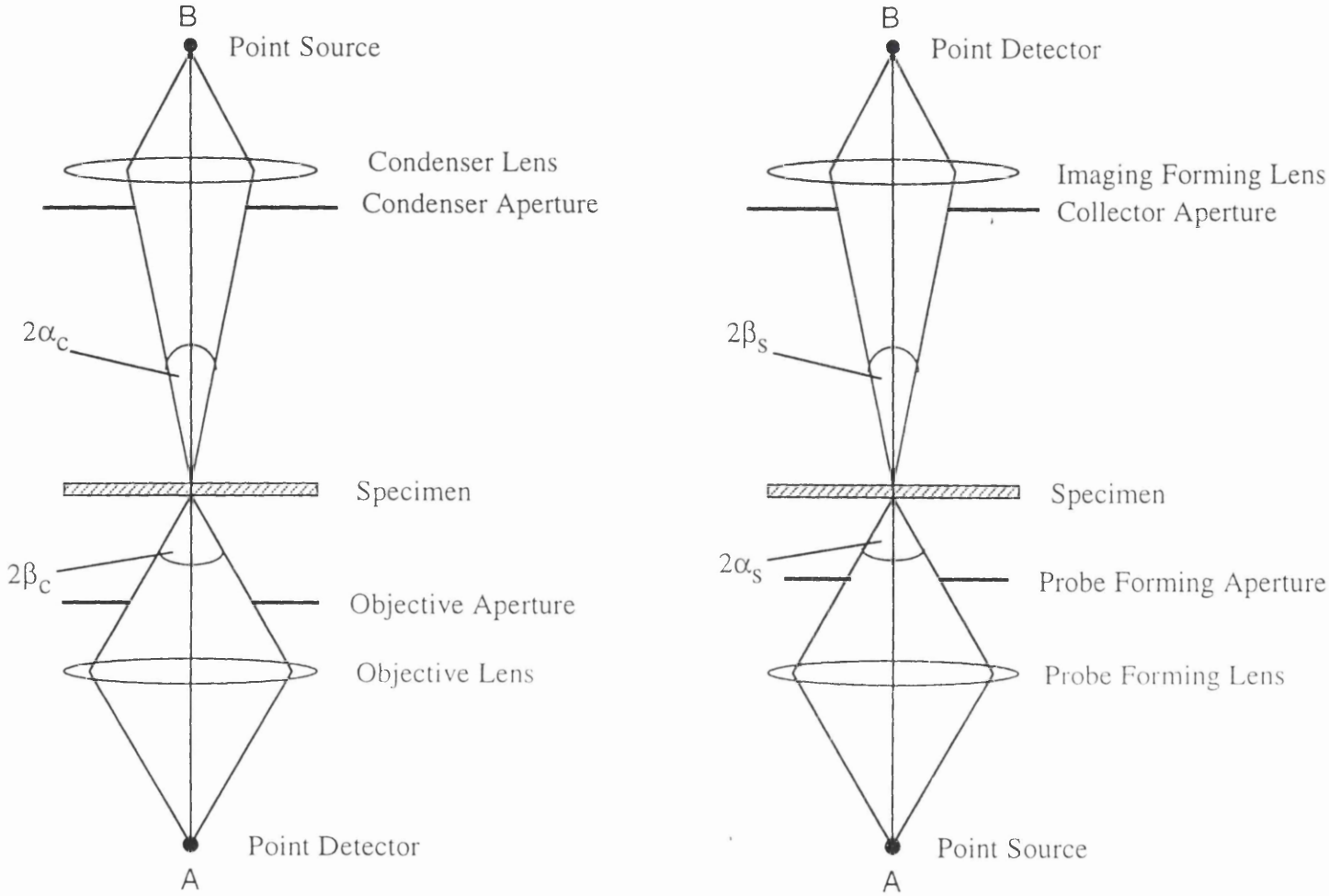

Figure 2.10 : Schematic diagram showing the reciprocal relationship between essential elements for CTEM and STEM.

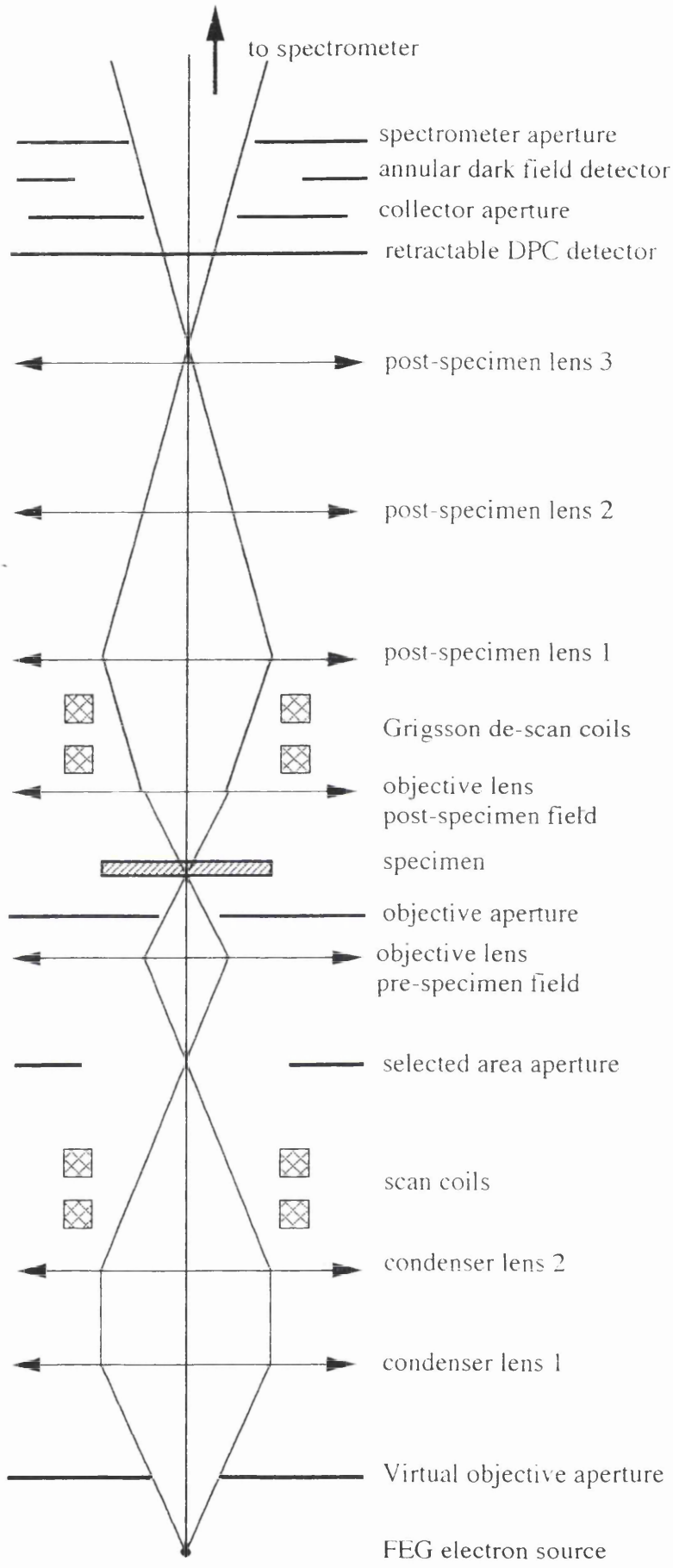

Figure 2.11 : Schematic diagram of the VG HB5 STEM.

the cathode tip is ~100nm. The cathode is held at a negative potential ~3kV relative to the extracting anode, creating an electric field $>5x10^9$V/m at the tip surface. As a result electrons are emitted which can "tunnel" through the potential barrier. A cathode current density of between 1000 and 10^6A/cm^2 can be obtained. To reduce emission fluctuations the field emission tip is used in a vacuum of 10nPa or better. A second anode accelerates the electrons up to energies of 100keV. A virtual objective aperture (VOA) defines the angular convergence of the probe. The spatial resolution is limited by the size of the probe, which is determined by the condenser and objective lenses. The HB5 is equipped with two condenser lenses C1 and C2. The sample is immersed in the intense magnetic field of the objective lens so that the prefield of this lens acts as a third condenser lens. In normal imaging mode either C1 or C2 condenser lens is used to transfer an image of the virtual cross-over produced by the gun on the selected area aperture plane. The objective lens produces the final focusing on the sample. The probe forming semi-angle α_S is defined by the objective aperture. The choice of C1 or C2 depends on the particular experiment ; C2 allows the formation of a smaller probe on the specimen whilst the total current in the probe is greater when using C1.

The post specimen lenses allow the angular distribution of the electrons transmitted through the specimen to be matched to the size and shape of the electron detectors by choosing a suitable camera length (Craven & Buggy, 1981). The HB5 is fitted with several detectors, those of interest are shown in figure 2.11. A small axial or bright field detector collects electrons which have lost energy through small-angle, inelastic scattering. There are two interchangeable annular dark field (ADF) detectors which collect electrons scattered at large angles, with respect to the directly transmitted beam. The collection semi-angles of these detectors are 20mrad and 40mrad. Figure 2.12 presents a ray diagram illustrating image formation using these two detectors. The HB5 has two additional detectors. The first is a detector system consisting of an

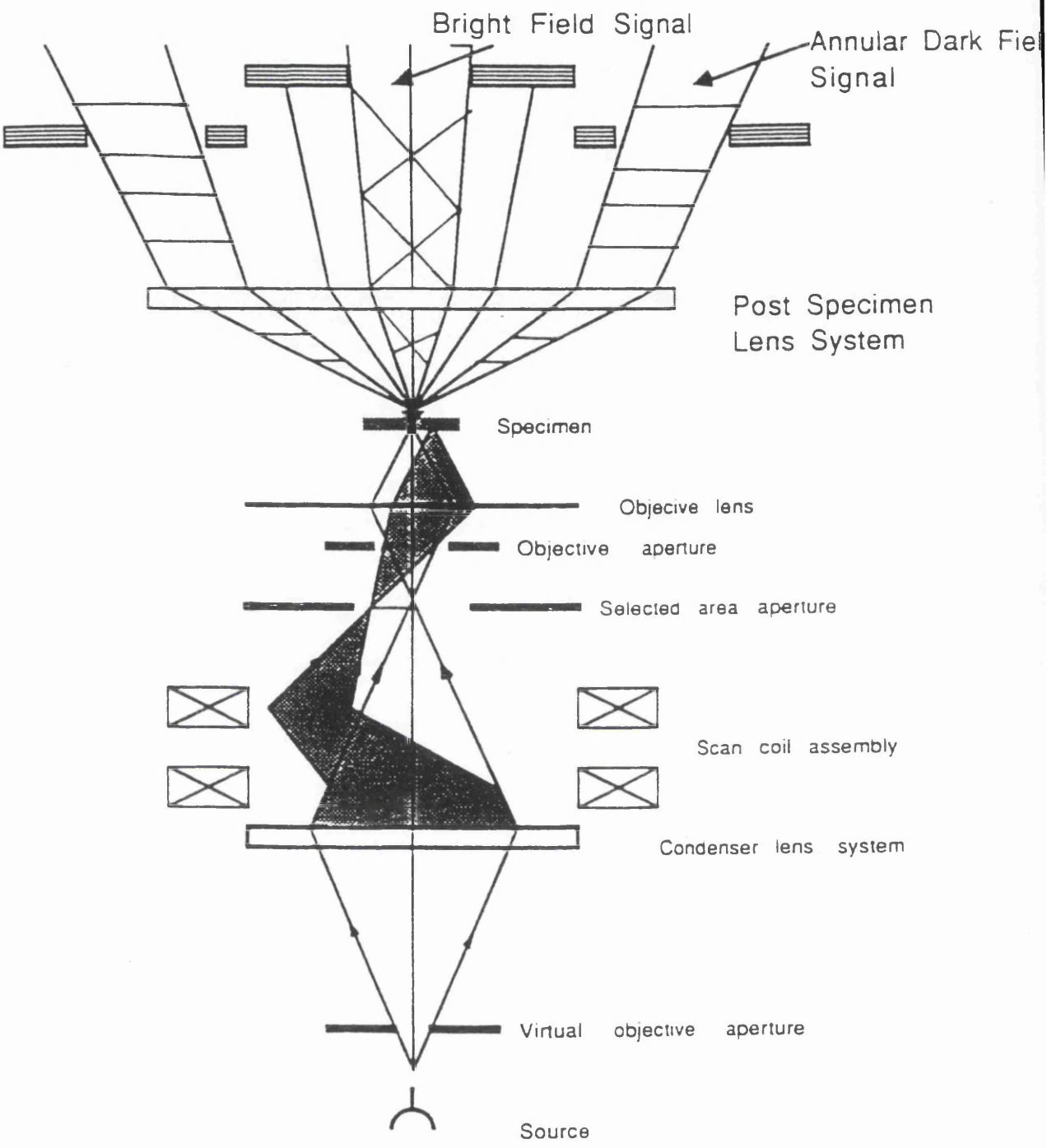

Figure 2.12: Ray diagram illustrating brightfield and darkfield imaging modes in the STEM (McColgan, 1990).

outer annular quadrant photodiode detector with an inner quadrant photodiode detector. This is mounted on a retractable carriage and positioned in the column below the annular dark field detector. The inner quadrant detector comprises a silicon p-n junction split into four sections separated by inactive strips. The signals from all four quadrants can be added together to give an incoherent bright field image. It is also possible for the difference signal from any two opposite quadrants from each detector to be obtained. These difference signals are, for small shifts, directly proportional to angular shifts of the electron beam across the detector. This gives differential phase contrast which represents the gradient of the object parallel to the scan direction. Further details regarding this mode of imaging are presented in chapter 4. The second detector is a GATAN model 666 parallel detection electron energy loss spectroscopy (PEELS) spectrometer. Electrons transmitted through the specimen are directed into the spectrometer where they are dispersed, according to their kinetic energy, by a second order aberration-corrected magnetic sector to form a spectrum. Since the collection angles of the ADF detectors are large, a smaller spectrometer aperture is normally used to define the collection angle of the PEELS spectrometer. The electron energy loss spectrum provides useful information about the chemical composition, electronic and structural properties of a specimen. A more detailed description of this spectrometer is given in chapter 5.

2.7 Image Formation In The STEM

The STEM uses a field emission source, thus it is assumed that electrons are emitted from a point source. The wave incident on the specimen is given by the Fourier transform of the transfer function of the objective lens :

$$\psi_1(\mathbf{r}) = \Im[A(\mathbf{u}) \exp\{i\chi(\mathbf{u})\}] \qquad (2.20)$$

where $A(\mathbf{u})$ and $\chi(\mathbf{u})$ are the same as defined in equation 2.9. The image is produced by recording the variation of the detected signal as the incident beam is scanned across the specimen. The equivalence of this can be considered as the specimen being moved relative to a fixed beam so that the wave at the exit surface of the specimen can be written as :

$$\psi_e(\mathbf{r},\mathbf{R}) = \psi_i(\mathbf{r}) \cdot q(\mathbf{r} - \mathbf{R}) \tag{2.21}$$

where $\mathbf{R}$ is the vector giving the translation of the specimen relative to the fixed incident beam and $q(\mathbf{r} - \mathbf{R})$ is the transmission function of the specimen given by:

$$q(\mathbf{r} - \mathbf{R}) = \exp\left[-i\sigma\phi(\mathbf{r} - \mathbf{R})\right] \tag{2.22}$$

The wave amplitude on the detector plane is then :

$$\begin{aligned}\Psi(\mathbf{u},\mathbf{R}) &= \Im\left[\psi_e(\mathbf{r},\mathbf{R})\right] \\ &= \Im\left[\psi_i(\mathbf{r}) \cdot q(\mathbf{r} - \mathbf{R})\right] \\ &= Q(\mathbf{u}) * A\left(\mathbf{u} \cdot \exp\{i\chi(\mathbf{u})\}\right)\end{aligned} \tag{2.23}$$

The intensity distribution in the detector plane is given by :

$$\begin{aligned}I(\mathbf{u}) &= \left|\Psi(\mathbf{u},\mathbf{R})\right|^2 \\ &= \left|Q(\mathbf{u}) * A(\mathbf{u}) \cdot \exp\{i\chi(\mathbf{u})\}\right|^2\end{aligned} \tag{2.24}$$

The signal, $J(\mathbf{R})$, produced by the STEM detector is obtained by integrating the intensity distribution, $I(\mathbf{u})$, over the detector surface described by a detector sensitivity function $D(\mathbf{u})$ such that :

$$J(\mathbf{R}) = \int_{?} I(\mathbf{u},\mathbf{R}) D(\mathbf{u}).d(\mathbf{u}) \qquad (2.25)$$

For a thin weakly scattering specimen the transmission function given in equation 2.22 can be reduced to

$$q(\mathbf{r}) = 1 - i\sigma\phi(\mathbf{r} - \mathbf{R}) - \frac{1}{2}\sigma^2\phi^2(\mathbf{r} - \mathbf{R}) \qquad (2.26)$$

so that

$$Q(\mathbf{u}) = 1 - iQ_1(\mathbf{u}) - Q_2(\mathbf{u}) \qquad (2.27)$$

where

$$Q_1(\mathbf{u}) = \sigma\ \Phi(\mathbf{u}) \text{ and } Q_2(\mathbf{u}) = \frac{1}{2}\sigma^2\Phi(\mathbf{u})*\Phi(\mathbf{u}) \qquad (2.28)$$

Q_1 and Q_2 are complex and can therefore be written in terms of their real (R) and imaginary (I) components :

$$Q_1(\mathbf{u}) = Q_{1R}(\mathbf{u}) + iQ_{1I}(\mathbf{u}) \quad Q_2(\mathbf{u}) = Q_{2R}(\mathbf{u}) + iQ_{2I}(\mathbf{u}) \qquad (2.29)$$

Neglecting all terms of order higher than 2 in $\sigma\Phi(\mathbf{u})$ the intensity on the detector plane can now be written as :

$$\begin{aligned} I(\boldsymbol{u}) = {} & A^2 + 2A\cos\chi\left[(Q_{1R} + Q_{2I}) * A\,\mathrm{sinc} - (Q_{2R} - Q_{1I}) * A\cos\chi\right] \\ & - 2A\sin\chi\left[(Q_{1R} + Q_{2I}) * A\cos\chi + (Q_{2R} - Q_{1I}) * A\,\mathrm{sinc}\right] \\ & + \left|Q_1 * A\sin\chi\right|^2 + \left|Q_1 * A\cos\chi\right|^2 \end{aligned} \qquad (2.30)$$

The normal phase contrast bright field STEM image for weak phase objects is obtained by considering only the first order terms of equation (2.30), by replacing Q_{1R} and Q_{1I} by $\sigma\Phi_R$ and $\sigma\Phi_I$ and putting Q_{2R} and Q_{2I} equal to zero in the second and third terms. The last two terms give a first approximation to the STEM dark field image.

For the bright field imaging case the integral in equation 2.25 is zero for the detector aperture tending to zero. It is also zero if the detector aperture is of diameter equal or greater than that of $A(\mathbf{u})$. For a very small centrally placed detector aperture of radius $\mathbf{u}_0$, $\cos\chi = 1$ and $\sin\chi = 0$ so that the STEM image signal is given by :

$$J(\mathbf{R}) = \pi\mathbf{u}_0^2\left[1 + \sigma\phi(\mathbf{R}) * \Im[A(\mathbf{u})\sin\chi(\mathbf{u})]\right] \tag{2.31}$$

This expression corresponds to the expression for bright field phase contrast in the CTEM (equation 2.13) where the image contrast is described directly as the projected potential smeared out by a spread function. The $\mathbf{u}_0^2$ term implies that for small apertures the image signal is low. The situation can be improved by increasing the size of the detector however calculation of the image signal becomes more complex and is given by :

$$\begin{aligned} J(\mathbf{R}) = & \int \Im[D(\mathbf{u})]\cdot\Im[A(\mathbf{u})] \\ & + 2\sigma\phi_e(\mathbf{R}) * \begin{Bmatrix} \Im[A(\mathbf{u})\sin\chi(\mathbf{u})]\left(\Im[D(\mathbf{u})] * \Im[A(\mathbf{u})\cos\chi(\mathbf{u})]\right) \\ -\Im[A(\mathbf{u})\cos\chi(\mathbf{u})]\left(\Im[D(\mathbf{u})] * \Im[A(\mathbf{u})\sin\chi(\mathbf{u})]\right) \end{Bmatrix} \end{aligned} \tag{2.32}$$

In the weak phase approximation the image contrast is again a linear representation of the projected potential but the spread function is more complex. The objective is then to choose the form of the detector function and defocus value in such a way as to make the spread function as narrow and intense as possible in order to achieve the best possible resolution and contrast.

Investigations of the width and contrast of the spread function as a function of the detector aperture size have been calculated by Butler (1982). Theoretical predictions and recorded images have shown that as the detector size is increased while there is improved signal to noise the resolution of the images is reduced. By referring to the reciprocity principle, increasing the size of the STEM detector is equivalent to extremely incoherent illumination in the CTEM resulting in poor phase contrast.

In STEM bright field imaging the collection efficiency is given by $(b_s/\alpha_s)^2$ where α_s is the angle subtended by the probe and β_s the angle subtended by the detector. These parameters are critical, particularly in lattice imaging. In a STEM lattice image the electron distribution in the detector plane is a convergent beam electron diffraction (CBED) pattern consisting of a series of circular disc-shaped diffraction spots. The radius of the discs is determined by the probe half angle α and the position of the scattering angle $\theta = 2\theta_B = \lambda / d$. Spence and Cowley (1977) have shown that for a lattice image to be formed there must be an overlap of the diffracted discs. The intensity in the regions where there is overlap is dependent on both the probe position and lens aberrations. Formation of the lattice fringes requires a sufficiently large probe angle, $\alpha > 2\theta_B$, to allow overlap and a small axial detector placed in the overlap region. Since the signal to noise ratio is dependent on the detector dimensions then a large collection angle would appear to be beneficial. However, Cowley and Au (1978) have shown that as this angle approaches the dimensions of the probe angle the contrast of the lattice fringes decreases to zero. To achieve STEM lattice images with comparable contrast and signal to noise of CTEM lattice images the specimen must be irradiated with a considerably larger electron dose. This makes standard STEM lattice imaging unsuitable for lattice imaging of radiation sensitive specimens. As a result of the poor collection efficiency in STEM more complex detector systems have been developed to make more efficient use of the electrons in the STEM. A technique based on the DPC mode of microscopy,

utilising a quadrant detector developed by Morrison et al. (1980) is described in Chapter 4. This technique provides simultaneous topographic and lattice fringe images.

Chapter 3

CTEM IMAGING AND DIFFRACTION STUDIES OF HALOGENATED COPPER PHTHALOCYANINE PIGMENTS.

3.1 Introduction

As discussed in Chapter 1, the colouring properties of the CPC pigments are strongly dependent on the size, shape and distribution of the pigment particles and on their internal structure. This chapter describes the application of diffraction and imaging techniques available on the CTEM to investigate various samples of industrially prepared halogenated CPC pigments. Section 3.2 describes the various samples investigated and their colouring properties. Diffraction patterns provide information on the internal structure of the pigmentary particles. Section 3.3 presents the results obtained from the diffraction studies of single pigment particles. Analysis of these patterns is presented in section 3.4. The diffraction studies revealed that the CPC crystals contain twin structures and these are discussed in section 3.5. Section 3.6 presents a discussion of the implications of the results of the analysis of the diffraction patterns. Low magnification images provide information on the size, shape and distribution of the pigment particles. Low magnification images acquired from the various

samples are presented in section 3.7. Lattice images provide information on the internal structure of the pigments, the extent of crystallinity and defects in the crystal structure. The principles and instrumental considerations for lattice imaging are described in section 3.8. Lattice images acquired from the various samples are presented in section 3.9. Details of a technique devised to investigate the structure of small aggregates using diffraction are presented in section 3.10. Analysis of the diffraction studies of these small aggregates is described in section 3.11. Conclusions about the investigations using imaging and diffraction are presented in section 3.12.

3.2 Samples investigated

Studies of three groups of industrially prepared samples of highly chlorinated (~14.5 Cl atoms/molecule) pigments were made. The first group of pigments were two samples of a paint pigment, A1 and A2, prepared using the same process but taken from different batches which exhibited different colouring properties. Sample A1 gave a standard colour strength and hue and good dispersibility. Sample A2 was a poor pigment which gave a strong blue bright colour and poor dispersibility. The second group of pigments were two samples of a plastic pigment, B1 and B2, prepared using the same process but from batches with different colouring properties. Sample B1 gave a standard colour strength, hue and brightness and good colour development. Sample B2 was a poor pigment which gave a weak blue colour and poor colour development. The final group of pigments were four samples of plastic pigments, C1, C2, C3 and C4, each prepared using a different process and giving different levels of colour development. Samples C1 and C2 gave the best colour development followed by sample C3 and finally sample C4 which gave the poorest colour development.

3.3 Diffraction studies of highly chlorinated particles of CPC pigment

As shown in chapter 2, the minimum selectable diameter from which diffraction patterns can be obtained using selected area diffraction (SAD) is ~0.2μm. The dimensions of a single pigment particle are significantly less than this, at ~50nm, and to be able to select a single particle for analysis would require a low particle density covering the carbon support film. An alternative method, used by McColgan (1990), analysed areas with a high particle density using SAD. In this way there was the possibility of a particle in the correct orientation to present a prominent reciprocal lattice plane to the incident beam, while the other particles contributed to the background intensity. However, using the convergent beam electron diffraction (CBED) technique detailed in chapter 2, it was possible to record electron diffraction patterns from areas with dimensions of the order of a single particle from samples with a high particle density.

Using a condenser aperture of 40μm diameter and the smallest spot size available, it was possible to focus the electron probe down to an area with a diameter ~40nm. It was then relatively easy to place this probe on a single particle in this area and switch to diffraction mode to record the diffraction pattern. To determine the lattice parameters from the spot spacings on the micrographs, an accurate measurement of the camera length was required. This was achieved by analysing the diffraction pattern from a cubic Au sample for which the lattice parameter is known. This gave a camera length of 24.3 ± 0.5cm for a nominal value of 30cm.

Around thirty diffraction patterns were recorded from areas containing small aggregates of particles, in the highly chlorinated sample A1. Figures 3.1(a) - (o) show a selection of diffraction patterns obtained from this sample. Around 75% of the diffraction patterns were similar to those shown in figures 3.1(a) - (i), where the outer lines were streaked while the central line of spots was preserved. While the majority of the diffraction patterns recorded were spot patterns, around

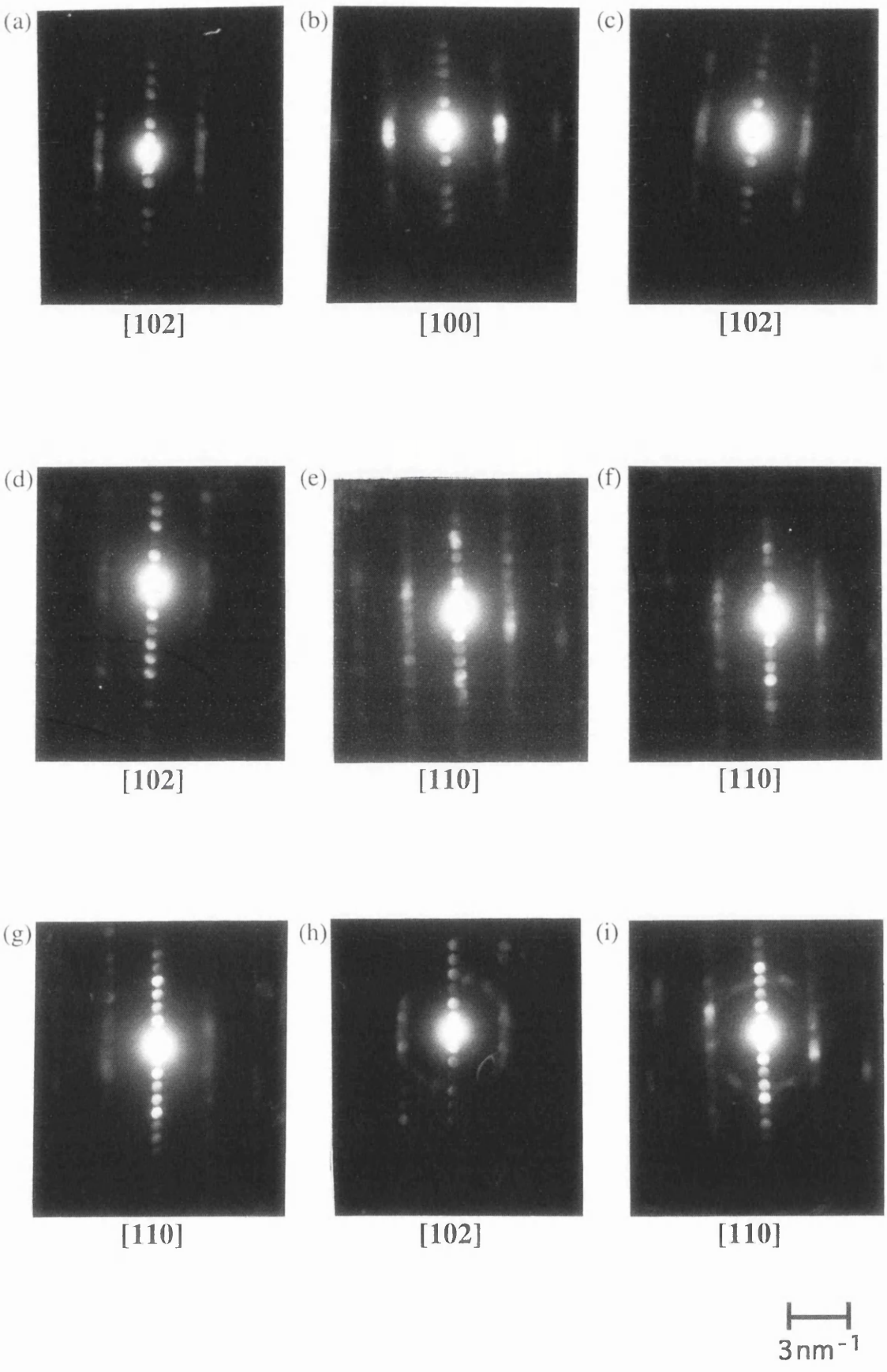

Figure 3.1(a) -(i) : Diffraction patterns recorded from a highly chlorinated CPC paint pigment.

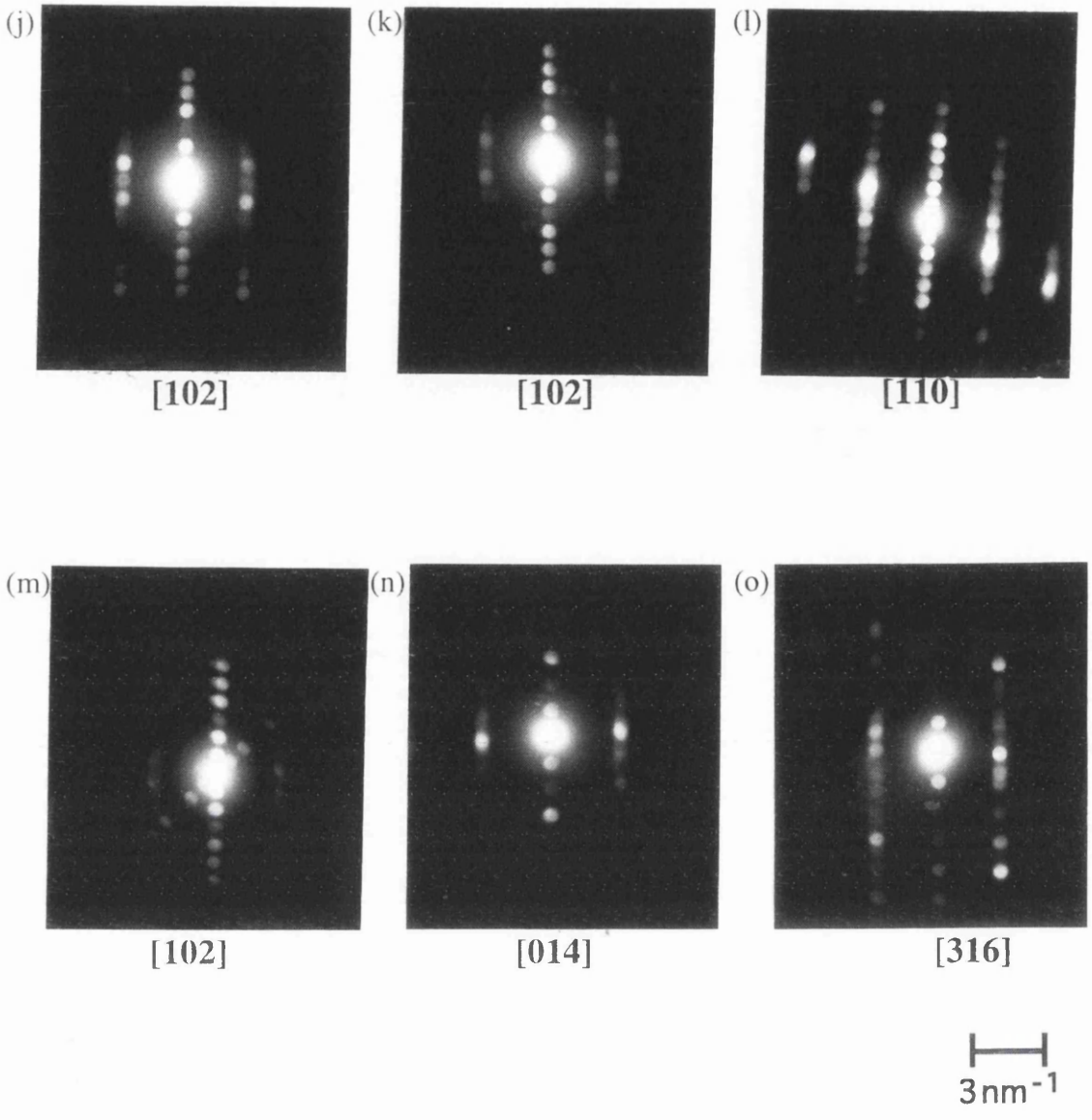

Figure 3.1(j) - (o) : Diffraction patterns recorded from a highly chlorinated CPC paint pigment.

one third also contained what appeared to be a ring pattern as shown in figures 3.1(h) & (i). The ring patterns occurred due to the diffraction pattern being recorded from an area containing several overlying particles which are randomly oriented with respect to each other and thus contribute to the background intensity. In about 20% of the diffraction patterns the outer lines had a small degree of streaking, as shown in figures 3.1(j) and (l). These streaks indicate an element of disorder predominantly along one particular direction. This is discussed further in section 3.5. A few diffraction patterns similar to that shown in figure 3.1(m) were recorded. The diffraction patterns shown in figures 3.1(n) and (o) were observed only once.

3.4 Analysis of diffraction patterns from single pigment particles

The "Diffract" software package was used to generate diffraction patterns from a CPC crystal matrix for various zone axes. By comparing the theoretically generated diffraction patterns with the experimentally obtained patterns, the zone axes of the experimental diffraction patterns could be determined.

The crystal structure of the CPC pigment was taken to be that of epitaxially prepared fully chlorinated CPC. This was found by Uyeda et al. (1981) to be a monoclinic c-face centred lattice with the following unit cell dimensions:

a = 1.962nm

b = 2.61nm

c = 0.376nm

$\beta = 116.5^{o}$

Space Group C2/c or C2/m

Figure 3.2 shows the relative orientation of the real reciprocal lattice axes for the monoclinic crystal structure.

Figures 3.3 (a) - (i) show the geometry of various diffraction patterns generated using the "Diffract" program for various zone axes. From the patterns shown in figure 3.3, it is clear that many of them are superficially very similar. Identification of the zone axis is complicated by the streaking present on the outer line of spots in the actual patterns. The most easily determined parameters on the patterns are the spacing of the spots along the centre line (i.e. the centre line spot spacing) and the perpendicular separation of the lines (i.e. the perpendicular distance to the outer line). The line spot ratio is defined as the ratio between the perpendicular distance to the outer line and the centre line spot spacing. Thus determination of the line spot ratio is the simplest way of starting the identification of the zone axis of the recorded patterns. The calculated spacings and line spot ratio, for various zone axes are presented in table 3.1. The distances are given in terms of the reciprocal of the real space distance i.e. for a 1.3nm plane spacing, the spot spacing is denoted as $(1.3nm)^{-1}$.

Table 3.2 presents the measured line spot ratios for the recorded diffraction patterns. By comparing the measured line spot ratio with the calculated ratios in table 3.1, possible zone axes were determined. Table 3.2 also provides additional information, including measured spacings and angles between reflections. This information was used to eliminate some of the possible zone axes and thus determine the actual zone axis. In certain cases there was only one possible zone axis, as shown for diffraction pattern 29, and no additional information was required. The following discussion gives some examples of how the zone axes were determined for the patterns shown in figure 3.1. At first sight the diffraction patterns, similar to those shown in figures 3.1(a) - (l), appeared to have similar centre line spot and perpendicular line spacings. Detailed analysis of these patterns revealed several different zone axes. The diffraction pattern shown in figure 3.1(h) has a line spot ratio of 3.47 ± 0.07. From table 3.1, this pattern

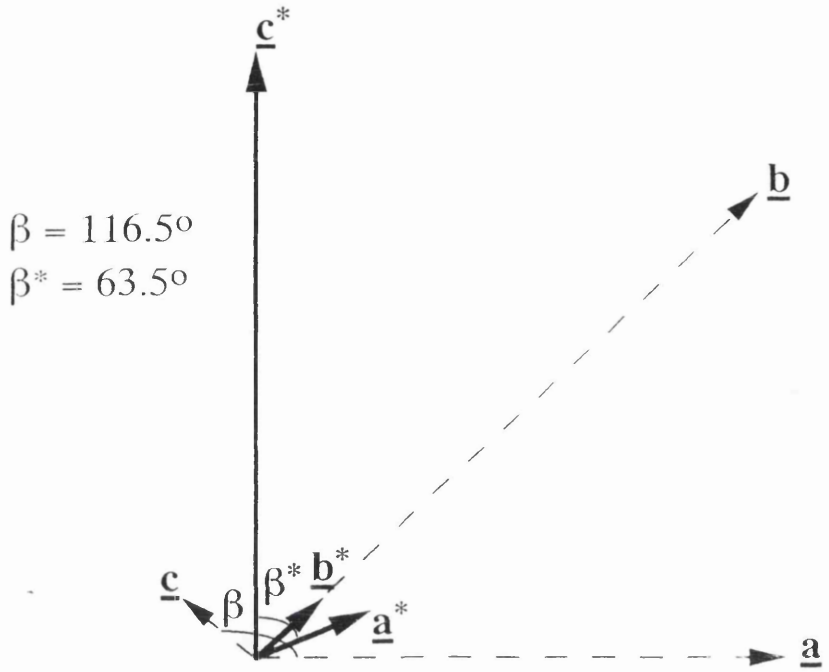

Figure 3.2 : Orientation of the real and reciprocal lattice axes for the monoclinic crystal structure

Centre Line Spot Spacing = 1.457nm^{-1}
Perpendicular Line Spacing = 0.362nm^{-1}
Line Spot Ratio = 4.02

Figure 3.3(a) Diffraction Pattern for a [110] Zone Axis

Centre Line Spot Spacing = 1.457nm^{-1}
Perpendicular Line Spacing = 0.376nm^{-1}
Line Spot Ratio = 3.88

Figure 3.3(b) Diffraction Pattern for a [1$\bar{1}$2] Zone Axis

Centre Line Spot Spacing = 1.457nm^{-1}
Perpendicular Line Spacing = 0.334nm^{-1}
Line Spot Ratio = 4.36

Figure 3.3(c) Diffraction Pattern for a [112] Zone Axis

Centre Line Spot Spacing = 1.305nm^{-1}
Perpendicular Line Spacing = 0.337nm^{-1}
Line Spot Ratio = 3.88

Figure 3.3(d) Diffraction Pattern For A [100] Zone Axis

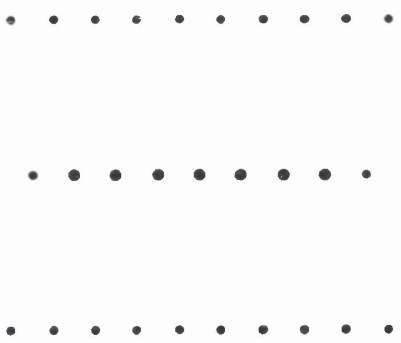

Centre Line Spot Spacing = 1.305nm^{-1}
Perpendicular Line Spacing = 0.362nm^{-1}
Line Spot Ratio = 3.61

Figure 3.3(e) Diffraction Pattern For A [101] Zone Axis

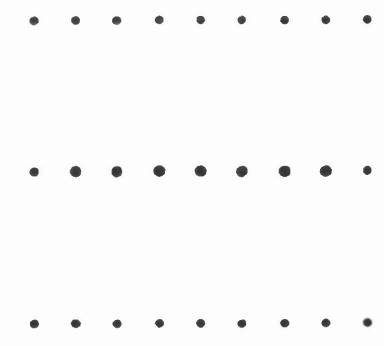

Centre Line Spot Spacing = 1.305nm^{-1}
Perpendicular Line Spacing = 0.375nm^{-1}
Line Spot Ratio = 3.48

Figure 3.3(f) Diffraction Pattern For A [102] Zone Axis

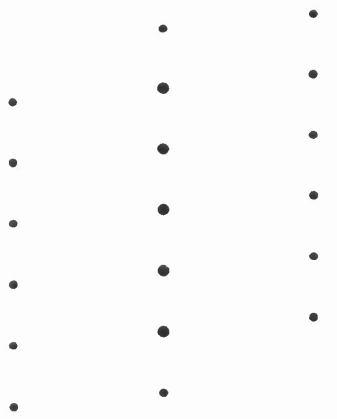

Centre Line Spot Spacing = 0.878nm^{-1}
Perpendicular Line Spacing = 0.376nm^{-1}
Line Spot Ratio = 2.33

Figure 3.3(g) Diffraction Pattern For A [010] Zone Axi3

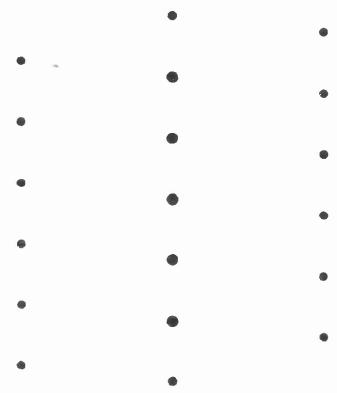

Centre Line Spot Spacing = 0.878nm^{-1}
Perpendicular Line Spacing = 0.372nm^{-1}
Line Spot Ratio = 2.36

Figure 3.3(h) Diffraction Pattern For A [011] Zone Axis

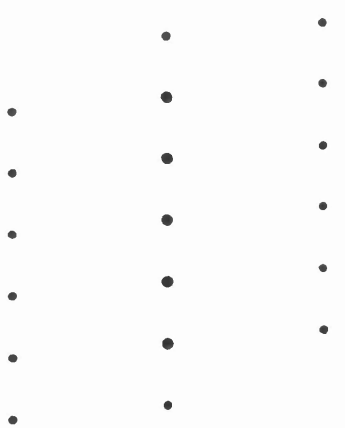

Centre Line Spot Spacing = 0.878nm^{-1}
Perpendicular Line Spacing = 0.361nm^{-1}
Line Spot Spacing = 2.43

Figure 3.3(i) Diffraction Pattern For A [012] Zone Axis

Centre Line Spot Spacing = 0.780nm^{-1}
Perpendicular Line Spacing = 0.369nm^{-1}
Line Spot Ratio = 2.11

Figure 3.3(j) Diffraction Pattern For A [314] Zone Axi3

Centre Line Spot Spacing = 0.780nm^{-1}
Perpendicular Line Spacing = 0.375nm^{-1}
Line Spot Ratio = 2.08

Figure 3.3(k) Diffraction Pattern For A [316] Zone Axis

Centre Line Spot Spacing = 0.780nm^{-1}
Perpendicular Line Spacing = 0.375nm^{-1}
Line Spot Ratio = 2.08

Figure 3.3(l) Diffraction Pattern For A [318] Zone Axis

Zone Axis	Inner Line Spot (hkl)	Outer Line Spot (hkl)	Angle	Inner Spot Spacing (nm)	Outer Spot Spacing (nm)	Perp. Line Spacing (nm)	Line/Spot Ratio
100	020	001	90.00	1.305	0.337	0.337	3.87
101	020	$\bar{1}11$	82.11	1.305	0.358	0.361	3.61
$10\bar{1}$	020	111	83.31	1.305	0.304	0.306	4.26
102	020	$\bar{2}01$	90.00	1.305	0.375	0.375	3.48
$10\bar{2}$	020	201	90.00	1.305	0.276	0.276	4.73
103	020	$\bar{3}11$	81.88	1.305	0.368	0.358	3.64
$10\bar{3}$	020	311	84.58	1.305	0.247	0.240	5.41
$1\bar{1}0$	110	001	68.27	1.457	0.337	0.363	4.02
110	$1\bar{1}0$	001	68.27	1.457	0.337	0.363	4.02
$1\bar{1}2$	110	$\bar{1}11$	72.45	1.457	0.358	0.375	3.88
$1\bar{1}\bar{2}$	110	$1\bar{1}1$	65.59	1.457	0.304	0.334	4.36
$2\bar{1}0$	240	001	74.56	0.524	0.337	0.350	1.50
010	$\bar{2}00$	001	116.50	0.878	0.337	0.377	2.33
011	200	$\bar{1}\bar{1}1$	74.28	0.878	0.358	0.372	2.36
$01\bar{1}$	200	$\bar{1}11$	74.28	0.878	0.358	0.372	2.36
012	200	$0\bar{2}1$	64.40	0.878	0.326	0.361	2.43
013	200	$\bar{1}\bar{3}1$	75.37	0.878	0.334	0.345	2.54
014	200	$0\bar{4}1$	66.64	0.878	0.299	0.326	2.70
$3\bar{1}4$	130	$\bar{1}11$	75.92	0.780	0.358	0.369	2.11
$3\bar{1}\bar{4}$	130	$1\bar{1}1$	81.28	0.780	0.304	0.308	2.54
$3\bar{1}6$	130	$\bar{2}01$	88.22	0.780	0.375	0.375	2.08
$3\bar{1}\bar{6}$	130	201	72.43	0.780	0.276	0.289	2.69
$3\bar{1}8$	130	$\bar{2}21$	73.89	0.780	0.360	0.375	2.08
$3\bar{1}\bar{8}$	130	$2\bar{2}1$	83.68	0.780	0.270	0.272	2.87

Table 3.1 : Calculated spacings and line spot ratios, for various zone axes, in fully chlorinated CPC.

Pattern	Line/Spot Ratio	Possible Zone Axes	Additional Information	Zone Axis
1	2.07±0.04	[3$\bar{1}$4] [3$\bar{1}$6] [3$\bar{1}$8]	The angle between the reflections is 87±1 degrees	[3$\bar{1}$6]
2	2.64±0.05	[014] [3$\bar{1}$6]	The centre line spot spacing is 0.87±0.05nm	[014]
3	3.47±0.07	[101] [102]	The angle between reflections is 90±1 degrees	[102]
4	3.47±0.07	[101] [102]	The angle between reflections is 90±1 degrees	[102]
5	3.47±0.07	[101] [102]	The angle between reflections is 90±1 degrees	[102]
6	3.47±0.07	[101] [102]	The angle between reflections is 90±1 degrees	[102]
7	3.47±0.07	[101] [102]	The angle between reflections is 90±1 degrees	[102]
8	3.47±0.07	[101] [102]	The angle between reflections is 90±1 degrees	[102]
9	3.49±0.07	[101] [102]	The angle between reflections is 90±1 degrees	[102]
10	3.51±0.07	[101] [102]	The angle between reflections is 90±1 degrees	[102]
11	3.51±0.07	[101] [102]	The angle between reflections is 90±1 degrees	[102]
12	3.53±0.07	[101] [102]	The angle between reflections is 90±1 degrees	[102]
13	3.53±0.07	[101] [102]	The angle between reflections is 90±1 degrees	[102]
14	3.53±0.08	[101] [102]	The angle between reflections is 90±1 degrees	[102]
15	3.53±0.08	[101] [102]	The angle between reflections is 90±1 degrees	[102]
16	3.55±0.07	[101] [102]	The angle between reflections is 90±1 degrees	[102]
17	3.77±0.07	[100] [11$\bar{2}$]	The centre line spot spacing is 1.27±0.07nm	[100]
18	3.79±0.08	[101] [102]	The angle between reflections is 82±1 degrees	[101]
19	3.93±0.08	[100] [110] [11$\bar{2}$]	The centre line spot spacing is 1.42±0.07nm and angle between reflections is 68±1 degrees	[110]
20	3.95±0.08	[100] [110] [11$\bar{2}$]	The centre line spot spacing is 1.42±0.07nm and angle between reflections is 68±1 degrees	[110]
21	3.95±0.08	[100] [110] [11$\bar{2}$]	The centre line spot spacing is 1.42±0.07nm and angle between reflections is 68±1 degrees	[110]
22	3.98±0.08	[100] [110] [11$\bar{2}$]	The centre line spot spacing is 1.42±0.07nm and angle between reflections is 68±1 degrees	[110]
23	4.00±0.08	[100] [110] [11$\bar{2}$]	The centre line spot spacing is 1.42±0.07nm and angle between reflections is 68±1 degrees	[110]
24	4.00±0.08	[100] [110] [11$\bar{2}$]	The centre line spot spacing is 1.42±0.07nm and angle between reflections is 68±1 degrees	[110]
25	4.00±0.08	[100] [110] [11$\bar{2}$]	The centre line spot spacing is 1.42±0.07nm and angle between reflections is 68±1 degrees	[110]
26	4.00±0.08	[100] [110] [11$\bar{2}$]	The centre line spot spacing is 1.42±0.07nm and angle between reflections is 68±1 degrees	[110]
27	4.00±0.08	[100] [110] [11$\bar{2}$]	The centre line spot spacing is 1.42±0.07nm and angle between reflections is 68±1 degrees	[110]
28	4.00±0.09	[100] [110] [11$\bar{2}$]	The centre line spot spacing is 1.42±0.07nm and angle between reflections is 68±1 degrees	[110]
29	4.19±08	[10$\bar{1}$]		[10$\bar{1}$]

Table 3.2 : Measured line spot ratios for the diffraction patterns recorded from sample A1.

could only be assigned the [102] zone axis. The centre line spot spacing of 1.27 ± 0.07nm^{-1} and perpendicular line spacing of 0.36 ± 0.02nm^{-1} would support this assigned zone axis. Figure 3.1 (l) had a line spot ratio of 4.00 ± 0.08 which gave possible zone axes of [100], [110] and [1 $\bar{1}$ 2]. However, the pattern had a centre line spot spacing of 1.42 ±0.08nm^{-1} which would eliminate the [100] zone axis. The angle between reflections is 68 ± 1^{o}, indicating that the diffraction pattern could only be assigned the [110] zone axis. The diffraction pattern shown in figure 3.1(b) had a line spot ratio of 3.77 ± 0.07. From table 3.1, possible zone axes for this pattern were [100] and [1 $\bar{1}$ 2]. The pattern has a centre line spot spacing of 1.27 ± 0.07nm^{-1} and a perpendicular line spacing of 0.33 ± 0.02nm^{-1}, thus the only possible zone axis is the [100]. The diffraction pattern shown in figure 3.1(n) has a line spot ratio of 2.64 ±0.05. From table 3.1 this indicated possible zone axes of [014] and [3 $\bar{1}$ $\bar{6}$]. The centre line spot spacing of figure 3.1(n) is 0.87 ±0.05nm^{-1} and thus can only be assigned the [014] zone axis. In the same way this technique was used to determine the zone axis for all the recorded diffraction patterns. A histogram of the various zone axes observed is presented in figure 3.4. It is clear that there are two zone axes which predominate, these being the [102] and [110] zone axes. The remaining zone axes are observed infrequently and neither appears to be observed more readily than the others. Similar results were obtained for all the pigment samples listed in section 3.2. An attempt is made in section 3.6 to try to determine why certain zone axes predominate. Before this can be considered, however, the presence of twin structures in the CPC crystal must first be considered.

3.5 Twinning in chlorinated CPC

In unhalogenated CPC, there are essentially two ways in which effectively planar molecules can stack together and these are shown schematically in figures

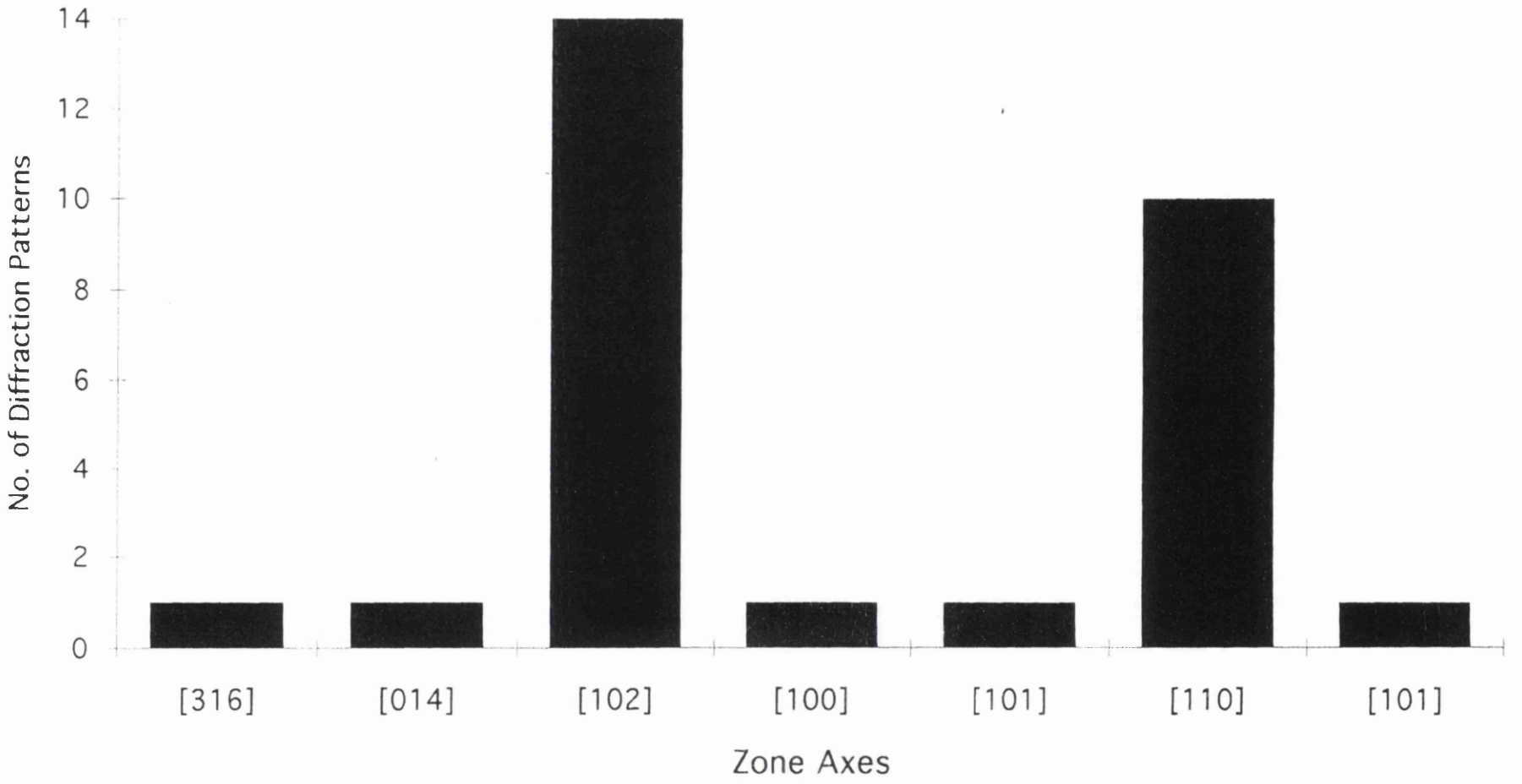

Figure 3.4 : Histogram of the observed zone axes.

3.5(a) and (b). The major differences between α and β CPC has been discussed by Fryer et al. (1981). In the α phase, all the molecules are stacked in parallel, whereas in β-phase, the planar molecules are stacked in zig-zag columns, such that the copper atom in one molecule is above a nitrogen atom in the underlying molecule. The crude CPC blue pigments, used to manufacture the pigments studied in this work, consist of β-phase crystals (Inman, 1967, Smith & Easton, 1966). After the halogenation and pigmentation processes, the highly chlorinated CPC's are made up of α-phase crystals (Fryer, 1977). The observed streaking in the diffraction pattern indicates that deviations in this stacking sequence are present. There are several defect models which can explain the presence of streaks in diffraction patterns [Andrews et al. (1971)]. A common feature of these is that ordering is altered along one direction while being preserved in the other. Streaking is then introduced along the direction in which a departure from the periodic structure can be viewed. Drummond (1985) has suggested that for highly chlorinated pigments the most probable explanation for the observed streaks is twinning. A twin structure is obtained by a rotation of 180^{o} of the original matrix, about a particular orientation, known as the twin axis. The plane perpendicular to the twin axis is known as the twin plane. In the case where the twin plane lies parallel to the electron beam, the twin axis is then parallel to the reciprocal lattice plane corresponding to the original diffraction pattern, and the twin diffraction pattern is immediately obtained by a simple rotation. In highly chlorinated CPC the twin structure is formed by a rotation about the [110] or $[1\bar{1}0]$ axes where the $(1\bar{1}0)$ and (110) planes are the respective twin planes, as shown in figure 3.6(a). A rotation of 180^{o} about the twin axis corresponds to a mirror image of the matrix diffraction pattern across the twin axis as shown in figure 3.6(b). As can be seen in figure 3.6(b) for diffraction patterns with a [110] zone axis it is relatively easy to determine the position of the twin spots since the twin axis lies in the plane of the diffraction pattern. The result of twinning on the diffraction pattern with a [102] zone axis is more difficult to determine since in this case the twin

(a)

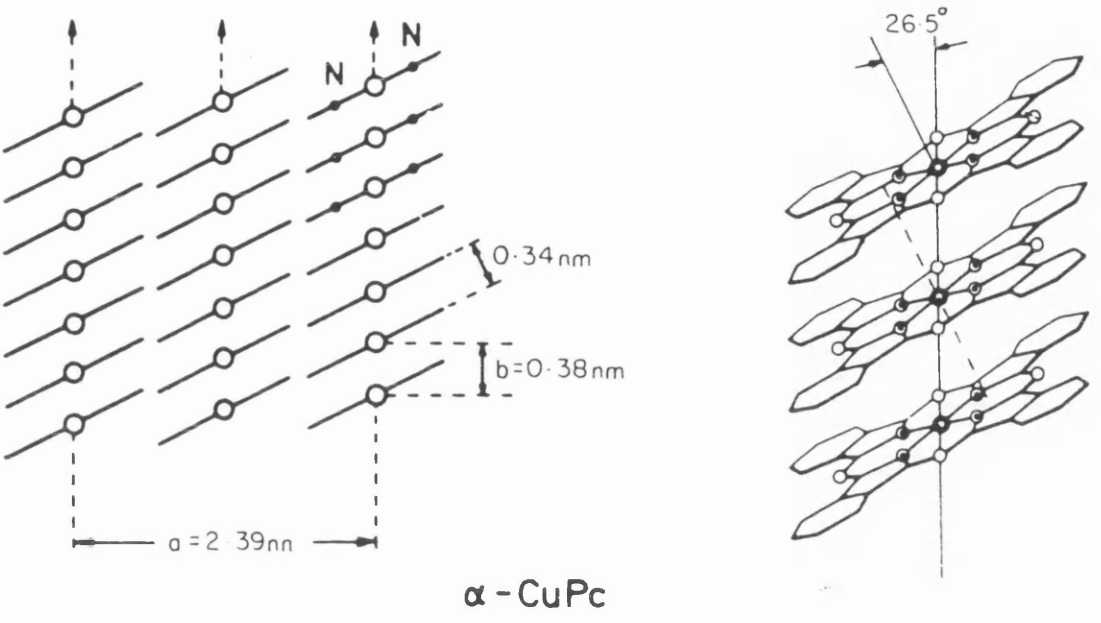

(b)

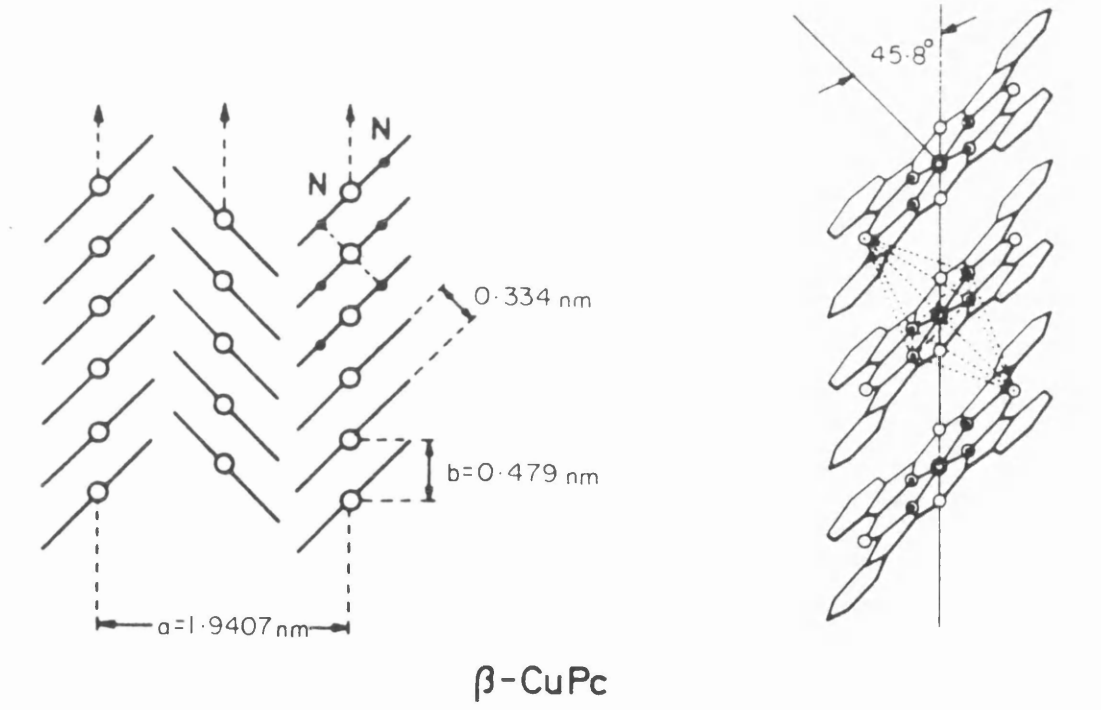

Figure 3.5(a) & (b) : Stacking of α and β copper phthalocyanine (after B. Honigmann).

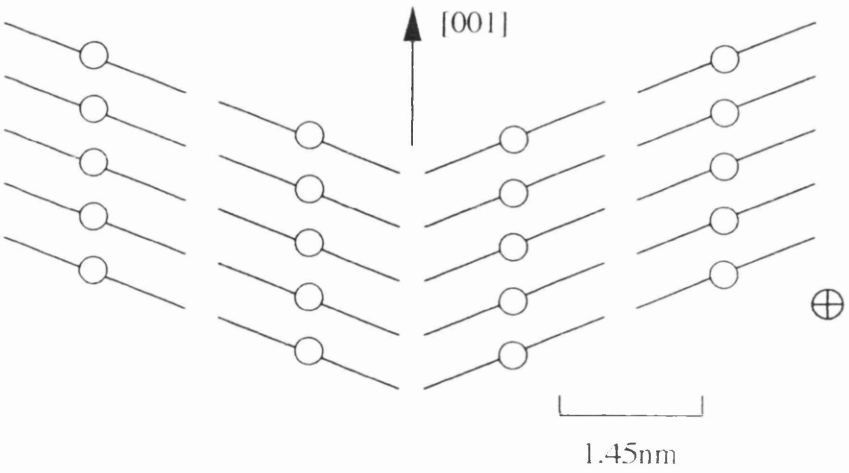

Figure 3.6(a): Schematic diagram of a twinned structure.

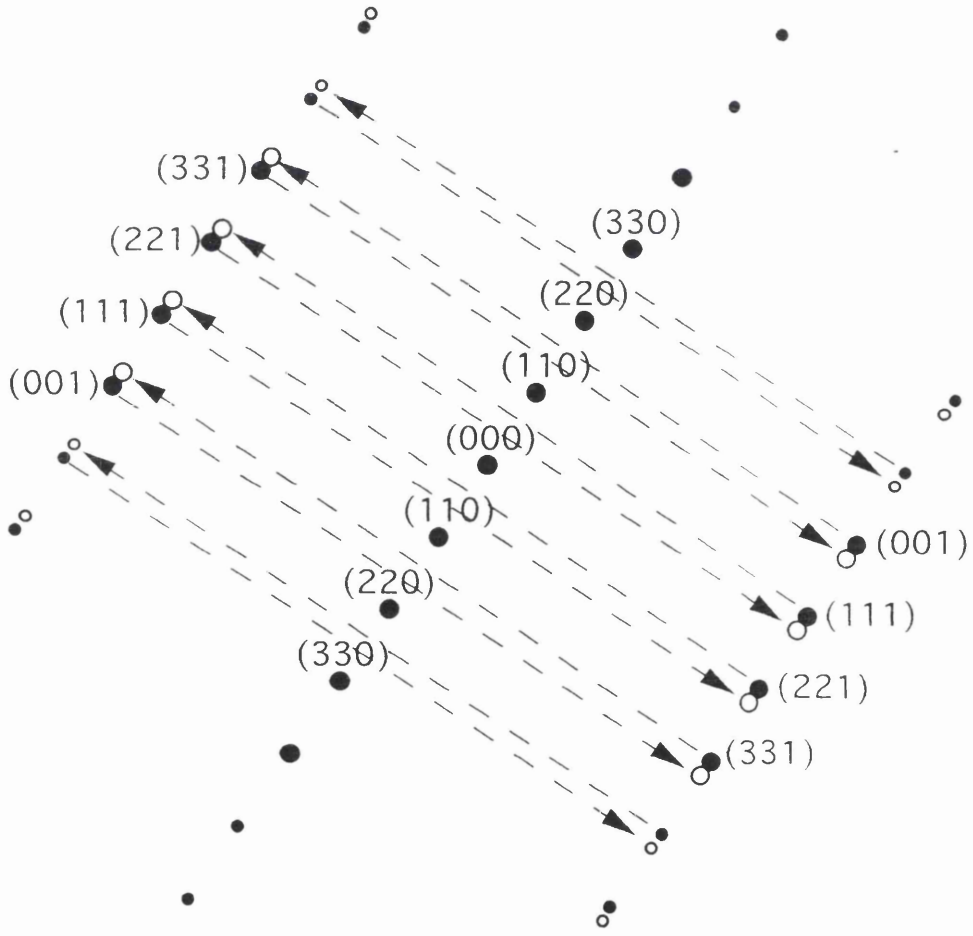

Figure 3.6(b): Plot of the twin spots (open circles) due to twinning about the [110] axis

orientation has no prominent zone axis parallel to the electron beam. The implications of twinning are considered further in the following section.

3.6 Discussion of results from diffraction studies

As mentioned in the previous section, CPC's can exhibit either an α or β crystallographic structures. Highly chlorinated CPC pigments, such as examined here, adopt only the α–type stacking sequence. In this case, the crystals are composed of molecules stacked in parallel to form long oblique columns with the c-axis running parallel to the long dimension (figure 3.5(a)). Since [102] and [110] zones are observed most frequently, it seems reasonable to suggest that the particles are faceted and that these facets are perpendicular to either [102] or [110]. In order to explain why these zone axes are observed frequently while the [100], [014], $[3\bar{1}6]$ and $[10\bar{1}]$ are rarely observed, it is important to understand how the pigmentary material is formed. According to Honigmann (1966), initial CPC crystals form crystalline aggregates which agglomerate into larger non-crystalline agglomerates. The crystalline aggregates are held together by relatively weak Van der Waals forces. Thus the various solvents and surfactants in the pigmentation process break down both the agglomerates and the crystalline aggregates into smaller crystalline particles. These particles would tend to be elongated along the c-axis, since the molecules are tightly bound in this direction. This morphology has been observed previously (McColgan, 1990).

If the particles are elongated along their c-axis then, after deposition by the spraying technique, they will tend to lie flat with the c-axis approximately in the plane of the carbon support film. Indeed, the c-axis and the [102] zone axis are approximately perpendicular (92^{o}). However, it is clear that the particles do not lie in random orientations, with the c-axis in the plane of the film, since the low index [010] zone axes are perpendicular to c and yet were never observed.

Similarly, the $[3\bar{1}6]$ zone lies at ~95° to the [001] and was observed only rarely. However, the angle between the [110] zone axis and the c axis is approximately 105°, and so the occurrence of this zone axes is somewhat more difficult to explain.

Zones perpendicular to the c-axis have the form ($u\underline{a} + v\underline{b} + 2.4u\underline{c}$). For such a zone to be parallel to the normal to the (hkl) planes, the following relationship must be satisfied :

$$(ha^* + kb^* + lc^*) \wedge (u\underline{a} + v\underline{b} + 2.4u\underline{c}) = 0. \qquad (3.1)$$

since $\underline{g}_{hkl}$ is the normal to the planes. Few planes satisfy this relationship exactly. Restricting the choice of planes to those containing the c-axis, i.e. (hk0) planes, then those whose normals are nearly parallel to [uv(2.4)u] minimise :

$$\sin\theta = \frac{[uvw] \times \underline{g}_{hk0}}{[uvw]\,|\underline{g}_{hk0}|} \qquad (3.2)$$

Table 3.3 shows the observed zone axes and the planes nearly normal to them. The plane which is closest to being normal to the common zone [102] is (100). The closest plane normal to [110] is (120), however these are non-parallel by approximately 16°. Furthermore, there are no low index planes (hkl) which are normal to [110].

Figure 3.7 shows the CPC structure looking down the [001] direction and terminated with various facets. This figure shows the $(1\bar{2}0)$ which is equivalent to the (120) plane. It is unclear as to why the apparently prevalent facets, (100) and (120), should form while the (010) and (110) facets are infrequent. However, the particle morphology is a consequence of crystal growth and pigmentation mechanisms and may not correspond to the faces which might be expected from the molecular structure.

u	v	w	h	k	l	theta(degrees)
1	0	2	1	0	0	4.02
1	0	2	1	1	0	34.14
1	0	2	2	1	0	19.01
1	1	0	1	2	0	15.78
1	1	0	1	3	0	17.26
1	1	0	3	8	0	16.26
1	1	0	1	1	0	26.83
1	1	0	1	-3	0	61.48
3	-1	6	2	-1	0	8.56
3	-1	6	1	-1	0	8.38
3	-1	6	3	-1	0	14.18
3	-1	6	3	-2	0	4.22
0	1	4	1	4	0	35.69
1	0	0	3	1	0	29.16
1	0	-1	3	1	0	37.38

Table 3.3 : Observed zone axes and the planes nearly normal to them.

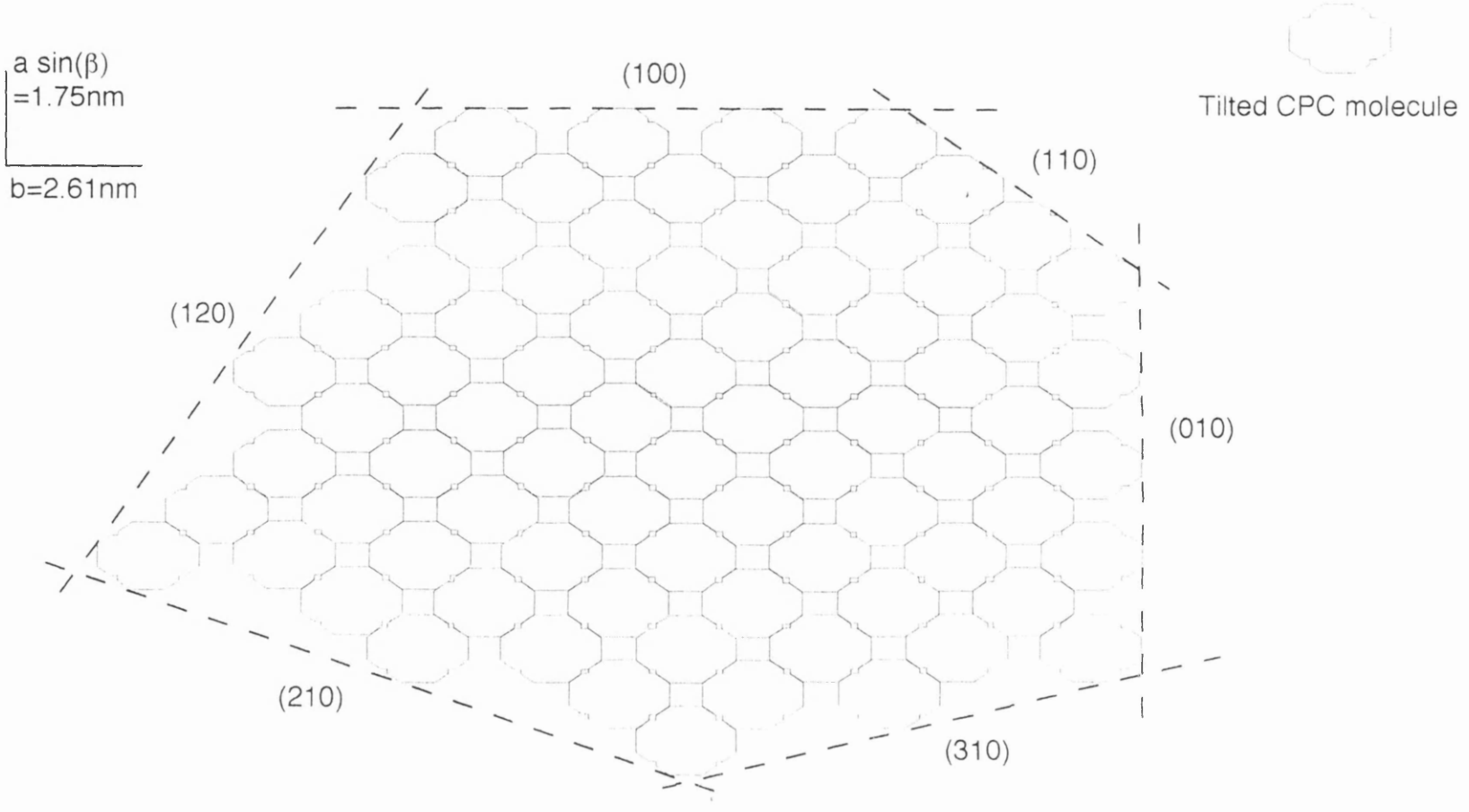

Figure 3.7 : CPC structure looking down [001] direction.

It may be that the actual facets have random rather than exactly regular arrays of steps and so only approximate to the observed normals. The presence of such steps is closely tied up with traditional ideas of crystal growth/dissolution. The step would normally be considered not to run the whole length leaving a corner site somewhere along its length. This corner site allows a single additional molecule to match a face and two edges and is the site with the greatest binding energy on a {110} type facet. Such a corner site is shown schematically in figure 3.8(a). This model of crystal growth seems reasonable in a molecule by molecule growth mechanism but it is difficult to see how a twin would nucleate in such a mode. It would seem more likely that to get a twin forming on a {110} type plane, a section of crystal which had grown in the twinned form already would have to land on the plane, as in figure 3.8(b). It is difficult to believe that a very long length could orient itself correctly to do this. More likely is that short lengths of column adhere to nucleate the twin and this then grows either by single molecules or small sections adding on. This micro-twinning model reveals that non crystallographic boundaries are formed where twinned and non-twinned regions come together. If twin nucleation occurs in this way, then the material could contain many fine microtwins and lots of non-crystallographic boundaries.

Turning to twinning in more detail, two possible models for the twinning mechanism will be discussed. In the first, model A, several possible orientational variants exist. Figure 3.9 shows the various orientations that can occur due to twinning about the $(1\bar{1}0)$ and (110) planes. If region 1 has a (110) twin boundary with region 2 then it could also have a $(1\bar{1}0)$ twin boundary with region 3 i.e. there are now three orientations present. If region 2 twins on a (110) plane, it will generate a fourth twin and so on. As a consequence some regions of crystals will meet in a way that requires a non-crystallographic boundary to occur. The number of orientations could continue to grow if twinning continued. Diffraction patterns were calculated, using Diffract, for the simultaneous presence of regions 1, 2 and 3 shown in figure 3.9. Since it has been suggested that the material

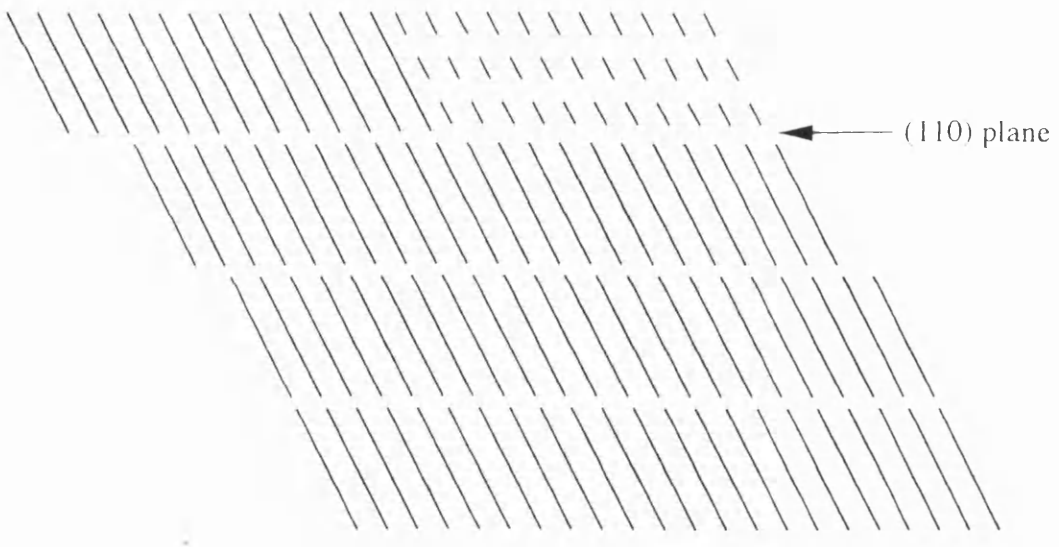

Figure 3.8(a) : Schematic corner site on a {110} plane. Dashed lines show molecule missing from top layer.

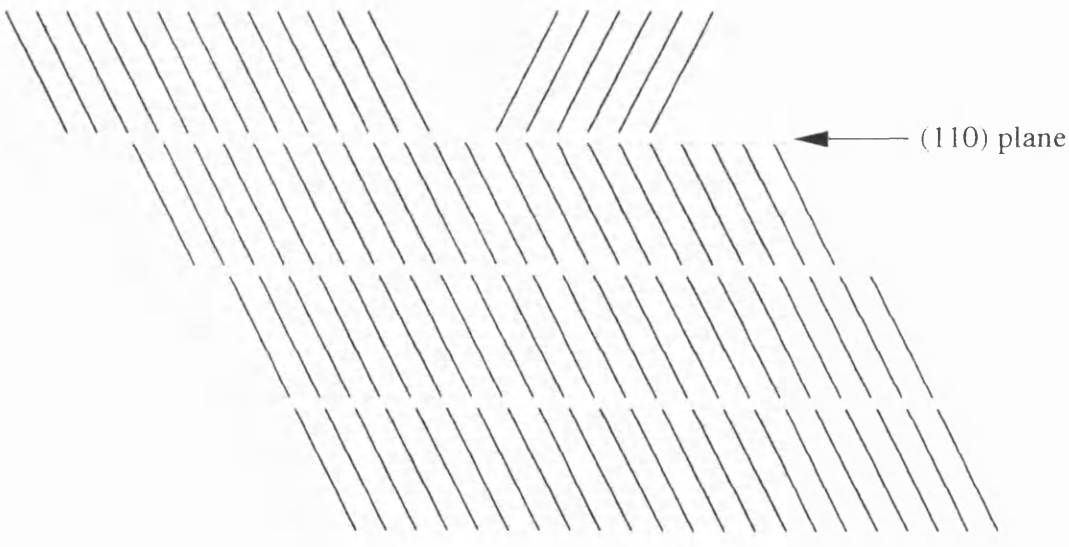

Figure 3.8(b) : A section of twin formed by the addition of a block of twinned material

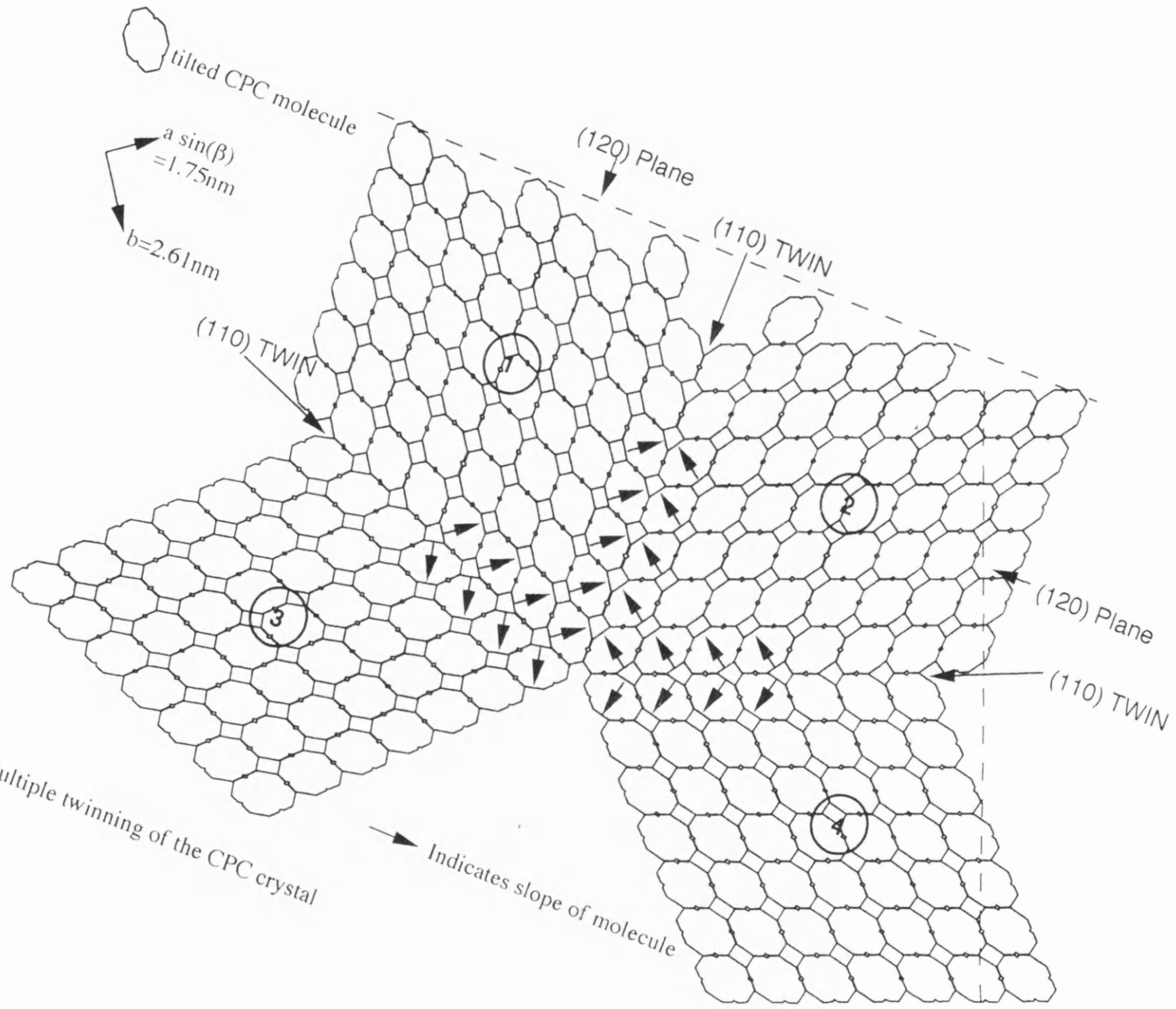

Figure 3.9 : Multiple twinning of the CPC crystal

consists of fine microtwins, the twinned regions were limited to 10nm in width. Figures 3.10(a) and (b) shows the resulting diffraction patterns for [110] and [102] zone axes, respectively. For the [110] zone axis, it is possible that as the number of twins increases the spots are smeared to form streaks, as was observed in the recorded diffraction patterns (figure 3.1). There are much fewer extra spots in the outer lines for the [102] zone axis. This is also consistent with the recorded diffraction patterns shown in figure 3.1, where the diffraction patterns which have a [102] zone axis appear much less streaked than those with a [110] zone axis. The large number of diffraction patterns with a [110] zone axis which were heavily streaked suggests that twinning is extensive, as was suggested by the microtwin model. It also reflects the small energy difference that is involved when the columns of molecules bind in almost equivalent orientations.

The various twin orientations presented in figure 3.9 show that the {120} planes are essentially preserved by the appropriate mirror action. It is this plane which is the closest low index plane normal to the [110] zone axis. However, as stated earlier, the normal to this plane is inclined to the [110] zone by approximately 16°. It is also difficult to see why twinning would encourage the (100) facet.

The second model for the twinning mechanism, model B, is now discussed. The crude material used in the manufacture of the halogenated CPC pigments adopts the β-type crystal structure. The pigmentation process produces crystals of the α-phase, as shown in figure 3.5(a). Whilst it is possible that the original crystal facets corresponded to low index β-phase planes, after transformation the facets may not correspond to low index α-phase planes. This may be an explanation for the facets normal to the observed [110] zone axis. However, not enough information on the transformation mechanism is available and therefore this is only speculative. Since unhalogenated CPC with a β-type structure is used to produce chlorinated CPC in the α-phase, this may explain the presence of twins in this structure. The herring bone structure of the β-phase is

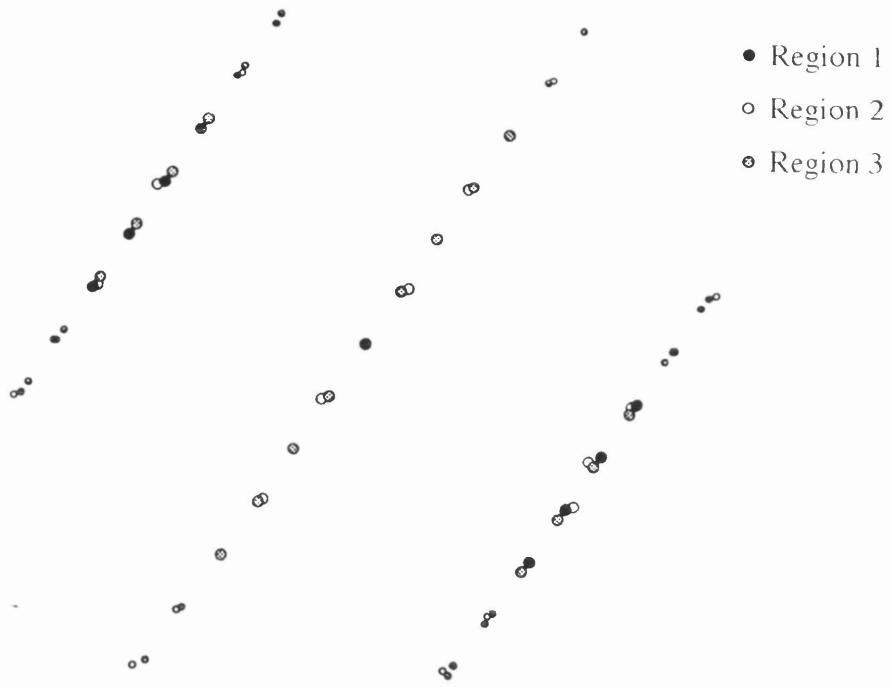

Figure 3.10(a) : Diffraction pattern for a [110] zone axis. CPC crystal twinned about the (110) and (110) planes.

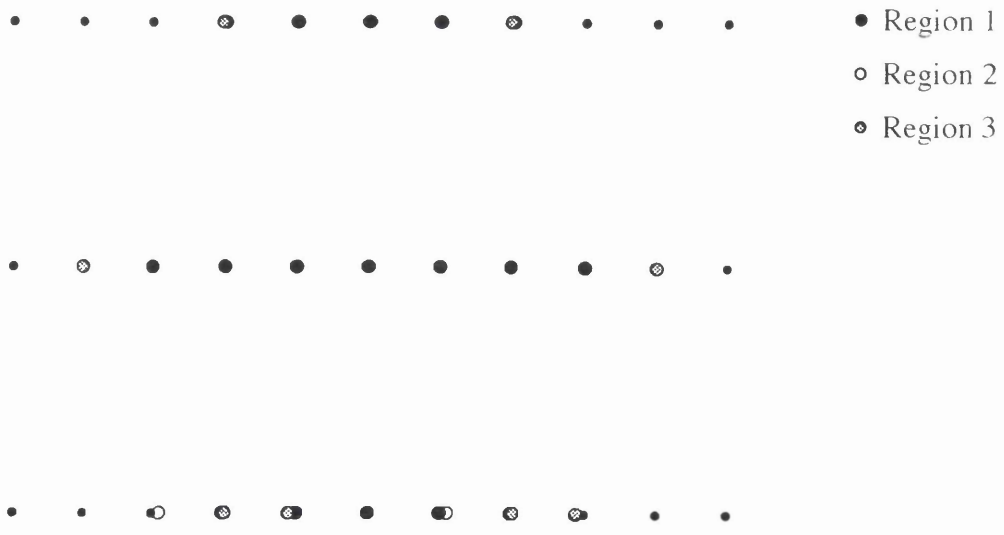

Figure 3.10(b) : Diffraction pattern for a [110] zone axis. CPC crystal twinned about the (110) and (110) planes.

similar in some ways to the twin structure shown in figure 3.6(b) and observed in the chlorinated CPC studied here. It seems reasonable to suggest that during the transformation from the β to α phase this twin structure is formed. This model implies that the twins come from an original β crystal so that only two orientations will be present; the "matrix" and "twin" orientations. The implications of models A and B for the lattice images are discussed later.

The faceting may also be a result of how the pigmentation process breaks down the intermediate material into smaller aggregates. It may be that the particles are broken down along particular facets. It is known that the larger aggregates are split at weak areas where defects are present. One such area may be where non-crystallographic boundaries occur as a result of twinning (figures 3.8(b)). In this case the most likely facets would be the (110) or $(1\bar{1}0)$ planes. However, if these facets are formed and the particles lie on them on the support film, they would not present a prominent zone axis to the electron beam.

It is clear that several factors can affect the morphology of the CPC particles. The exact processes involved are not clear and only assumptions about mechanisms can be made. Thus there is no method of predicting the faceting on the particles. The subject of particle morphology is considered further in section 3.9 and in the following chapter.

3.7 Low magnification results

As mentioned in the introduction to this chapter, low magnification images provide information about the size, shape and distribution of the pigment particles. For a pigment to give any appreciable colouring strength the aggregates of pigment powder must be broken down to less than one micron in size. A series of low magnification images were recorded for each sample in order that a comparison of the samples from different batches and the samples produced using

different processes could be compared. It was observed that in every sample the pigments did not break down to their primary particles but were made up of small aggregates consisting of several primary particles. Figures 3.11(a) & (b) and 3.11(c) & (d) show images recorded from the paint pigment samples A1 and A2, respectively. The first noticeable difference between these two samples was the greater number of large dark clumps of material in the poor sample A2. The particles in sample A1 are rod-like in shape with a maximum dimension of ~100nm, whereas, in sample A2 the particles are generally smaller with a maximum dimension of ~50nm. These observations are helpful in explaining why sample A2 has a poor dispersibility and gives a strong blue bright colour. Smaller particles can come into contact with each other more intensively and frequently due to their greater surface area so that the forces of attraction, van der Waals forces, come into play more readily. Thus the particles tend to form more compact aggregates, making it more difficult to disperse them. The high strength of attraction also means that particles which have been separated can form flocculates. While the flocculates can be broken up by shear or rapid stirring they are quickly reformed and the pigment never achieves its potential colour strength. Flocculation could be the cause of the strong blue bright colour of sample A2 since one effect of this phenomenon is a change in hue.

Figures 3.12(a) & (b) and 3.12(c) & (d) show images recorded from the plastic pigment samples B1 and B2 respectively. The main difference between the standard pigment, B1, and the poor pigment, B2, is the wider particle size distribution in sample B2. It has been suggested by Merkle and Herbst (1968) that a wide size distribution is detrimental to the dispersibility of a pigment and thus would explain the poor colour development of sample B2.

Images recorded from the samples prepared using different processes are presented in figures 3.13(a) - (d). The most notable difference between the four samples is the shape of the pigment particles. The edges of the particles in sample C1 and C2 are rounded and have maximum dimensions ~50-100nm. The particles

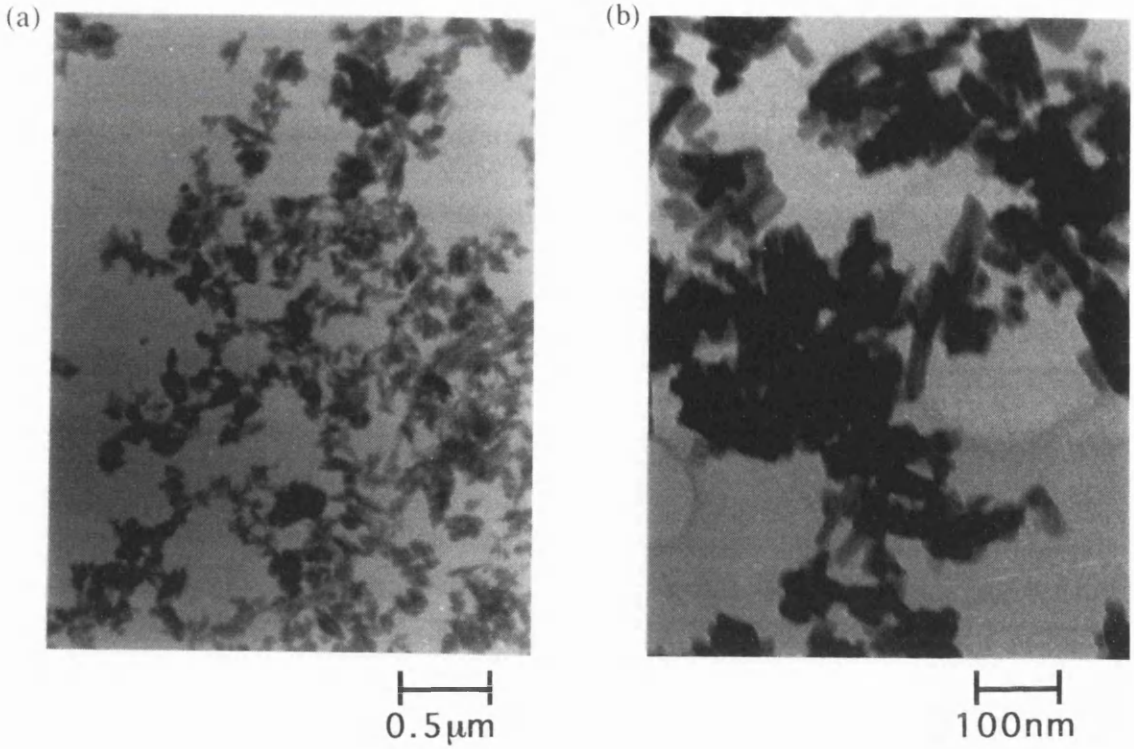

Figure 3.11(a) & (b) : Low magnification images recorded from sample A1.

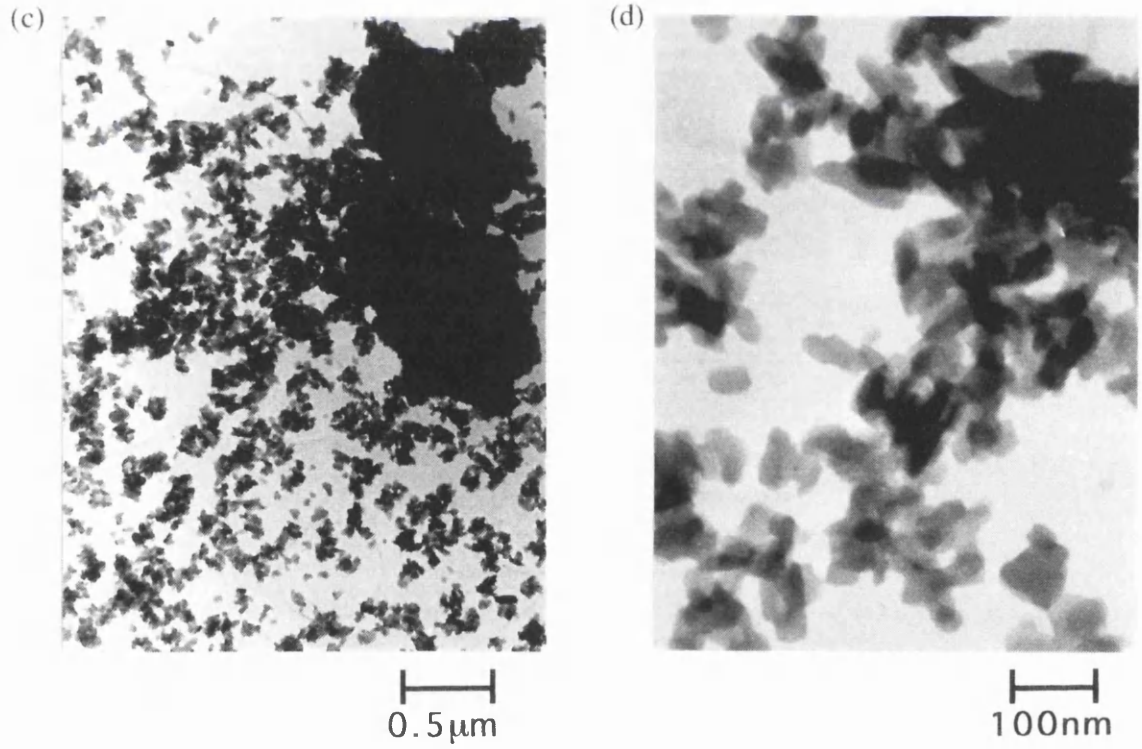

Figure 3.11(c) & (d) : Low magnification images recorded from sample A2.

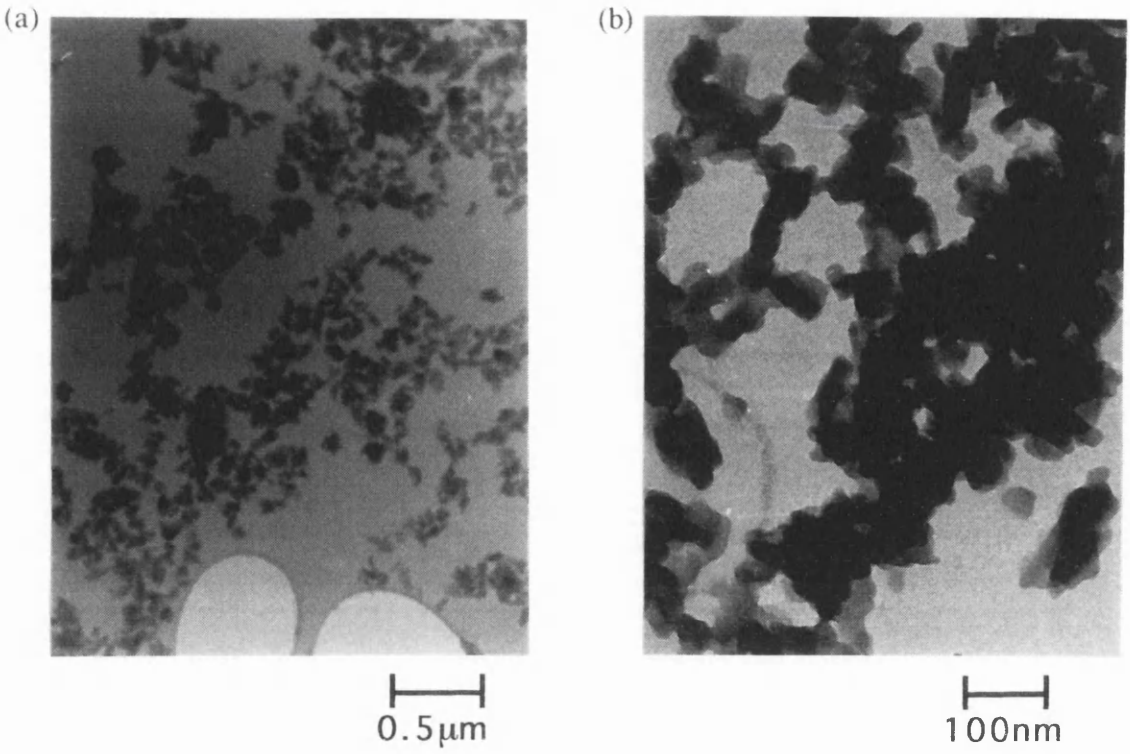

Figure 3.12(a) & (b) : Low magnification images recorded from sample B1.

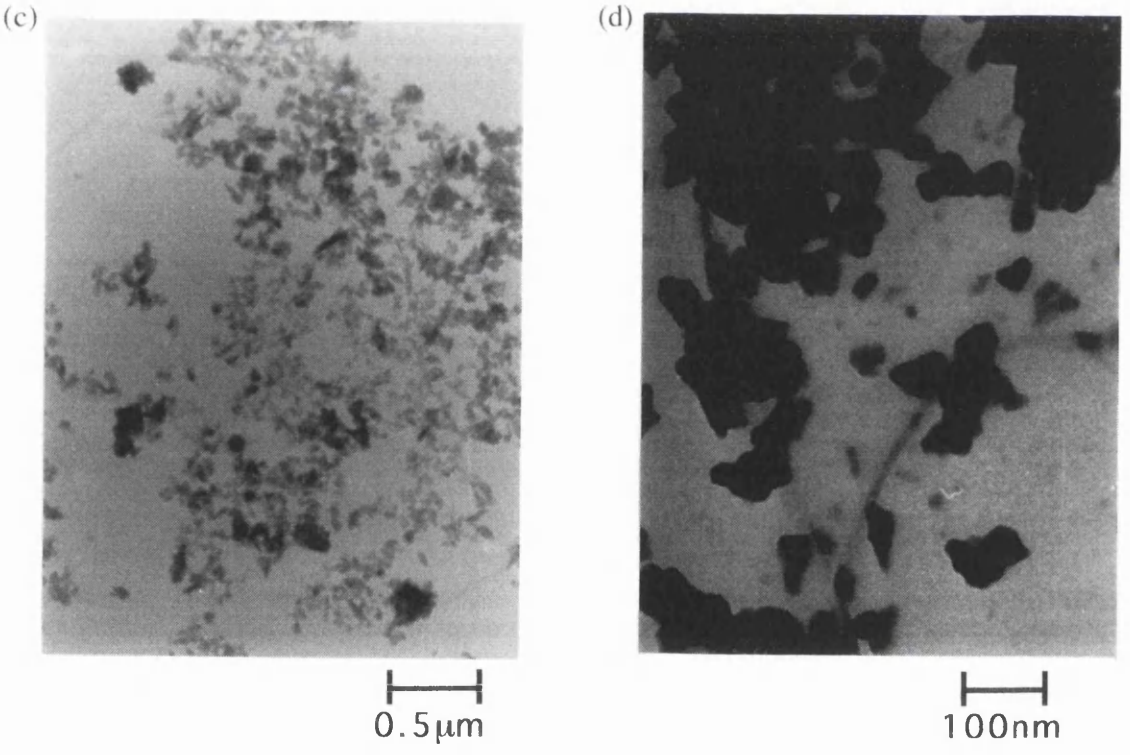

Figure 3.12(c) & (d) : Low magnification images recorded from sample B2.

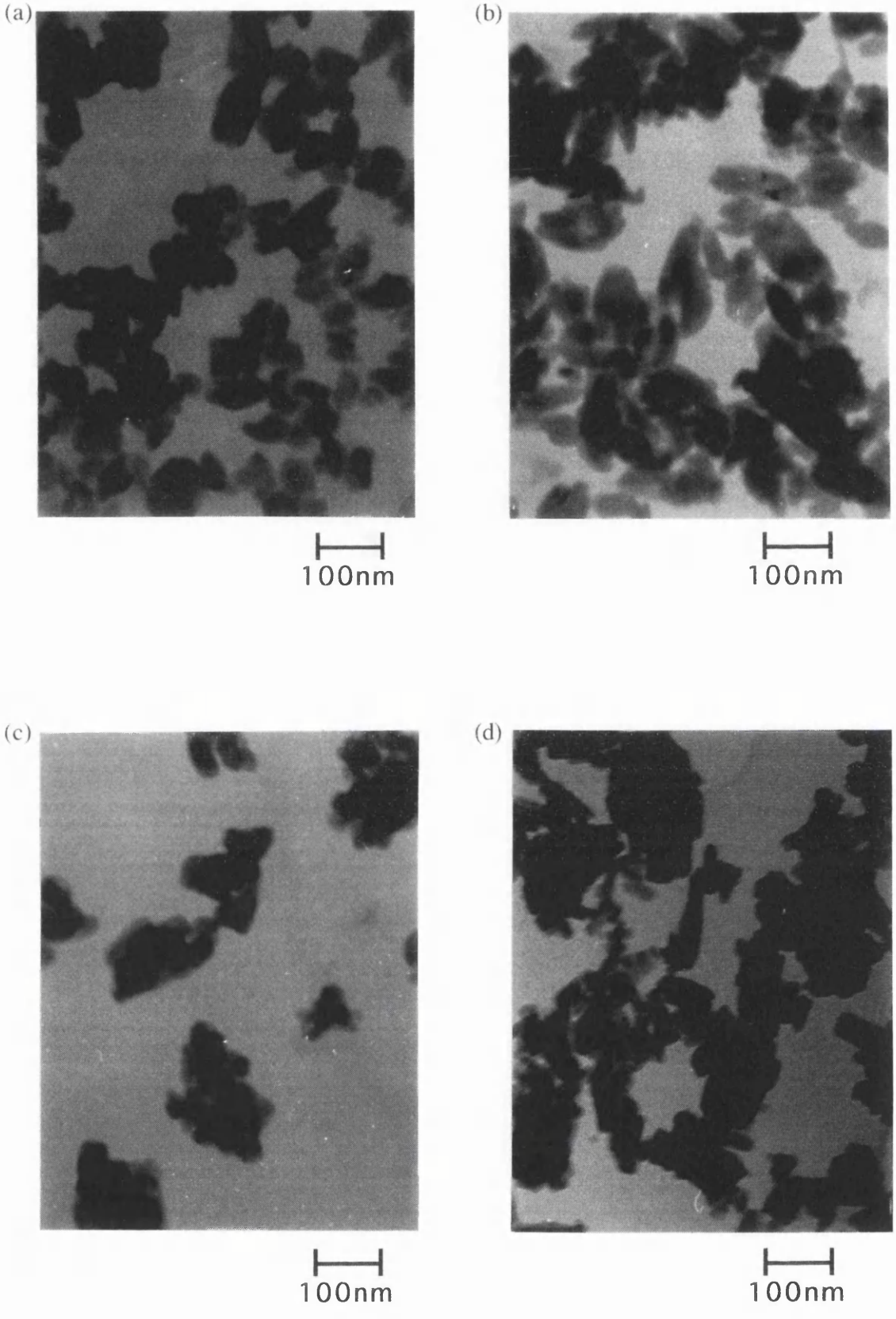

Figures 3.13(a) - (d) : Low magnification images recorded from samples C1 - C4, respectively.

in sample C3 are more brick shaped with rounded corners and have maximum dimensions ~50-100nm. The particles in sample C4 are rod-like with straight edges and many of the particles have a maximum dimension ~200nm. These observations are useful in explaining why samples C1 and C2 give the best colour development, sample C3 is the next best and sample C4 has the poorest colour development. The area of possible contact between particles in which the edges are rounded is limited and thus the probability of these particles reaggregating in the application medium is reduced. However, in a pigment containing particles with long straight edges there is a larger possible area of contact between the particles and thus there is a greater probability of reaggregation of particles in the application medium.

3.8 Instrumental considerations in lattice imaging

A lattice image is formed when the transmitted beam and one or more of the diffracted beams are allowed to pass through the objective aperture. Figure 3.14 shows a schematic diagram of the formation of a lattice image for the two beam case of the undeflected beam and one Bragg reflection. The angle between the transmitted beam and the Bragg reflected beam is $\alpha=2\theta_B$. The transmitted and diffracted beams can be made to recombine in the image plane to form interference fringes with a separation dM, where d is the interplanar spacing in the crystal and M is the magnification of the electron optics. To obtain high contrast lattice fringes it is important that highly coherent illumination is incident on the specimen. This was achieved using a 40μm condenser lens and a spot size of 3. A further important factor in being able to resolve the lattice fringes is the correction of the objective lens astigmatism. The lattice fringes in highly chlorinated CPC are visible at magnifications of 200kX - 250kX and it is also important when recording these lattice fringes that the incident electron dose be kept as low as

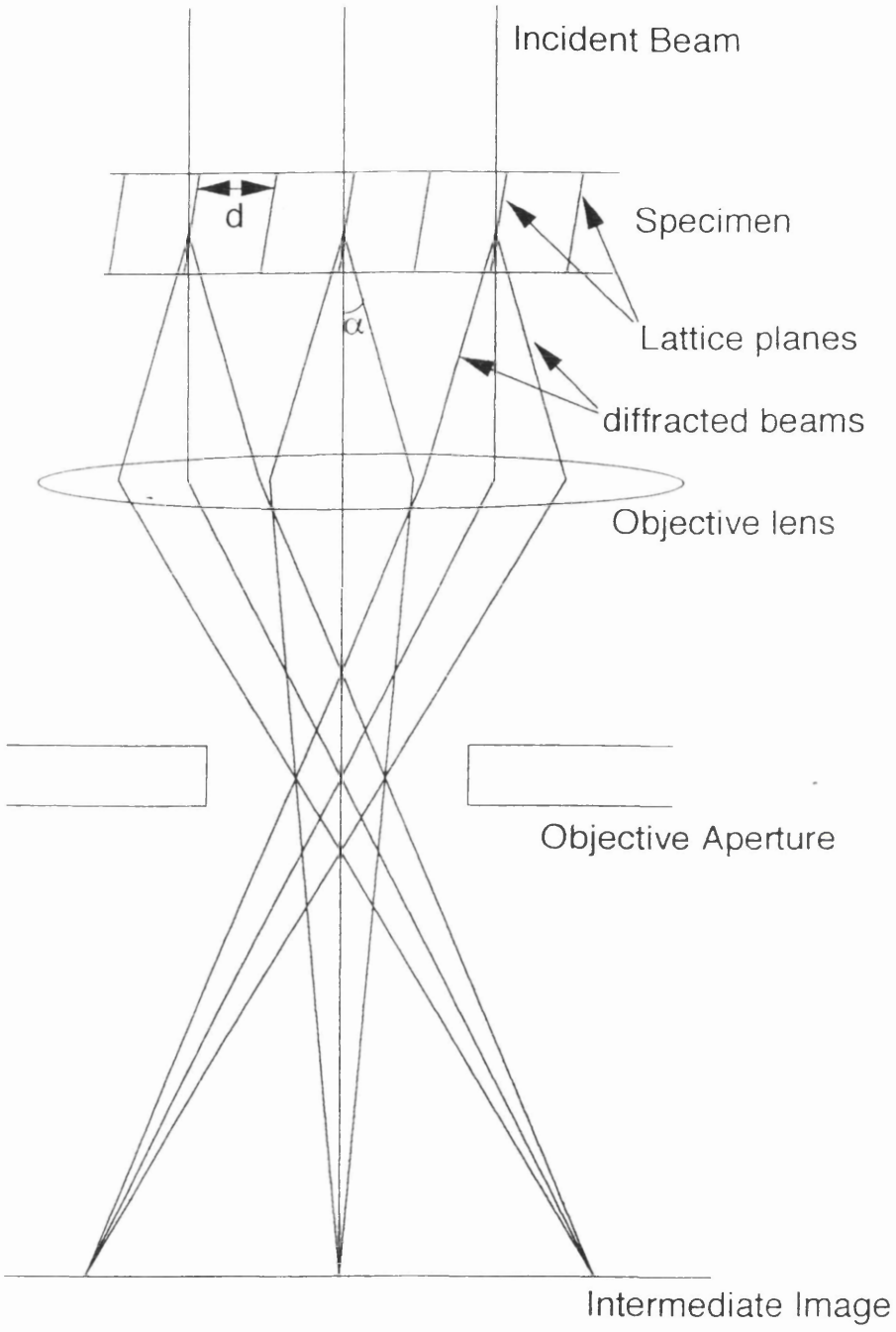

Figure 3.14 : Schematic diagram showing formation of a lattice image

possible to minimise the damage to the specimen. One way in which this can be achieved is to record the lattice images using fast photographic emulsions which allow low exposure times to be employed. To satisfy this requirement CEA Reflex-15 x-ray film was used in this project. This allowed high contrast lattice images to be recorded with an exposure time of 1s and a current density of ~1pAcm^{-2} (as measured at the viewing screen). As this corresponds to a dose of ~1Ccm^{-2} which is substantially less than the critical dose (the dose necessary to reduce diffraction spot intensities to 1/e of their pristine value) for these materials, the images recorded are virtually free from damage.

3.9 High magnification results

Lattice images from the highly chlorinated pigment samples are shown in figures 3.15 - 3.17. Figures 3.15(a) - (b) show lattice images recorded from the paint pigment sample A1. These images contain lattice fringe spacings of 1.40 ± 0.05nm, which correspond to the $(1\bar{1}0)$ plane spacing. In figure 3.15(a) there are areas of darker contrast than others, indicating areas of different thickness. This observation together with the size and shape of the aggregate would indicate that it was made up of several pigment particles. However, the lattice fringes are continuous across this aggregate indicating that it is probably an aggregate of particles which have not been broken down by the pigmentation process. Similar aggregates were observed in all the samples investigated. Several of the lattice images showed areas similar to those shown at **a** in figure 3.15(b). There may be two possible explanations for these areas. The lattice fringes may have been destroyed as a result of beam damage. Alternatively, this may be a twinned region formed following model A, described in section 3.6 It was also noted that in many of the lattice images the fringes do not extend to the particles edges. Radiation damage is probably the most likely explanation for this. Fryer (1984) showed how

(a)

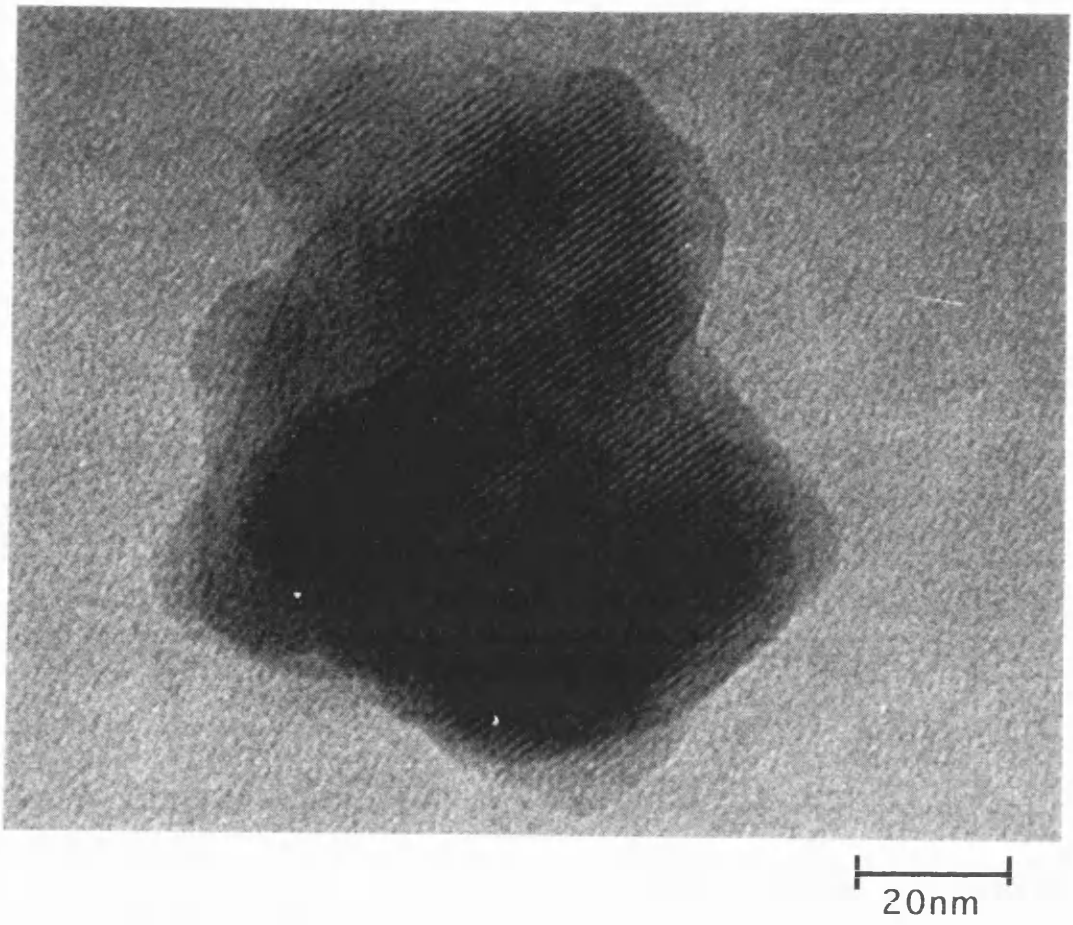

(b)

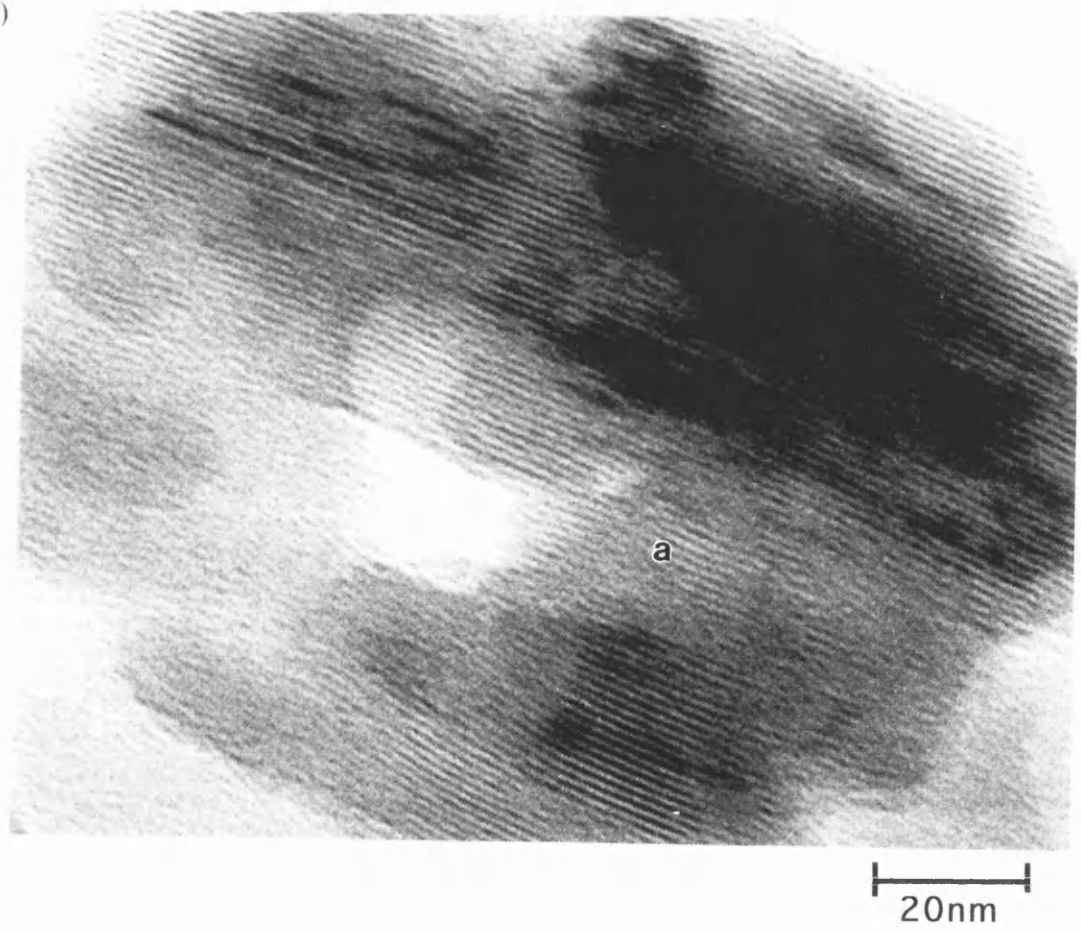

Figures 3.15(a) & (b) : Lattice images recorded from sample A1.

(c)

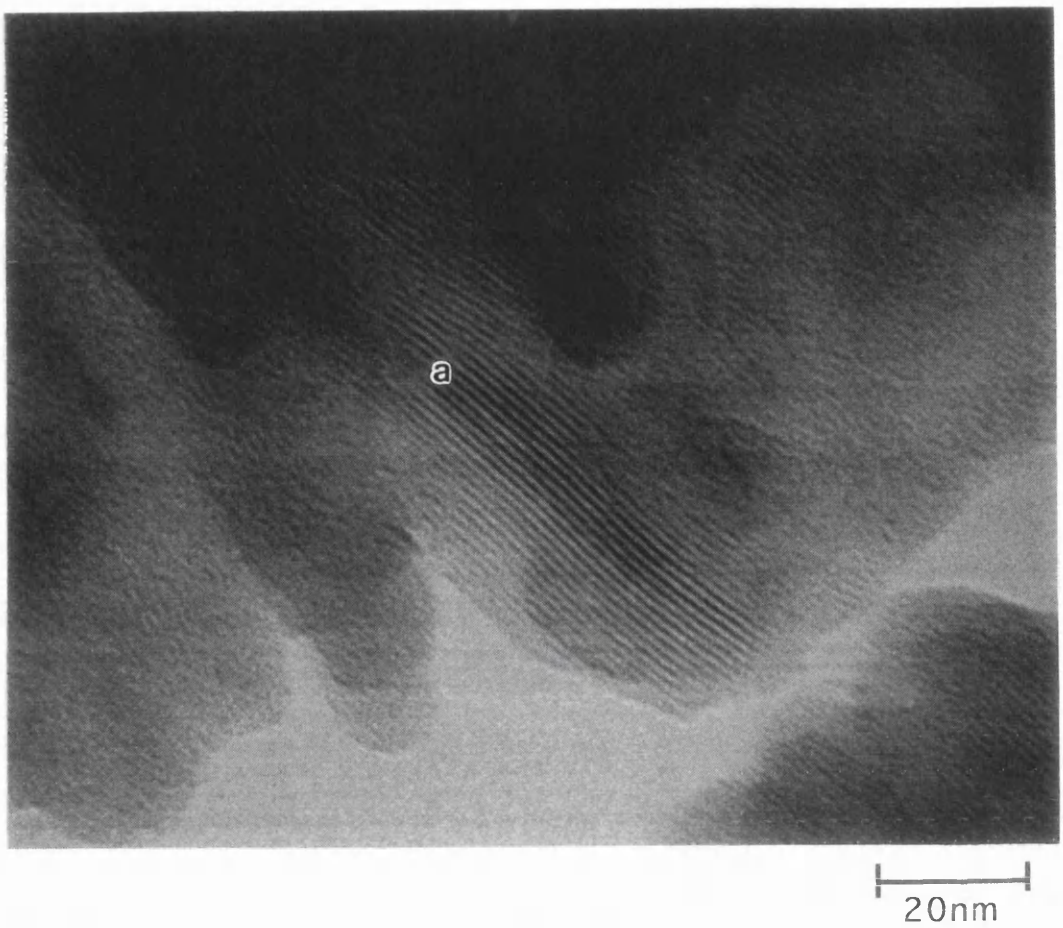

(d)

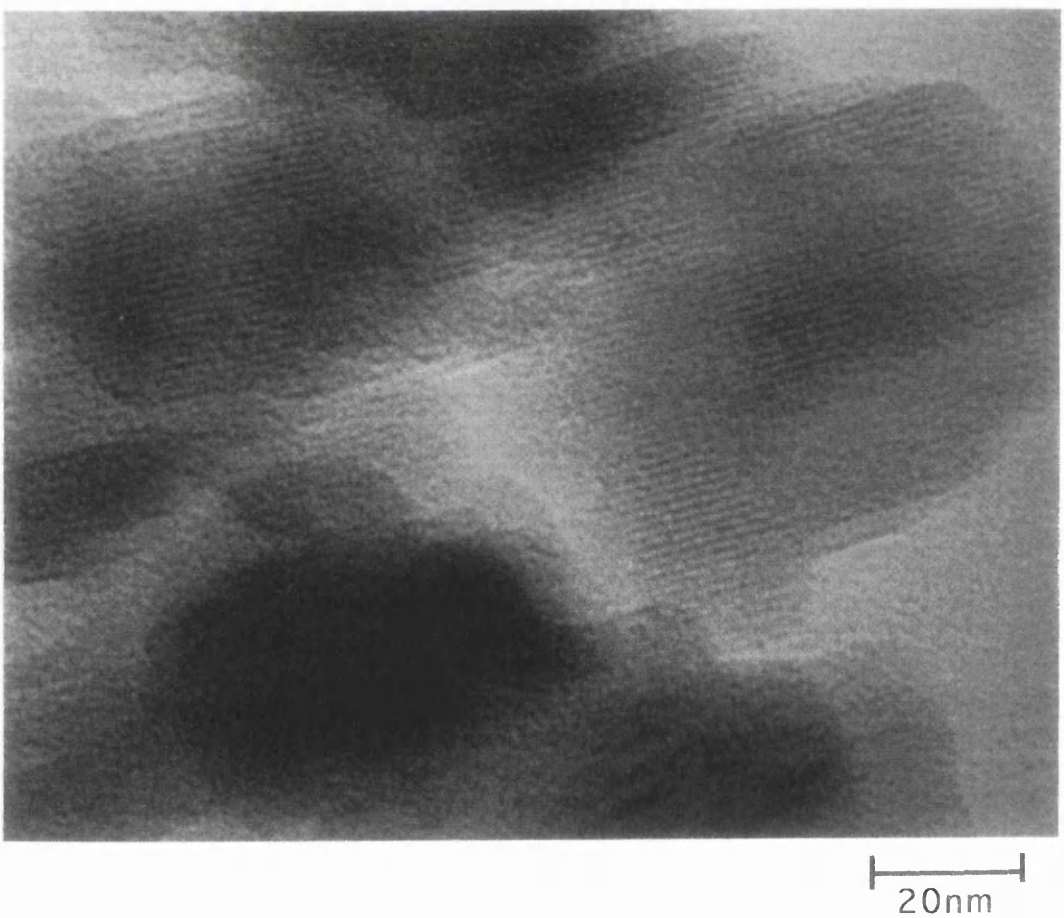

Figures 3.15(c) & (d) : Lattice images recorded from sample A2.

(a)

(b)

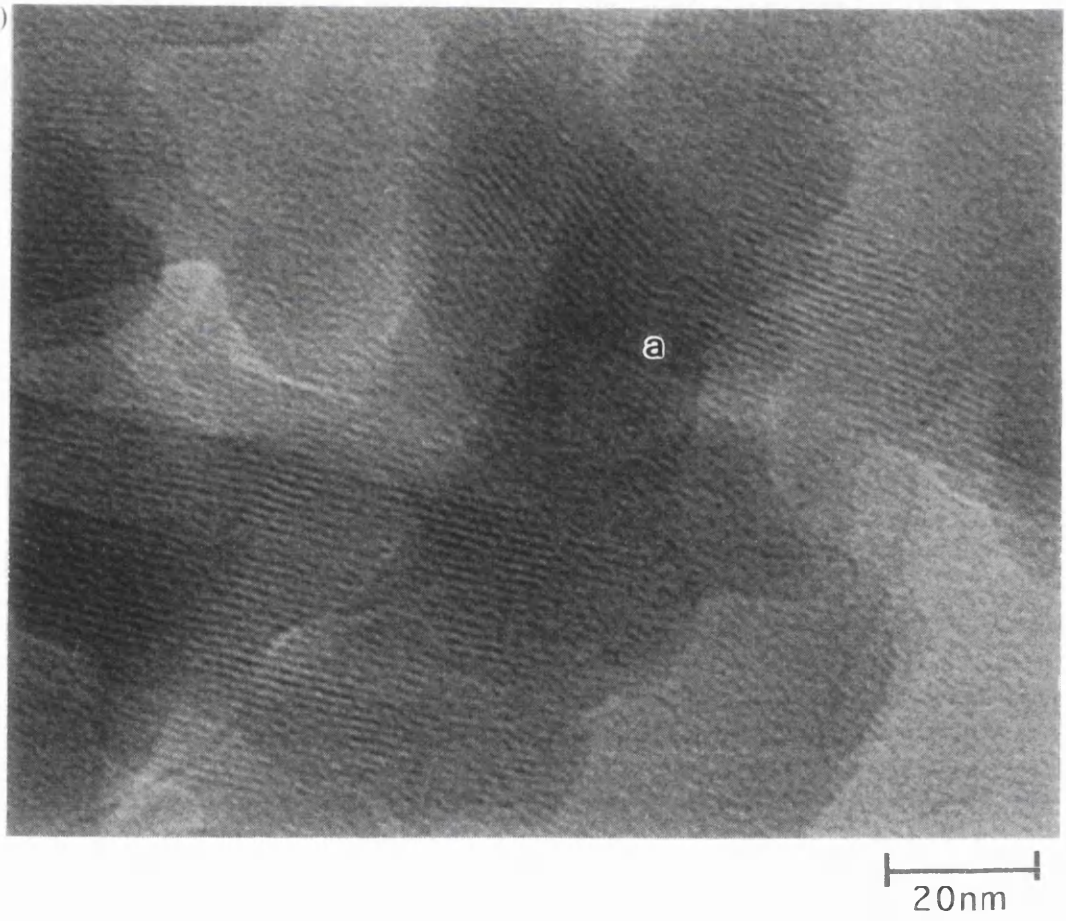

Figures 3.16(a) & (b) : Lattice images recorded from samples B1 and B2, respectively.

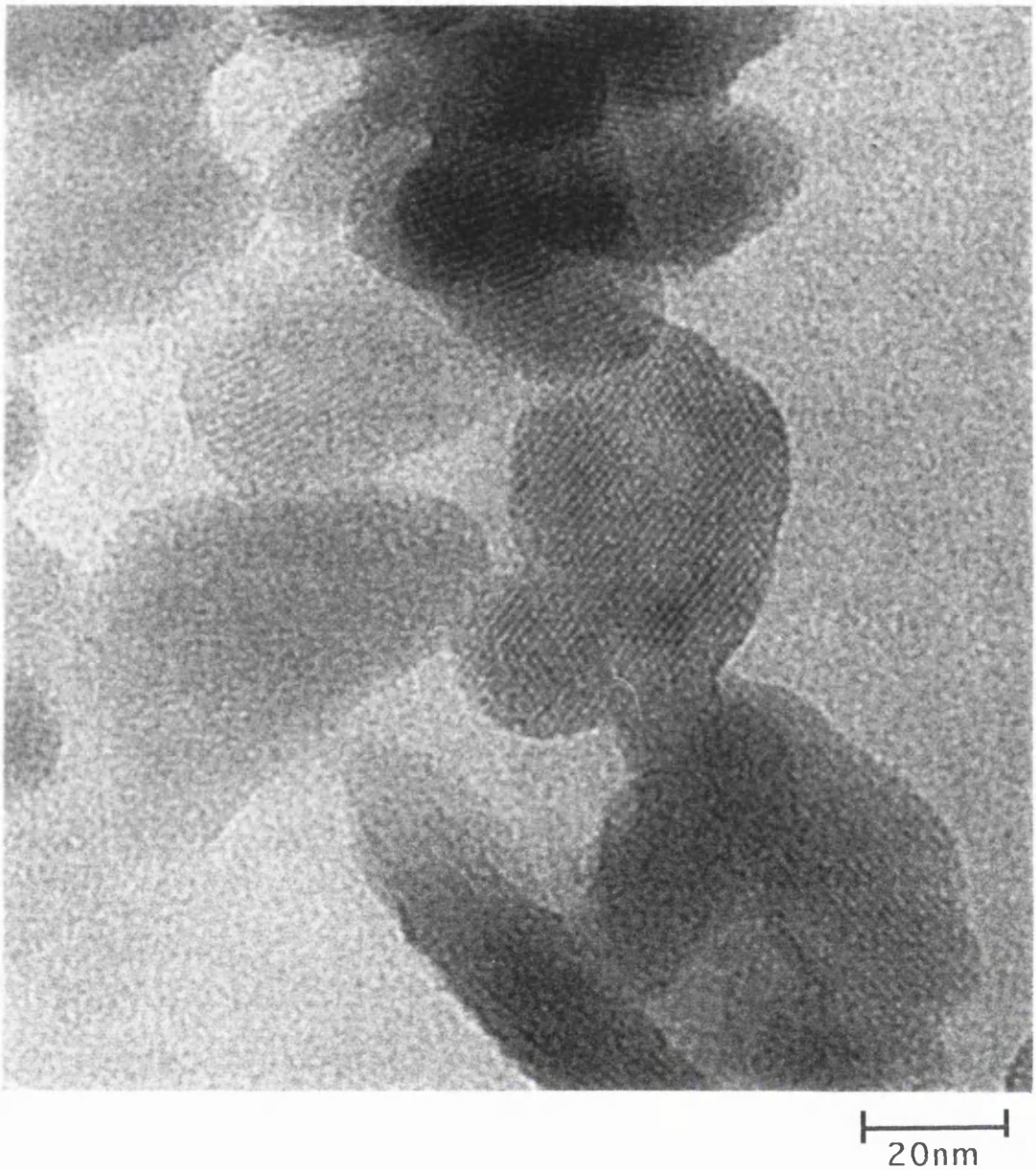

Figure 3.17(a) : Lattice image recorded from sample C1.

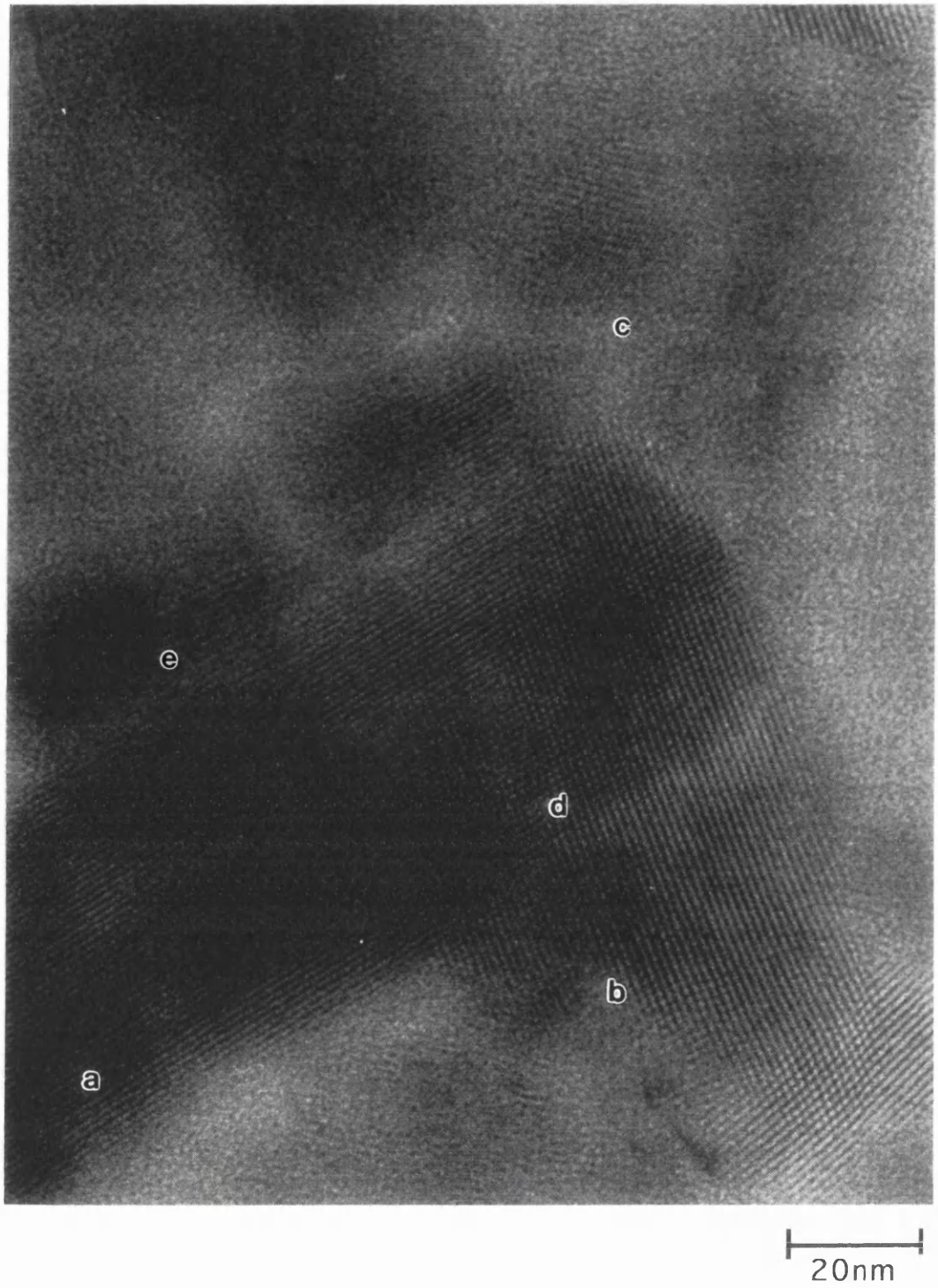

Figure 3.17(b) : Lattice image recorded from sample C2.

(c)

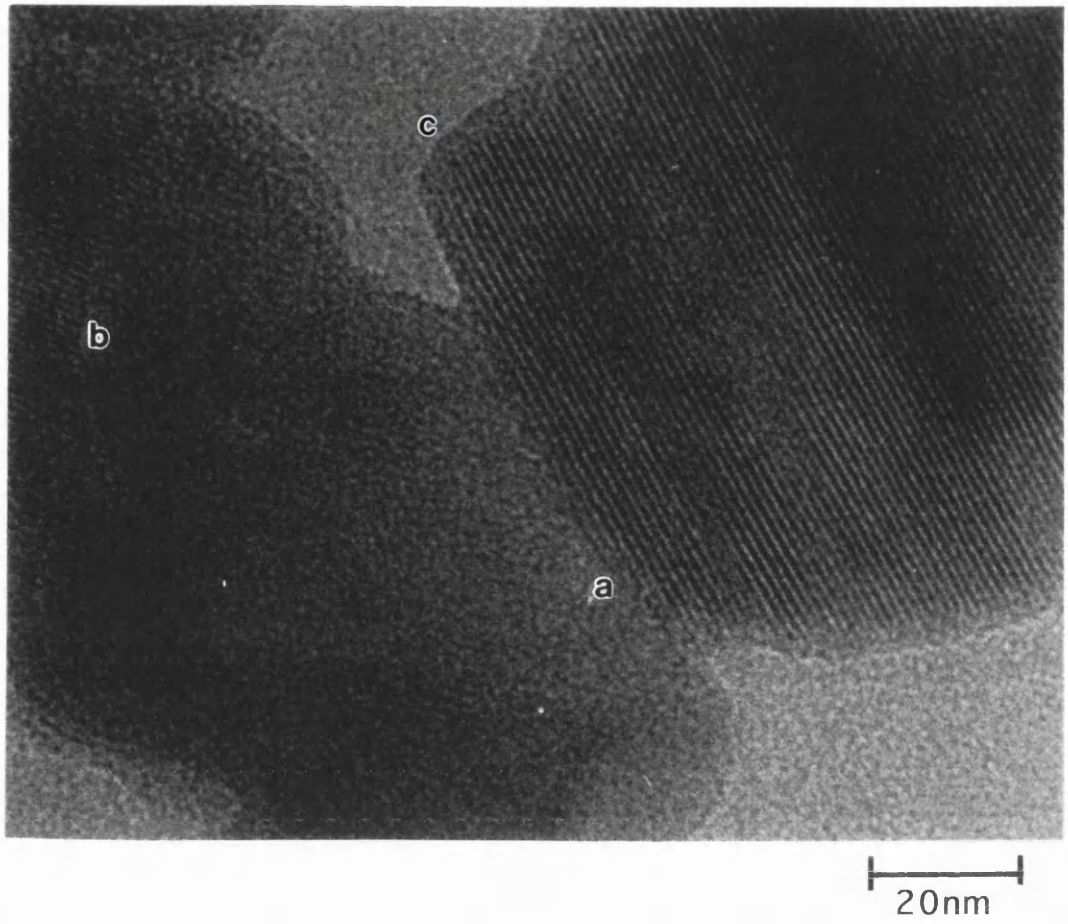

(d)

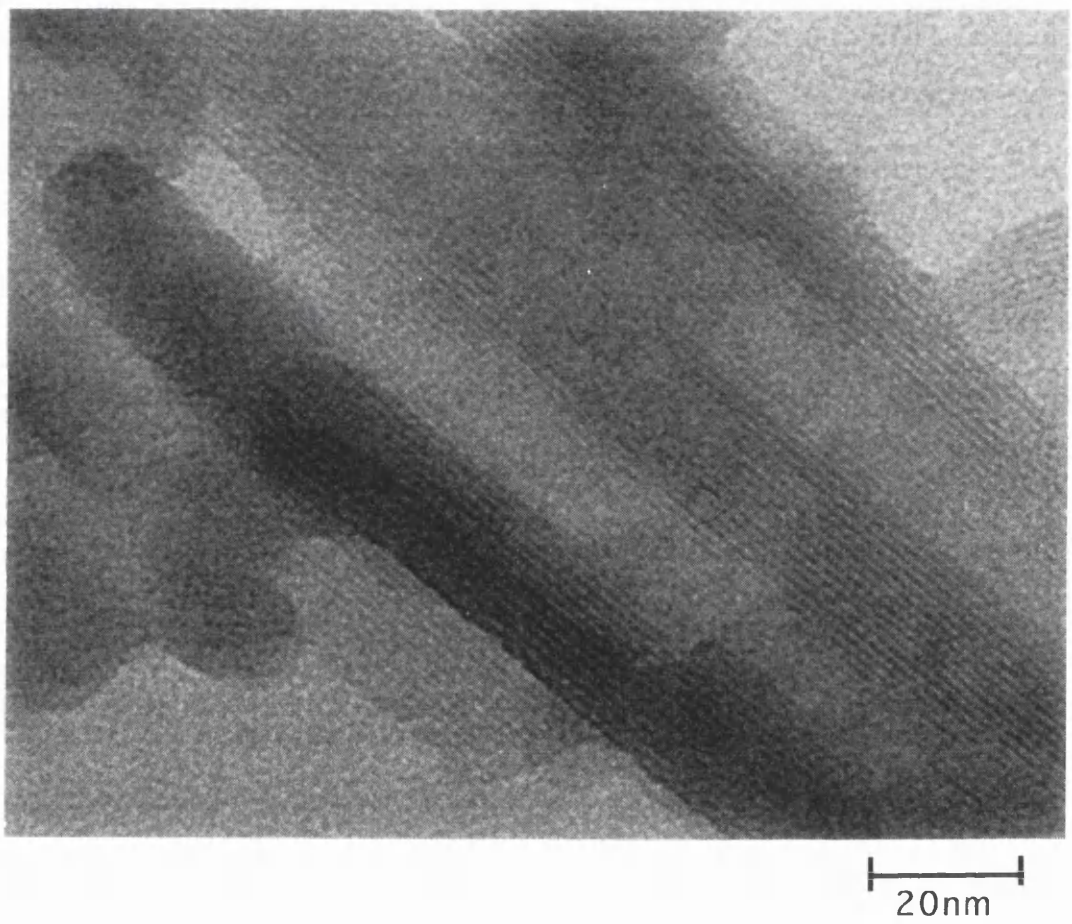

Figures 3.17(c) & (d) : Lattice images recorded from sample C3 & C4, respectively.

radiation damage develops in chlorinated CPC crystals. The crystal detail will first start to disappear around the crystal edges because of the increased probability of any displaced chlorine atoms there being able to diffuse out of the crystal. In the crystal bulk, the molecules are more tightly bound and, since this makes it more difficult for the large chlorine atoms to move around, recombination is much more likely. However, at crystal defects molecules are not generally as well packed and the rate of damage is increased in these areas. Section 3.6 showed that as a result of twinning non-crystallographic boundaries would occur. If the twinning model A operates within these particles, it is reasonable to expect that radiation damage would be observed at the consequent non-crystallographic boundaries.

Figures 3.15(c) and (d) are lattice images recorded from the paint pigment sample A2. Both these images contain lattice fringe spacings of 1.40 ± 0.05nm. Another feature frequently observed in all the lattice images are edge dislocations, which can be clearly seen at **a** in figure 3.15(c). Near the dislocation the crystal is highly strained, as can be seen by the bending of the lattice fringes around this area. There is also some loss of lattice fringe detail in this area indicating that radiation damage has occurred.

Figures 3.16(a) and (b) show lattice images from the plastic pigments B1 and B2 respectively. Both images show lattice fringe spacings of 1.4 ± 0.05nm. At **a** in figure 3.16(a) there again appears to be areas in which the lattice fringes are lost. In figure 3.16(b), whilst there is severe bending of the lattice fringes at **a**, they do remain almost continuous throughout the particle.

Lattice images from samples C1, C2, C3 and C4 are presented in figures 3.17(a) - (d) respectively. In figure 3.17(a) there is an area of crossed lattice fringes. Both fringe spacings are 1.40 ± 0.05nm and the angle between the fringes is 68^{o}. These the fringes correspond to the (110) and $(1\bar{1}0)$ lattice plane spacings. This indicates a zone axis of [001] i.e. the c-axis is parallel to the incident beam and thus the image is a projection of the planar molecules stacked in columns.

The image shown in figure 3.17(b) shows several lattice fringe spacings of 1.24 ± 0.05nm and 1.40 ± 0.05nm at **a** and **b**, respectively. There is also a small region of fringes at **c** with spacings of 0.86 ± 0.05nm. The 0.86nm lattice fringe spacings were observed infrequently and correspond to the (200) lattice plane spacings. This image also shows an area of crossed lattice fringes at **d** with spacings of 1.4nm and 1.3nm. If this area of crossed fringes occurred in a single particle the angle between the fringes would be 58^{o}, however, the angle was measured to be 79^{o} indicating that the crossed fringes are a result of overlapping particles. The other areas of this image showing crossed lattice fringes are also the result of overlying particles. There is also a small area of what looks like beating fringes at **e**. The spacing of these fringes is 1.61 ± 0.05nm which do not correspond to any of the plane spacings observed using diffraction. This type of beat pattern or parallel Moiré pattern occurs when two crystals of different spacing overlap to produce a structure with a double periodicity. Figure 3.17(c) shows lattice fringe spacings of 1.40 ± 0.05nm and 1.24 ± 0.05nm at **a** and **b**, respectively. In this image, as with many of the other images recorded from the various samples, it is clear that the lattice fringes do not appear to extend to the edges of the particles. It is clear from this image that at **c**, close to the particle edge, the lattice fringes are slightly bent. Bending of the lattice fringes and variations in lattice fringe intensity, where the lattice fringes are perpendicular to the particle edge, can occur due to changes in the thickness of the particle at its edge (Hirsch et al. 1977). Figure 3.17(d) contains lattice fringe spacings of 1.40 ± 0.05nm. As in the previous lattice images, there are areas where the contrast is reduced or lost, giving "patchy" lattice fringes on the particles.

In all the samples investigated, lattice fringe spacings of 0.36nm were not observed. A much greater dose is required to observe these fringes with the same contrast as shown in the images presented here. However, at such a high dose the lattice fringes are destroyed by radiation damage.

It was suggested that particles lie with their elongated c-axis along the carbon support film. It is clear from the images of the pigment particles that this is true for the majority of particles. This is further confirmed by the very small number of lattice images showing single particles with crossed lattice fringes. The crossed lattice fringes occur when the [001] direction is parallel to the incident electron beam and therefore perpendicular to the carbon film.

The lattice images revealed that the particles contain many dislocations and there are many localised areas within the particles where the crystal detail is lost. This may correspond to regions which have been damaged by the electron beam or regions containing crystallographic defects, or both. Similarly, whilst many particles were observed showing $(1\bar{1}0)$ lattice fringes, very few were observed which showed clear (020) lattice fringes. From the diffraction studies, approximately equal numbers of particles showing these different lattice fringes would be expected. However, twinning on {110} will disrupt (020) and may decrease the contrast of these lattice fringes. The multiple orientations of twins formed by model A would also be expected to disrupt all of the {110}'s. Only regions exhibiting the correct orientation to the electron beam would be expected to produce lattice fringes. Other, either underlying or adjacent, twins would reduce the contrast and give "patchy" areas in the lattice images. Twins formed by model B will only exhibit two orientations and when this twin plane is perpendicular to the electron beam, no degradations (due to twinning) in the lattice fringe contrast would be expected. Unfortunately, insufficient evidence is available to suggest whether only one, or perhaps both, of these models operates.

3.10 Diffraction studies of small aggregates of highly chlorinated CPC pigment

It was noted, in section 3.5, that the pigment samples did not consist of many separated single particles with dimensions ~50nm but contained many small aggregates, with dimensions ~100-200nm. It cannot be discerned from these low magnification images if these small aggregates are made up of single particles which have come together after pigmentation or, if they are small clumps of material which have not been broken down by the pigmentation process. Lattice images revealed several small aggregates in which the lattice fringes were continuous across them. This would seem to suggest that these are aggregates of particles which have not been broken down by the pigmentation process. However, it is not clear from these images if the zone axis changes across the particles and thus particles have come together at the correct faces to produce continuous lattice fringes. A better method in determining how these aggregates were formed is to record diffraction patterns at steps across the aggregate, thus allowing the line/spot ratio to be determined at each point.

It was not possible to use the CTEM in imaging mode to select an aggregate and then switch to diffraction mode and record the diffraction patterns at steps across it. This was due to the fact that a single step turn of the electrical shifts, which corresponded to a step of ~50nm in imaging mode, corresponded to a much greater distance in diffraction mode. Thus to record diffraction patterns at the required step size across the aggregate would mean continually switching between imaging and diffraction mode. This was not a viable method due to the sensitivity of the material to radiation damage.

In an attempt to gain better control of the probe position a new technique was devised which involved operating the microscope in scanning mode. Using a condenser aperture of 40μm and the largest STEM spot size, a probe size ~20nm was obtained. The probe size was estimated from the blurring of the images of the

aggregates, recorded at a magnification ~150kX. With the STEM attachment the microscope could be operated in diffraction mode while viewing a transmission electron image (TEI) of the specimen on the CRT. The TEI allowed a suitable aggregate to be selected. Aggregates were chosen which were bigger than the smallest particle which was resolved in the TEI image and was therefore assumed to be an aggregate seen in normal CTEM imaging. Using the picture scan facility on the STEM unit, the area scanned by the probe was reduced to ~40nm x 40nm. The ability to change the location of the scanned area allowed it to be stepped across the aggregate, while a diffraction pattern was recorded at each step.

3.11 Results of diffraction studies of small aggregate

Figures 3.18(a) - (e) show a selection of TEI's of aggregates together with the diffraction patterns recorded at steps across them. Figure 3.18(a) shows the TEI and diffraction patterns from an aggregate from sample A1. The central line of the second diffraction pattern clearly shows deviations from a straight line. This pattern was compared with those produced by Diffract (Figures 3.3(a) - (l)). However, a zone axis which would produce this pattern could not be found. The pattern shown in figure 3.3(c) does show a non-straight central line of spots for a zone axis $[1\bar{1}2]$. This is the result of the large lattice parameters which give rise to planes of spots in the reciprocal lattice with small separations. This means that the crystal may be oriented in such a way that some reciprocal lattice points lie very close to the zero order layer. Because the crystal is thin, these reflections are excited but lie off the line of zero order spots. The shape of this centre line is not the same as that shown in the second diffraction pattern of figure 3.18 but it does show that it is possible to obtain a diffraction pattern with this effect. The same effect is not observed in the other two diffraction patterns from this aggregate. The streaks in final diffraction pattern also appear to be slightly rotated compared

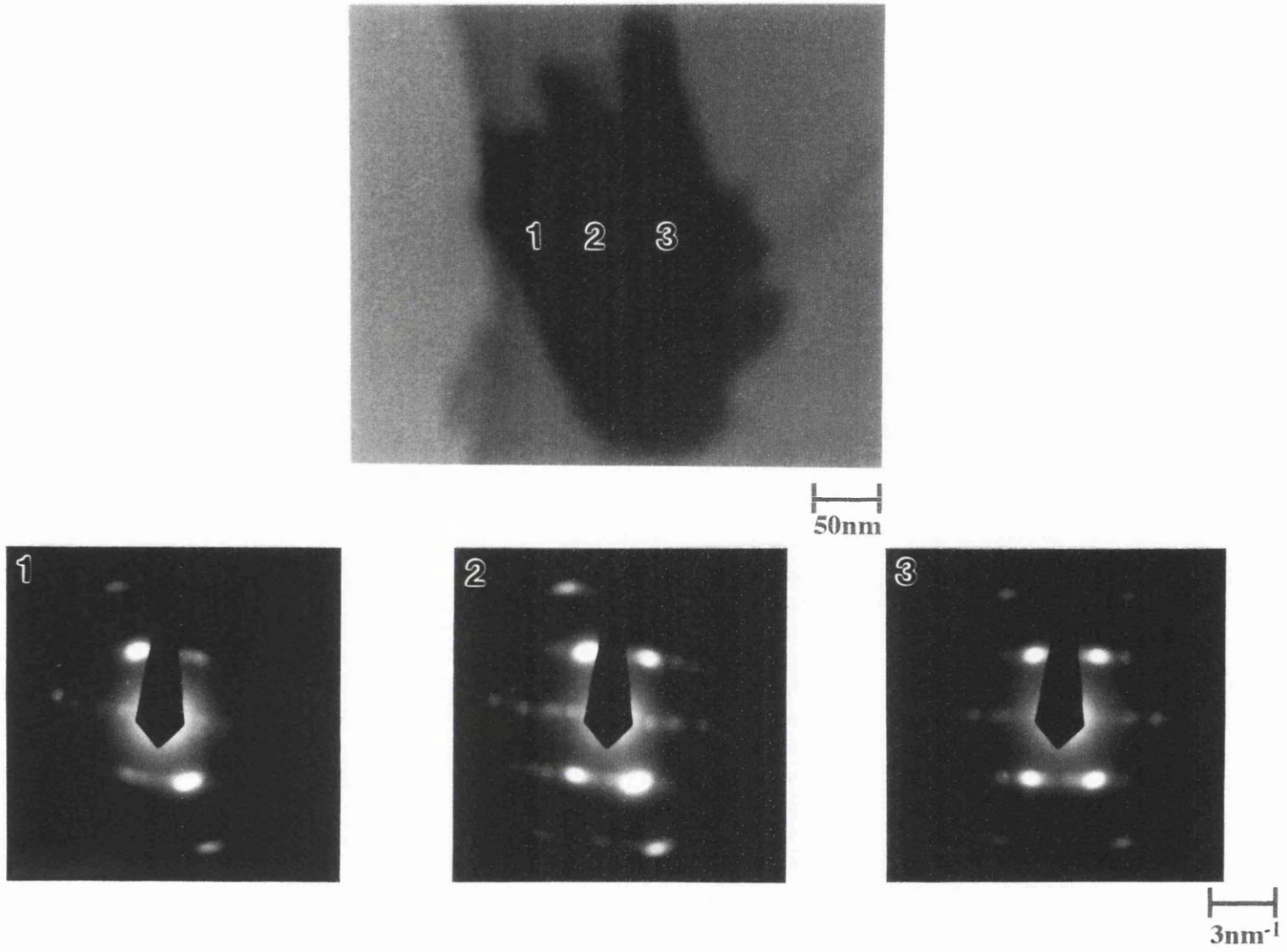

Figure 3.18(a) : TEI and diffraction patterns recorded from an aggregate from sample A1.

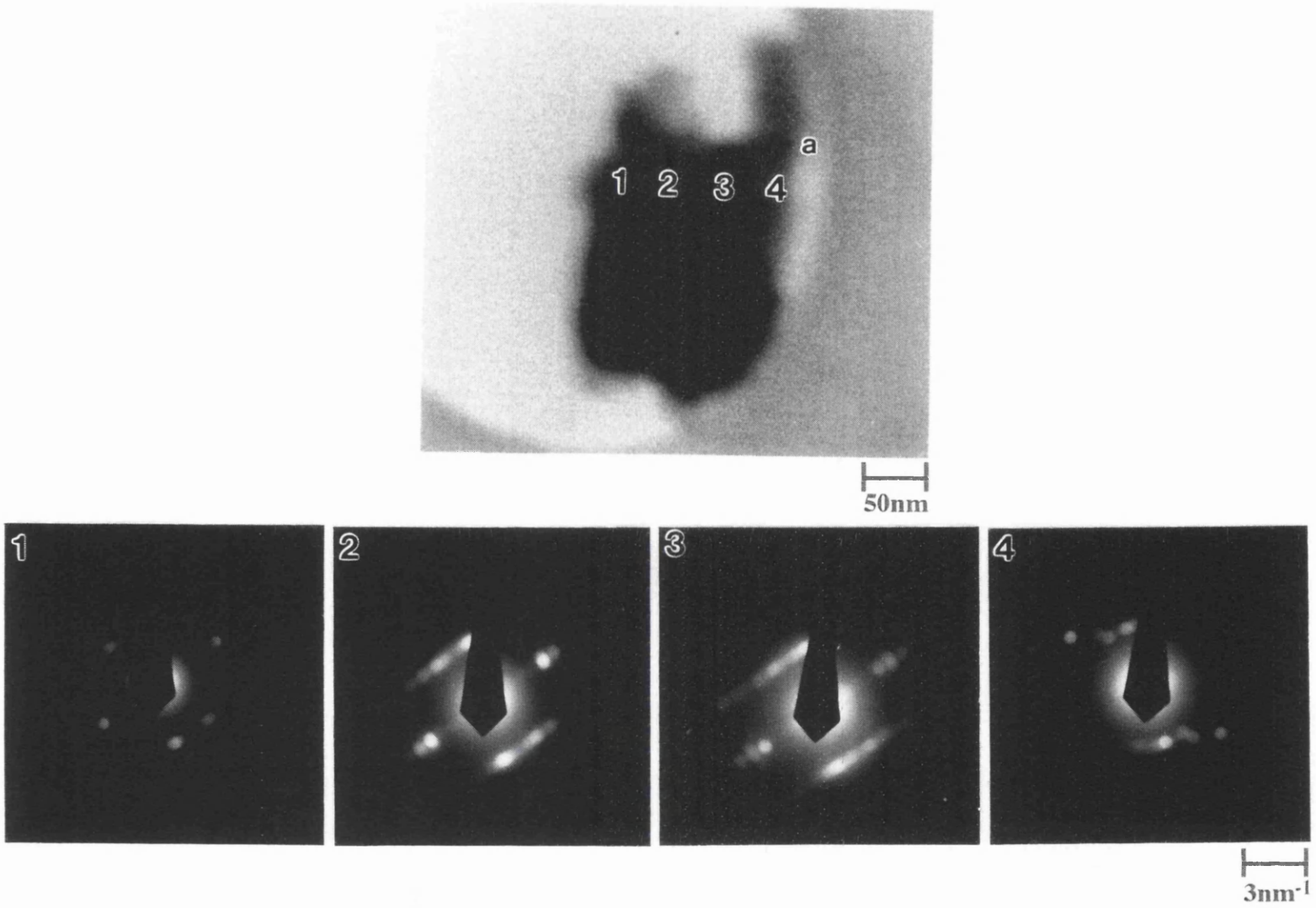

Figure 3.18(b) : TEI and diffraction patterns recorded from an aggregate from sample A1.

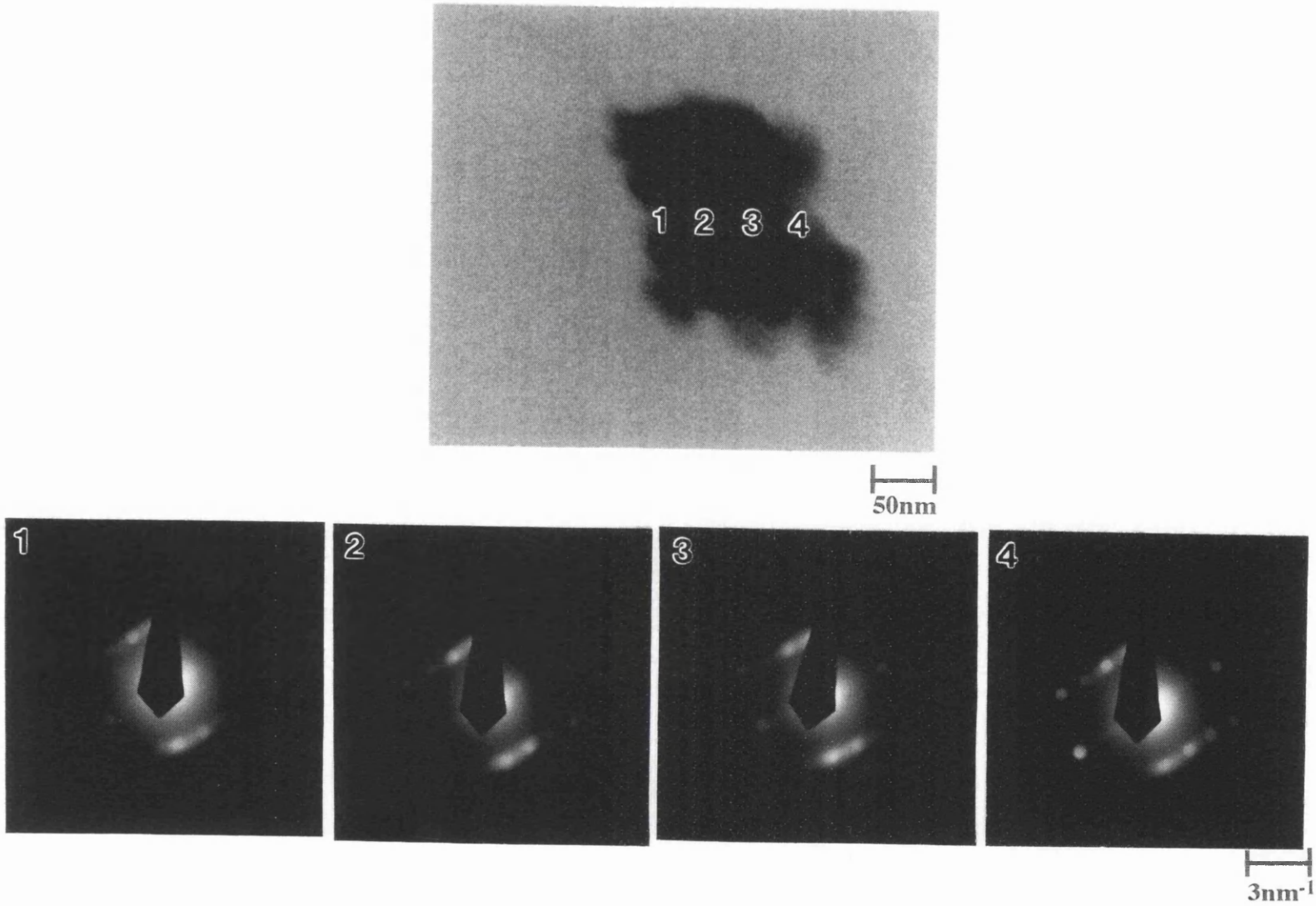

Figure 3.18(c) : TEI and diffraction patterns recorded from an aggregate from sample A2.

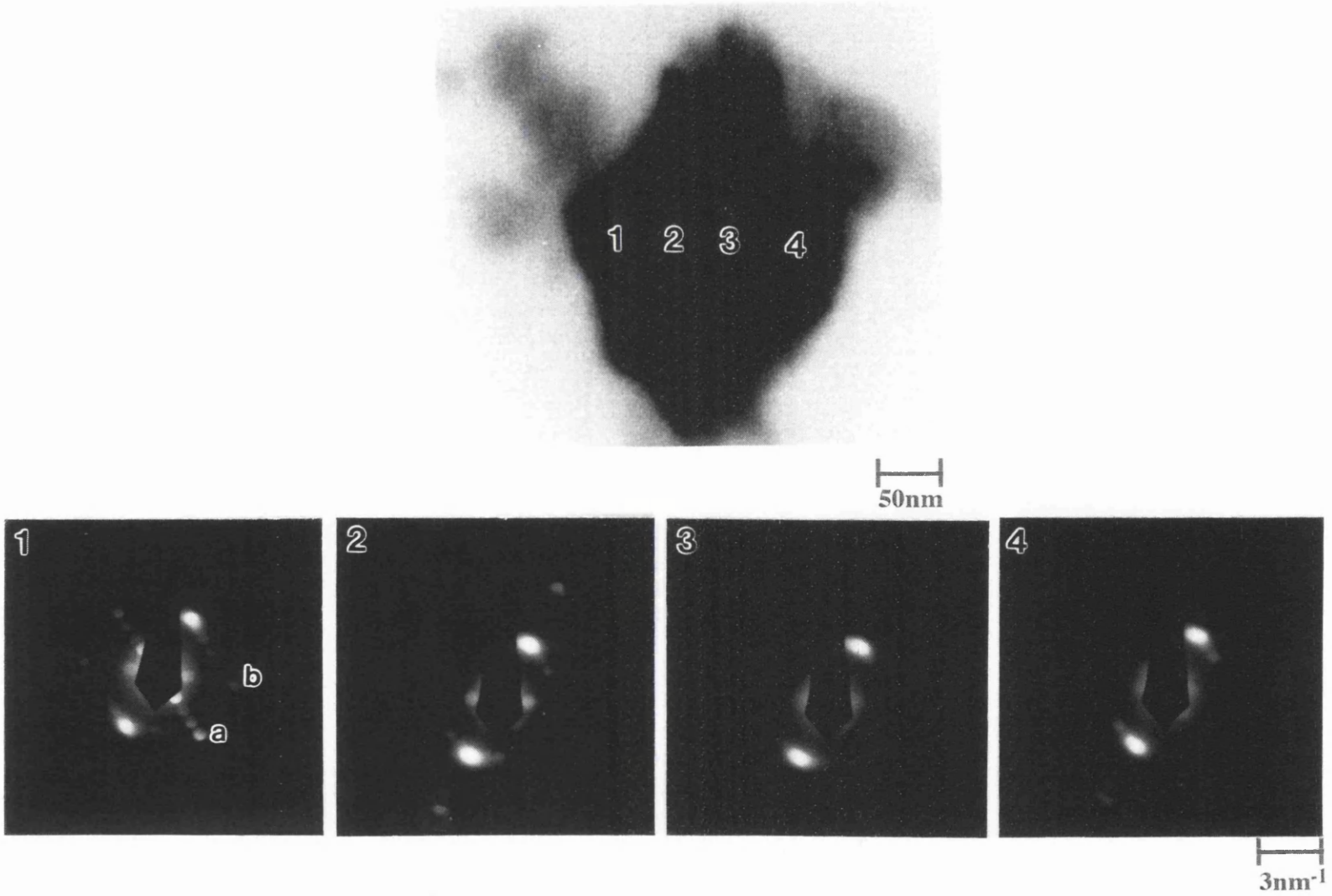

Figure 3.18(d) : TEI and diffraction patterns recorded from an aggregate from sample C1.

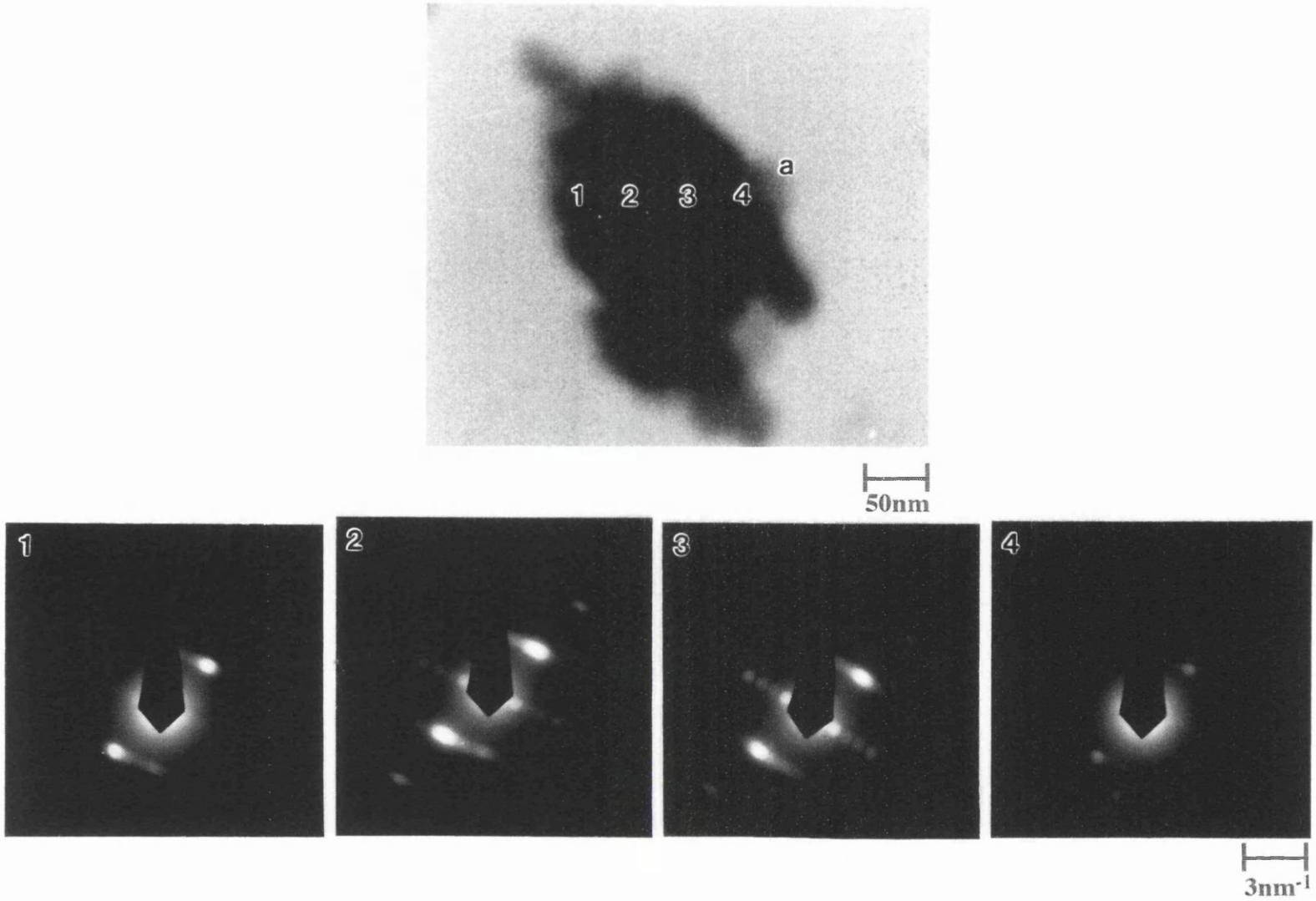

Figure 3.18(e) : TEI and diffraction patterns recorded from an aggregate from sample C4.

to those in the previous patterns. It is possible that this is a reaggregation of particles or it is an aggregate which has been attacked during the pigmentation process but pigmentation is incomplete. Part of the aggregate has broken away during this process but has not completely separated from the rest of the aggregate and thus gives rise to the diffraction patterns shown. The TEI and diffraction patterns shown in figure 3.18(b) are also from sample A1. The first three diffraction patterns have the same orientation, line/spot ratio and the angle between the brightest regions of streaks is the same. This indicates that these diffraction patterns are from an aggregate which has not been broken down by the pigmentation process. The final diffraction pattern consists of two separate orientations, one which is the same as in the previous patterns and another which lies at ~20^{o} to this. This suggests that a separate piece of the pigmentary material has attached itself to the aggregate. It can be seen from the TEI that there does appear to be a piece of material at **a** which has attached itself to the aggregate. Figure 3.18(c) shows the TEI and diffraction patterns recorded from an aggregate from sample A2. The diffraction patterns from this aggregate have the same orientation and the angle between the brightest regions of streaks is the same. This indicates that this is an aggregate which has not been broken down by the pigmentation process. The diffraction patterns and TEI shown in figure 3.18(d) are from an aggregate from sample C1. The first diffraction pattern shows two central line of spots, in directions **a** and **b**, at an angle of ~50^{o} to one another and are probably due to two particles overlapping. In the next diffraction pattern only the central line of spots from direction **a** remain, however, there is still some evidence of orientation **b** in the outer lines. In the next diffraction pattern only the brightest region of streaks are visible. The streaks appear to be in an arc but this is probably due to the overlap of the two orientations observed in the previous patterns. The final diffraction pattern shows streaking mainly in direction **b**. The position and angle between the brightest regions of streaks is unchanged in all the diffraction patterns. The fact that two orientations are observed in all the

diffraction patterns would seem to indicate that there are two aggregates overlaying one another at different orientations. Unfortunately this cannot be confirmed from the TEI. Figure 3.18(e) shows the TEI and diffraction pattern recorded from an aggregate in sample C4. The first three diffraction patterns have the same orientation and the angle between the brightest region of streaks is the same. This indicates that it is an aggregate which has not been broken down in the pigmentation process. However, there does appear to be a variation in the degree of crystallinity of the structure, as shown by the variation in perfection of the central line of spots. The final diffraction pattern shows two orientations to be present, one of which is the same as that observed in the previous patterns, while the other is at ~90^{o} to this. This is probably due to a piece of pigment material which has attached itself to the aggregate, as shown on the TEI at **a**.

Over 50 aggregates, consisting of only a few pigment particles, were investigated and around 80% appeared to be aggregates which had not been broken down in the pigmentation process. The diffraction patterns in several of these aggregates have the same crystal normal but there has been some rotation about it, as in figure 3.18(a). This indicates that during the pigmentation process these aggregates have been attacked by the acids and part of the aggregate has been dislodged but pigmentation is incomplete. The remaining aggregates appeared to be a group of particles which had recombined after pigmentation.

3.12 Conclusions

In this chapter results obtained from diffraction and imaging studies of highly chlorinated CPC pigments have been presented. Samples taken from different batches and samples produced using different processes were compared in order to determine any differences in their physical characteristics which would help to explain their various colouring properties. Diffraction studies of these

samples showed no obvious differences in the crystalline structure of samples from different batches. The studies also indicated that the particles have particular facets. However, since the particle morphology depends on several factors, it is difficult to determine not only exactly why certain facets are prevalent but which facets are formed. The highly chlorinated pigments adopt an α-type stacking sequence and the large number of diffraction patterns with streaks indicate that deviations from this type of stacking can readily occur. Previous studies of highly chlorinated CPCs have shown that twinning of the CPC crystal is the most likely reason for this. From the diffraction studies, two twinning models have been suggested, producing multiple and single crystallographic variants, respectively.

The low magnification images revealed that the pigments did not consist of single pigment particles with dimensions ~50nm but contained a large number of aggregates consisting of several particles. These images also showed that for two samples of a paint pigment, produced using the same process, different particle sizes were present. This explains the different performance of these pigments. Similarly, for two samples of a plastic pigment, again produced using the same process, a wide particle size distribution can also affect the colouring properties of the pigment. Images obtained from a group of samples, produced using different processes, also showed variability in the shape of the particles. This is also known to affect pigment performance. Analysis of the high magnification images showed no obvious differences in the crystallinity of the various samples. In many small aggregates, the lattice fringes were continuous across the aggregate. However, since CTEM images provide no information on the topography of the pigmentary material, it is difficult to determine if these are aggregates which have not been broken down by the pigmentation process .

Diffraction patterns recorded at steps across the aggregates indicated that the majority of these have not been broken down by the pigmentation process. To investigate this in greater detail, DPC imaging in a STEM was used. The results from these investigations are presented in the following chapter.

Chapter 4

DIFFERENTIAL PHASE CONTRAST IMAGING OF HALOGENATED COPPER PHTHALOCYANINE PIGMENTS

4.1 Introduction

In chapter 3 CTEM images of the CPC pigments provided information on the size and distribution of pigment particles. However, these images revealed little information about the topography of the particles. Diffraction studies of small aggregates suggested that most of them were aggregates, of the size of several particles, which had not been broken down by the pigmentation process. Changes in the relative orientation of some of the diffraction patterns recorded at steps across the aggregates suggested that these aggregates had been attacked in some way but the pigmentation was incomplete. However, it was not possible to confirm this from the CTEM images. A technique based on the differential phase contrast (DPC) mode of microscopy can provide simultaneous topographic information and high contrast lattice fringes. The DPC image is formed by using the difference signals from a split or quadrant detector as the probe is scanned across the specimen. Section 4.2 gives an introduction to the theory of DPC image formation in the STEM. A modification to the DPC detector system developed by Chapman et al.

(1990) is described in section 4.3. These sections borrow heavily from the work of Chapman et al (1990), Dekkers and De Lang (1977) and Chapman (1995). The instrumental considerations for DPC microscopy are discussed in section 4.4. In section 4.5, the imaging conditions for recording DPC images from CPC pigment particles are discussed. The images obtained are presented and discussed in section 4.6.

4.2 Introduction to DPC image Formation

It was Dekkers and De Lang (1974) who proposed using a circular detector split into two semi-circles and summing the contributions from both segments to produce a bright field image. They also produced images from the difference in the signals falling on both halves of the detector, as the electron beam was scanned across the specimen. These so-called DPC images are linearly related to the phase gradient of the specimen transmittance in a direction perpendicular to the split in the detector. An extension to this detector system was proposed by Hawkes (1978) and Rose (1977) and developed as the quadrant detector by Morrison et al (1980). This system allowed both components of the phase gradient to be obtained without rotation of either the specimen or detector through 90^0. The aim of this section is to discuss the principles of DPC imaging, with particular reference to obtaining topographic and structural information.

Figure 4.1 shows schematically how topographic contrast arises in the DPC imaging mode. Small shifts of the bright field cone away from the symmetry position are related to the thickness gradients in the specimen. The electrons, focused to a small probe in the plane of the specimen, are deflected through an angle α_D that is proportional to the thickness gradients integrated along an electron trajectory. Due to the deflection by the specimen, the electron distribution on each quadrant is not the same and difference signals from opposite quadrants provide a

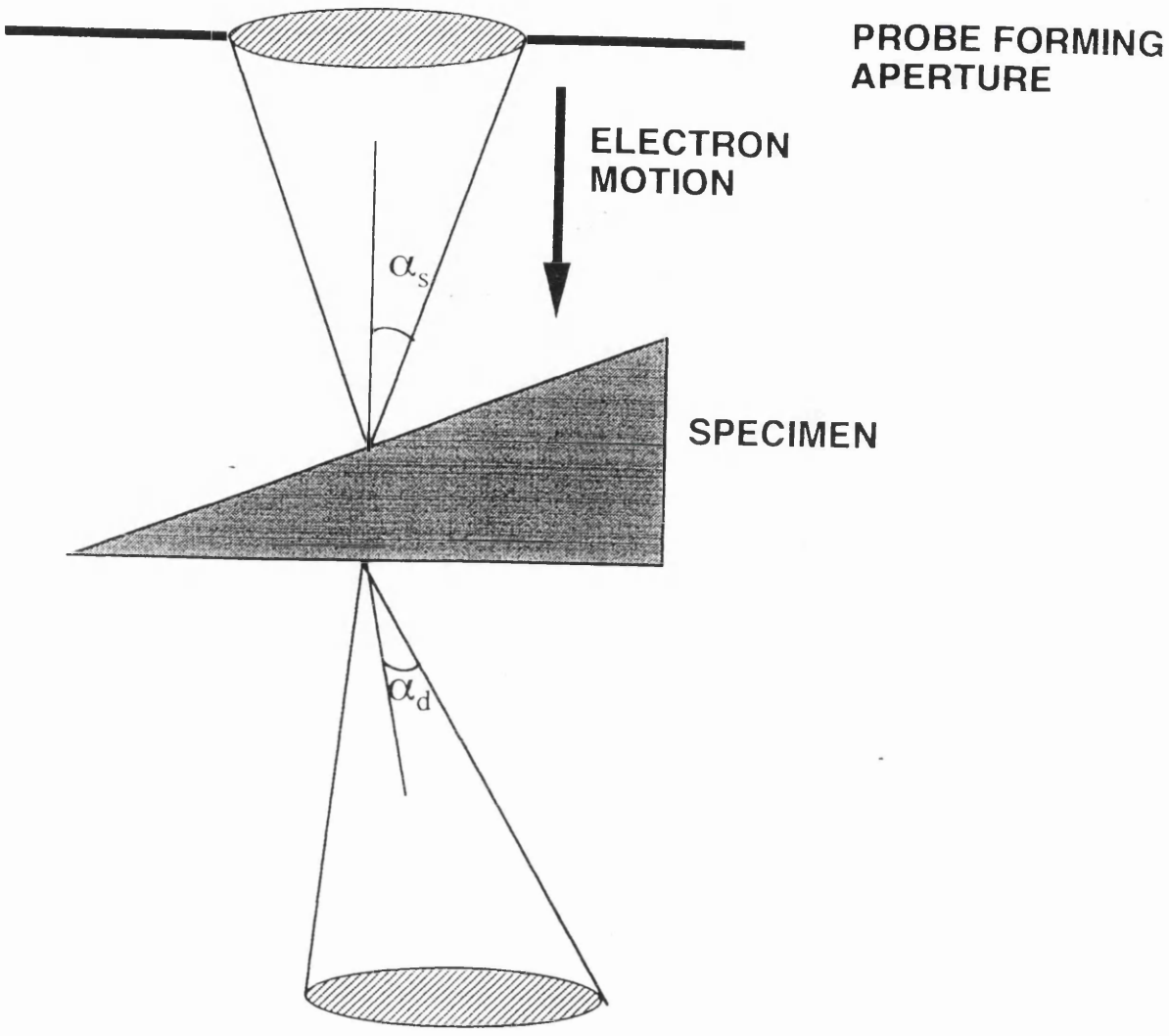

Figure 4.1 : Schematic diagram showing how topographic contrast arises in the DPC imaging mode.

quantitative measure of the components of the deflection angle. Images derived from the difference signals can be regarded as maps of two orthogonal components of the thickness gradient.

For a crystalline specimen of thickness $t(\boldsymbol{r})$ and internal potential function $V(\boldsymbol{r}, z)$ the phase excursion of the incident electron wave is given by (Chapman et. al., 1978)

$$\phi(\boldsymbol{r})=\frac{\pi}{\lambda E_0}\int_0^{t(\boldsymbol{r})} V(\boldsymbol{r}, z)\mathrm{d}z \qquad 4.1$$

where λ is the electron wavelength, E_0 the energy of the electron beam and z is the co-ordinate along the optic axis. Assuming the potential variation along the z-axis is negligible equation 4.1 can be rewritten as

$$\phi(\boldsymbol{r})=\frac{\pi}{\lambda E_0}[V(\boldsymbol{r})t(\boldsymbol{r})] \qquad 4.2$$

Therefore the two components of the phase gradient of the specimen transmittance in the orthogonal directions x and y are given by

$$\nabla_x\phi(\boldsymbol{r})=\frac{\pi\nabla_x(V(\boldsymbol{r})t(\boldsymbol{r}))}{\lambda E_0} \qquad 4.3$$

$$\nabla_y\phi(\boldsymbol{r})=\frac{\pi\nabla_y(V(\boldsymbol{r})t(\boldsymbol{r}))}{\lambda E_0} \qquad 4.4$$

The above expressions show that, at low resolution where the variation in the mean inner potential is below the resolution limit, the images obtained are to a good approximation directly proportional to the thickness gradient $t(\boldsymbol{r})$.

To reveal the internal structure of the particles by DPC lattice imaging requires that the diffracted beams emerging from the specimen overlap with the unscattered primary beam. In the case of a weakly scattering one-dimensional object, with the phase varying sinusoidally with periodicity Λ, the specimen transmittance can be written as

$$h(x)=1+i\phi_0 \sin\left(\frac{2\pi x}{\Lambda}\right) \qquad 4.5$$

If the specimen is illuminated by a coherent probe, the electron wave leaving the specimen consists of an unscattered cone of angular radius α_S together with two diffracted cones of the same angular radius but displaced from the primary cone by an angle $\lambda/\Lambda=\theta_B$, where λ is the electron wavelength. A schematic diagram showing the overlap of the diffraction discs is shown in figure 4.2 For the overlap condition to be satisfied requires $\alpha_s>\theta_B$.

The resulting image $S(x)$, formed by differencing signals from opposite segments of the quadrant detector, has as its Fourier transform $S(k_x)$, which can be written as

$$S(k_x) = \tau(k_x)\, \Phi(k_x) \qquad 4.6$$

where k_x is the spatial frequency and is equivalent to $1/\Lambda$, $\tau(k_x)$ is the linear phase transfer function of the imaging system and $\Phi(k_x)$ is the Fourier transform of $\phi(x)$.

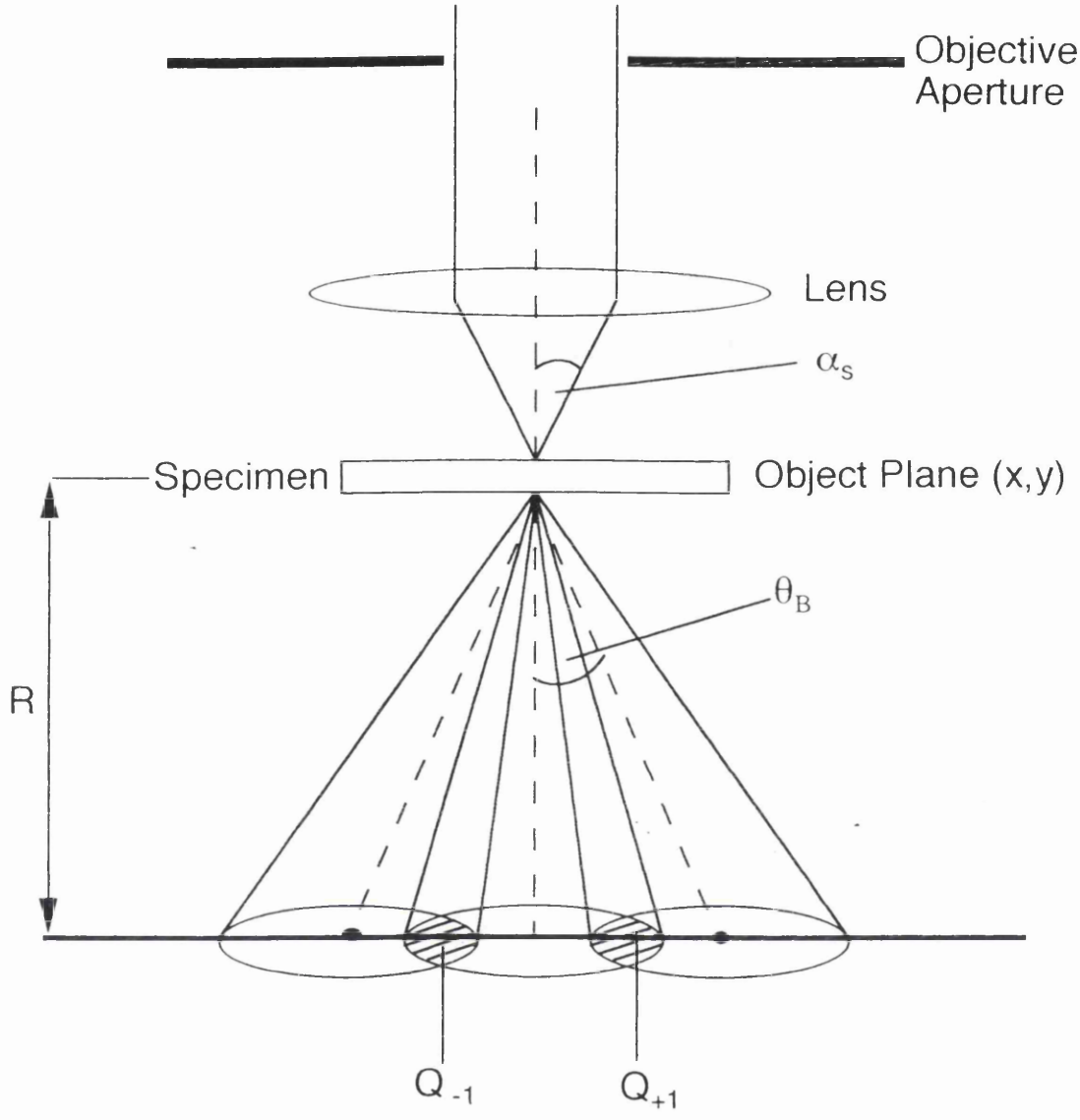

Figure 4.2 : Schematic diagram showing the overlap of discs in the diffraction pattern

Since it is the phase gradient rather than the phase function which is of interest it is convenient to rewrite equation 4.6 in the form

$$S(k_x) = T(k_x)\,\nabla\Phi(k_x) \qquad 4.7$$

where, using the standard Fourier relations $T(k_x) = \tau(k_x)/2\pi i k_x$ (Chapman et. al., 1990).

Only the areas involving overlap between the unscattered and diffracted beam carry information in a difference image. The overlap areas which contribute to the difference image A-C from the quadrant detector are shown hatched in figure 4.3. In figure 4.3 the displacements in the detector plane are shown in terms of spatial frequency rather than in terms of scattering angles so that equations 4.6 and 4.7 are directly applicable. Thus the probe angle α_s is replaced by the maximum spatial frequency component in the probe k_α, which is given by α/λ, and the separation of the circles becomes k_x for the phase sinusoid under consideration. If the hatched areas in figure 4.3 are denoted by $P(k_\alpha, k_x)$ the transfer function can now be written as

$$T(k_x) = P(k_\alpha, k_x)/2\pi^2 k_\alpha^2 k_x \qquad 4.8$$

where as already noted, $P(k_\alpha, k_x)$ can be calculated using simple geometry. Figure 4.4 shows the variation of $T(k_x)$ expressed as a function of the reduced spatial frequency $k_r = k_x/k_\alpha$ for a standard quadrant detector. The graph shows $T(k_x)$for various values of κ ,which is defined as the ratio of the radius of the detector k_a to that of the bright field cone k_α. It can be seen that information transfer falls monotonically with increasing spatial frequency and finally ceases at a reduced

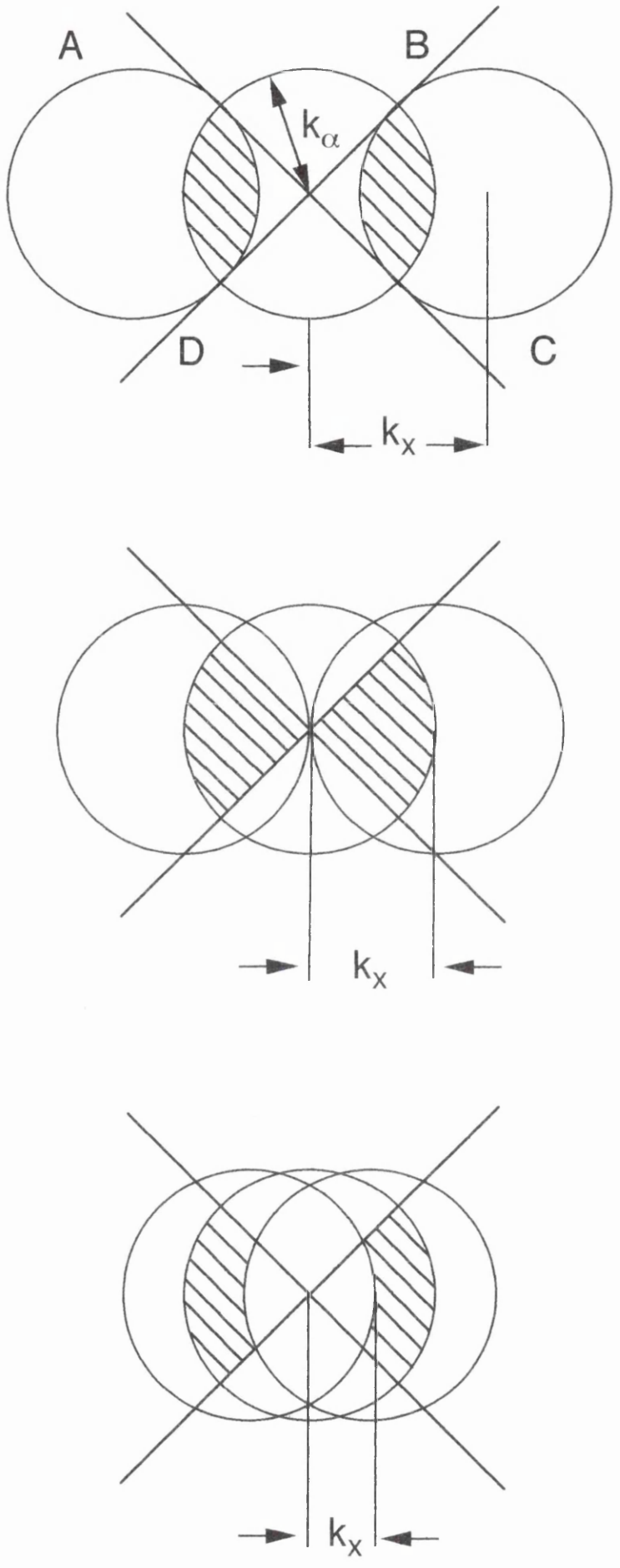

Figure 4.3 : The electron intensity distributions in the plane of a solid quadrant arising from weak phase sinusoids of three different periodicities.

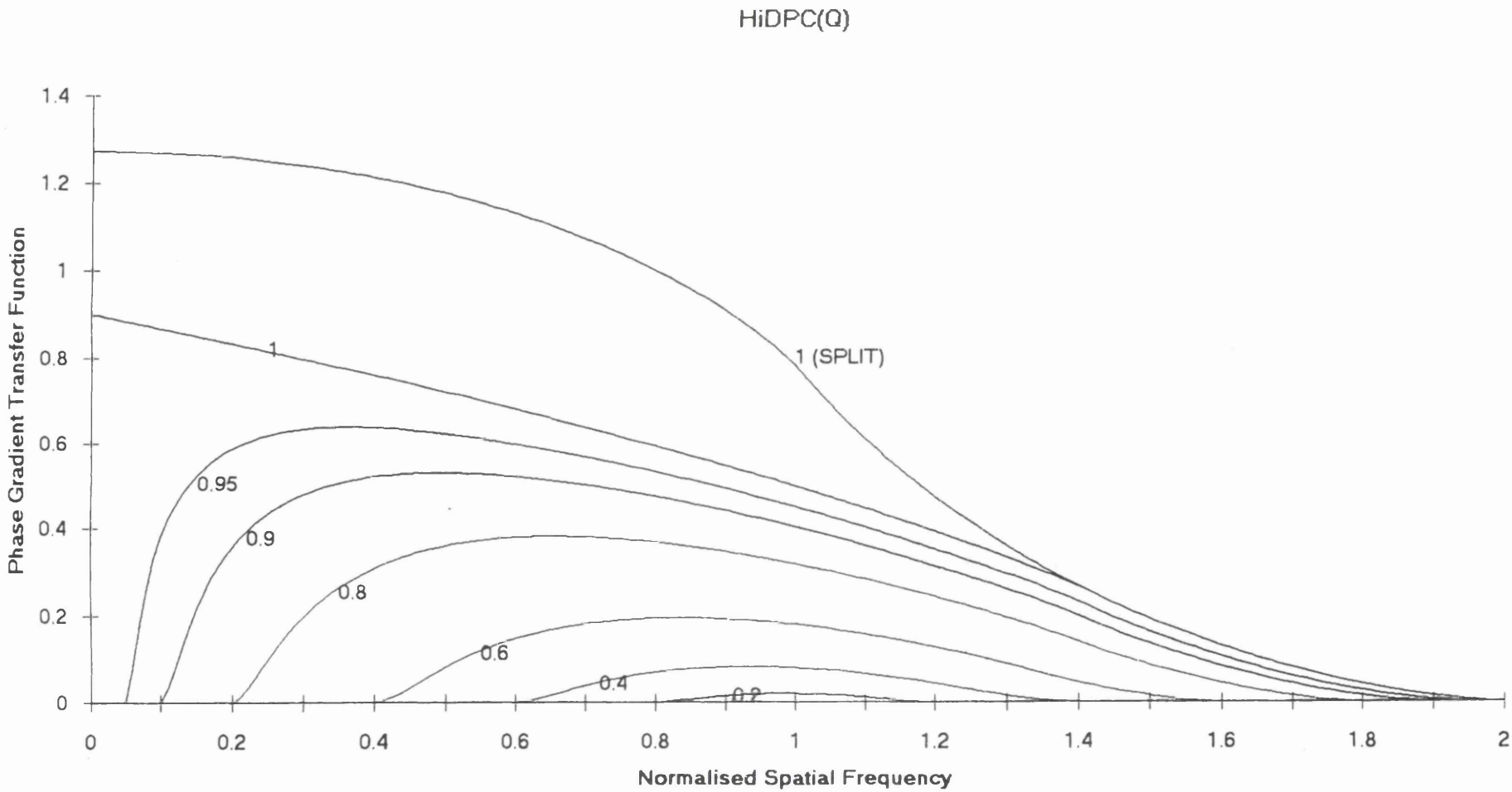

Figure 4.4 : Variation of the phase gradient transfer function with reduced spatial frequency for standard quadrant detectors with different values of κ.

spatial frequency of 2, which corresponds to a cut-off in real space of all periodicities $\Lambda < \lambda/2\alpha$. It is apparent that the form of the transfer function is well suited to the efficient transfer of low spatial frequency information which represents topographic detail in the pigment particles. The (110) lattice fringe spacings of ~1.4nm, represent a reduced spatial frequency of ~0.5 for α_s of ~5mrad and thus it is clear from figure 4.4 that images of the pigment particles containing both topographic and lattice information simultaneously can be obtained using the standard DPC imaging technique (McColgan and Chapman, 1989). However, some of the topographic detail on the pigment particles can be swamped by the lattice fringes and an improved analysis of the structure of the pigment particles could be achieved if the topographic and lattice information are separated out.

Chapman et al (1990) have developed a modification to the DPC detector geometry which allows substantial changes to be made in the efficiency with which different spatial frequencies in the specimen structure are transferred to the image. This modified DPC system allows images to be obtained in which there is an appreciable separation of the topographic and lattice information. The following section describes the modified DPC imaging mode and its characteristics.

4.3 The modified DPC imaging mode

In order to separate the lattice image information from the topographic information in the image a more rapid supression of information at mid-band spatial frequencies is required. Thus it is desirable to increase the signal to noise ratio of low spatial frequency components whilst reducing that of those components of higher spatial frequency. The converse is true for obtaining images in which the topographic information is removed and only the lattice spacings are observed, Chapman et al (1990) achieved this by dividing the detector into eight segments to take the form of an outer annular quadrant detector surrounding an inner solid

quadrant detector as shown in figure 4.5. The effect of this modification for the three periodicities and the area of overlap contributing to the difference image A - C, considered in figure 4.3, is shown in figure 4.6. It is clear that there is very little difference in the signal detected at low and high spatial frequencies compared to that detected using the solid quadrant detector, whilst the value of $P(k_\alpha, k_x)$ is appreciably reduced in the mid-band region. The degree to which the mid-band spatial frequency components are suppressed depends on the radius k_i of the inner solid quadrant detector relative to that of the bright field cone k_α, the ratio of which is denoted by κ. Images formed using only electrons falling on the inner detector reveal high spatial frequency information with virtually no interference from low spatial frequency components. Scattering of the electron beam by a lattice potential results in a change of the intensity distribution within the bright field cone rather than a shift in its position. Thus in contrast to the low spatial frequency case most of the useful signal at higher spatial frequencies comes from the inner detector. As can be seen from figure 4.6 loss of the contribution from the extremities of the overlap area is of little consequence.

Figure 4.7 shows the variation of $T(k_x)$ (for the outer annular detector) measured as a function of k_i for various values of κ between $\kappa = 0$ (which corresponds to the standard quadrant detector system) and $\kappa = 0.95$ (which corresponds to a detector system in which only the extremities of the bright field cone are detected by the outer annular detector). LoDPC denotes that the measured values of $T(k_x)$ are for the outer annular detector where most of the useful signal at low spatial frequencies comes from. Figure 4.7 clearly shows that taking the difference signal from opposite quadrants of an annular quadrant detector rather than from a solid quadrant detector leads to a reduction in the signal detected or leaves it unchanged depending on the values of k_i and κ. However, the performance of an imaging system is primarily judged by the signal to noise ratio in the resulting image. Assuming only Poisson noise need be considered, the noise in a difference image is dependent simply on the total number of electrons detected. It

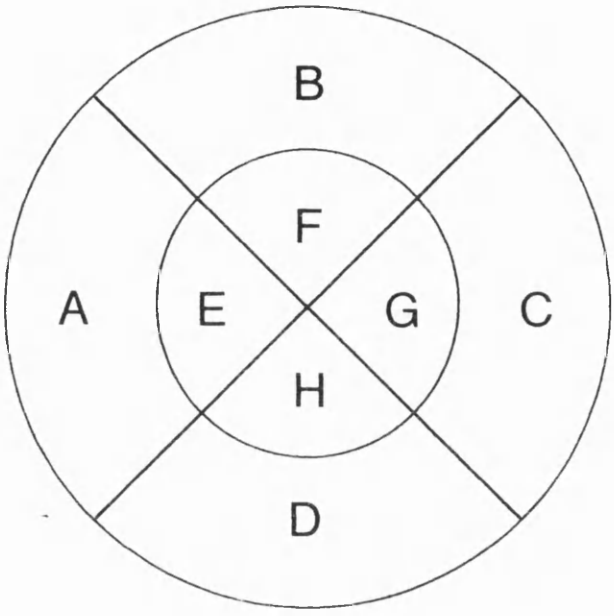

Figure 4.5 : Schematic disgram of the eight segment DPC detector.

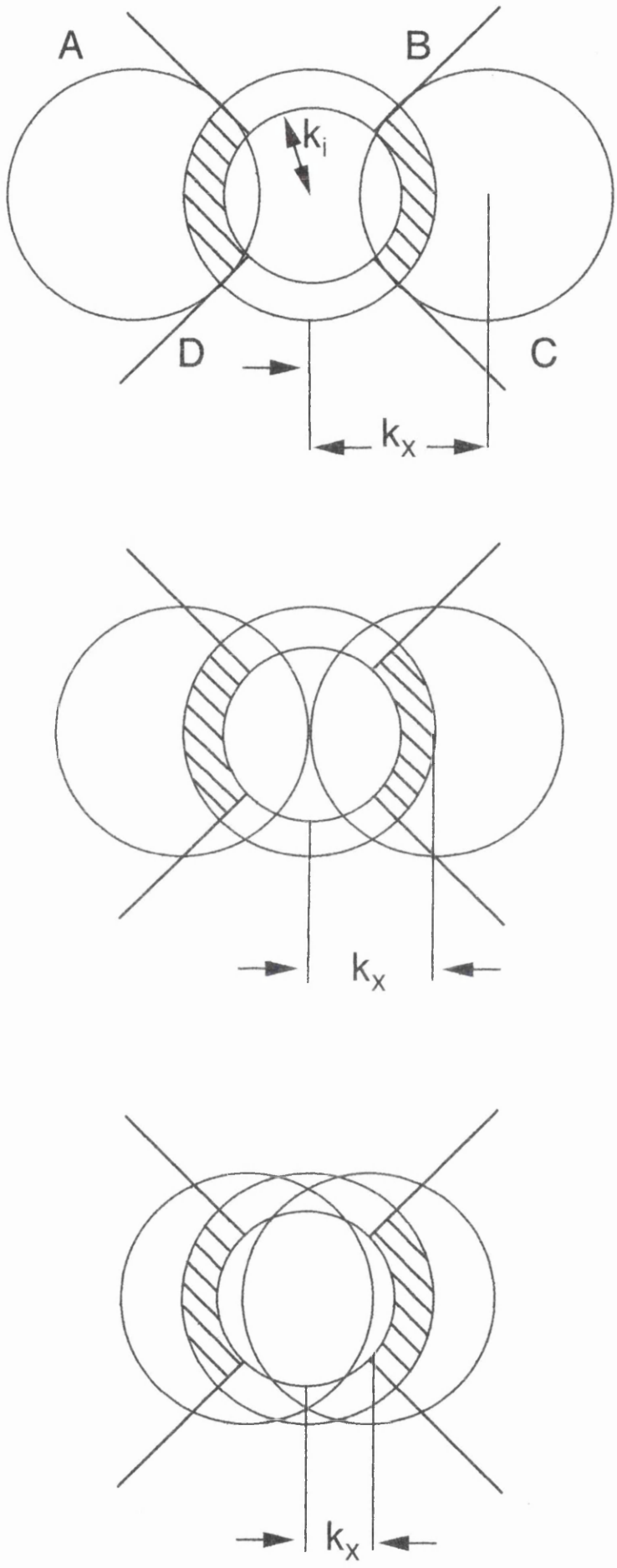

Figure 4.6 : The electron intensity distributions in the plane of an annular detector arising from weak phase sinusoids of three different periodicities.

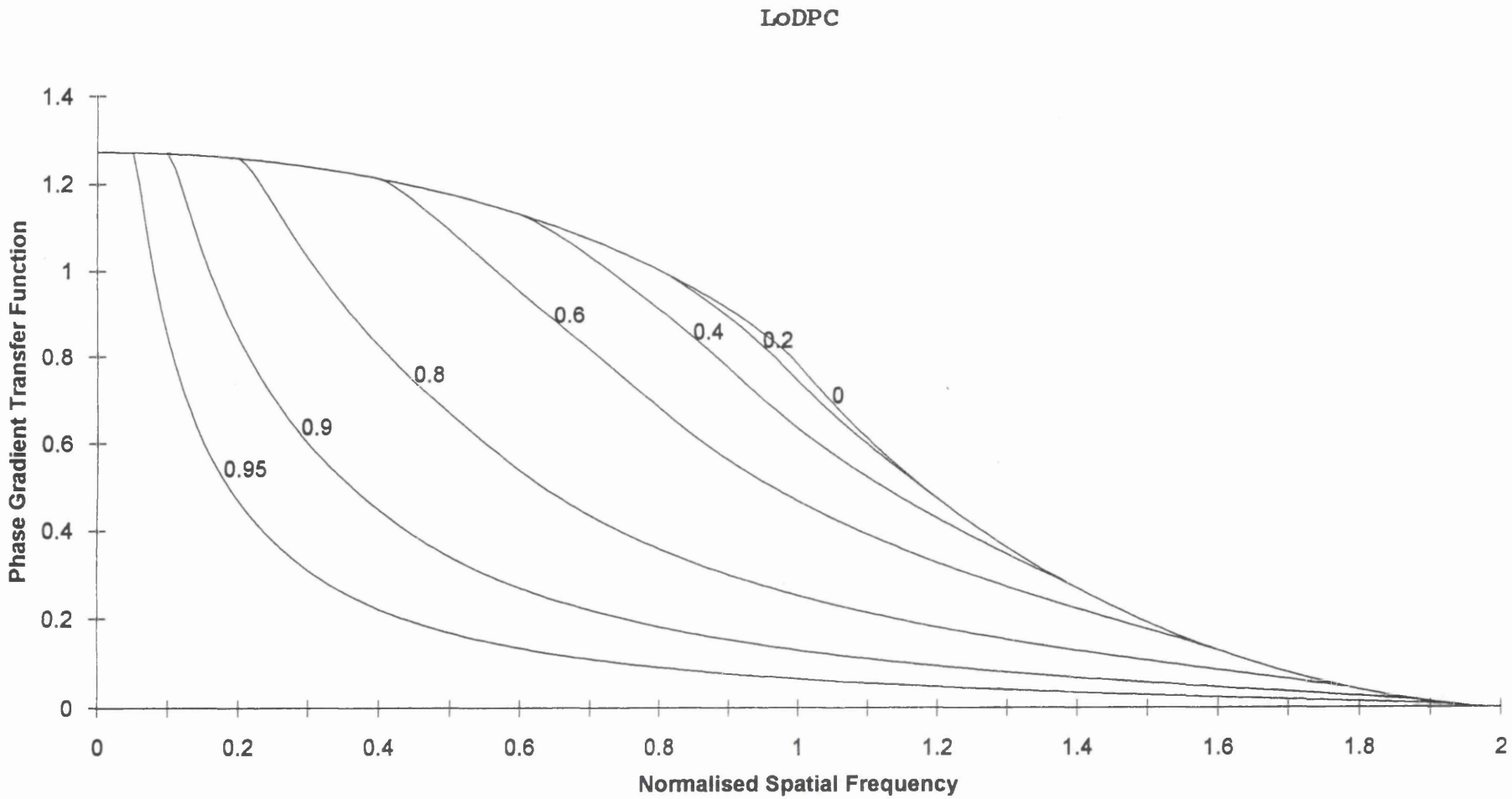

Figure 4.7 : Variation of the phase gradient transfer function with reduced spatial frequency for outer annular detectors with different values of κ.

can be shown that the signal to noise ratio as determined by the geometry of the detector, is directly proportional to $P(k_r, \kappa)/k_r\left(1-\kappa^2\right)^{1/2}$ (Chapman et. al., 1990). Figure 4.8 shows the variation of the signal to noise ratio as a function of k_r for various values of κ (again for LoDPC). This clearly shows the full advantage of the annular detector over the standard quadrant detector for investigating the topography of the pigment particles. At low spatial frequencies the signal to noise ratio is enhanced whilst in the mid-band it is reduced leading to an overall improvement of approximately an order of magnitude by using a detector with κ =0.9 as opposed to one with κ = 0.

Figures 4.9 and 4.10 show the variations of $T(k_x)$ and the signal to noise ratio, respectively, (from the inner quadrant detector) measured as a function of k_r for various values of κ. In these figures HiDPC indicates that the measured values of $T(k_x)$ and the signal to noise ratio are for the inner solid quadrant detector. Figures 4.9 and 4.10 show that suppression of the low frequency components depends on the values of both k_r and κ. For κ = 1 (i.e. $k_i=k_\alpha$) the diameter of the bright field cone is equal to the diameter of the inner quadrant detector and thus none of the low spatial frequency information is lost. As the value of κ is decreased more of the signal arising from the electrons at the periphery of the cone is lost and thus the greater the amount of low spatial frequency information is lost.

A simple physical argument using figure 4.6 can be used to explain how the separation of topographic and lattice information from the pigment particles is achieved using this detector system. As mentioned in the previous section the effect of a change in thickness is primarily to introduce a small deflection into the electron beam. Thus in the detector plane the principal result is a slight shift of the bright field cone Figure 4.6 shows that in the low frequency case virtually all the area of overlap falls on the outer detector. It should be noted that at low spatial frequencies where the two diffracted beams overlap their contributions are in anti-phase, signal cancellation occurs and no phase information can be derived from electrons falling on these portions of the detector. Thus, it is clear that omission of the contribution

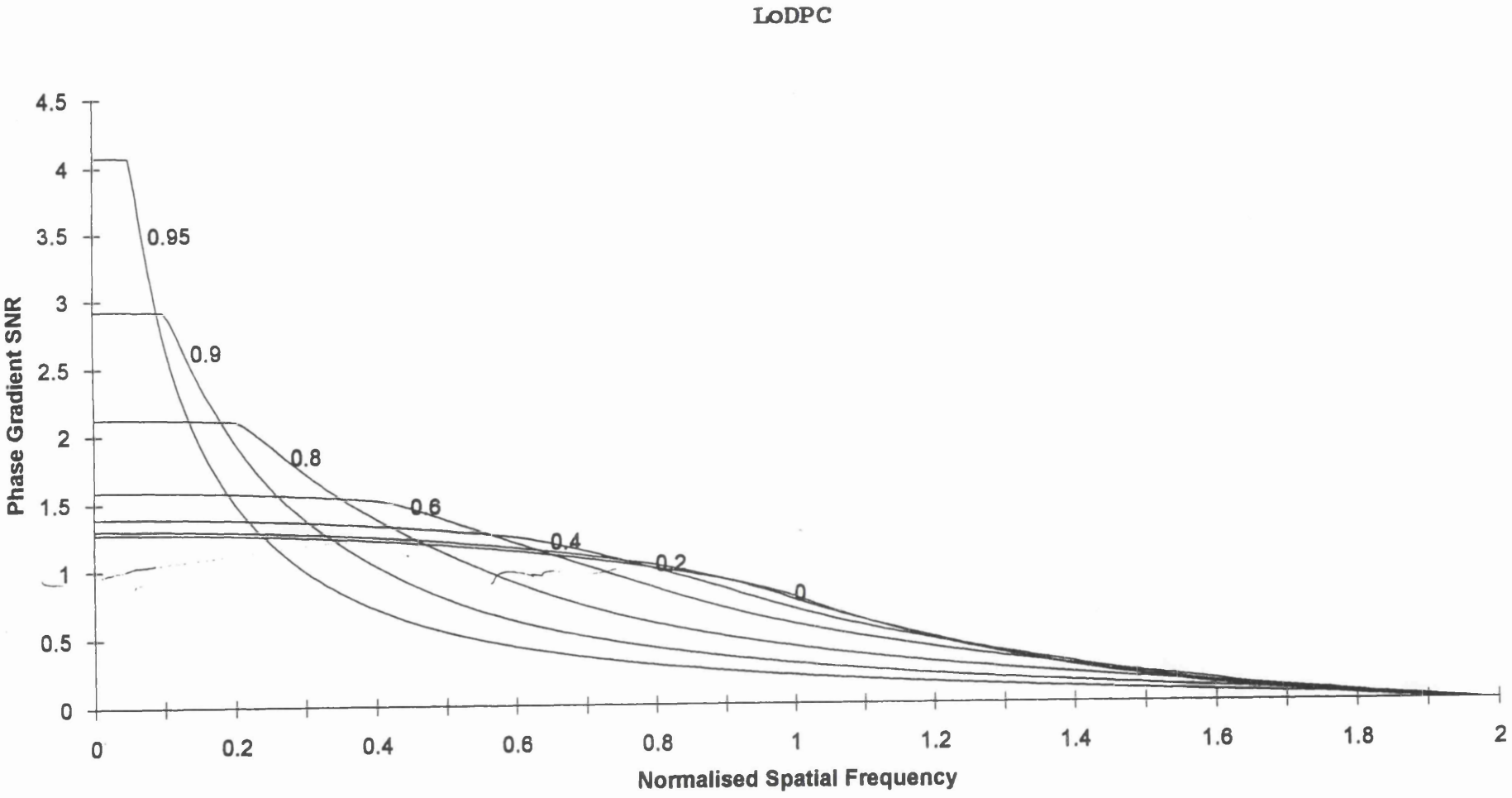

Figure 4.8 : Variation of the signal to noise ratio with reduced spatial frequency for outer annular detectors with different values of κ.

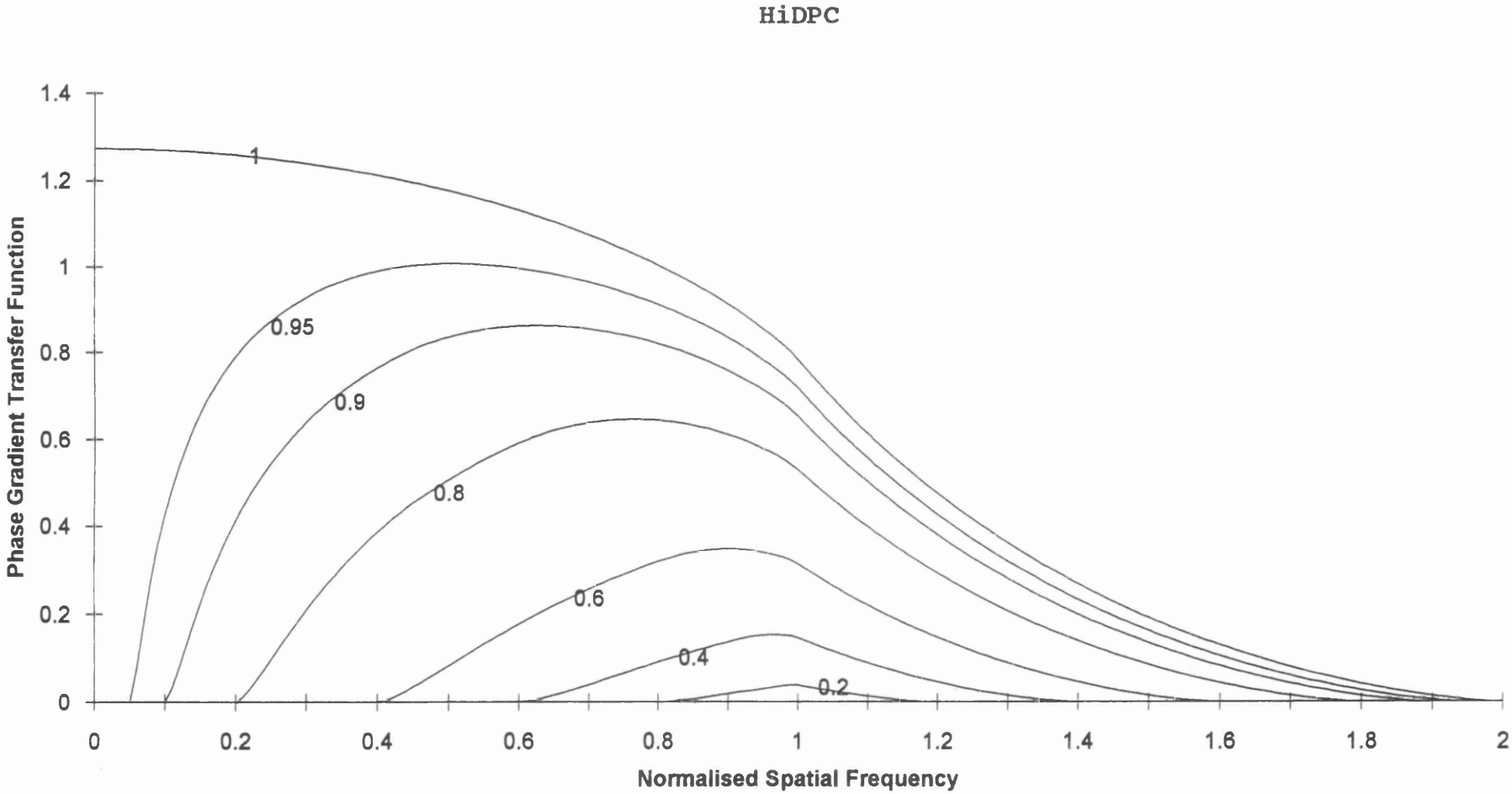

Figure 4.9 : Variation of the phase gradient transfer function with reduced spatial frequency for inner quadrant detectors with different values of κ.

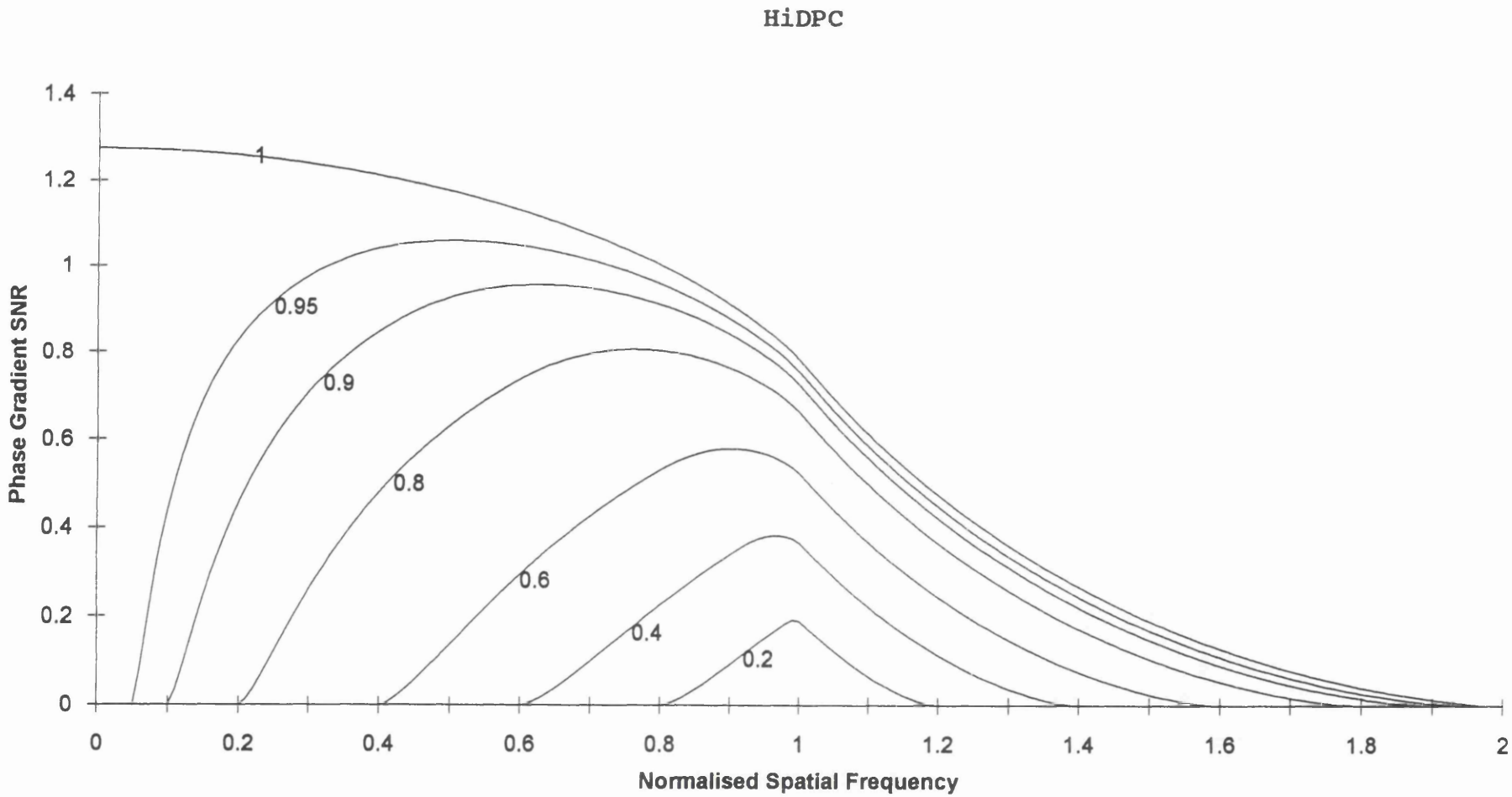

Figure 4.10 : Variation of the signal to noise ratio with reduced spatial frequency for inner quadrant detectors with different values of κ.

from the inner solid quadrant detector has no effect on the efficiency with which the shift is detected, and the signal can be thought of as arising entirely from those electrons near the periphery of the bright field cone. Since the electrons in the centre of the cone contribute nothing to the signal but considerably to the noise it is desirable to choose a value of κ which is just sufficient to ensure that there is always a non-zero signal on each outer segment of the detector.

This discussion has so far used a number of simplifying assumptions, the most important being that the system was aberration free. In practice, however, the phase contrast transfer function (PCTF) is affected by lens aberrations and defocus. The effects of these aberrations were first introduced in chapter 2 of this work and are expressed in equation 2.10. This equation can be rewritten in terms of the spatial frequency k_x , as

$$W = -\frac{C_s \lambda^3 k_x^4}{4} + \frac{\Delta f \lambda k_x^2}{2} \qquad 4.9$$

and expressed as a function of the reduced spatial frequency k_r, becomes

$$= -\frac{C_s \alpha_s^4 k_r^4}{4\lambda} + \frac{\Delta f \alpha_s^2 k_r^2}{2\lambda} \qquad 4.10$$

$$= -Ck_r^4 + Dk_r^2 \qquad 4.11$$

where

$$C = \frac{C_s \alpha_s^4}{4\lambda} \qquad 4.12$$

and

$$D = \frac{D \Delta a_s^2}{2\lambda} \qquad 4.13$$

As shown in figure 2.6, the characteristic feature of the PCTF curves is that they oscillate about zero so that different spatial frequency components in the object appear in the image with positive and negative contrast, whilst those for which the PCTF is zero are not imaged at all. The transfer of the widest range of spatial frequencies is achieved by balancing the effects of spherical aberration and defocus. The value of optimum defocus or Scherzer defocus (Scherzer, 1949) is given by $\Delta f = (C_S\lambda)^{1/2}$, thus at optimum defocus $D=(C)^{1/2}$. The optimum imaging conditions for DPC imaging of pigment particles is discussed in section 5.5.

4.4 Instrumental considerations for DPC imaging

The investigations were carried out using the eight segment annular detector described in the previous section and shown in figure 4.5. The radius of the inner annulus is fixed but the area of detector covered by the bright field cone can be changed by varying the excitation of the post specimen lenses. Thus the value κ, the ratio of the radius of the inner annulus, k_i, to the radius, k_α, of the bright field cone, can be varied.

All investigations were carried out in an extended VG HB5 STEM. The high brightness source of a field emission gun is particularly suitable for producing a small probe on the specimen. The Link Analytical detectors comprised two sets of four pn junction diodes fabricated on single silicon crystals. The upper set in the shape of an annular quadrant, was mounted on top of, but electrically isolated from, the lower set which was in the form of a standard quadrant detector. The inner radius of the annular quadrant was 12mm and its outer radius was 25mm.

The HB5 provides considerable flexibility in the probe forming conditions for imaging. The electron optical components used in imaging consisted of a single condenser lens C2 plus the highly excited objective lens. An objective lens apertures of 30μm was used in these investigations and subtends an angle of

5mrad. A further discussion of the imaging conditions is presented in the following section.

Descan coils, situated before the first PSL, were used to ensure that in the absence of any specimen interaction the electron distribution in the detector plane remained stationary about the centre of the detector, irrespective of the position of the probe in the specimen plane.

Signals from the detector could either pass through an analogue electronic signal mixing unit, the outputs from which were used to form the video signals to the display monitors, or acquired digitally. Image acquisition in digital mode was performed using a Link AN10000 image acquisition and processing system. Initial images of the pigment particles were recorded at a resolution of 256x256 at 8 bits per pixel. However, the particles were found to damage too rapidly and much of the lattice fringe information was lost. The damage was reduced by acquiring images with a resolution of 512x512 at 16 bits per pixel at a lower magnification. Two difference images were formed, the first using the signal combination A-C, which yields the topographic images and the second combination of F-H which provides images showing the internal structure of the particles.

4.5 Imaging conditions for DPC microscopy

As mentioned in the previous section the imaging condition used was the condenser lens C2 and a 25μm ROA. The effects of the aberrations on the information transferred from the specimen were calculated using a computer programme written by Dr. A. McLeod of the Department of Physics and Astronomy at the University of Glasgow. This programme allows the phase gradient transfer function (PGTF) and phase gradient signal to noise ratio (PGSNR) to be calculated for various values of C and D. The functions are plotted

as a function of the reduced spatial frequency k_r for structures, within the specimen, at various angles between 0^O and 90^O to the incident electron beam.

In the HB5 STEM $C_s \approx$ 3.5mm and it is this value which is used to calculate the value of C for a 30μm ROA's. From this value D was calculated and thus an optimum defocus was obtained. These values are given below

ROA = 30μm

α = 5mrad

$C \approx 0.15$

$D = \sqrt{(C)} \approx 0.38$

Optimum defocus = 1138Å

These values of C and D were used to calculate the phase gradient transfer function (PGTF) from the inner and outer quadrant detectors, for various values of κ. The results of these calculations are shown in figures 4.11(a) & (b). It is known that the most frequently observed lattice fringes have a spacing of ~1.4nm. Work carried out by McColgan (1990), using DPC to reveal topographic information in halogenated CPC's, showed that it was possible to reveal thickness variations of the order of one or two molecules in thickness (~5nm). Reduced spatial frequencies of 0.15 and 0.57 for the 30μm, corresponding to dimensions of 1.3nm and 5nm respectively, are marked on the plots. Figure 4.11(a) shows that when the diameter of the bright field cone equals the diameter of the inner quadrant, at both low and high spatial frequencies the signal is enhanced. As the bright field cone is increased in size to κ=0.9, a large amount of the information at low spatial frequencies is lost. A further decrease of κ to 0.8 removes more of the signal at low spatial frequencies. However, at this value of κ the PGTF is reduced. A further reduction in κ reduces it even further. Thus values of κ of between ~0.8 - 0.95 are best for recording the high spatial frequency information, at the optimum defocus.

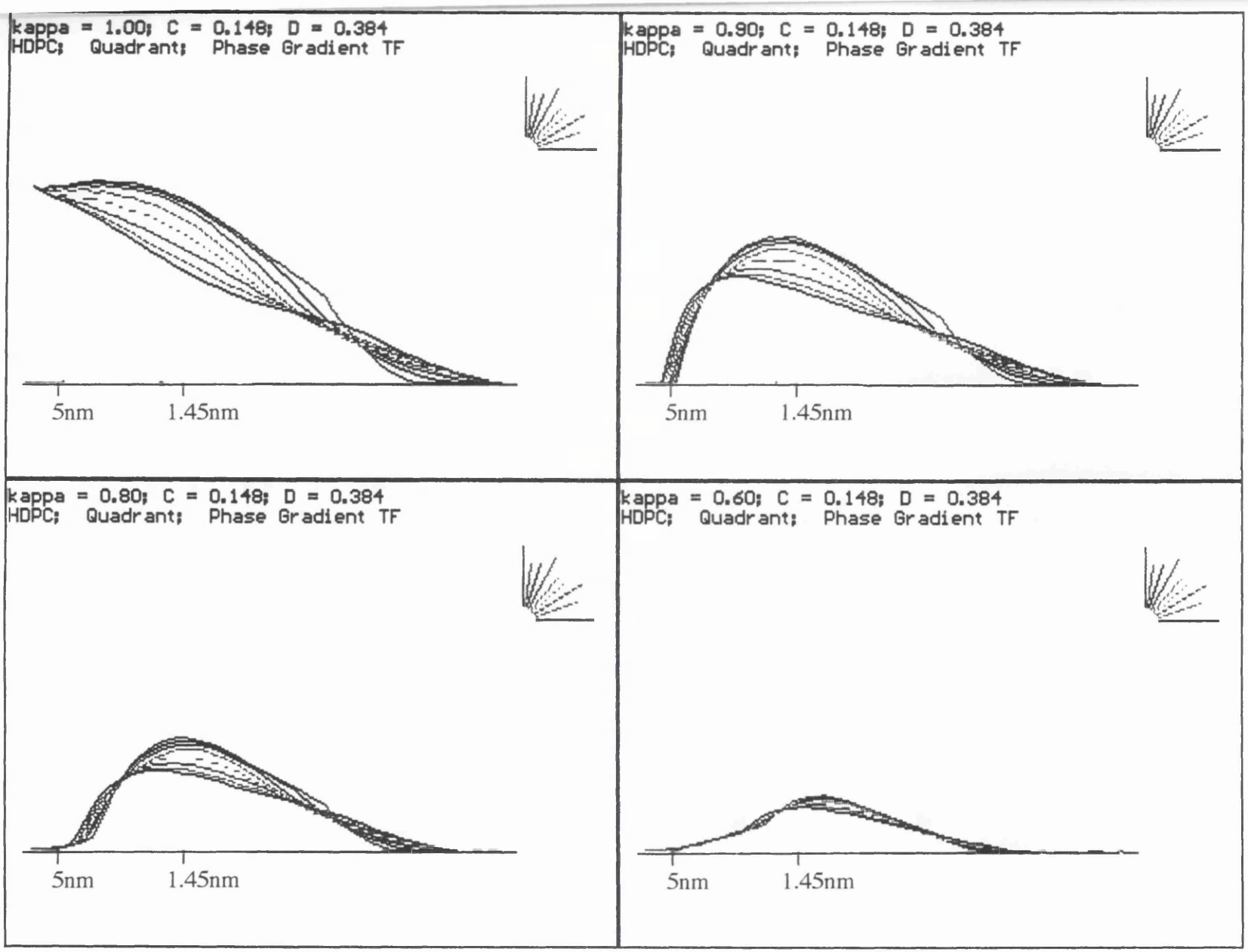

Figure 4.11(a) : Variation of the phase gradient transfer function with reduced spatial frequency for the inner quadrant detector with different values of κ ($C_s \approx 3.5$mm, $\Delta f \approx 1138$Å).

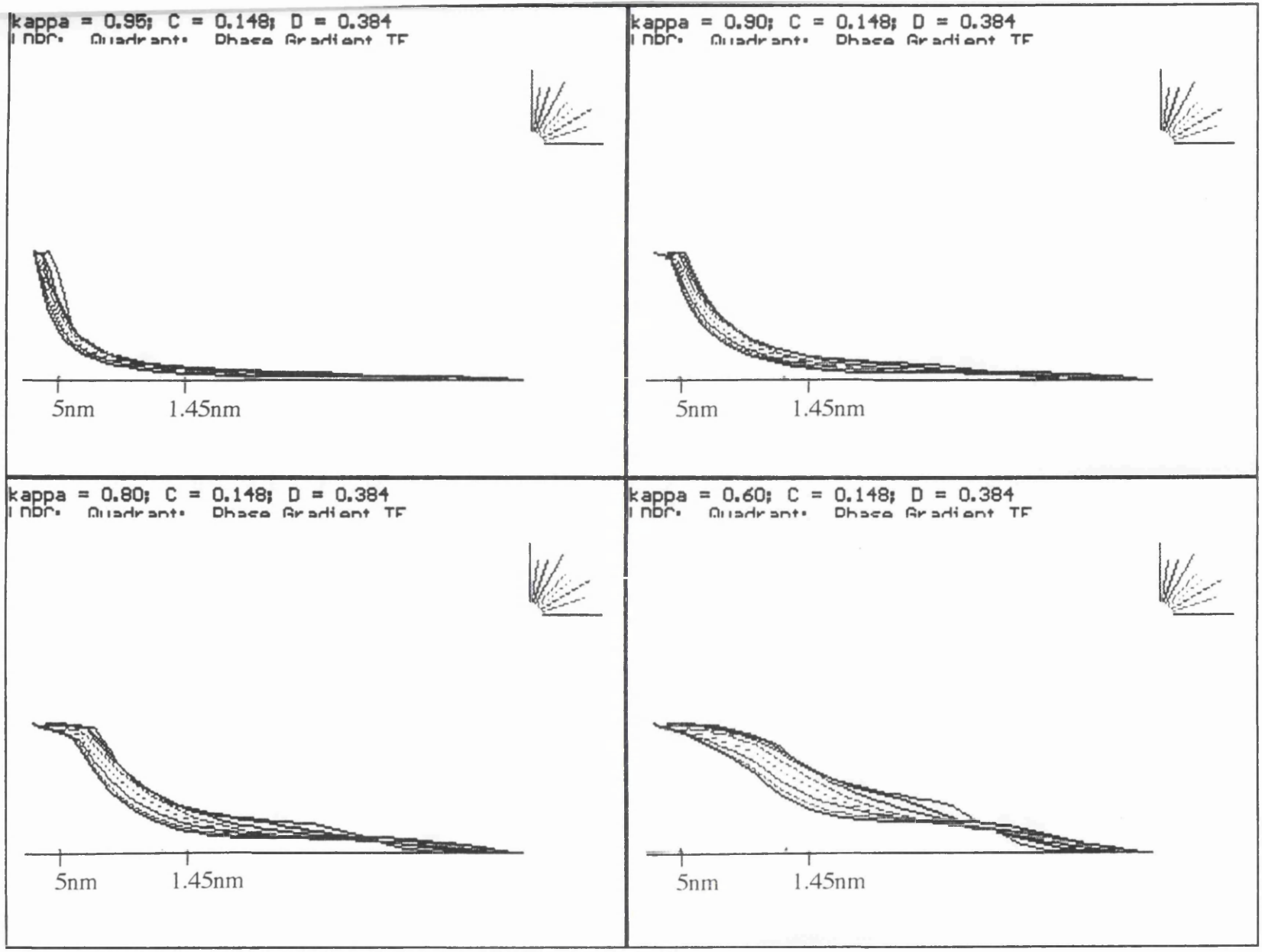

Figure 4.11(b) : Variation of the phase gradient transfer function with reduced spatial frequency for the outer annular detector with different values of κ (C_s≈3.5mm, Δf≈1138Å).

Figure 4.11(b) shows that for κ = 0.95 the signal at normalised spatial frequencies >0.3, equivalent to <3nm, is very low. Thus, for these conditions, lattice information from the CPC particles would be lost. However, for low spatial frequencies ~5nm, the signal transferred is still relatively low. For a κ of 0.9 the signal at high spatial frequencies is greatly diminished, while the transfer of the signal at spatial frequencies >4nm is better than for κ = 0.95. As the value of κ is further reduced, whilst the signal at low spatial frequencies is transferred, the signal contains more high spatial frequency information . The graphs shown in figures 4.11(b) indicate that a κ value between ~0.8 - 0.9 are the best conditions for imaging features which have a low spatial frequency. To record separate lattice and topographic images simultaneously the ideal conditions are κ = 0.9 at a defocus of ~1138Å. Images recorded using the modified DPC technique are presented in the following section.

4.6 Experimentally obtained DPC images from highly chlorinated CPC

Using the imaging conditions described in the previous section, several images were recorded from highly chlorinated, industrially produced pigment particles. A selection of typical images are presented in figures 4.12(a) - 4.14(b). The arrow on each image shows the direction of differentiation. Two images were recorded simultaneously from each area. The first image provides information on the topography of the particles. The second image provides information on the internal structure of the particles, through the presence of lattice fringes. As mentioned in the introduction to this chapter, it is hoped that these images will provide more information on the aggregates, previously studied using CTEM imaging and diffraction techniques.

(a)

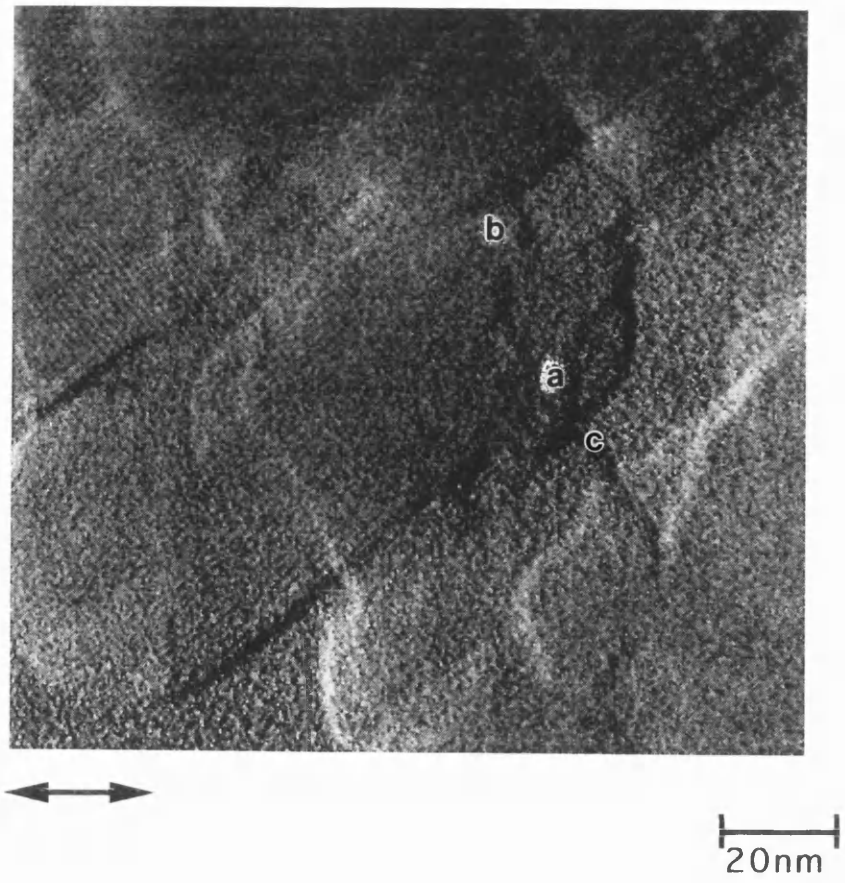

(b)

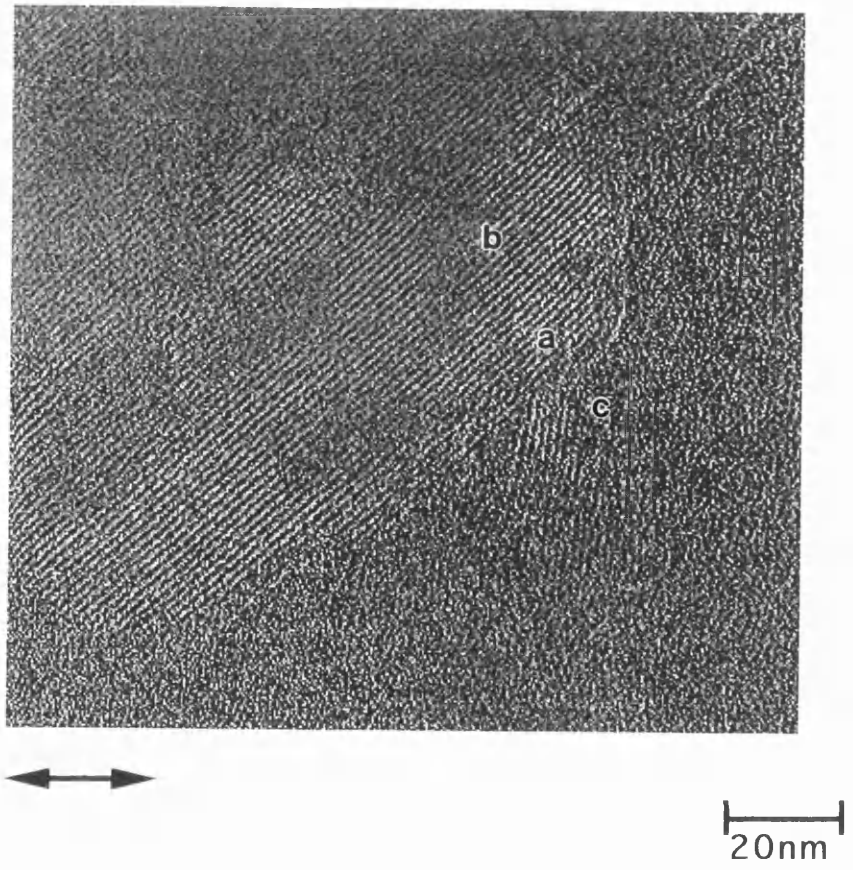

Figure 4.12(a) & (b): Topographic and lattice images of a small aggregate of particles.

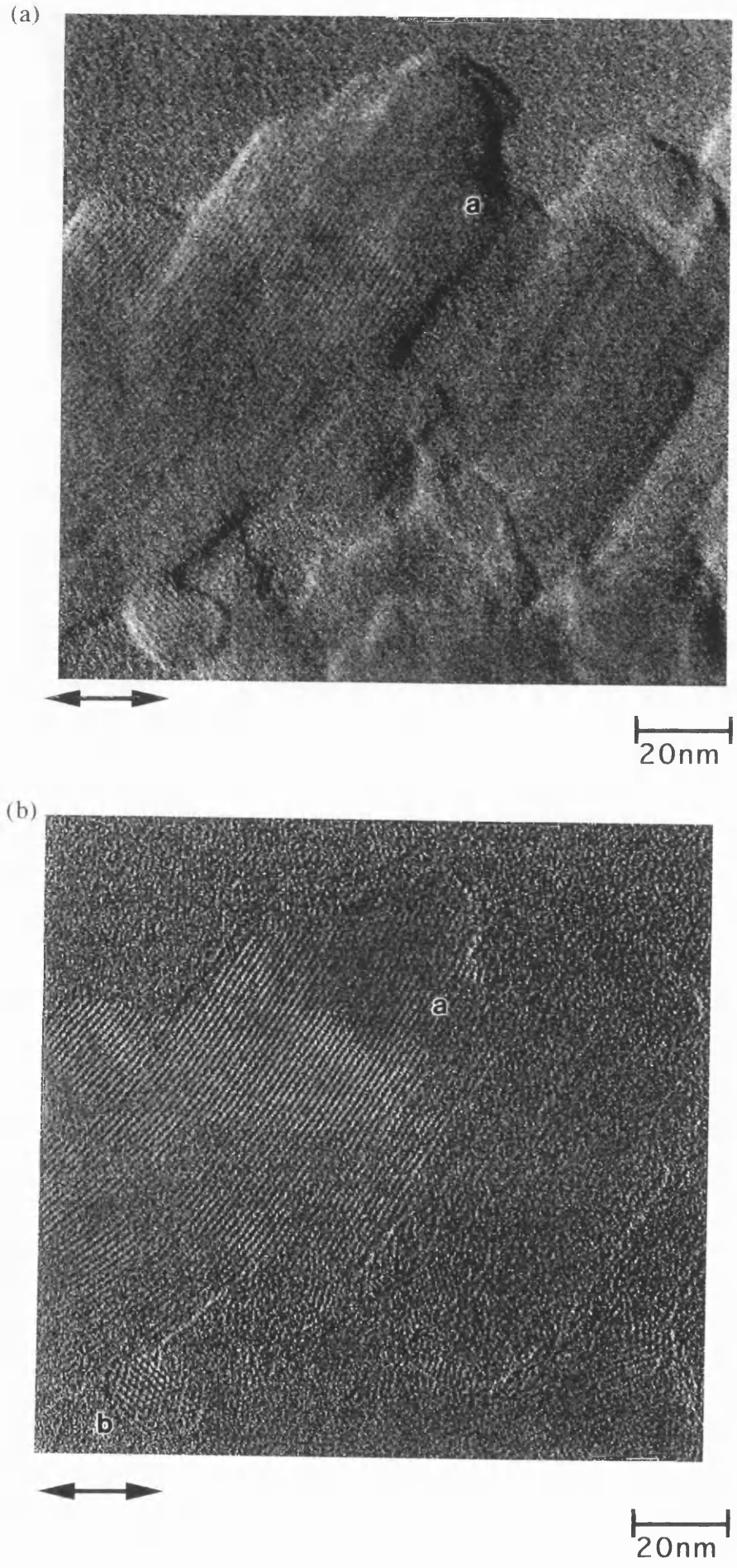

Figure 4.13(a) & (b): Topographic and lattice images of a small aggregate of particles.

(a)

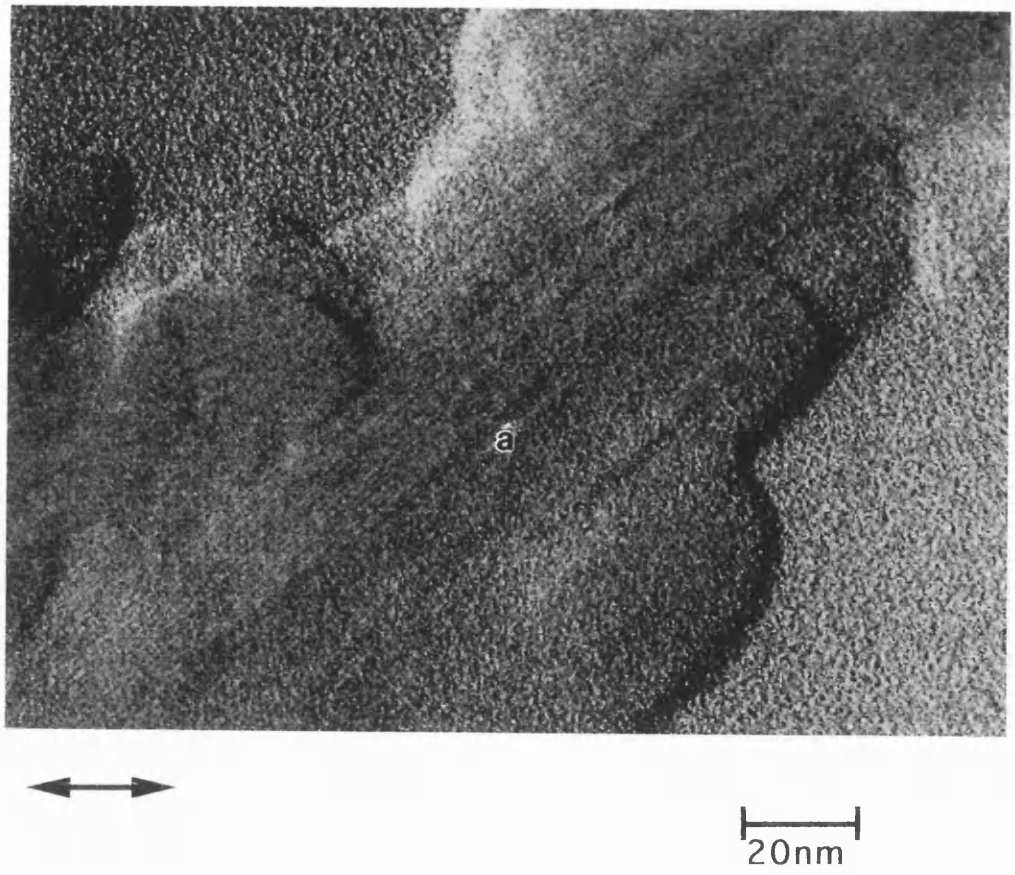

(b)

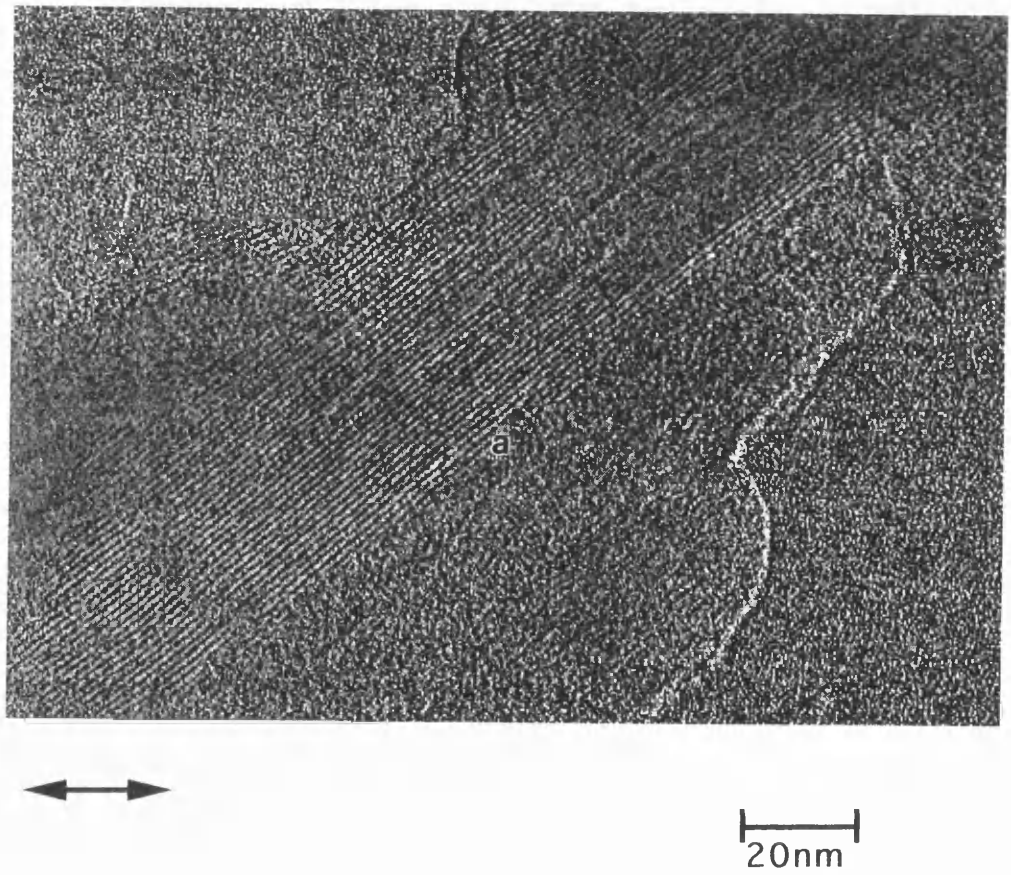

Figure 4.14(a) & (b): Topographic and lattice images of a small aggregate of particles.

Figure 4.12(a) shows a topographic image of an aggregate of what appears to be several particles. The edges of the particles are clearly discernible and it appears that there are several overlaying particles. There are also some irregular features on the surface. In the previous chapter, diffraction studies were carried out to determine if these are aggregates which have not been broken down by the pigmentation process or, if they are a reaggregation of particles. The lattice image shown in figure 4.12(b) shows that at **a** and **b** (also marked in figure 4.12(a)) the lattice fringes carry on across what appears to be overlaying particles. This suggest that these are not areas of particle reaggregation but that this is an aggregate which has not been broken down by the pigmentation process. These steps at the particle edge appear to be areas which have been attacked during the pigmentation process but the process is incomplete. The feature marked **c** appears to be another step on the surface of the aggregate, however, the lattice fringes from the same area are in a different direction to the rest of the fringes. It is possible that this is a piece of material which has attached itself to the aggregate.

Figure 4.13(a) shows a topographic image of another aggregate of particles. At **a** the edge of the particle appears to show a terraced structure, while the surface of the aggregate is by comparison, relatively flat. Again the lattice fringes at **a**, in figure 4.13(b), show that these are not overlaying particles but an aggregate which has not been broken down by the pigmentation process. The lattice fringes at **b** are almost perpendicular to those at **a**. This demonstrates the ability of this technique to image lattice fringes in nearly all directions except those parallel to the direction of differentiation. This area is probably a second aggregate.

Figure 4.14(a) shows another aggregate of material. The terraced structure at the edge of the particles is clearly visible. There appears to be a large area at **a** in which the surface has irregular features. In the corresponding lattice image, shown in figure 4.14(b), the lattice fringes are continuous across this feature. These irregular features may be a result of the pigmentation process which is attacking the particle along the length of the aggregate. Alternatively it may be a result of the

crystal growth process. As discussed in chapter 3, long chains of approximately planar molecules are formed. These columns are then attracted by weaker Van der Waals forces. The irregular surface may arise from the stacking of the planes of molecules.

Whilst in CTEM imaging all pixels are acquired simultaneously, thus reducing the dose incident on the beam sensitive material, STEM images offer other advantages. DPC images provide simultaneous information regarding the topography and internal structure of the pigment particles. These images have confirmed the conclusion, in chapter 3, that many of the aggregates are large particles which have not been broken down by the pigmentation process. The images have also shown that the particles are not completely smooth and that the edges of the particles are terraced and the surface of the particles have irregular features.

Chapter 5

ANALYSIS OF HIGHLY CHLORINATED COPPER PHTHALOCYANINES USING ELECTRON ENERGY LOSS SPECTROSCOPY

5.1 Introduction

As discussed in Chapter 1, the colouring properties of CPC pigments depend markedly on the degree of halogenation, the relative amounts of each halogen present and the physical form of the pigment particles. Thus there is considerable interest in studying the particle to particle variations within the pigment. Previous work by McColgan et al (1990) used energy dispersive x-ray (EDX) analysis to measure the halogen to copper ratios from a number of different samples with differing degrees of halogenation. By recording a sequence of spectra they were able to extrapolate to zero dose to obtain the original halogen to copper ratios. They determined the Cl:Cu ratio to an accuracy of ~0.5 Cl atoms per molecule in highly chlorinated CPC. However, to attain this level of accuracy, each area analysed had to contain ~1500 pigment particles. In addition, the specimen was cooled to 110K, reducing the rate of chlorine loss by a factor of 3 relative to that at room temperature. The related technique of electron energy loss

spectroscopy with parallel detection (PEELS) has a very much higher detection efficiency for the primary electrons that cause the ionisations resulting in characteristic x-rays. Its sensitivity, for microanalysis of low atomic number elements, is greater, by a factor of 100 - 1000, compared to that of EDX (Egerton, 1980). Thus it is possible to investigate CPC pigments with a spatial resolution which cannot be achieved using EDX. Initial estimates suggested that it should be possible to analyse a single pigment particle, with dimensions ~50nm, at room temperature (Craven, 1989). The ability of the PEELS system to record the electrons inelastically scattered by low atomic number elements meant that the carbon and nitrogen ionisation edges could be recorded. Further to this, it was possible to record the carbon, chlorine, nitrogen and copper ionisation edges simultaneously. It is known that not every CPC molecule has a copper atom at its centre and that this atom can be replaced by two hydrogen atoms or some other transition metal such as iron. This chapter provides an introduction to EELS and its application to the study of highly chlorinated CPC pigments.

Section 5.2 gives a description of the electron energy loss spectrum. The methods of recording an energy loss spectrum are described in section 5.3. Section 5.4 gives details of the analysis of an electron energy loss spectrum and the information available from it. The experimental technique used in the investigations of highly chlorinated CPC pigments is described in section 5.5. The accuracy of the analysis of highly chlorinated CPC was determined by analysing a highly chlorinated, surfactant free material prepared in the laboratory as a standard. To do this, films with thicknesses in the range 50 - 100nm were grown epitaxially on KBr by evaporation. The techniques used to analyse spectra are described in sections 5.6. and 5.7. The problems which have to be overcome when analysing CPC spectra are discussed in section 5.8. Techniques which have been developed to overcome these problems and the results of the analyses are presented in sections 5.9 - 5.13. The technique described in section 5.13 was then applied to the investigation of epitaxial films of an industrially prepared sample.

Section 5.14 presents the results of this investigation. A discussion of the results obtained from the epitaxial films of the standard and industrially prepared samples is presented in section 5.15. The technique was then applied to study samples of pigment particles of the industrially prepared CPC material. The results of this investigation are presented in section 5.16. Section 5.17 presents a summary of the use of PEELS in analysing CPC material.

5.2 The electron energy loss spectrum

Electron energy loss spectroscopy involves the analysis of the energy distribution of a beam of electrons after it has passed through a specimen. The technique can provide a wealth of information about thin solid specimens (Egerton 1986). To limit the effects of multiple scattering, specimens for use with 100keV electrons must be less than ~100nm thick and preferably less than 50nm thick. In practice, specimens with a $t/\lambda < 0.5$ are desirable, where t is the thickness of the specimen and λ is the total mean free path for inelastic scattering.

When fast electrons travel through a thin specimen, they may be transmitted through the specimen unscattered, elastically scattered or inelastically scattered. In elastic scattering, the incident electrons interact with the Coulomb field of each atomic nucleus and very little energy is exchanged. Electrons are inelastically scattered by Coulomb interaction with the atomic electrons and there is a gain of energy by the scattering atoms and an equal loss of energy by the fast electrons. Since the energy gains are dependent on the atomic properties of the specimen, information about the specimen can be obtained by analysing the energy of the transmitted electrons using an electron spectrometer. A typical electron energy loss spectrum is shown in figure 5.1. The zero loss peak represents those electrons which have been elastically scattered and those which are unscattered. It also includes quasi elastic scattering i.e. electrons which have

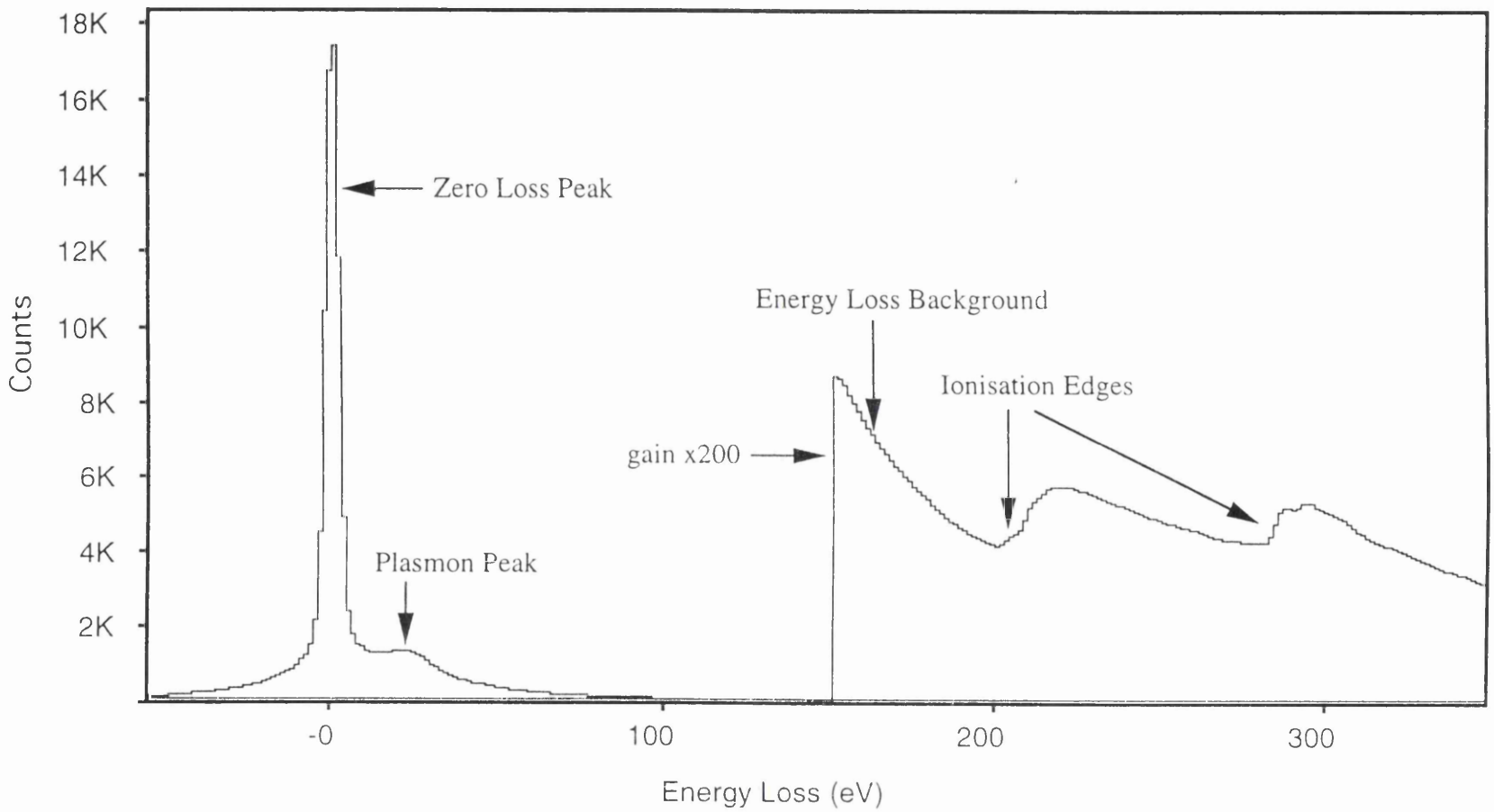

Figure 5.1 : A typical electron energy loss spectrum.

excited vibrational modes (~ meV at most). Since the energy exchange in elastic scattering is small the width of this peak is a measure of the energy resolution of the system (Krivanek et al, 1987). In electron microscope systems, the resolution of the system is determined by both the resolution of the spectrometer and the energy spread of the electrons produced by the electron gun and neither is affected by the other. The Gatan model 666 PEELS on the VG microscopes HB5 STEM, operating at 100keV beam energy, can give a resolution of < 0.4eV. In addition to inelastic collisions with individual electrons, the fast electrons can excite collective oscillations of the outer electrons. These scattering events are called plasmons and are visible as one or more peaks below 50eV. Except in the case of extremely thin specimens, there is a high probability that the fast electrons will undergo more than one inelastic event, so that the plasmon peaks are repeated at multiples of the plasmon energy $\hbar\omega_p$ where ω_p is the plasmon frequency. If λ_p is the mean free path for excitation of one plasmon, the probability P_n of exciting n plasmons in a specimen of thickness t is given by Poisson statistics

$$P_n = \frac{1}{n!}\left(\frac{t}{\lambda}\right)^n exp\left(-\frac{t}{\lambda_p}\right) \qquad (5.1)$$

λ_p depends on the elemental composition of the specimen and is of the order of 100nm for 100keV electrons. The energy range covering the zero loss peak and the plasmon peaks is referred to as the 'low-loss' region. The local thickness of a specimen can be measured from analysis of the low-loss spectrum (Egerton & Cheng, 1987). At higher energy losses the spectrum falls rapidly forming a spectral background which results from excitation of atomic shells of lower binding energy. Superimposed on this background are ionisation edges which correspond to the excitation of inner-shell (core) electrons. In figure 5.1 this region of the spectrum has been scaled by a factor of 200. These edges take the form of an abrupt rise in intensity followed by a more gradual decrease to become

part of the background for higher energy edges. The edge threshold corresponds to the binding energy of a particular atomic shell. This energy depends upon the type of shell (K, L etc.) and the atomic number of the excited atom. These edges can therefore be used to identify the elements present in the sample. If the energy loss spectrum is calibrated to within a few percent, elements present in the sample are identified by comparing the energies of observed edges with tabulated values (Egerton 1986, Ahn and Krivanek 1983). In order to quantify the spectra, it is necessary to subtract the background from under the ionisation edges. From the edge intensities it is possible to determine the elemental concentrations in the sample and this is described in section 5.7.

5.3 Electron energy loss spectra recording

There are two main methods of electron detection, these being serial and parallel recording systems. Figure 5.2(a) shows the ray paths of a typical serial EELS system. Electrons which pass through the spectrometer entrance aperture (SEA) are bent through 90^{o} by a magnetic prism. Since the magnetic force (Bev) is equal to the centripetal force mv^2/R, the bending radius R is smaller for electrons of lower kinetic energy and the exit beam is dispersed, with the less energetic electrons deflected through a larger angle. A narrow slit is placed at the exit to the spectrometer and by varying the strength of the magnetic prism different energy electrons are scanned across it and onto the detector. In this way, a plot of energy loss versus intensity can be obtained The slit selects intensity from a well defined energy range. The width of the slit may be increased thus increasing the number of electrons entering the spectrometer but the energy resolution of the signal is degraded. The problem with a serial recording system is that it makes inefficient use of the electrons passing through the spectrometer since almost 99.9% of them (for 1000 channels) are absorbed by the energy-

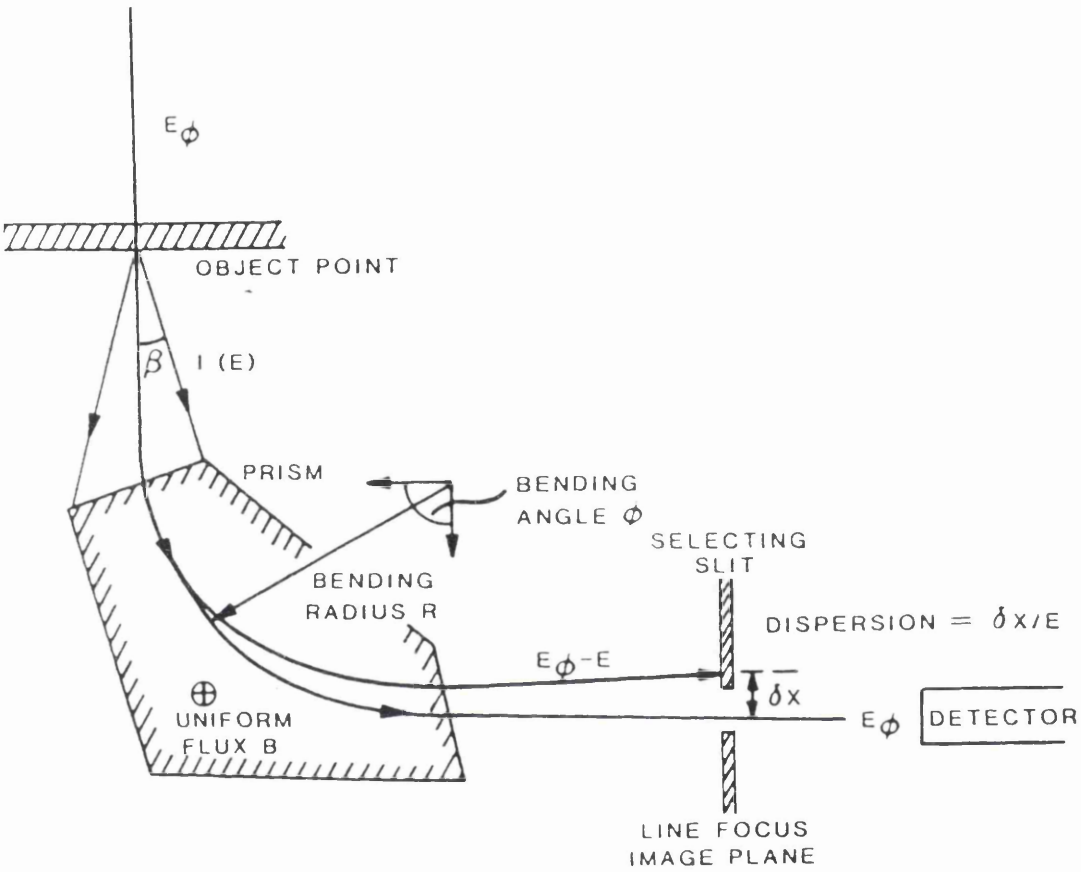

Figure 5.2(a): Ray paths of a typical serial EELS system.

selecting slit. By replacing the slit with a position sensitive detector, all energy losses are recorded simultaneously. This system is referred to as parallel electron energy loss spectroscopy (PEELS). The experimental work described in the following sections was performed on an EELS system with parallel detection. Figure 5.2(b) shows the Gatan model 666 parallel-recording spectrometer used to record the spectrum in this work. The action of the magnetic prism is the same as for the serial EELS system. A set of quadrapole lenses (Q1 - Q4) precedes the detector in order to magnify the dispersion in the vertical direction. In this way the energy dispersion is matched to the spatial resolution of the detector so that the latter is not the limiting factor. Each photodiode behaves like a capacitor, and before recording a spectrum, all the diodes are charged to the same potential. During spectrum acquisition, electron-hole pairs created by light emission in the thin yttrium aluminium garnet (YAG) scintillator cause the diodes to discharge by an amount proportional to the local electron intensity. At the end of the acquisition period, the charge remaining on each diode is sampled in turn. The resulting signal is digitised and stored as one channel of the spectrum. The design and performance of the parallel detection system is described in more detail in Krivanek et. al. (1987).

There are several departures from ideal behaviour in such systems. The diodes also discharge by thermal generation of electron-hole pairs, giving rise to a background or 'dark current' in the energy-loss spectrum. This effect is corrected for by taking a readout with no electrons incident on the scintillator. This is then subtracted from the EELS data inside the computer. This also corrects for any DC offset in each diode. Being an electrical insulator, the YAG scintillator accumulates internal charge in strongly irradiated regions. This has the effect of locally increasing its conversion efficiency. This artefact can be reduced by 'annealing' the scintillator with a broad (undispersed) beam for several minutes at the start of each day. Stray scattering generated by the very intense zero loss peak hitting the solid material of the spectrometer can be a severe problem in parallel-

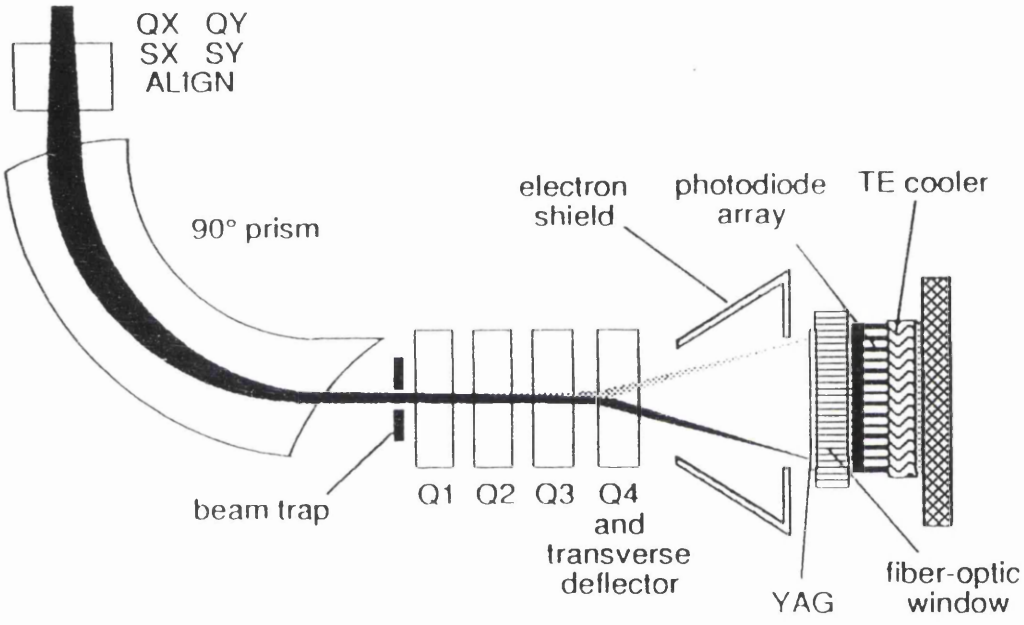

Figure 5.2(b): Principle components of the Gatan model 666 parallel-detection electron-energy loss spectrometer.

recording detectors. This effect has been reduced in the Gatan spectrometer by means of a beam-trap. Thus when the energy loss is sufficiently large, the zero loss peak enters a "Faraday cage" from which the scattered electrons are unlikely to reach the detector.

The Gatan system used allows spectra to be recorded in several ways. The set-up and control of spectra recording is done using the Gatan EL/P software. There are two banks of memory which can each record and store eight spectra. The system also allows the set-up of six configurations which can be selected to record spectra. Each configuration includes : (1) the integration period i.e. the time spent recording the spectra, (2) the Voltage Scanning Module (VSM) setting, which positions the spectra on the diode array, (3) the number of readouts per acquisition. The option to acquire a single spectrum or a sequence of spectra is also available after set-up is complete. A sequence of spectra can be acquired to a memory bank, thus there are 8 spectra per sequence, or a greater number of spectra can be acquired to disk. To record a spectrum, the system is set to acquire using a selected configuration. During acquisition the spectrometer collects the signal from the sample for the selected integration time. At the end of the acquisition period an end of read (EOR) signal is set high and the signal is readout to the computer display, which takes around 20msec after which time the EOR signal goes low. Throughout the process the diodes never stop accumulating. The cycle continues until the operator hits the space bar on the computer. This indicates to the system to stop the acquisition. At this point, if the system is set-up to record a single spectrum, the system continues integrating until the EOR signal goes low and the last recorded spectrum is read out. The system then stops acquiring spectra. If the system has been configured to record a sequence of spectra to a memory bank, it will hold the current spectrum in the first memory and the spectrometer will continue to record and store spectra until a further seven EOR's have elapsed. In this way, a sequence of eight spectra are recorded. In the same way, larger sequences of spectra can be recorded to disk.

The use of this system and a beam blanking facility used to record spectra for the investigations of CPC material is described in section 5.5.

The Gatan EL/P software is also used to analyse the acquired spectra and the information available from an EELS spectrum is described in the following section.

5.4 Information available from EELS spectra

The experimental work described in the following sections is concerned mainly with the use of the energy loss spectra for the determination of concentration ratios. However, the energy loss spectrum not only provides quantitative information on the elemental concentrations but it can also be used to determine the specimen thickness. The thickness of the sample is determined from the probability of inelastic scattering. The probability P_0 of no inelastic scattering is represented by the area I_0 under the zero loss peak, relative to the total area I_t beneath the complete spectrum. This probability can also be determined from equation 5.1 by setting n=0 to get

$$P_0 = I_0 / I_t = \exp(-t/\lambda_t) \qquad (5.2)$$

$$t/\lambda_t = \ln(I_t/I_0) \qquad (5.3)$$

The value of λ_t depends on the sample material, the incident electron energy and the probe angle. Ideally this can be determined from a calibration sample whose thickness has been determined by other means. However, it is known that for 100keV electrons the value of λ_t is of the order of 100nm, thus an estimate of thickness is available immediately (Egerton & Cheng, 1987). Egerton has an equation to predict λ_t to within 20% based on a fit to available data.

The height of an ionisation edge above the underlying background gives a rough indication of the amount of the element present. Quantitative measurements on each ionisation edge provide an estimate of the chemical composition of the material being analysed (Isaacson and Johnson, 1975 and Egerton, 1978). This is discussed further in section 5.7.

There are other types of information which can be obtained from analysis of these ionisation edges. The ionisation edges have a characteristic basic shape which can be calculated on the basis of atomic physics. Superimposed on these basic edge shapes is a fine structure. Energy loss near-edge fine structure (ELNES) consists of oscillations of intensity in the region up to 50eV above the threshold. This fine structure is related to the chemical state of the atom in the solid (Weng et al 1989) and can also give information on defect states (Batson 1988). Beyond 50eV from the ionisation threshold, fine structure oscillations become weak but they continue for an energy range comparable to the threshold energy. This extended electron energy loss fine structure (EXELFS) provides information on the nearest neighbours of particular types of atom. From the damping of EXELFS oscillations, it is possible to measure the amount of thermal or static (local) disorder in a material.

5.5 Experimental technique

The pigment particles themselves are relatively inhomogeneous and may vary in composition. In the electron microscope they are subject to radiation damage. For these reasons, initial investigations using PEELS were carried out using epitaxial films of the CPC samples. In this way, it was possible to have reproducibility thus allowing the performance limits of the technique to be established. It was also possible to study the effects of sample thickness

systematically. Epitaxial films ~50nm thick were prepared using the specimen preparation technique described in chapter 1.

In order to determine the smallest area from which reliable results could be gained, the experiment was performed over a range of areas with various diameters. The diameter of the area irradiated was set by defocusing the condenser lens a known amount. The diameter was determined by measuring the size of the resulting damaged area on an annular dark field image of the region. Figure 5.3 shows a typical image recorded from an irradiated area of epitaxial material.

Spectra were recorded using the GATAN 666 UHV PEELS spectrometer on the extended VG Microscopes HB5 operated at 100kV. The probe current was 0.2nA, as measured on the electrically isolated real objective aperture. Data was collected with the spectrometer aperture removed and only the larger of the interchangeable ADF detectors as the defining aperture. With PSL1 used at its standard setting this set-up gave a collection semi-angle of 40mrad. This allowed a large signal to be collected in the shortest time period, thus giving a larger signal to noise ratio for the small nitrogen edge, whilst minimising radiation damage. The 100μm VOA was used to define the probe giving a convergence semi-angle of 11mrad.

Since the CPC material is subject to radiation damage, it was necessary to record all ionisation edges simultaneously to allow the mass loss to be monitored. A suitable energy dispersion had to be selected to allow this to be done. The ionisation edges for the CPC material lie in the energy range 270eV for the Cl $L_{2,3}$ edge to the Cu L_1-edge at 1096eV. The minimum selectable nominal eV per channel which would allow simultaneous recording of the edges was 2eV/channel. The spectrometer was calibrated using this selected value at the start of each experiment. In each case the actual energy dispersion was found to be ~1.4±0.01eV/channel, which was sufficient to acquire the ionisation edges simultaneously. The start energy of the spectra on the diode array was determined

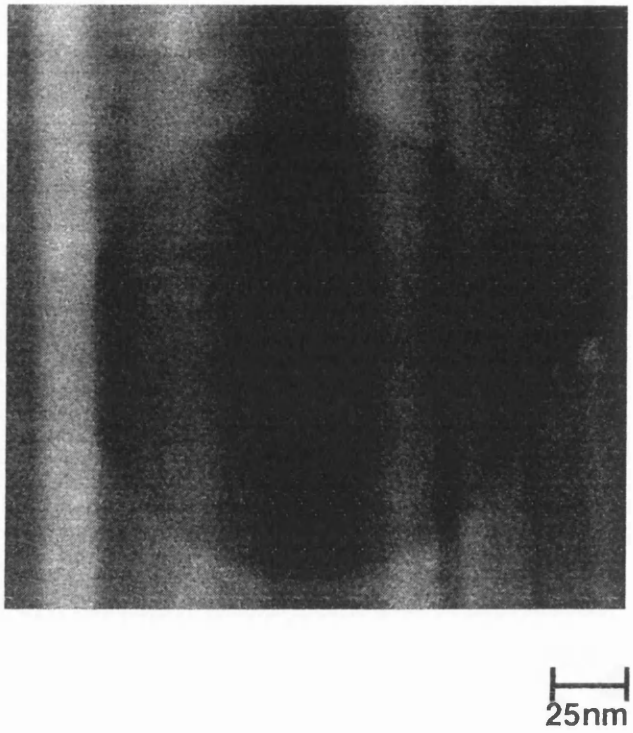

Figure 5.3 : Typical image of an irradiated area.

by two factors : (i) the necessity of having the ZLP in the beam trap so that the spectra contained no spurious background signal and (ii) the need to have enough background prior to the onset of the first edge to allow background subtraction. The problem of mass loss required a sequence of spectra to be recorded. This was done automatically, using a facility provided in the GATAN EL/P software, and a chemical analysis of the sample as a function of radiation dose was performed. By extrapolation of the results back to zero dose, an estimate of the initial composition of the material was determined.

The most important consideration during these experiments was that radiation damage was kept to a minimum prior to recording a sequence from the area under investigation. To reduce the radiation damage during experimental set-up, the PEELS system was used to synchronise the operation of specially built hardware units to control the beam blanking unit and the HB5. Before describing how this system was modified in order to limit the radiation damage, it is important to understand how it operates. Figure 5.4 shows a schematic diagram of the beam blanking units. The first hardware unit uses the End of Read (EOR) signal to control a timer which unblanks the electron beam for a time which can be set by the operator. At the end of the EOR signal, the beam is unblanked for this period and then blanked. Provision is made to override the blanking for normal operation. This unit is used to provide flexible signal attenuation to allow the low-loss region to be recorded without saturation and is used for most PEELS work. The second unit was built specifically for this project. The acquire sequence mode of the EL/P software starts the system displaying spectra continuously. When the space bar on the computer keyboard is hit, it keeps the existing spectrum in memory A, writes the one currently being acquired to memory B and the subsequent six spectra to the remaining six memories. When armed, the additional hardware unit forces the system to blank. While blanked, the acquire sequence mode can be invoked and an unirradiated area of specimen moved into position using the electrical shifts of the HB5. By pressing the initiate

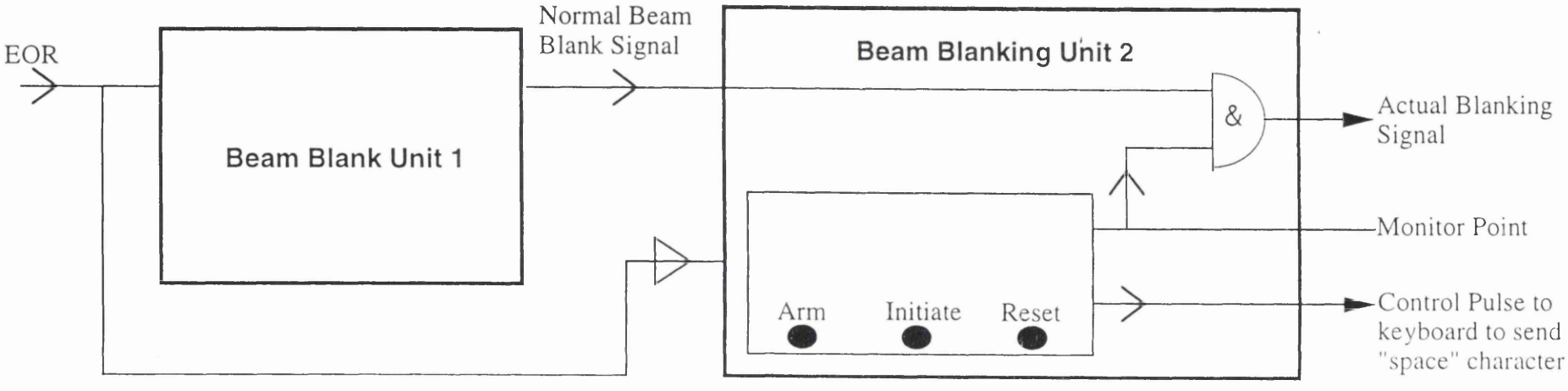

Figure 5.4 : Schematic diagram of the beam blanking units.

button, the hardware waits until the end of the next EOR pulse and unblanks the beam for the pre-set time and repeats this after the next seven EOR pulses. In this way, exactly eight spectra from the previously unirradiated area are recorded. To ensure that the computer acquires these eight spectra into the eight memories, a "space" character is sent to the computer after the second EOR pulse.

5.6 Separation of inner-shell ionisation edges

A typical spectrum recorded from the CPC material, showing the inner-shell ionisation edges, is presented in figure 5.5. Before quantifying the inner-shell ionisation edges, it is first necessary to remove the spectral background. This background has an approximate form AE^{-r} where E is the energy loss and A and r are constants. A and r can be found using a least squares fitting (or other) routine in a region prior to the edge threshold as shown in figure 5.6. In practice the fitting region should be ~50eV in width. Atomic theory predicts and it has been confirmed that r should lie in the range 2 to 6.5 (Egerton 1986). Higher values corresponding to large energy loss E or smaller collection semi-angle β. This modelling of the background is likely to be more accurate if the spectrum has first been deconvoluted to remove plural scattering (Leapman and Swyt, 1981) and if the instrumental background (arising from stray scattering around the electron detector) is low or has been subtracted (Craven and Buggy, 1981; Bentley et al, 1982). Measurement of the stray scattering was carried out prior to experiments on CPC samples and was found to be at a level low enough to be ignored without affecting the results of the analysis. Deconvolution is done using a fast-Fourier transform (FFT) algorithm which can process an extended range of energy loss in seconds using a computer. There are two distinct Fourier techniques which are used (Egerton, 1989). The Fourier-log method derives the single scattering distribution from a measured spectrum over an arbitrary range of energy,

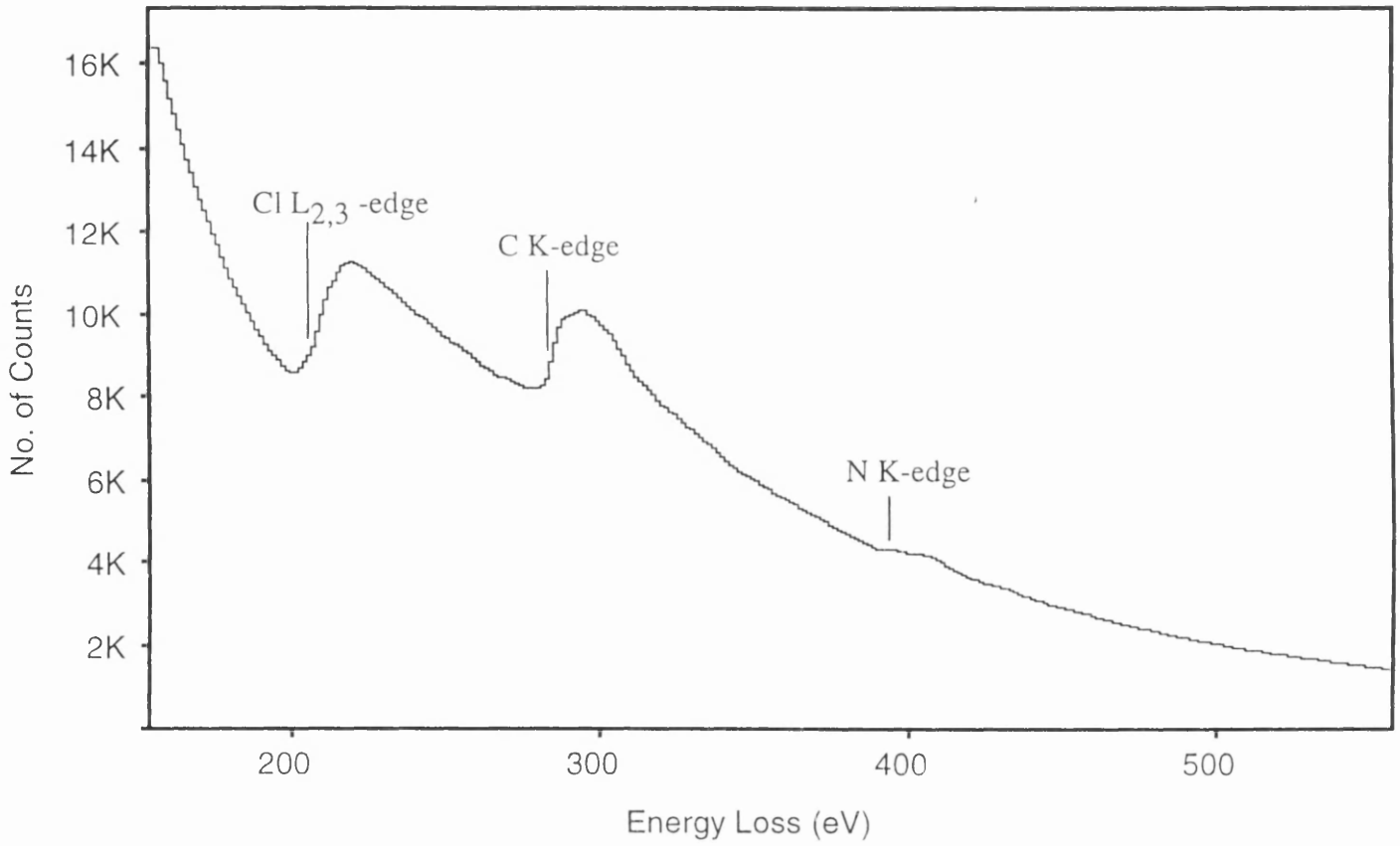

Figure 5.5 : Typical energy loss spectrum from highly chlorinated copper phthalocyanine.

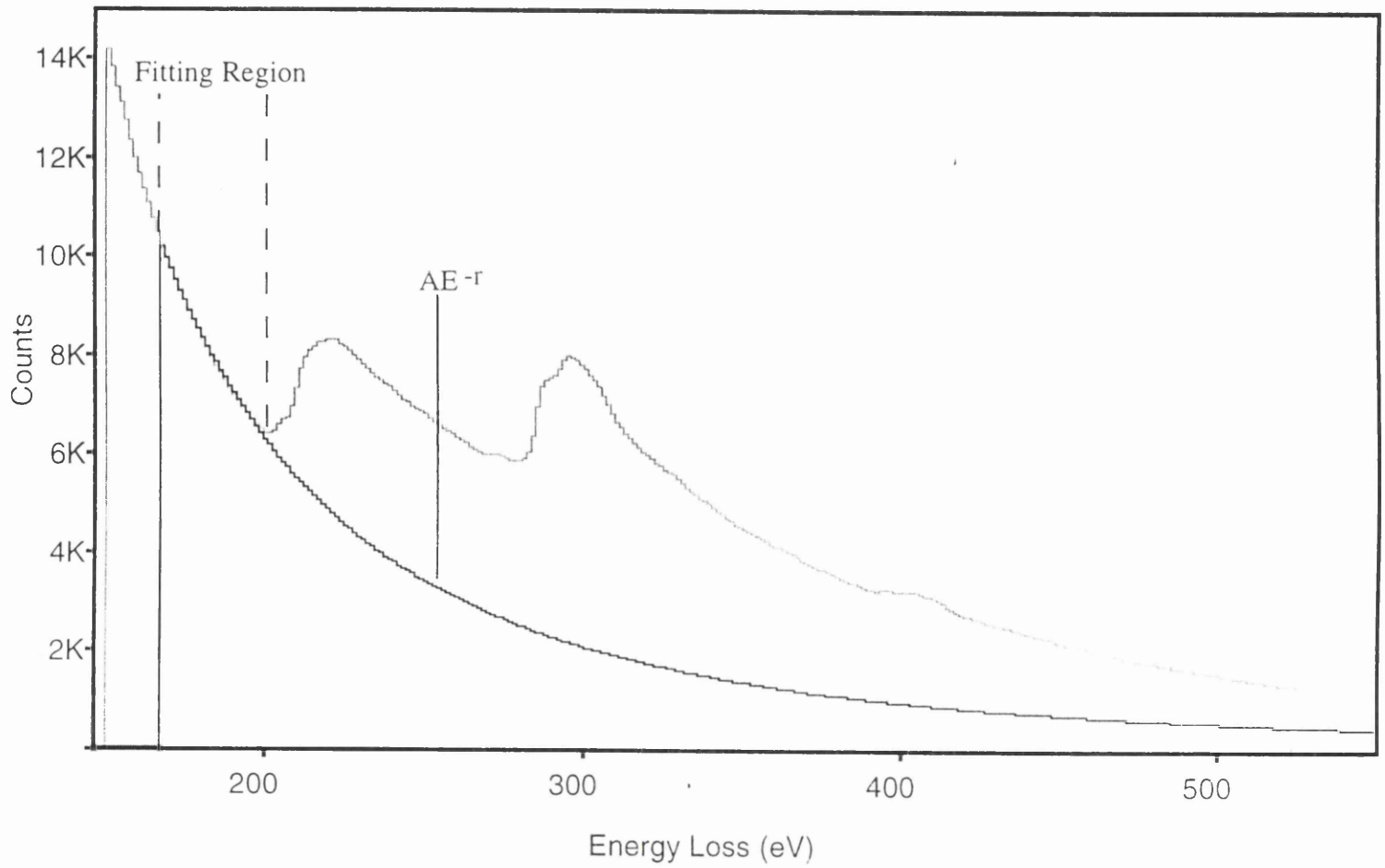

Figure 5.6 : Background calculation using an AE^{-r} form.

provided the zero-loss peak is included and any gain changes are first removed. The Fourier-ratio method removes plural scattering (inner-shell and low-loss) scattering from a core-loss profile whose pre-edge background has previously been removed. In this work the spectra were also sharpened prior to background subtraction. This involves using a deconvolution routine to recover some of the spectrum detail lost to the broad tails of the zero-loss peak.

5.7 Quantification of Ionisation Edges

Once the background has been subtracted from under the ionisation edge quantitative elemental analysis is usually carried out by integrating the core-loss intensity over an energy window of width Δ, starting at the ionisation threshold. The areal density N (the number of atoms per unit area of specimen) is found using the approximate formula (Egerton 1978)

$$I_c(\beta,\Delta) = N\,\sigma_c(\beta,\Delta)\,I_l(\beta,\Delta) \qquad (5.4)$$

$$N = \frac{1}{\sigma_c(\beta,\Delta)}\frac{I_c(\beta,\Delta)}{I_l(\beta,\Delta)} \qquad (5.5)$$

where $\sigma_c(\beta,\Delta)$ is a 'partial' cross-section for ionisation by electrons scattered through angles $< \beta$ and up to an energy loss Δ above the edge threshold and $I_l(\beta,\Delta)$ is the integrated intensity present in the low-loss part of the spectrum, including the zero-loss peak and all scattering up to an energy loss $E=\Delta$. The partial cross-section can be measured experimentally or calculated using various models (Leapman et al, 1978; Egerton 1979). The theoretical cross-section shapes for this work were obtained using the SIGMAK and SIGMAL programmes of Egerton (1986). The relative concentrations of two elements A and B can be found from :

$$\frac{N_A}{N_B} = \frac{I_C^A(\beta,\Delta)\sigma_C^B(\beta,\Delta)}{I_C^B(\beta,\Delta)\sigma_C^A(\beta,\Delta)} \qquad (5.6)$$

5.8 Problems of analysing CPC material

As mentioned in the introduction, the accuracy of the analysis was to be determined using a standard sample which was prepared in the laboratory at Zeneca to be highly chlorinated and surfactant free. Bulk analysis determined that the sample contained 15.3 Cl atoms/molecule. In order to determine the original composition of the material, a sequence of spectra were to be recorded and the results of the analysis extrapolated back to zero dose. Figures 5.7(a) & (b) show typical sequences of spectra recorded from diameters ~150nm and ~60nm, respectively. In each of the spectra, the background under the Cl $L_{2,3}$-edges has been subtracted. The backgrounds under the Cl $L_{2,3}$-edges of figures 5.7(a) & (b) were subtracted by fitting an AE^{-r} form prior to the edge threshold. This was done using the background subtraction routine provided in the GATAN software. Several fitting windows were tried to determine the stability of the results. It was found that the first few channels of the spectrum should not be included in the fitting window. The response of the detector in this local region is different but the detailed cause of the difference is not known. Figures 5.7a and b clearly show an increased rate of loss from the smaller area and also a decrease in the loss rate as the irradiation proceeds. To be able to determine the chemical composition it is necessary to measure quantitatively the inner shell ionisation edges in the energy loss spectrum.

There are a number of problems with the quantification process. It can be clearly seen from figure 5.7(a) that the least-squares fitting method of background subtraction, described in section 5.6 cannot be used to separate the Cl edges and the C K-edge. The Cl $L_{2,3}$ edge has not settled to an AE^{-r} shape due to the

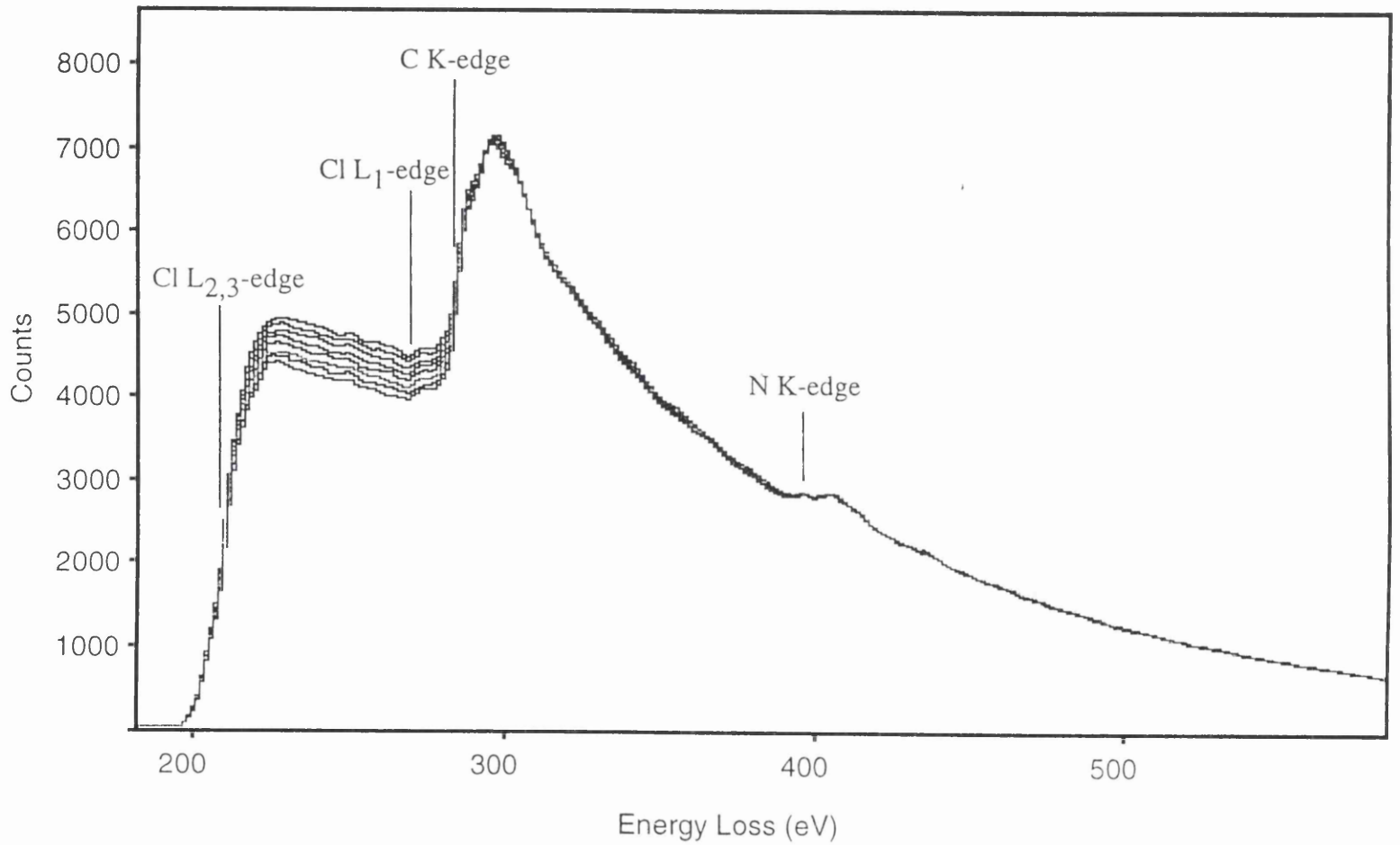

Figure 5.7(a) : A sequence of spectra recorded from an area 150nm in diameter

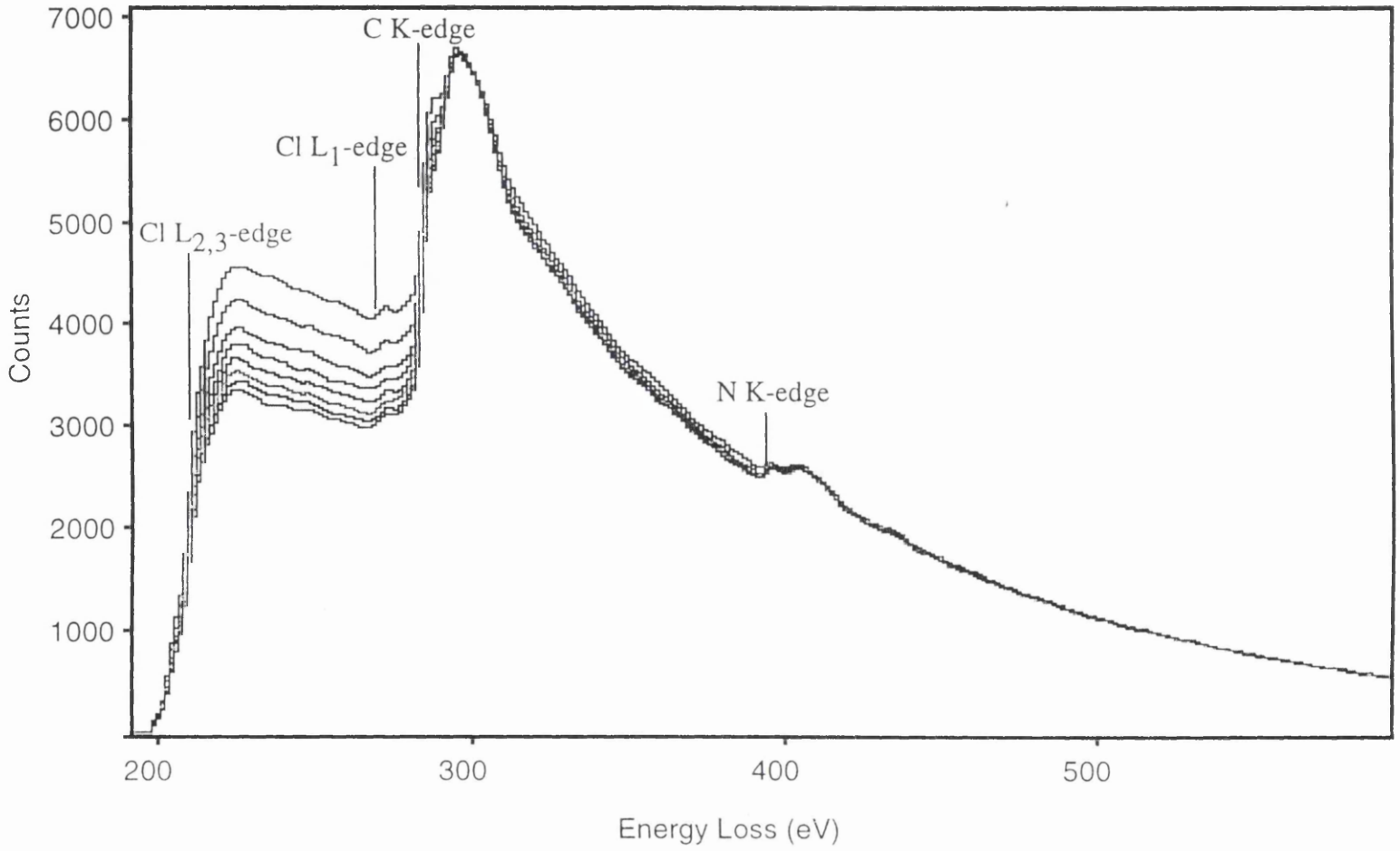

Figure 5.7(b) : A sequence of spectra recorded from an area 60nm in diameter.

proximity of the C K-edge. The shape is further perturbed by the Cl L_1 edge at 270eV. There is also a problem with the weak N K-edge. The EXELFS from the much stronger C K-edge prevent a sufficiently accurate background removal using an AE^{-r} fit. For these reasons a different method of calculating the background under the C and N K-edges had to be used.

Figures 5.7(a) & (b) show that as the probe diameter is reduced the rate of mass loss is increased. This presents problems in the extrapolation of the data to zero dose in order to determine the original composition.

The theoretical edge shapes, initially used to process the spectra are different from the edge shapes found experimentally. These problems and the methods used to overcome them are considered in the following sections. Several approaches were tried and the one which gave the most consistent results adopted.

5.9 Approximation to the single stage fitting process

As mentioned above the least-squares fitting process of background subtraction cannot be used to separate the C and N K-edges. The first method used to extract these edges was an approximation to the single stage fitting process of Steele et al (1985). This section describes how this method was applied to the spectra and the results of the data analysis.

Prior to extraction of the ionisation edges the dark currents were subtracted and the spectra were sharpened to remove the effects of tailing. The backgrounds under the Cl $L_{2,3}$-edges were subtracted as described above and then deconvoluted using the Fourier Ratio method (Egerton 1989).

In the approximation to the single-stage fitting process a trial background of the form AE^{-r} was calculated. This was done by choosing a value for r and calculating the constant A such that it forced the background form to pass through the spectrum immediately prior to the edge. The resulting edge shape for the first

spectrum in a sequence was compared to a SIGMAL2 (Egerton 1986) theoretical cross section. Figures 5.8 and 5.9 show such a comparison for the C K-edge and N K-edge, respectively. The value of r which gave the best agreement was used to process that edge for all spectra in that sequence. The elemental ratios were calculated using equation 5.6. Figures 5.10(a) - (c) show the Cl:C, C:N and N:Cl ratios for a number of sequences recorded using different probe diameters. The expected initial values for these ratios are 0.478, 4 and 0.523 respectively. The ratios are shown as a function of spectrum number rather than dose. Figure 5.10(a) shows that for diameters down to 150nm the rate of loss of chlorine is effectively linear. More specifically, at the largest probe diameter, after a dose of $\sim 8.5 \times 10^3$ C/m^2 (spectrum 8) the sample has lost only ~ 5% of its chlorine. At a probe diameter of 150nm, after a dose of $\sim 1.4 \times 10^5$ C/m^2 (spectrum 8) the sample has lost ~ 20% of its chlorine. As the dose is increased past this value, the rate of loss of chlorine slows down and at the smallest probe diameter, after a dose of $\sim 3 \times 10^6$C/m^2 (spectrum number 8) the sample has lost ~ 57% of its chlorine. There does not appear to be any loss of nitrogen as shown in figure 5.10(b). At the large probe diameters the C:N values vary by ~2.5%. At the smallest probe diameter the C:N ratio rises by only ~6% of its original value. Figure 5.10(c) reveals that at large probe diameters the loss of chlorine is ~5% as was found for the Cl:C ratios.

As mentioned in section 5.1, the original elemental ratios are determined by extrapolating to zero dose. Figures 5.10(a) and (b) show that for probe diameters down to 150nm the rate of mass loss appears to be linear. At smaller probe diameters the mass loss rate is non-linear and appears to be approaching a limiting value, called saturation below, as the dose increases. The methods of extrapolation for both data sets are described in the following section.

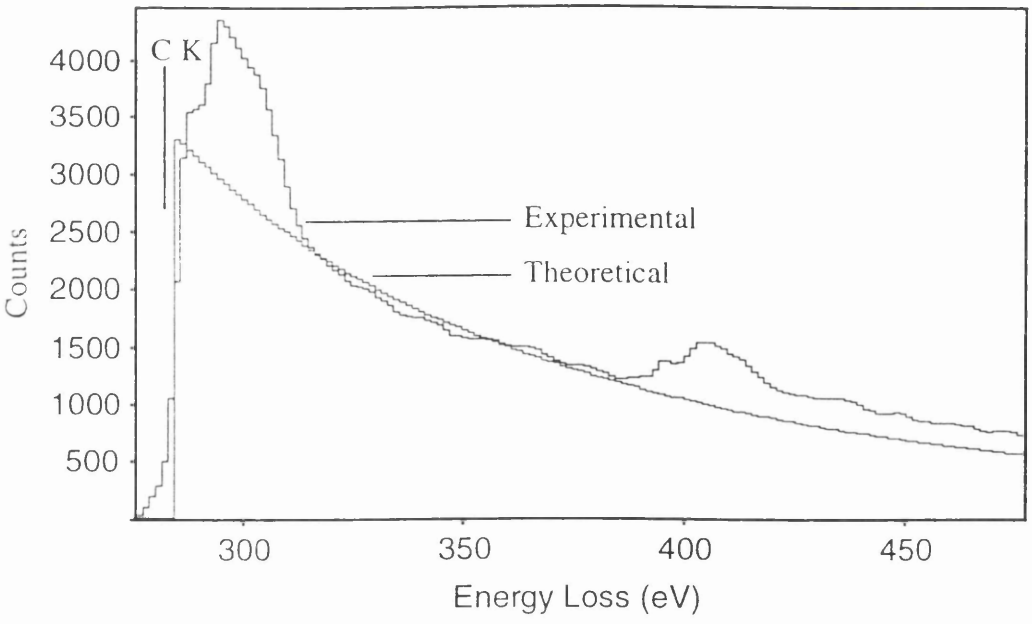

Figure 5.8 : Comparison of the theoretical and experimental carbon edge shapes.

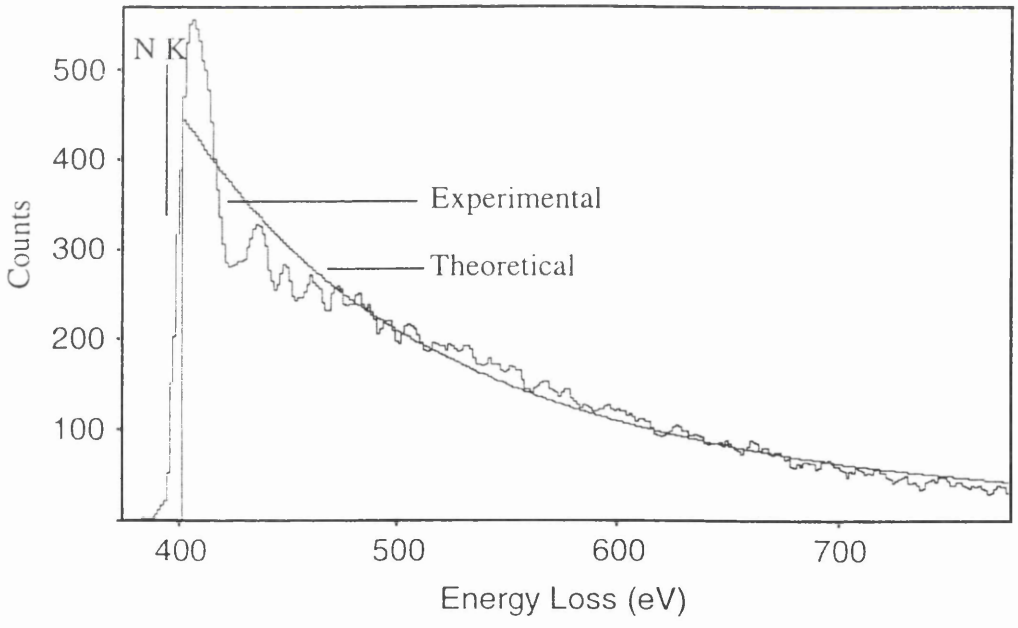

Figure 5.9 : Comparison of the theoretical and experimental nitrogen edge shapes.

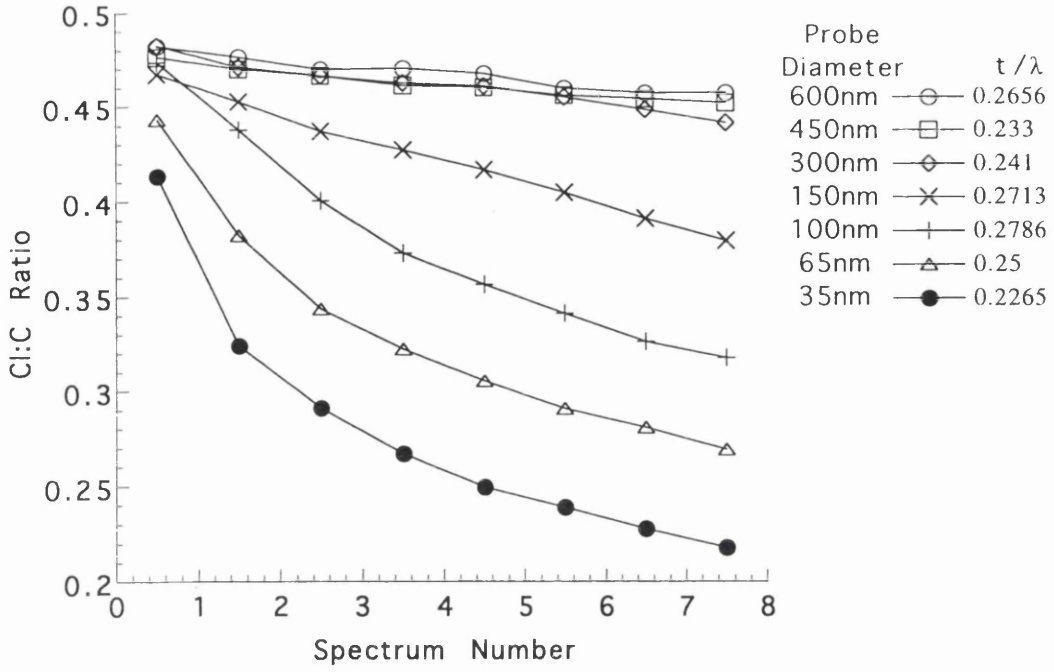

Figure 5.10(a) : Cl:C ratio as a function of spectrum number.

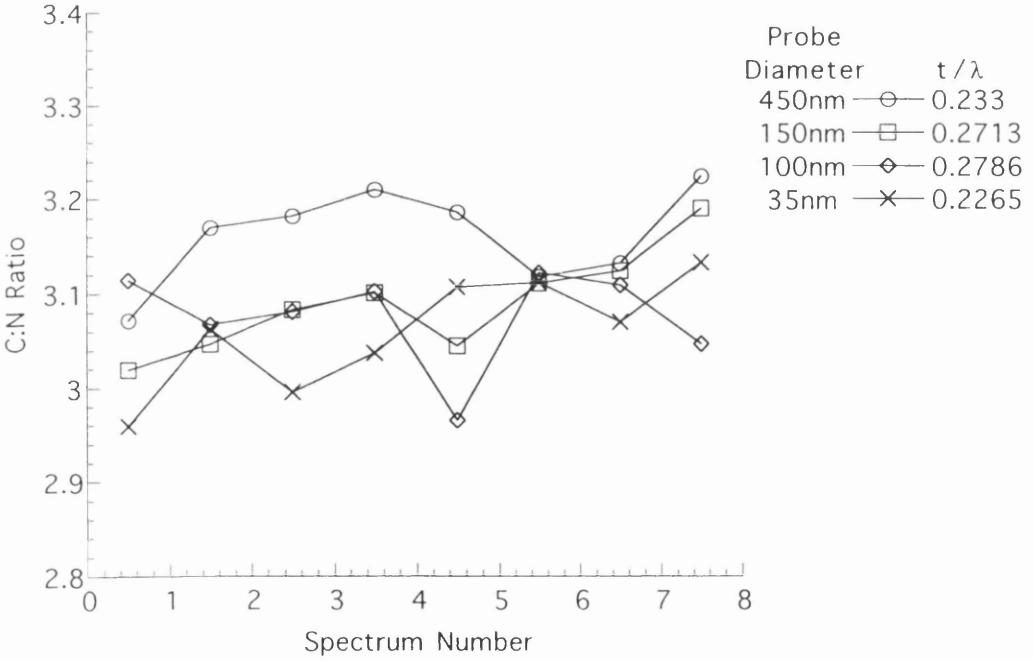

Figure 5.10(b) : C:N ratio as a function of spectrum number.

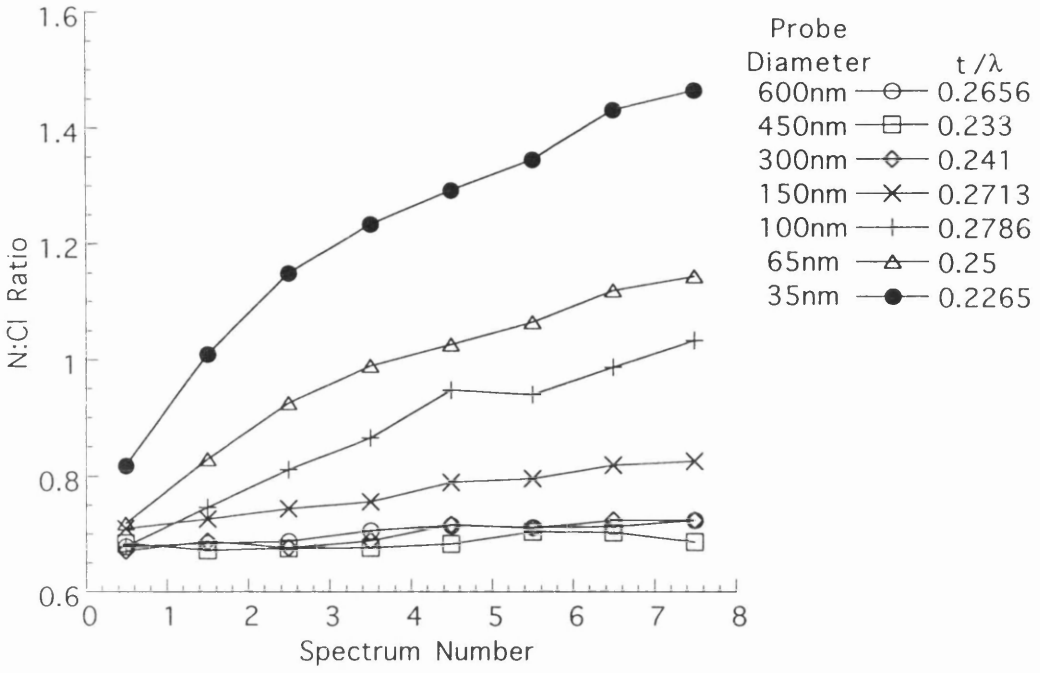

Figure 5.10(c) : N:Cl ratio as a function of spectrum number.

5.10 Extrapolation of Elemental Ratios and Error Analysis

In order to obtain the composition of the undamaged material, accurate extrapolation procedures are required for the spectral series. For linear data sets, the fitting equations can be readily determined. The first part of this section gives details of the fitting procedure used and the determination of the errors involved. For non-linear data sets the determination of the original elemental ratios is more difficult since the form of the equation is not known. Details of the extrapolation method used for these data sets and the errors involved are given in the second part of this section.

As mentioned above the Cl:C and N:Cl ratios vary linearly with dose for probe diameters down to 150nm and thus can be modelled using an equation of the form

$$y_i = \alpha + \beta x_i + \varepsilon_i \qquad (5.7)$$

where y_i is the chlorine to carbon ratio, x_i is the dose, α and β are the intercept and gradient respectively and ε_i is the error due to counting statistics and background subtraction. α represents the composition of the undamaged material and the best estimate of it is given by using a least-squares fit

$$\alpha = \frac{1}{n}\left(\sum y_i - \beta \sum x_i\right) \qquad (5.8)$$

with

$$\beta = \frac{n\sum x_i y_i - \sum x_i \sum y_i}{n\sum x_i^2 - \left(\sum x_i\right)^2} \qquad (5.9)$$

where n is the number of spectra in each series.

The accuracy of the extrapolations was determined by calculating a $(100-\eta)\%$ confidence interval for the intercept. Thus the results from each spectral series are presented in the form $\alpha + \delta\alpha$ where, for a 95% confidence interval, $\delta\alpha$ is given by

$$\delta\alpha = t\left(n-2,1-\frac{1}{2}\eta\right)\left[\frac{\sum x_i^2}{n\sum\left(x_i-\bar{x}\right)^2}\right]^{1/2}\cdot S_1 \qquad (5.10)$$

where $t\left(n-2,1-\frac{1}{2}\eta\right)$ is the $\left(1-\frac{1}{2}\eta\right)$ percentage point of a distribution with $(n-2)$ degrees of freedom and

$$S_1 = \left[\frac{\sum\left(y_i-\alpha-\beta x_i\right)^2}{(n-2)}\right]^{1/2} \qquad (5.11)$$

Since the C:N ratio appears to be independent of dose at large probe diameters an even simpler model is applicable with the best estimate of the undamaged composition being given by the mean value of y_i. Thus

$$\alpha = \sum y_i / n \qquad (5.12)$$

In this case $\delta\alpha$ is given by

$$\delta\alpha = S_2/(n)^{1/2} \qquad (5.13)$$

where

$$S_2 = \left[\frac{\left(y_i-\alpha\right)^2}{(n-1)}\right]^{1/2} \qquad (5.14)$$

Analysis of the data using the expressions detailed above was carried out using the Excel spreadsheet package.

For the smaller probe diameters, where the ratios do not vary linearly with dose, an estimation of the extrapolated ratios and their associated error had to be made. Figures 5.11 and 5.12 show the Cl:C ratios, as a function of spectrum number, at probe diameters of 65nm and 35nm, respectively. It is not clear what form of fit should be applied to the data points since it is not known at what rate the Cl is lost at the start of irradiation. From the analysis of spectra from large probe diameters, the rate of loss of Cl at the beginning of irradiation is linear. Figures 5.11 and 5.12 show linear fits to the first two data points in each curve, extrapolated to zero dose. The initial slope of the graphs near the y-axis is probably steeper than the linear fits shown, and thus high order polynomial fits to all data points were also plotted. For simplicity the actual extrapolated value was taken to lie between these two values, with the error, $\delta\alpha$, being the difference between the two. If the overall shape of the graphs is considered, the linear extrapolation probably gives a value lower than the actual value. Whilst the polynomial fit may give a more reasonable value for the extrapolated ratio. By taking the extrapolated value to lie between these two points, the linear fit biases the value to the low side. As the probe diameter is decreased the biasing problem is made worse. The decision to use this method turned out not to be very critical and will be discussed later in this chapter.

5.11 Extrapolated Elemental Ratios Using Theoretical Cross-Sections

The results of the extrapolation of the Cl:C, C:N and N:Cl ratios are presented in tables 5.1 - 5.3 respectively. Also shown are the mean values α, together with the standard deviations ($\Delta\alpha$) and the standard errors of the means. The extrapolated values are plotted as a function of specimen thickness in figures

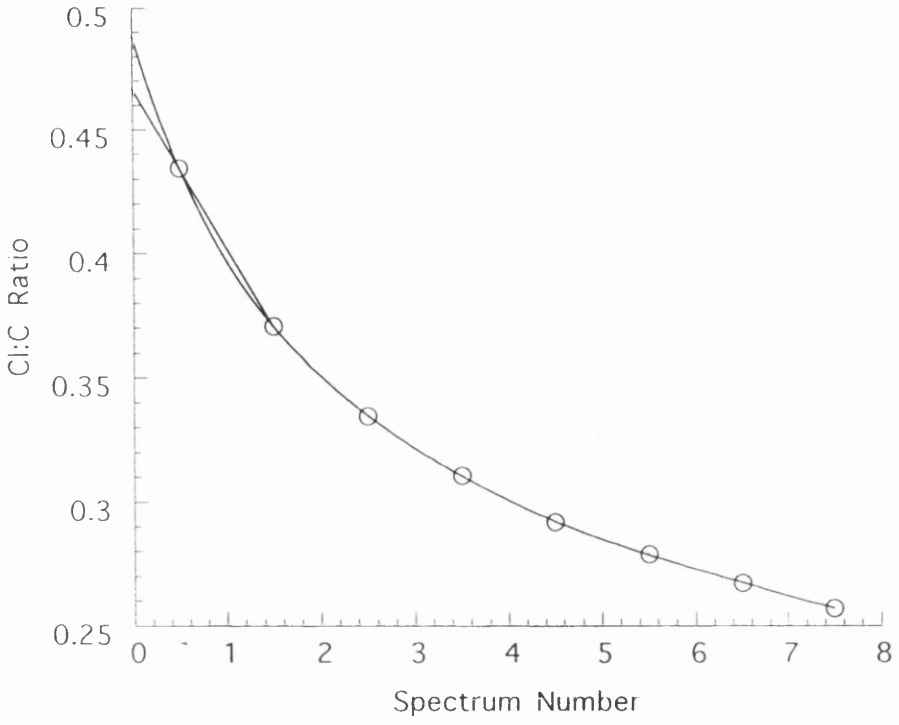

Figure 5.11 : Trial extrapolation values for the Cl:C ratios from an area 65nm in diameter

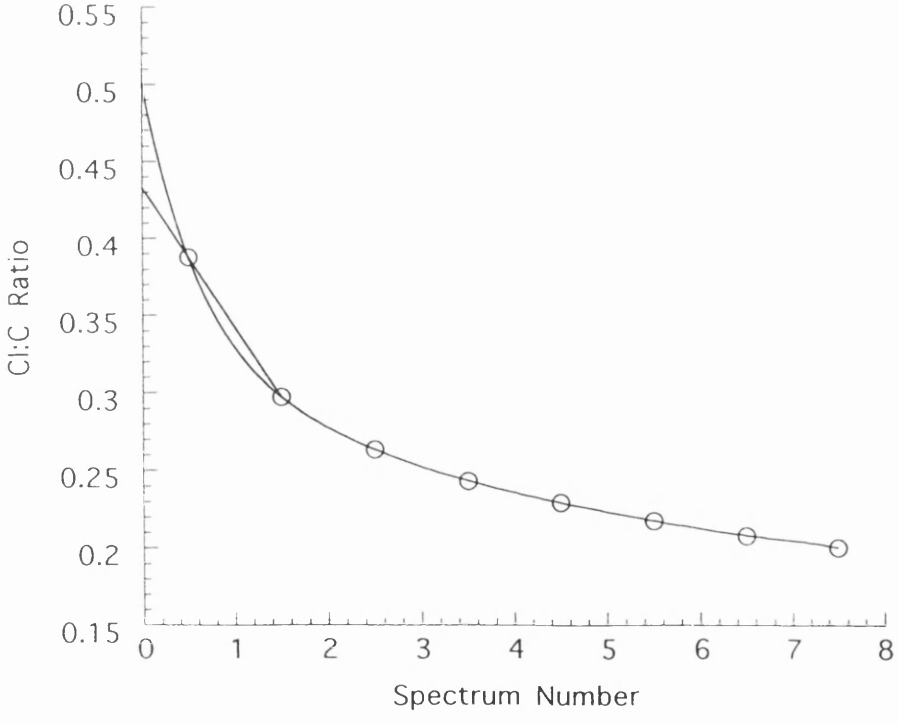

Figure 5.12 : Trial extrapolation values for the Cl:C ratios from an area 33nm in diameter.

Table 5.1. Results from analysis of standard sample using SIGMA cross-sections

Probe Diam. (nm)	Thickness (t/λ)	Extrpltd. Cl:C ratio (α)	Error ($\delta\alpha$)
600	0.241	0.466	0.001
600	0.245	0.474	0.001
600	0.265	0.487	0.002
600	0.266	0.482	0.002
600	0.280	0.469	0.002
600	0.280	0.473	0.001
450	0.269	0.490	0.003
450	0.233	0.475	0.001
300	0.303	0.488	0.002
300	0.241	0.481	0.002
150	0.271	0.471	0.001
150	0.275	0.475	0.002
100	0.279	0.495	0.003
100	0.256	0.482	0.004
65	0.250	0.481	0.008
65	0.248	0.477	0.011
35	0.227	0.491	0.031
35	0.244	0.466	0.031

Mean chlorine to carbon ratio = 0.479 ; standard deviation ($\Delta\alpha$) of distribution of results = 0.01 ; standard error = 0.002 .

Table 5.2. Results from analysis of standard material using SIGMA cross-sections

Probe Diam. (nm)	Thickness (t/λ)	Extrpltd. C:N ratio (α)	Error ($\delta\alpha$)
600	0.241	3.196	0.020
600	0.245	3.178	0.023
600	0.265	3.116	0.016
600	0.266	3.048	0.013
600	0.280	2.887	0.010
600	0.280	2.899	0.013
450	0.269	3.104	0.017
450	0.233	3.161	0.018
300	0.303	2.887	0.013
300	0.241	3.105	0.016
150	0.271	3.089	0.019
150	0.275	3.008	0.015
100	0.279	3.075	0.018
100	0.256	3.182	0.021
65	0.250	3.127	0.018
65	0.248	3.114	0.017
35	0.227	2.979	0.027
35	0.244	3.248	0.031

Mean carbon to nitrogen ratio = 3.078 ; standard deviation ($\Delta\alpha$) of distribution of results = 0.11 ; standard error = 0.03.

Table 5.3. Results from analysis of standard sample using SIGMA cross-sections

Probe Diam. (nm)	Thickness (t/λ)	Extrpltd. N:Cl ratio (α)	Error ($\delta\alpha$)
600	0.241	0.667	0.008
600	0.245	0.649	0.009
600	0.265	0.657	0.007
600	0.266	0.676	0.004
600	0.280	0.737	0.005
600	0.280	0.729	0.007
450	0.269	0.664	0.009
450	0.233	0.672	0.007
300	0.303	0.721	0.003
300	0.241	0.666	0.006
150	0.271	0.700	0.004
150	0.275	0.702	0.007
100	0.279	0.637	0.007
100	0.256	0.646	0.005
65	0.250	0.650	0.012
65	0.248	0.663	0.012
35	0.227	0.698	0.033
35	0.244	0.646	0.027

Mean nitrogen to chlorine ratio = 0.677 ; standard deviation ($\Delta\alpha$) of distribution of results = 0.03 ; standard error = 0.01 .

5.13(a) - (c). The best estimate of the undamaged Cl:C ratio together with its associated standard error is 0.479 ± 0.002. The C:N ratios shown in figure 5.13(b) clearly show some thickness dependence and, if the data point labelled (a) is assumed to be anomalous, the dependence is approximately linear. Thus the mean value of the C:N ratio derived using this approach is not meaningful. The extrapolated N:Cl ratios, shown in figure 5.13(c), show a much greater spread in the data points compared to the C:N ratio. The spread may be a result of signal noise which will have a greater affect on the Cl and N signals than the much greater C signal. If the data point (a) is again assumed to be anomalous, there would also appear to be some thickness dependence in the N:Cl ratio. However, this is difficult to determine due to the large data spread. The expected values for the extrapolated C:N and N:Cl ratios are 4 and 0.523, respectively. However, the experimental values lie around 3.076 and 0.677, respectively. This suggests that the intensity in the N K-edge may have been overestimated and thus the background subtraction method used here is not sufficiently accurate. As a result of these problems further discussion is left until the results of the modified data processing are discussed.

The approximation to the single stage fitting process and the use of theoretical cross sections for processing the data, has been shown to give various anomalies in the results. In an attempt to obtain better values for the C:N and N:Cl ratios and to reduce the effects of thickness on these values, a second method of analysis was developed. The following section describes the use of experimentally derived cross-sections (empirical cross-sections) to analyse the spectra.

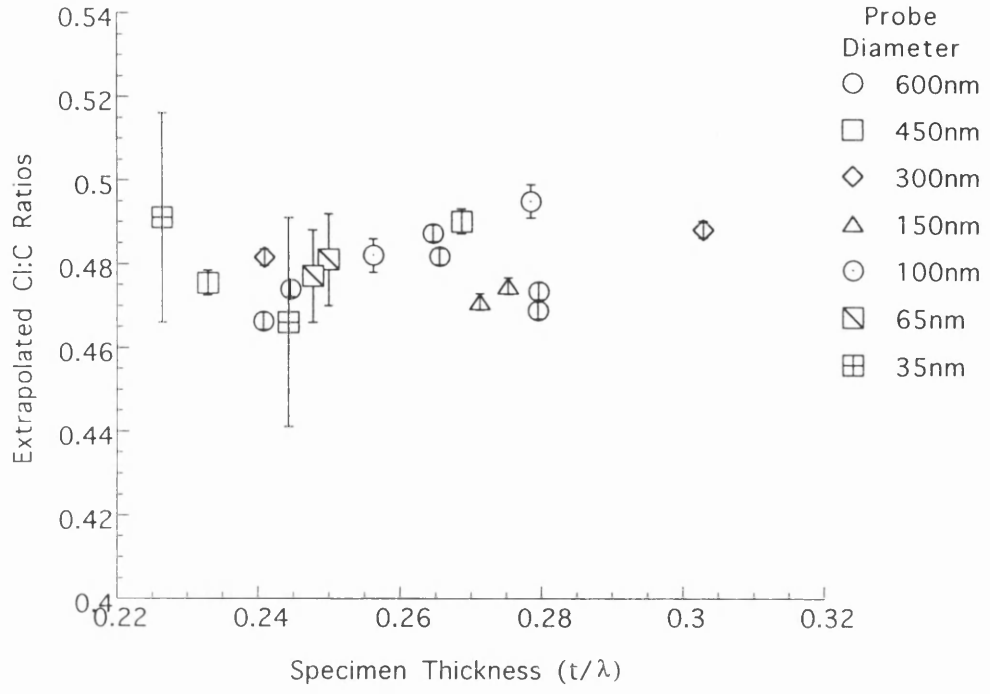

Figure 5.13(a) : Extrapolatd Cl:C ratios as a function of specimen thickness.

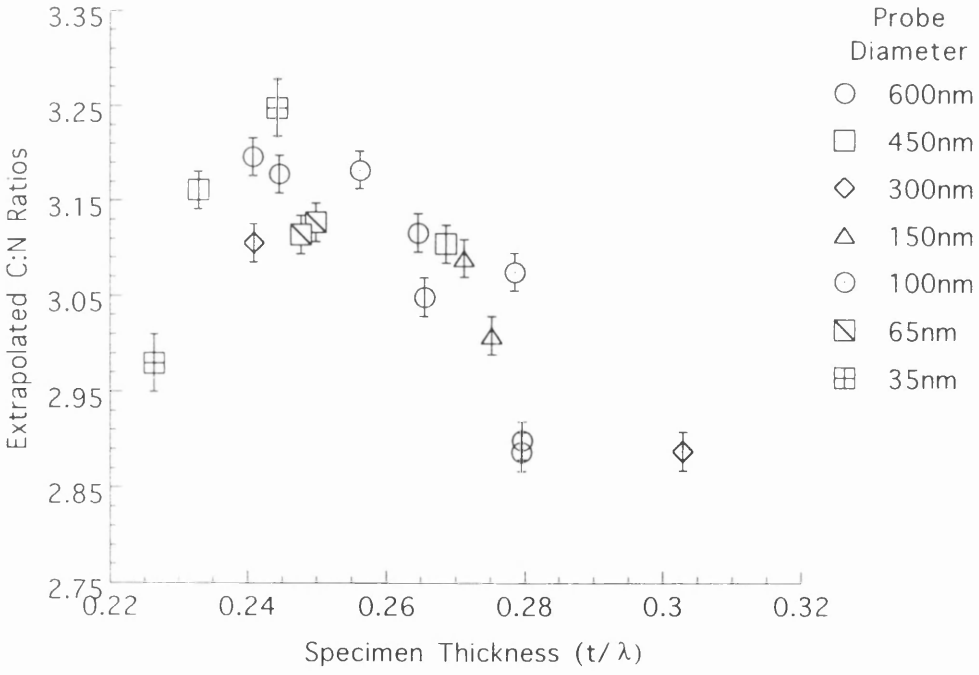

Figure 5.13(b) : Extrapolated C:N ratios as a function of specimen thickness.

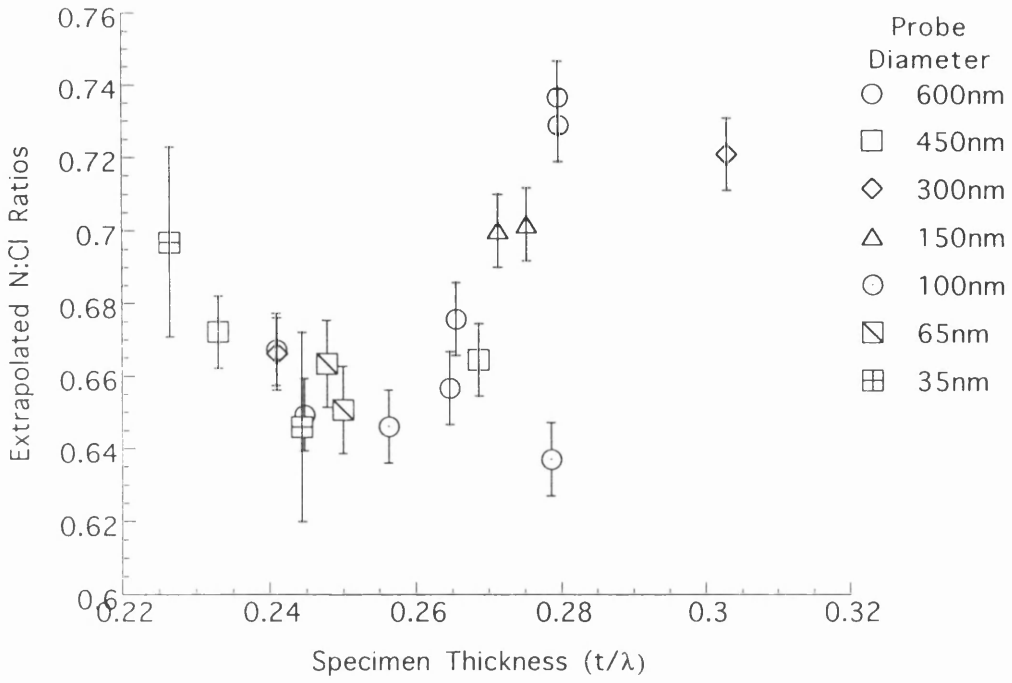

Figure 5.13(c) : Extrapolated N:Cl ratios as a function of specimen thickness.

5.12 Obtaining empirical cross-sections

In an attempt to improve the analysis of the CPC spectra it was decided to use empirical cross-section shapes to analyse the CPC spectra. The problem is that these edge shapes cannot be obtained directly due to the overlapping of other edges. This was overcome by extracting the part of the edges that was present in isolation and then extrapolating it in some way to obtain the full edge shape. These empirical cross sections were derived from a spectrum recorded from a large thin area of the standard sample. In this way there was little radiation damage to the area and the effects of plural scattering were minimised. The spectrum was both sharpened and deconvoluted. The background under the Cl $L_{2,3}$-edge was subtracted using the background subtraction routine in the GATAN software. As shown in figure 5.7(a), part of the Cl L_1-edge is underlying the C K-edge. In order to extrapolate the experimental Cl edge a theoretical SIGMAL2 Cl cross section was generated, aligned to the Cl-edge as shown in figure 5.14(a) and scaled to it over the energy range 270 - 272eV. This energy range was chosen because it lies after the Cl L_1-edge. The empirical Cl edge prior to 272eV was attached to the theoretical cross section after 272eV to produce the full single scattering experimental cross section as shown in figure 5.14(b). The empirical cross-section was then scaled to the theoretical Cl cross-section, over the energy range 210 - 265eV, to give the magnitude of the Cl edge shape.

This empirical cross section was then used to process the spectra. To do this it was scaled to the spectrum over an energy window (200 - 272eV) in the Cl edge and subtracted from the spectrum. The resulting C and N K-edges are shown in figure 5.15(a). It is clear that part of the C K-edge lies under the N K-edge and a similar extrapolation technique to that used to obtain the Cl edge is required. This was done using the theoretical SIGMAK C K-edge. The experimental C edge was matched to this spectrum over the energy window 345 - 385eV, as shown in figure 5.15(a). The experimental edge was then attached to the

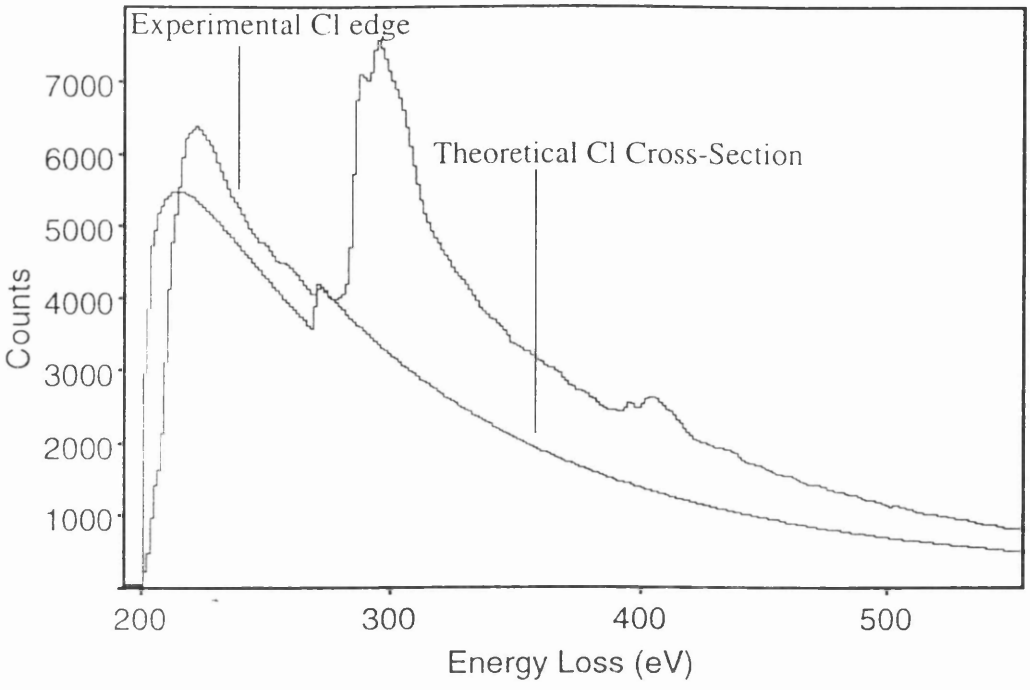

Figure 5.14(a) : The theoretical Cl edge scaled to the experimental Cl edge.

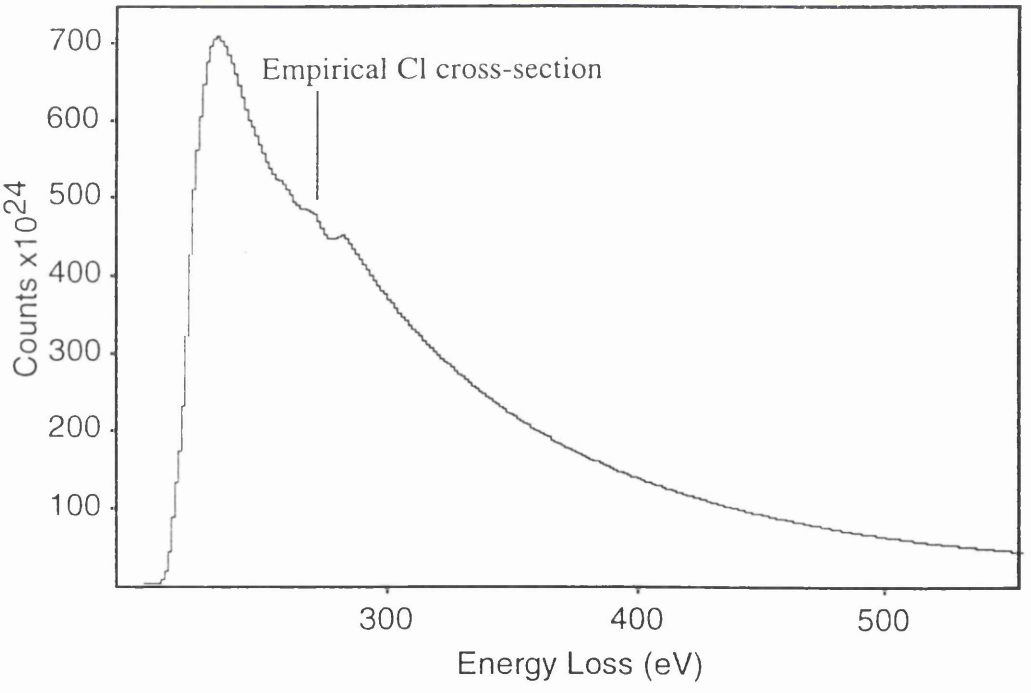

Figure 5.14(b) : Empirical Cl cross-section.

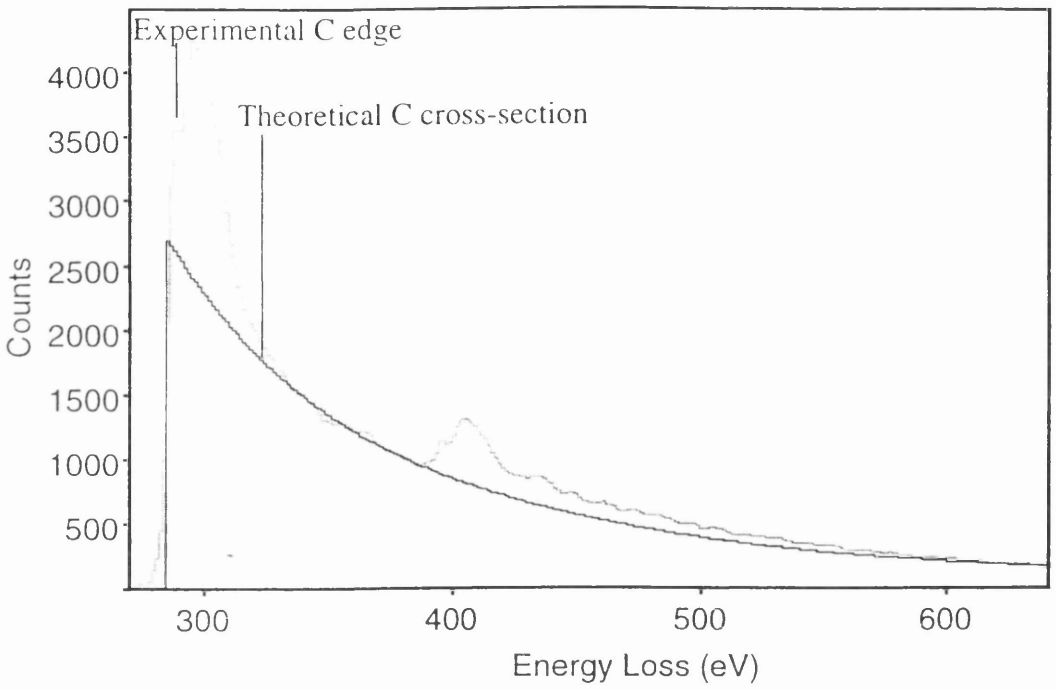

Figure 5.15(a) : The theoretical C K-edge scaled to the experimental C K-edge.

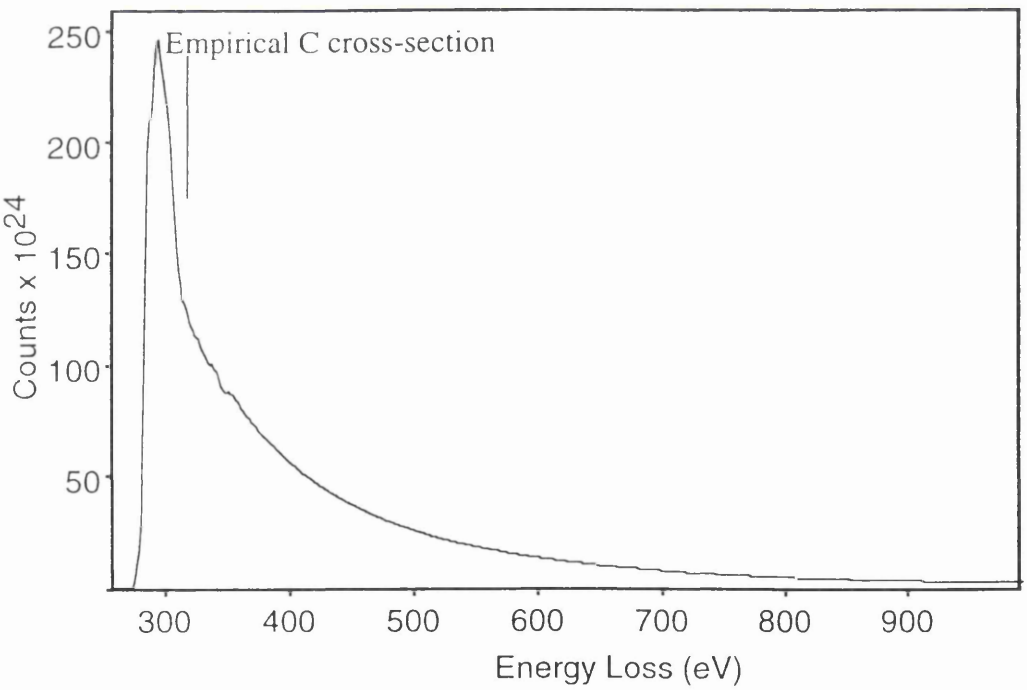

Figure 5.15(b) : Empirical C cross section.

theoretical cross section at 345eV. To produce the full single scattering experimental C K-edge shown in figure 5.15(b), the experimental edge was scaled to the theoretical edge shape over the energy range 345 - 500eV. This edge was scaled, over the energy range 345 - 385eV, to the spectrum shown in figure 5.15(a) and subtracted from it. The residual spectrum shown in figure 5.16 is the experimental N K-edge shape. This shape was scaled to the theoretical N K-edge shape over the energy range 425 - 500eV to give the full experimental single scattering edge shape. The shape of the empirical N K-edge is relatively poor and thus will affect the accuracy of the data analysis. These empirical cross sections were then used to analyse the same spectra processed using the theoretical cross sections.

5.13 Using empirical cross-sections to analyse the standard sample

The CPC spectra were both sharpened and deconvoluted as before and the background under the Cl edge was subtracted. The empirical Cl cross section was scaled to each spectrum, over the selected energy range and then subtracted from the spectrum to reveal the C K-edge as shown in figure 5.15(a). The empirical C cross section was similarly scaled to the spectrum and subtracted to reveal the N K-edge as shown in figure 5.16. The empirical N K-edge was then scaled to the spectrum over a selected energy range. The Cl:C ratio was determined by dividing the ratios of the intensity in the spectrum (I_C) to the empirical cross section (σ_χ) such that

$$\frac{N_{Cl}}{N_C} = \frac{I_c^{Cl}(\beta,\Delta)\sigma_c^{Cl}(\beta,\Delta)}{I_c^{C}(\beta,\Delta)\sigma_c^{C}(\beta,\Delta)} \qquad (5.15)$$

which is equivalent to equation 5.6. Similar equations were used to obtain the C:N and N:Cl ratios.

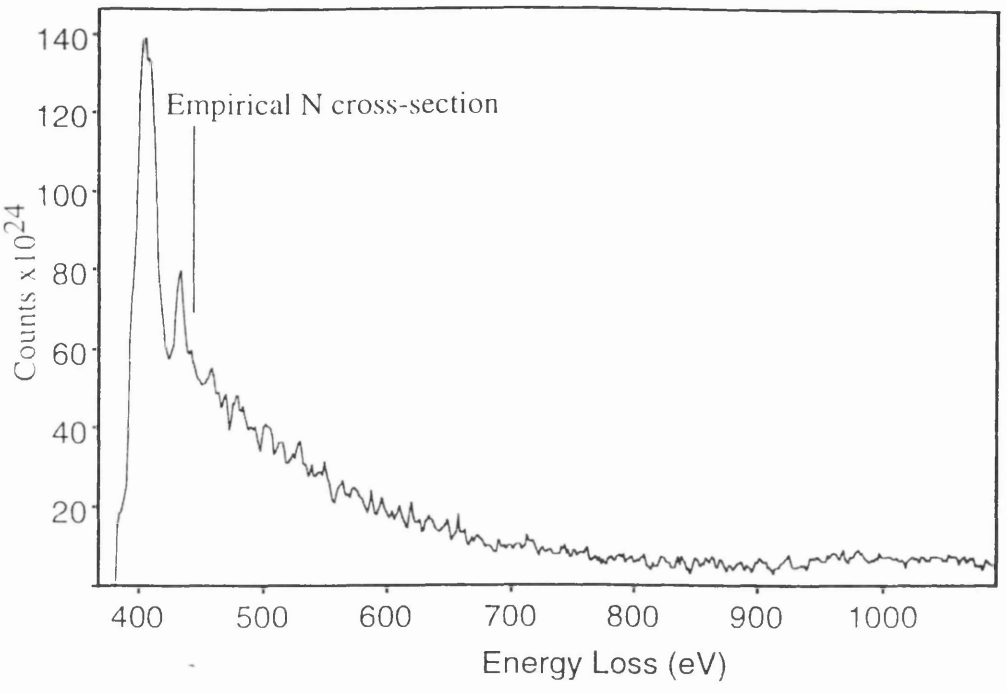

Figure 5.16 : Empircal N cross-section

The Cl:C, C:N and N:Cl ratios for various probe diameters are shown in figures 5.17(a) - (c). As in the previous analyses the Cl:C ratio is linear for probe diameters down to ~150nm. The amount of chlorine loss at the various probe diameters is also the same. The C:N ratios show no loss of nitrogen for large probe diameters down to ~ 300nm. At a probe diameter of 150nm there is a loss of nitrogen of ~ 10% and the rate of loss is linear. At smaller probe diameters, the initial loss of nitrogen is faster and drops with increasing dose. At the smallest probe diameter the sample has lost ~ 30% of its nitrogen. This result is different to the previous analysis where there was found to be only ~ 6% loss of the nitrogen content at the smallest probe diameter.

The methods of extrapolation to zero dose are the same as those described in section 5.10. The results of these extrapolations together with the standard deviations and standard errors in the extrapolated values are presented in tables 5.4 - 5.6. Graphs of the extrapolated ratios as a function of specimen thickness are presented in figures 5.18(a) - (c). The data point (a) in figures 5.18(b) & (c) which was assumed to be anomalous gives more reasonable values for the extrapolated C:N and N:Cl values in figures 5.13(b) & (c). The best estimate of the undamaged Cl:C ratio and its standard error is 0.505 ± 0.003. Figure 5.18(b) shows that the thickness dependence in the measured C:N ratios has been reduced. The extrapolated N:Cl values shown in figure 5.18(c) reveal that the spread of data is much reduced compared to that of the data set shown in figure 5.13(c). At first sight there does not appear to be any significant thickness dependence. The experimental C:N and N:Cl values lie around 4.706 and 0.424, respectively. These values are closer to the expected values of 4 and 0.532, than was obtained using the theoretical cross-sections. However, these values suggest that the nitrogen is underestimated whereas the previous technique overestimated the nitrogen. This is discussed further in section 5.15.

Further investigation of figure 5.18(b) appeared to show that the thickness dependence only held true for the large probe diameters. For this reason the data

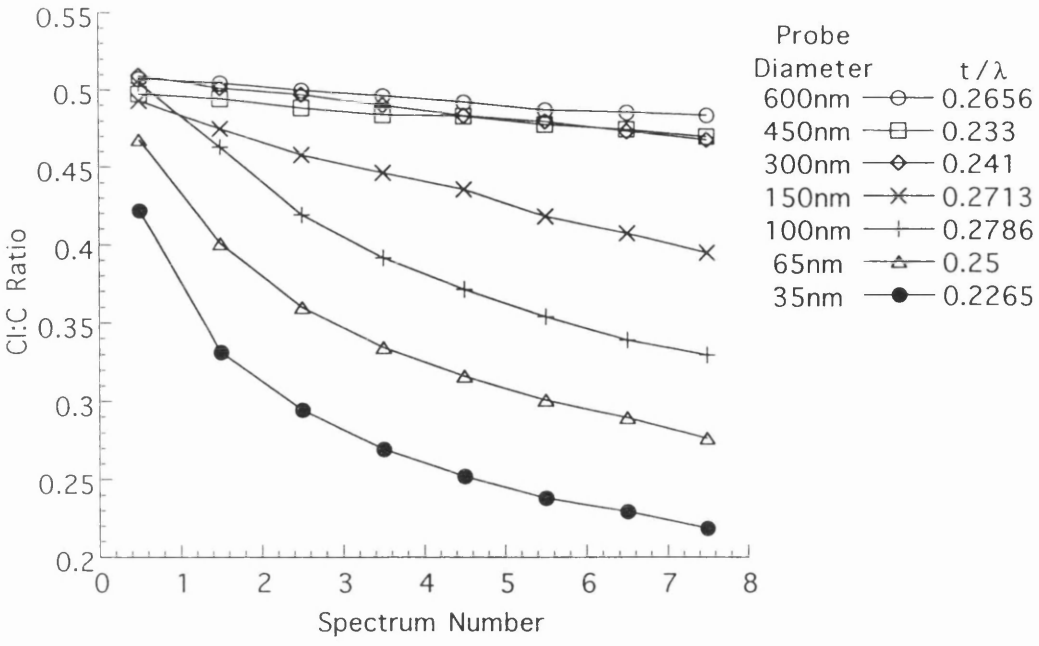

Figure 5.17(a) : Cl:C ratio as a function of spectrum number.

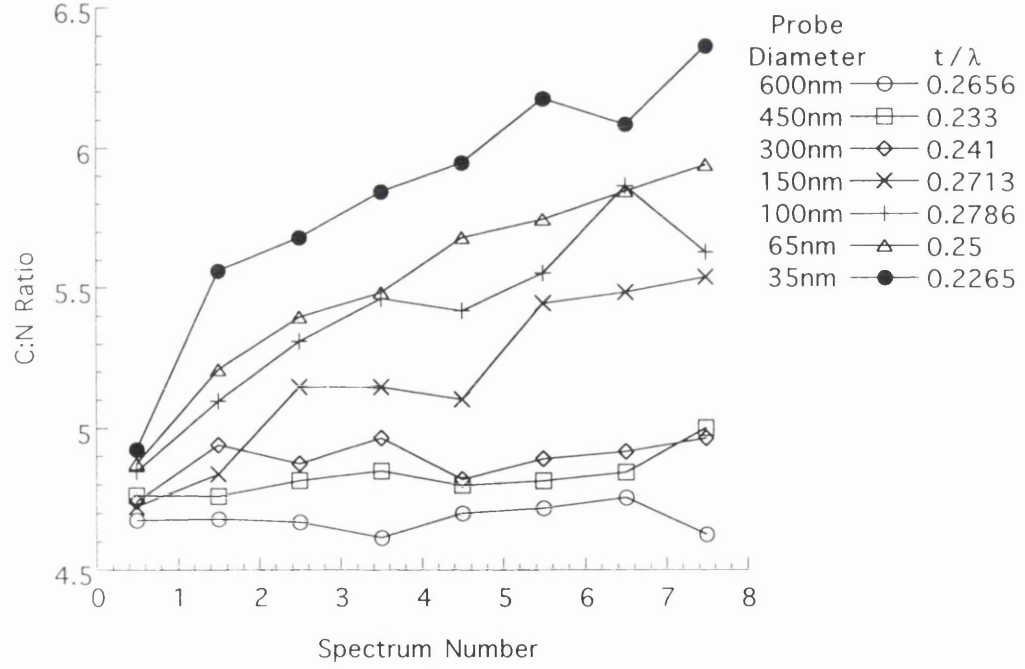

Figure 5.17(b) : C:N ratio as a function of spectrum number.

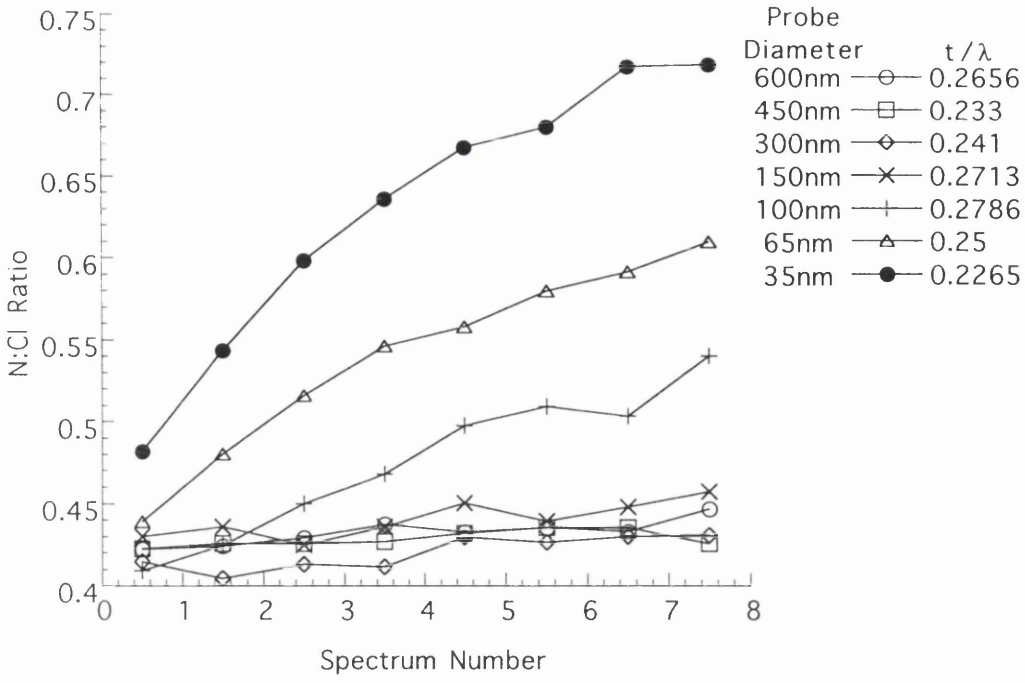

Figure 5.17(c) : N:Cl ratio as a function of spectrum number.

Table 5.4. Results from analysis of standard sample using empirical cross-sections

Probe Diam. (nm)	Thickness (t/λ)	Extrpltd. Cl:C ratio (α)	Error ($\delta\alpha$)
600	0.241	0.491	0.001
600	0.245	0.491	0.001
600	0.265	0.519	0.001
600	0.266	0.508	0.001
600	0.280	0.505	0.001
600	0.280	0.491	0.001
450	0.269	0.519	0.001
450	0.233	0.499	0.001
300	0.303	0.518	0.002
300	0.241	0.511	0.001
150	0.271	0.496	0.002
150	0.275	0.494	0.002
100	0.279	0.529	0.004
100	0.256	0.505	0.003
65	0.250	0.505	0.009
65	0.248	0.510	0.018
35	0.227	0.492	0.024
35	0.244	0.493	0.031

Mean chlorine to carbon ratio = 0.505; standard deviation ($\Delta\alpha$) of distribution of results = 0.012; standard error = 0.003.

Table 5.5. Results from analysis of standard sample using empirical cross-sections

Probe Diam. (nm)	Thickness (t/λ)	Extrpltd. C:N ratio (α)	Error ($\delta\alpha$)
600	0.241	4.786	0.025
600	0.245	4.768	0.016
600	0.265	4.662	0.016
600	0.266	4.678	0.017
600	0.280	4.459	0.034
600	0.280	4.506	0.019
450	0.269	4.667	0.022
450	0.233	4.733	0.027
300	0.303	4.340	0.038
300	0.241	4.824	0.051
150	0.271	4.711	0.068
150	0.275	4.828	0.045
100	0.279	4.695	0.030
100	0.256	4.826	0.030
65	0.250	4.675	0.040
65	0.248	4.623	0.040
35	0.227	4.565	0.062
35	0.244	4.983	0.113

Mean carbon to nitrogen ratio = 4.706; standard deviation ($\Delta\alpha$) of distribution of results = 0.124; standard error = 0.029.

Table 5.6. Results from analysis of standard sample using empirical cross-sections

Probe Diam. (nm)	Thickness (t/λ)	Extrpltd. N:Cl ratio (α)	Error ($\delta\alpha$)
600	0.241	0.428	0.004
600	0.245	0.425	0.003
600	0.265	0.412	0.003
600	0.266	0.421	0.003
600	0.280	0.450	0.007
600	0.280	0.451	0.004
450	0.269	0.413	0.004
450	0.233	0.423	0.003
300	0.303	0.444	0.004
300	0.241	0.406	0.004
150	0.271	0.425	0.005
150	0.275	0.417	0.003
100	0.279	0.403	0.005
100	0.256	0.418	0.005
65	0.250	0.415	0.006
65	0.248	0.426	0.006
35	0.227	0.444	0.009
35	0.244	0.412	0.009

Mean nitrogen to chlorine ratio = 0.424; standard deviation ($\Delta\alpha$) of distribution of results = 0.015; standard error = 0.003.

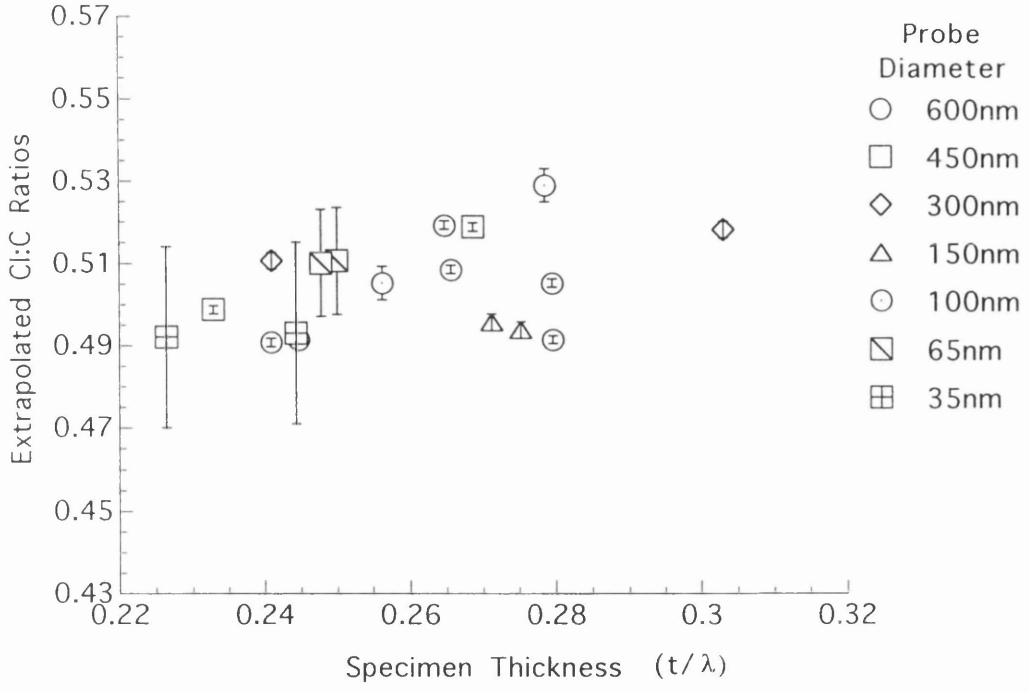

Figure 5.18(a) : Extrapolated Cl:C ratios as a function of specimen thickness.

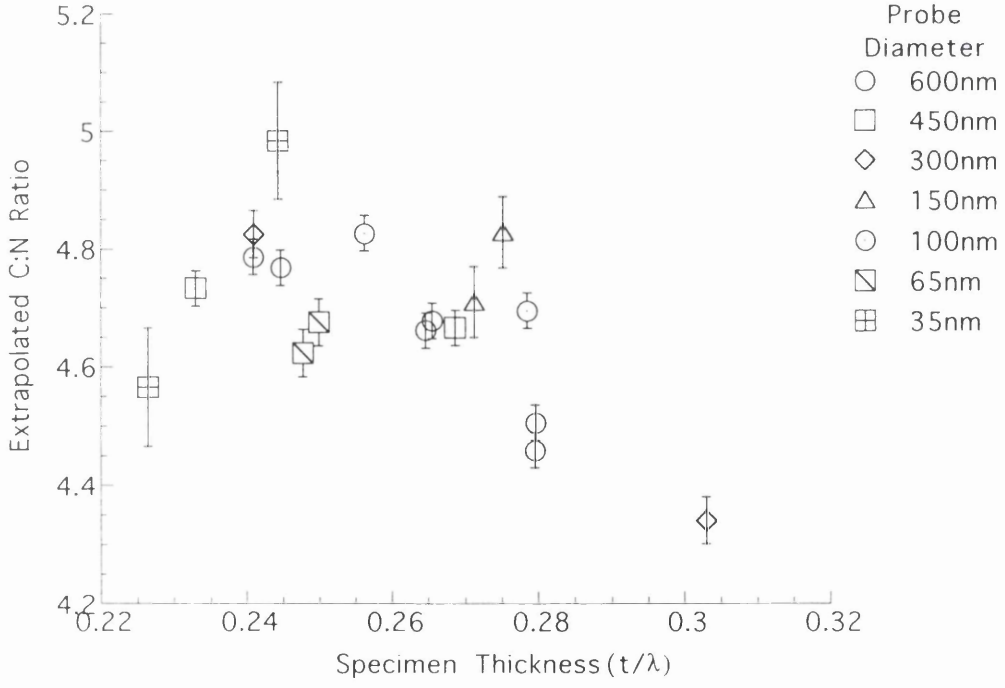

Figure 5.18(b) : Extrapolated C:N ratios as a function of specimen thickness.

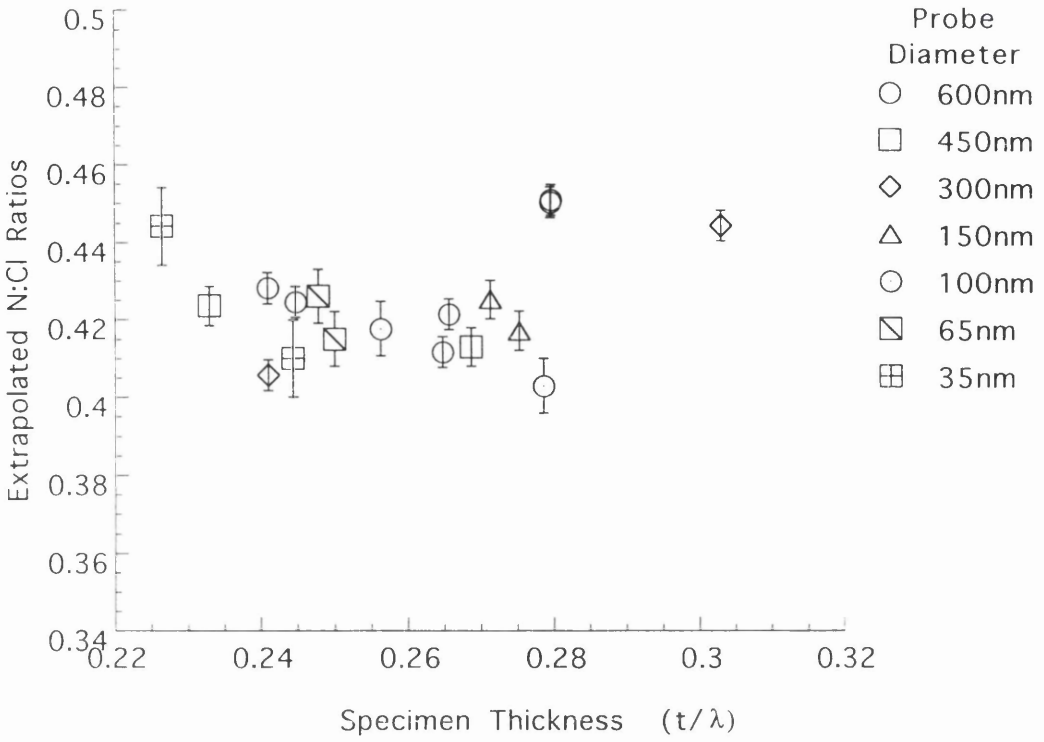

Figure 5.18(c) : Extrapolated N:Cl ratios as a function of specimen thickness.

sets shown in figures 5.18(a) - (c) were separated into results for large and small probe diameters. These results are shown in figures 5.19 - 5.21. The Cl:C ratios show no apparent thickness dependence for either large or small probe diameters, as shown in figures 5.19(a) & (b). Figure 5.20(a) & (b) show that for the C:N ratios the thickness dependence is approximately linear at large probe diameters, while for small probe diameters there does not appear to be any significant thickness dependence. From figure 5.21(a) it appears that there is also a small thickness dependence for the N:Cl ratio at large probe diameters. As with the C:N ratios the same thickness dependence is not observed for the small probe diameters, as shown in figure 5.21(b) These results are considered further in section 5.15.

The error in the extrapolated Cl:C and N:Cl ratios, $\delta\alpha$, is smaller than the standard deviation, $\Delta\alpha$, in the distribution of measured ratios. This is probably a result of overall fluctuations introduced by the technique as a whole. These fluctuations being a result of noise and the position of the spectrum on the diode array. Table 5.4 shows that a single point measurement of the Cl:C ratio deviates from the mean by < 0.012 (the standard deviation) in 65% of cases, by < 0.024 in 95% of cases and by < 0.036 in < 99.7% of cases. Therefore, if there are no other effects, the result of a single measurement should give an answer for Cl:C to 2% at a 65% confidence level or 4% at a 95% confidence level. Thus, it is possible to measure the Cl:C to within ±1/2 a Cl atom/molecule with a confidence of 95% in probe diameters down to 35nm in 50nm thick highly chlorinated copper phthalocyanines. From table 5.6, the deviation from the mean N:Cl ratio of 0.424 at a 95% confidence level is 0.03. Thus it is only possible to measure the N:Cl to within ± 1 Cl atom/molecule with a 95% confidence level in probe diameters down to 35nm. This is a considerable improvement over the spatial resolution attainable with EDX analysis. Thus the aim of being able to analyse individual particles with an accuracy of better than 0.5 chlorine atoms per molecule appears to be achievable.

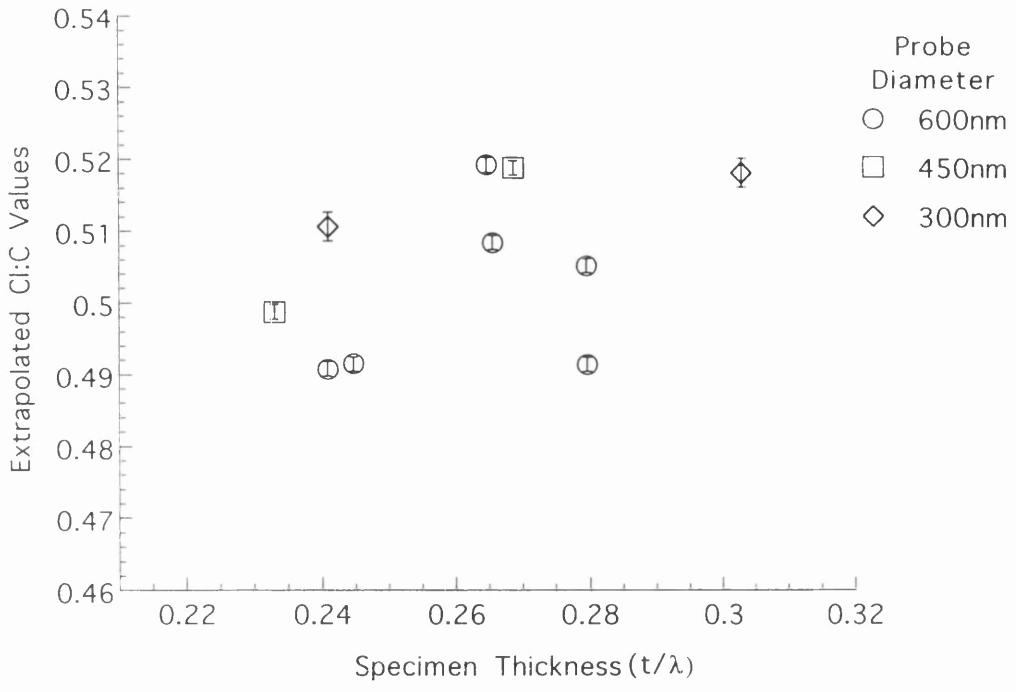

Figure 5.19(a) : Extrapolated Cl:C ratios for large probe diameters.

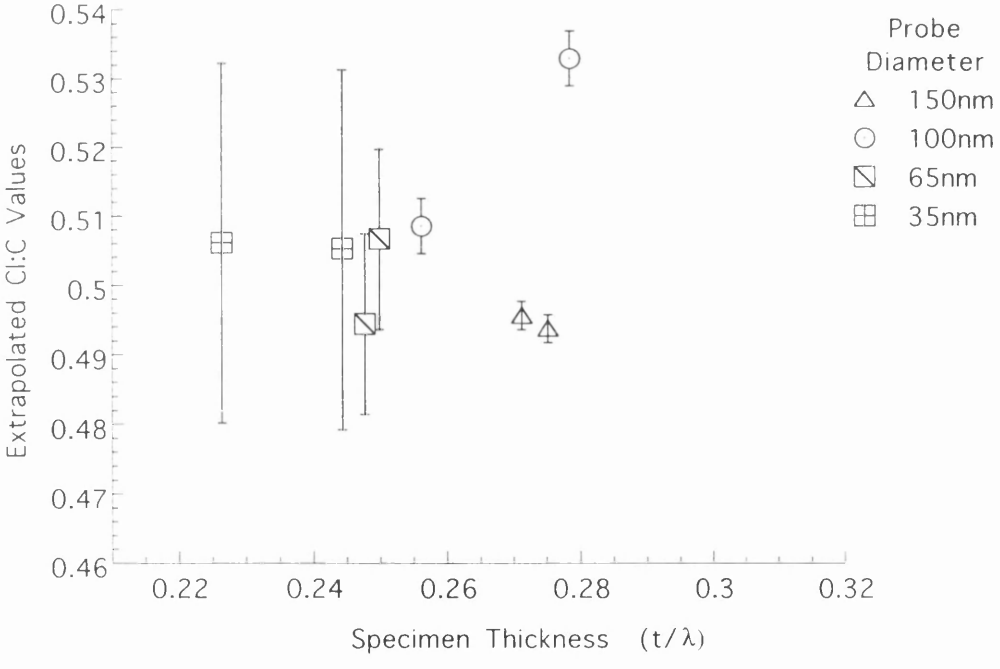

Figure 5.19(b) : Extrapolated Cl:C ratios for small probe diameters.

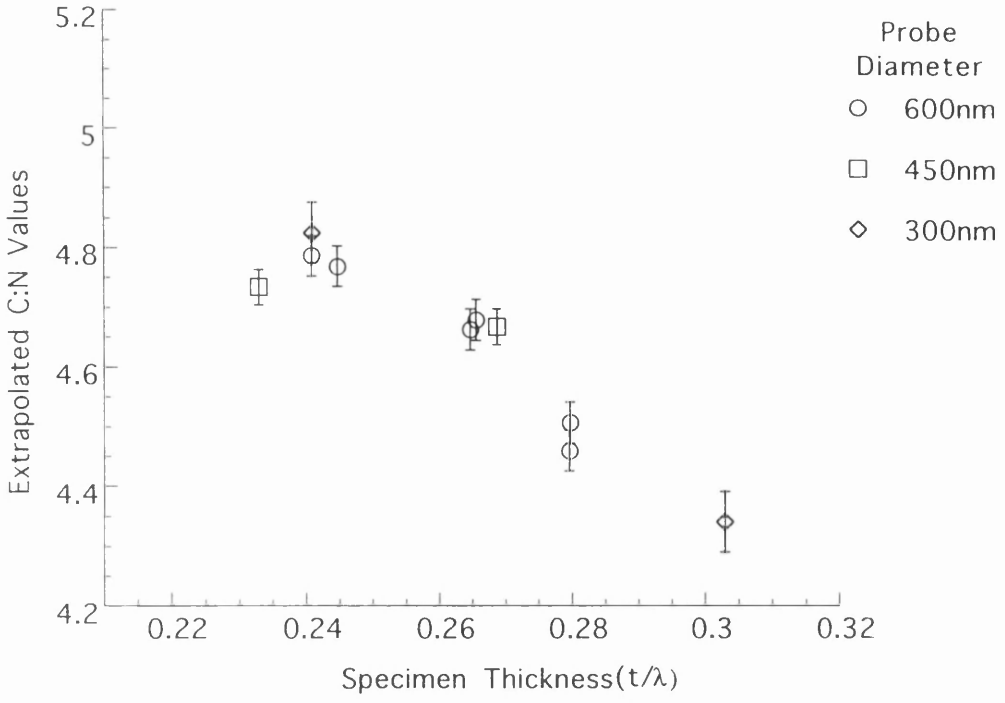

Figure 5.20(a) :Extrapolated C:N ratios for large probe diameters

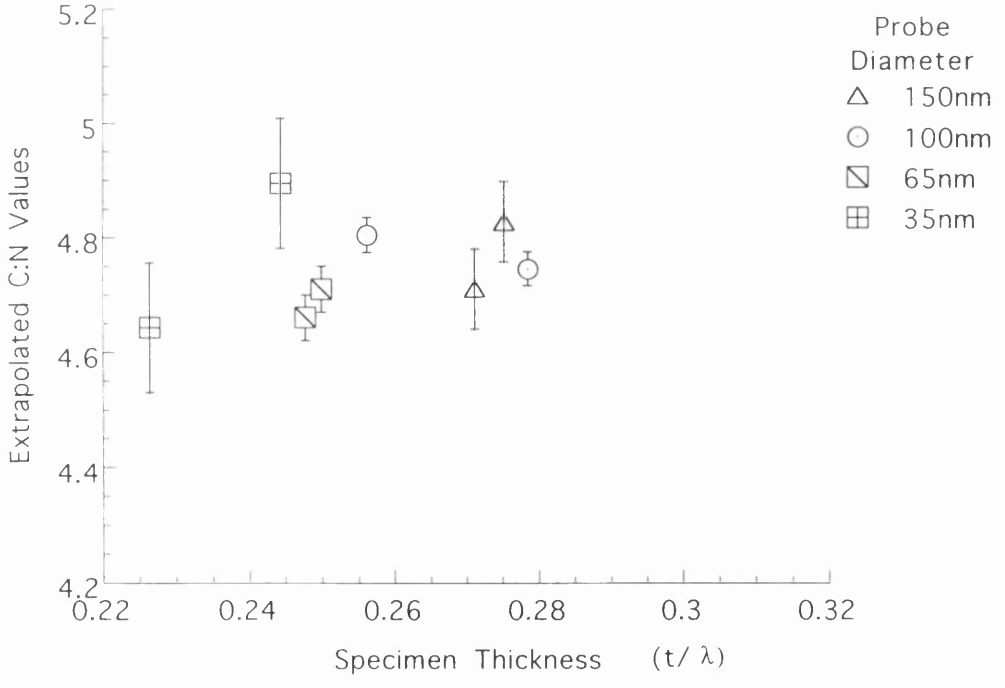

Figure 5.20(b) : Extrapolated C:N ratios for small probe diameters.

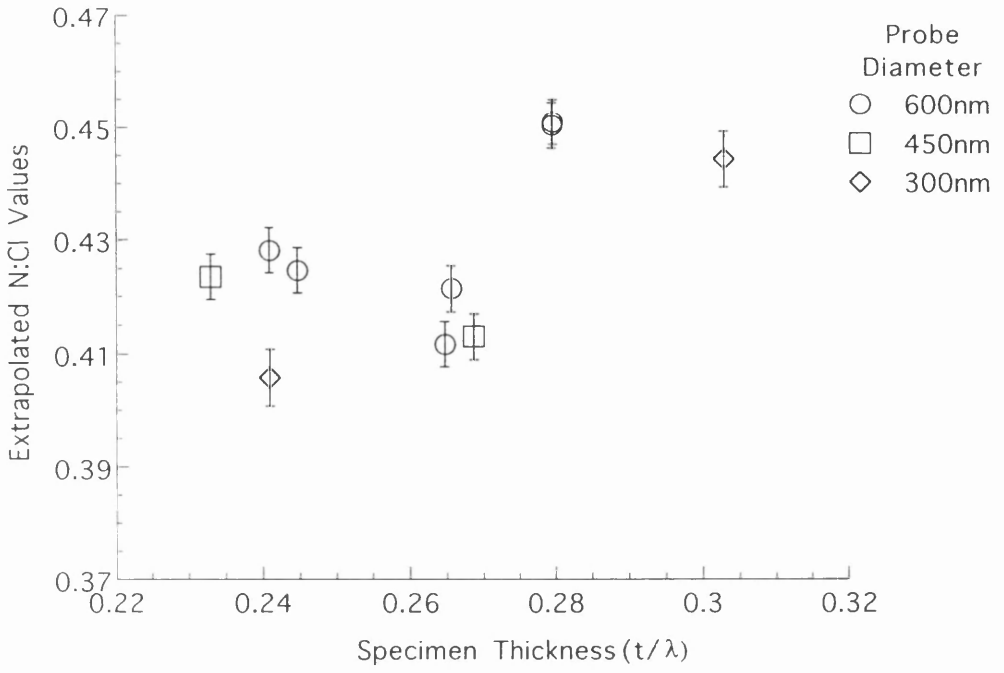

Figure 5.21(a) : Extrapolated N:Cl ratios for large probe diameters.

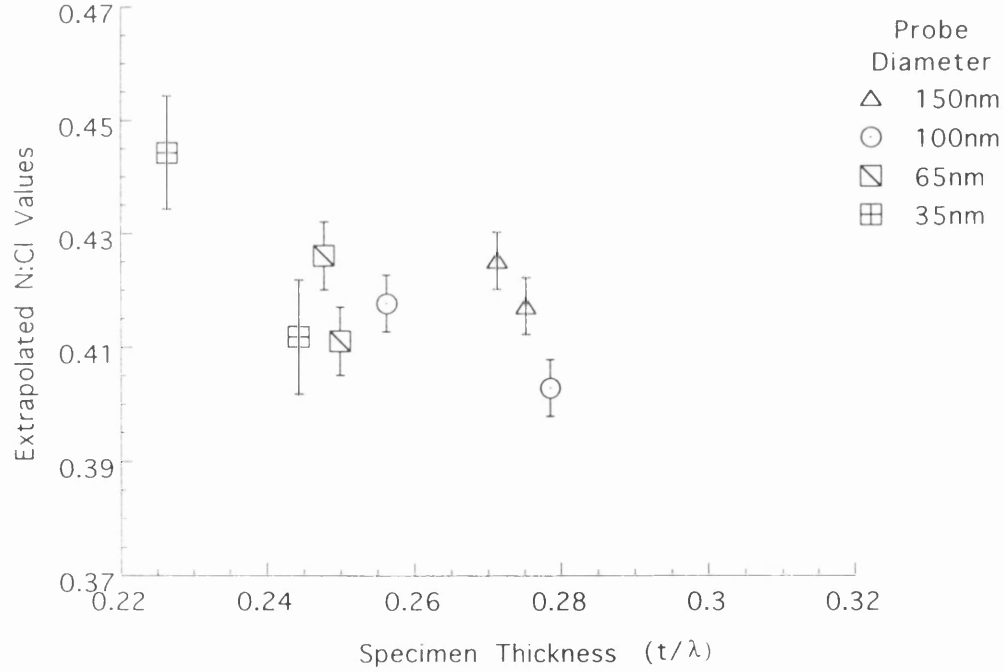

Figure 5.21(b) : Extrapolated N:Cl ratios for small probe diameters.

5.14 PEELS studies of industrially prepared highly chlorinated CPC

An industrially produced sample of a highly chlorinated CPC, containing an average of ~14.6 Cl atoms per molecule (determined by bulk analysis), was analysed using the experimental technique described in section 5.5. As before, investigations were carried out using epitaxial films of similar thickness to a single pigment particle. In this way a cross-check on the analysis procedure could be made prior to analysing pigment particles. Sequences of spectra were recorded for various probe diameters.

In the previous section, the accuracy with which it was possible to analyse samples of highly chlorinated CPC material using PEELS was determined to be < ± 0.5 Cl atoms per molecule on areas down to ~ 35nm in diameter. It should then be possible to analyse single pigment particles. The material analysed in the previous section was prepared in the laboratory to be approximately fully chlorinated and surfactant free and thus could be considered to be homogeneous. CPC pigments are produced on an industrial scale to have only an average number of chlorine atoms per molecule. A determination of any particle to particle variations within a pigment may explain the differing colouring properties of different pigmentary samples.

The samples of the industrially produced CPC were slightly thicker than the standard samples used. For this reason the integration time for each spectrum recorded was reduced to 1s. The spectra were processed using the empirical cross-sections derived to process the standard material. Figures 5.22(a) - (c) show the measured Cl:C, C:N and N:Cl ratios, respectively. For convenience the ratios are shown as a function of spectrum number. The graphs of the ratios are similar to those obtained for the standard sample. Figure 5.22(a) reveals a chlorine loss of between 1% and 3% for probe diameters of 600nm and 300nm respectively. At small probe diameters the loss of chlorine is linear for probe diameters down to 150nm, where after a dose of ~2 x 10^5 C/m^2 the sample has lost ~ 20% of is

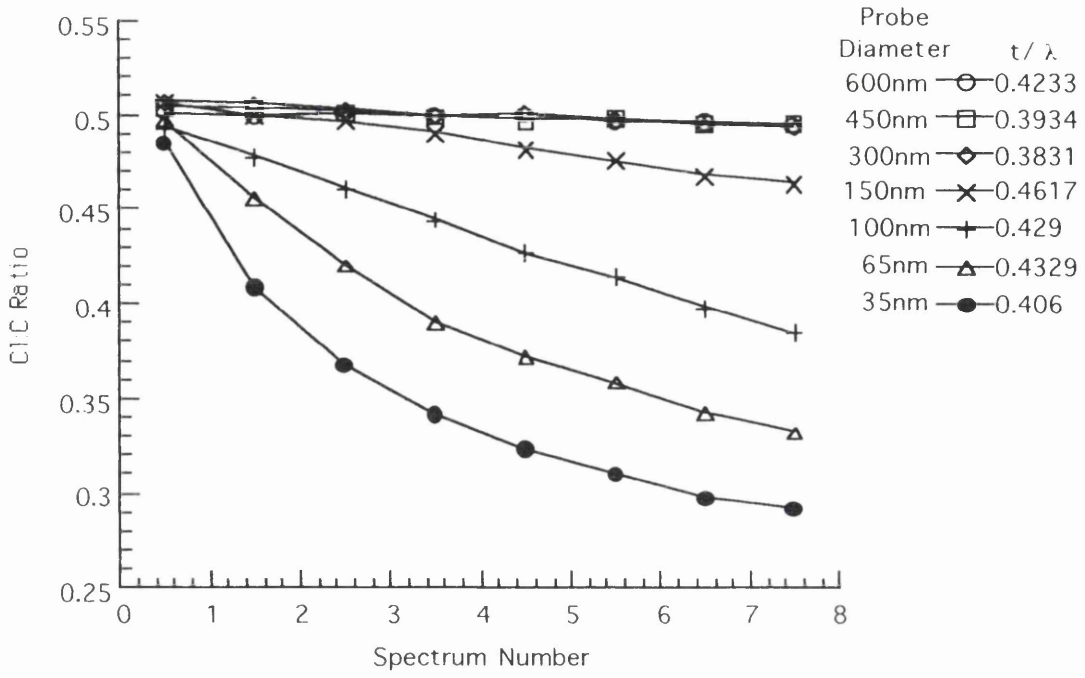

Figure 5.22(a) : Cl:C ratio as a function of spectrum number.

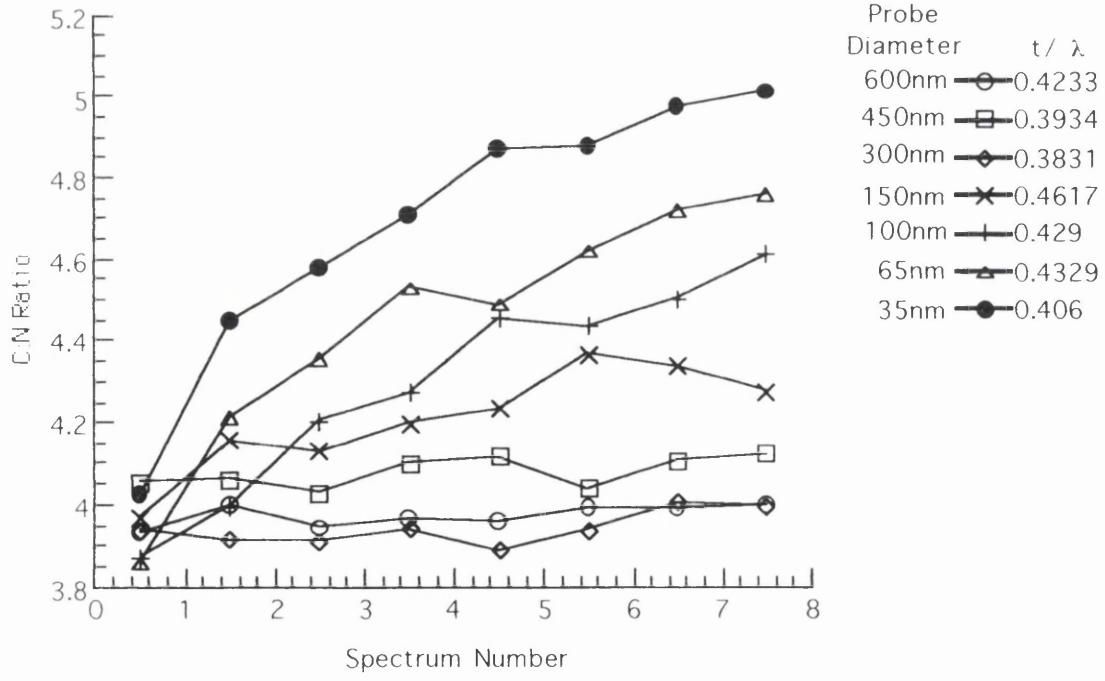

Figure 5.22(b) : C:N ratio as a function of spectrum number.

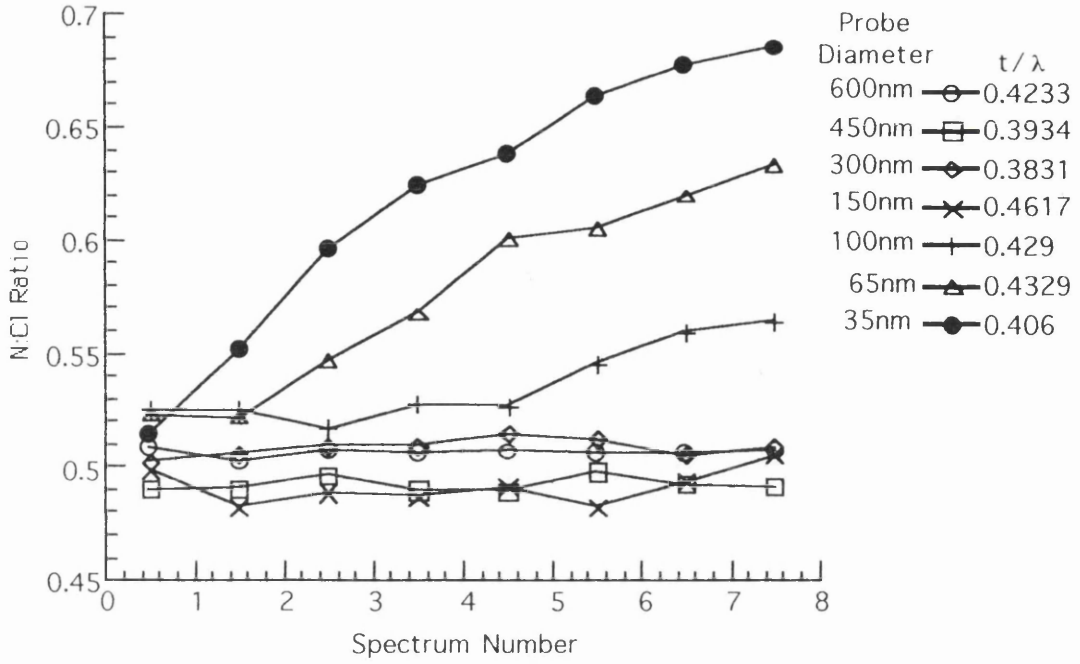

Figure 5.22(c) : N:Cl ratio as a function of spectrum number.

chlorine. As with the standard sample at larger doses the rate of chlorine loss slows down and at the smallest probe diameter, after a dose of ~ 2 x 10^6 C/m^2 , the sample has lost ~ 45% of its chlorine. Figure 5.22(b) shows a small loss of nitrogen for the large probe diameters which was not observed in the standard sample. The loss of nitrogen is ~ 1% and 3% for the 600nm and 300nm probe diameters respectively. The loss of nitrogen is linear down to probe diameters of 100nm where after a dose of ~ 2 x 10^6 C/m^2 the sample has lost ~ 15% of its nitrogen. Figure 5.22(c) reveals that for large probe diameters the N:Cl ratio is relatively unchanged. For small probe diameters the N:Cl ratio increases linearly with increasing dose for probe diameters down to 63nm.

Extrapolation of the ratios to zero dose was achieved using the same techniques employed for the standard sample. The results together with the standard deviation and standard error in the distribution of extrapolated values are presented in tables 5.7 - 5.9. Figures 5.23(a) - (c) show the extrapolated Cl:C, C:N and N:Cl ratios, as a function of specimen thickness, respectively. The best estimate of the undamaged Cl:C ratio is 0.517 ± 0.003, which is ~ 10% higher than the expected value of 0.456. The experimental values for the C:N and N:Cl ratios lie around 3.911 and 0.492, respectively. These values are much closer to the expected values of 4 and 0.548, respectively, than was obtained for these ratios in the standard sample. It would appear that in the thicker industrial sample the nitrogen is higher.

Figure 5.23(b) appears to show no thickness dependence in the C:N ratios. The ratios are separated into the results for large and small probe diameters as shown in figures 5.24 - 5.26. As was observed for the standard sample, the Cl:C ratios, in figures 5.24(a) & (b), do not appear to show any thickness dependence. In figure 5.25(a) the thickness dependence of the C:N ratio appears to be linear for the large probe diameters but the same dependence is not observed at small probe diameters presented in figure 5.25(b). Similarly for the N:Cl ratios, in figures 5.26(a) & (b), there appears to be a small thickness dependence for large

Table 5.7. Results from analysis of industrial sample using empirical cross-sections

Probe Diam. (nm)	Thickness (t/λ)	Extrpltd. Cl:C ratio (α)	Error ($\delta\alpha$)
600	0.423	0.502	0.001
600	0.397	0.510	0.001
450	0.394	0.504	0.001
450	0.367	0.516	0.001
300	0.458	0.520	0.001
300	0.393	0.515	0.001
300	0.383	0.508	0.001
150	0.378	0.535	0.001
150	0.462	0.510	0.001
100	0.345	0.504	0.001
100	0.429	0.500	0.001
65	0.391	0.521	0.002
65	0.433	0.520	0.003
65	0.476	0.526	0.005
35	0.366	0.532	0.009
35	0.406	0.537	0.019
35	0.467	0.532	0.013

Mean chlorine to carbon ratio = 0.517; standard deviation ($\Delta\alpha$) od distribution of results = 0.012; standard error = 0.003.

Table 5.8. Results from analysis of industrial sample using empirical cross-sections

Probe Diam. (nm)	Thickness (t/λ)	Extrpltd. C:N ratio (α)	Error ($\delta\alpha$)
600	0.423	3.943	0.015
600	0.397	3.981	0.017
450	0.394	4.041	0.018
450	0.367	4.100	0.016
300	0.458	3.782	0.017
300	0.393	4.031	0.018
300	0.383	3.896	0.015
150	0.378	3.692	0.018
150	0.462	4.025	0.048
100	0.345	4.205	0.023
100	0.429	3.743	0.048
65	0.391	4.447	0.050
65	0.433	3.620	0.089
65	0.476	3.889	0.067
35	0.366	3.720	0.040
35	0.406	3.773	0.062
35	0.467	3.600	0.069

Mean carbon to nitrogen ratio = 3.911; standard deviation ($\Delta\alpha$) of distribution of results = 0.222; standard error = 0.054.

Table 5.9. Results from analysis of industrial sample using empirical cross-sections

Probe Diam. (nm)	Thickness (t/λ)	Extrpltd. N:Cl ratio (α)	Error ($\delta\alpha$)
600	0.423	0.506	0.001
600	0.397	0.492	0.001
450	0.394	0.492	0.001
450	0.367	0.474	0.001
300	0.458	0.511	0.002
300	0.393	0.481	0.001
300	0.383	0.508	0.001
150	0.378	0.505	0.002
150	0.462	0.487	0.006
100	0.345	0.468	0.002
100	0.429	0.511	0.007
65	0.391	0.429	0.003
65	0.433	0.513	0.010
65	0.476	0.482	0.002
35	0.366	0.497	0.004
35	0.406	0.491	0.005
35	0.467	0.512	0.005

Mean nitrogen to chlorine ratio = 0.492; standard deviation ($\Delta\alpha$) of distribution of results = 0.021; standard error = 0.005.

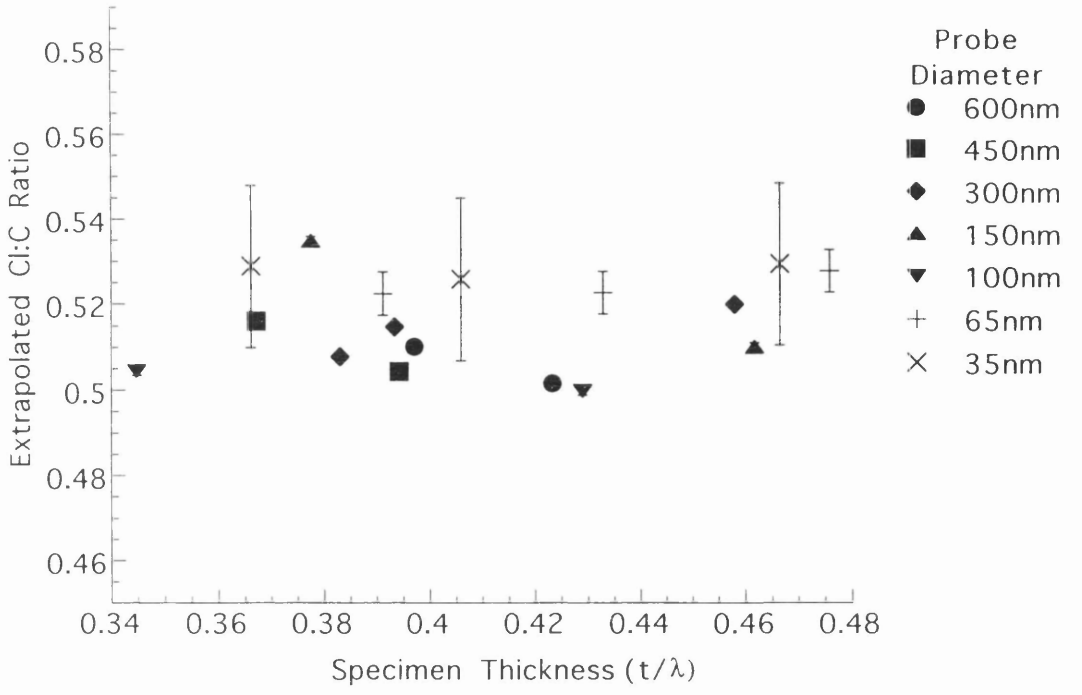

Figure 5.23(a) : Extrapolated Cl:C as a function of specimen thickness.

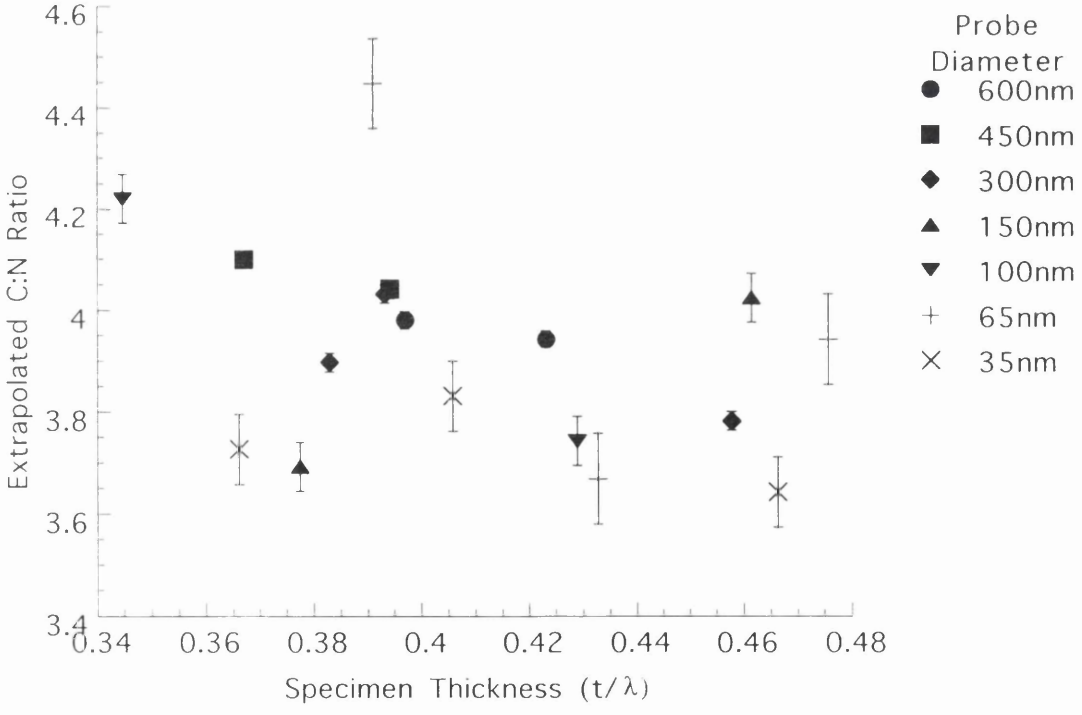

Figure 5.23(b) : Extrapolated C:N Ratios as a function of specimen thickness.

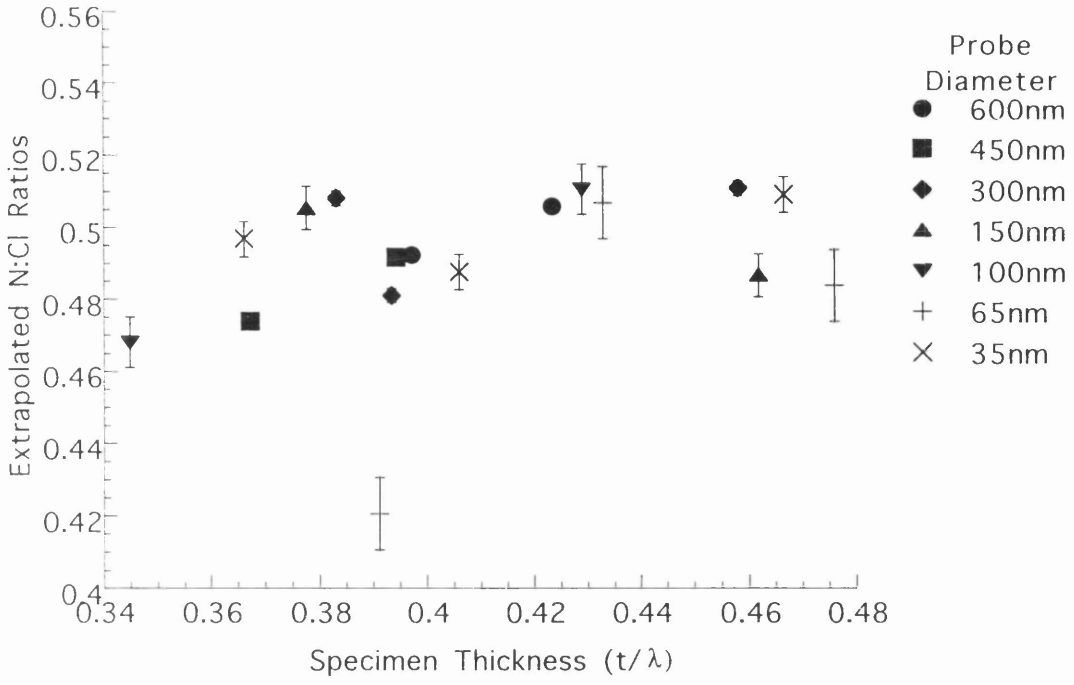

Figure 5.23(c) : Extrapolated N:Cl ratios as a function of specimen thickness.

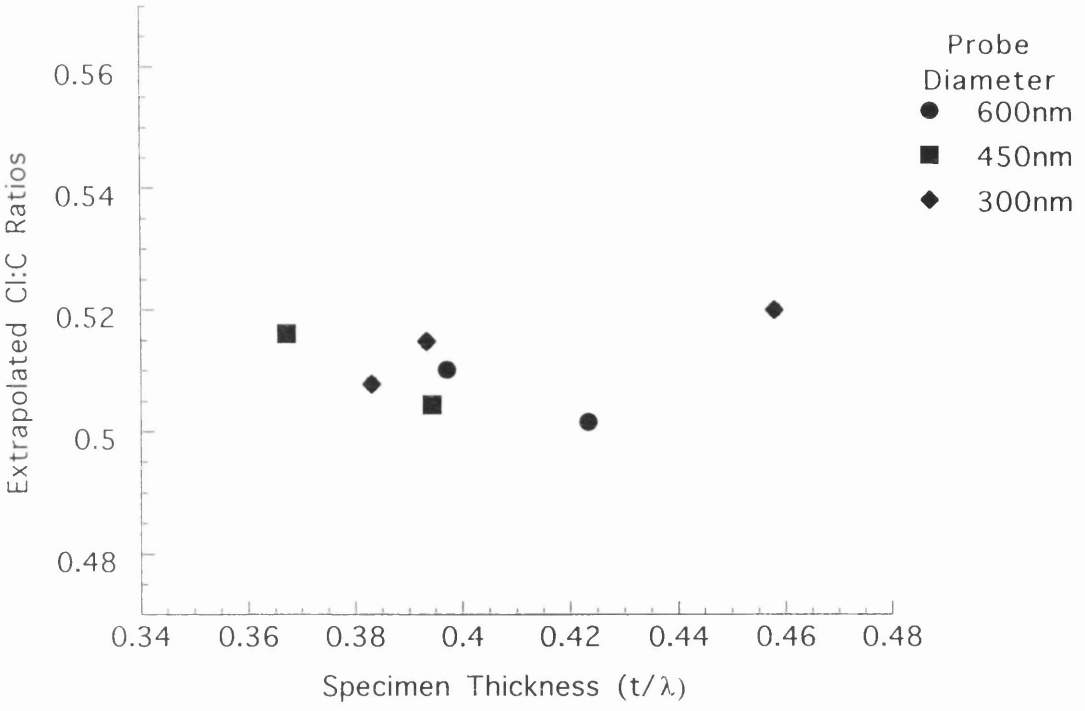

Figure 5.24(a) Extrapolated Cl:C ratios for large probe diameters.

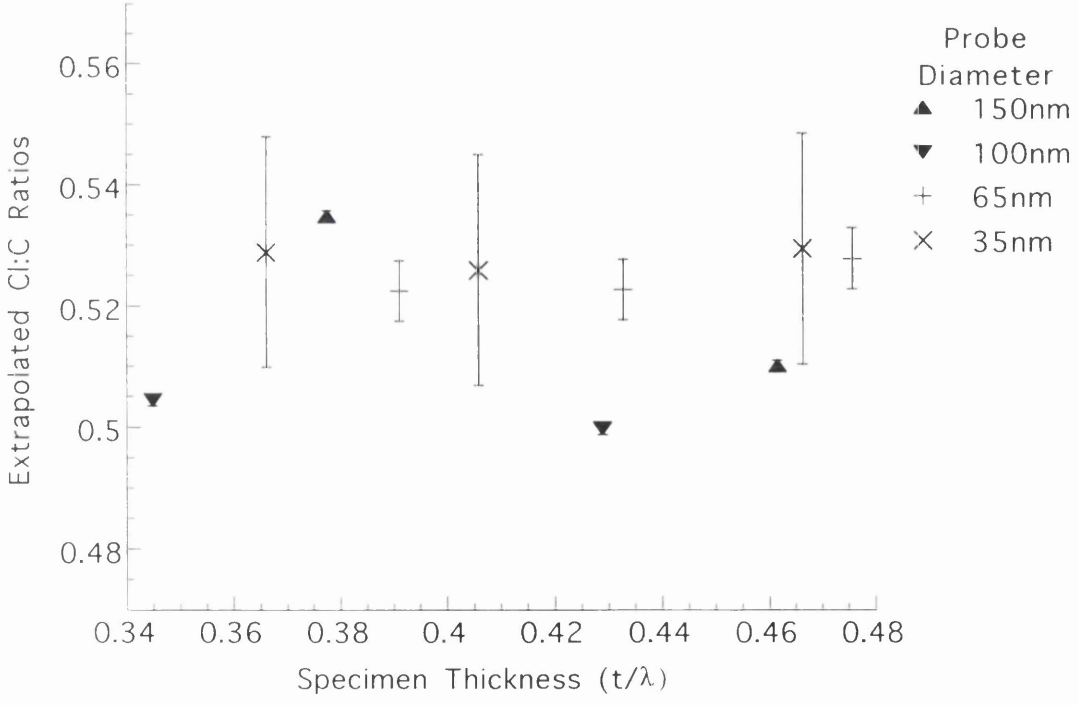

Figure 5.24(b) : Extrapolated Cl:C ratios for small probe diameters.

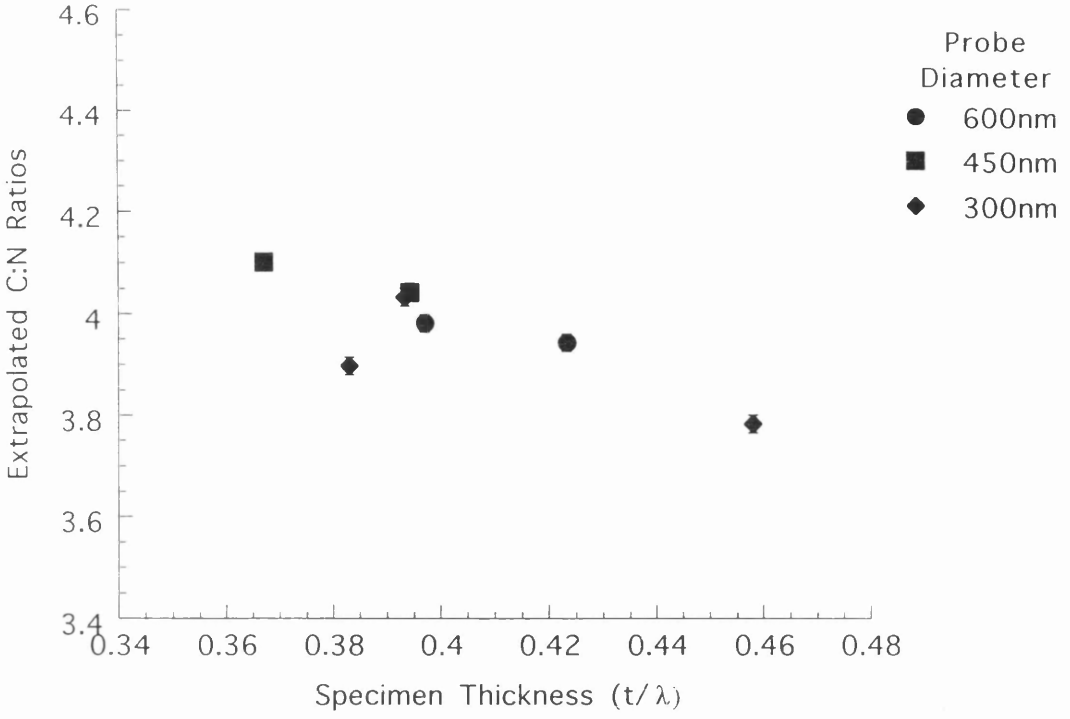

Figure 5.25(a) : Extrapolated C:N ratios for large probe diameters.

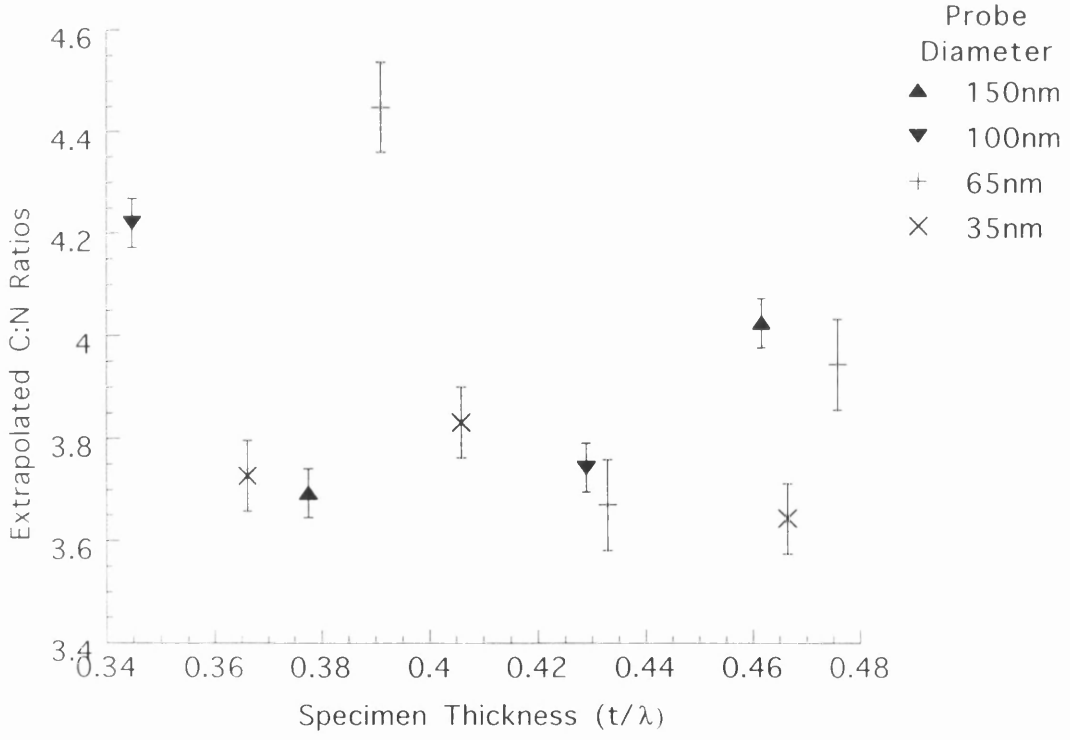

Figure 5.25(b) : Extrapolated C:N ratios for small probe diameters.

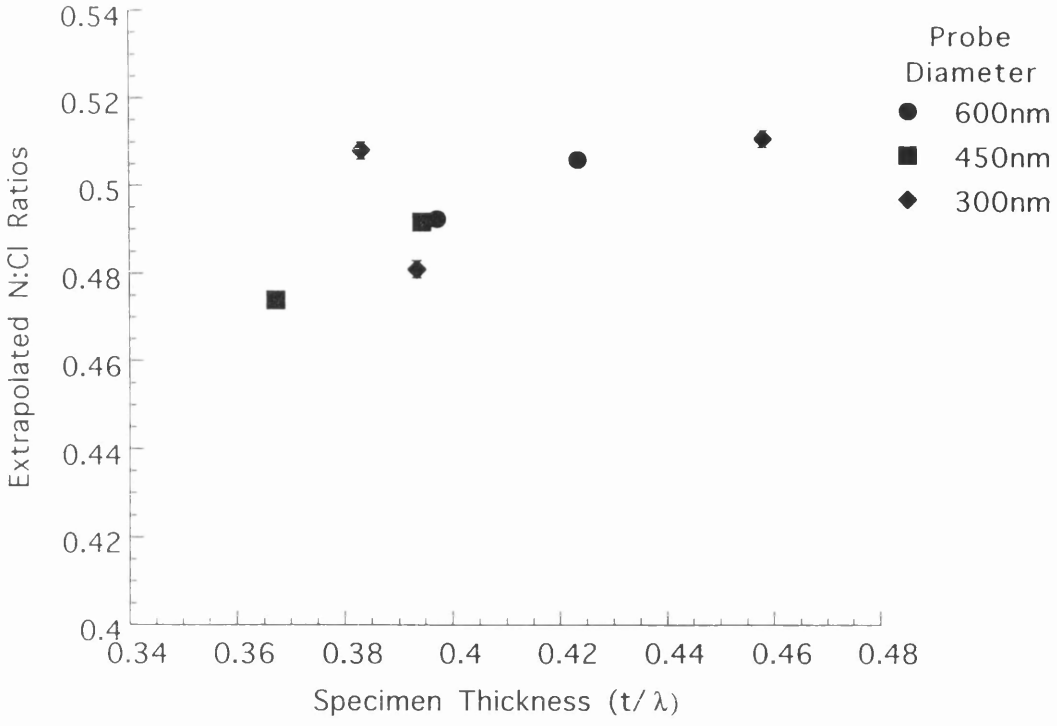

Figure 5.26(a) : Extrapolated N:Cl ratios for large probe diameters.

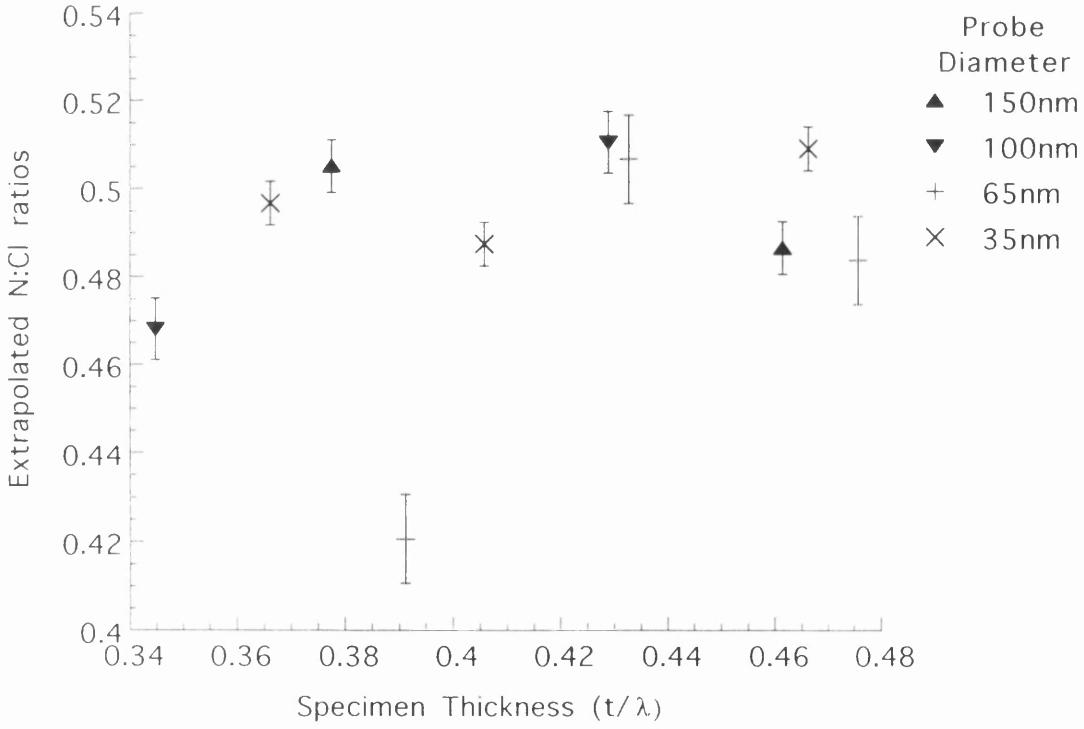

Figure 5.26(b) : Extrapolated N:Cl ratios for small probe diameters.

probe diameters which is not observed for the small probe diameters. The results for the industrial sample together with those for the standard sample are discussed in the following section.

5.15 Discussion of results for standard and industrial samples

The studies above have shown that, at large probe diameters, the Cl:C, C:N and N:Cl ratios vary linearly with respect to dose. At smaller probe diameters these ratios approach a saturation level. It is unlikely that all of the chlorine in the sample has been lost. Chlorine is known to be lost from an irradiated area by diffusion which is strongly temperature dependent (McColgan, 1990). As irradiation continues, chlorine continues to diffuse out of the area and free chlorine from the unirradiated area nearby diffuses back into the area. The processes of diffusion out and back diffusion approach an equilibrium level so that the Cl:C ratio approaches a saturation. The same processes of diffusion occur for the N and explains why the C:N ratios also approach a saturation level.

The results for both the standard and industrial samples were separated into those for large and small probe diameters. For both samples the previous discussion showed no demonstrable thickness dependence in the Cl:C ratios at either large or small probe diameters. The mean Cl:C ratios for the standard and industrial samples from PEELS were 0.505 ± 0.003 and 0.517 ± 0.003, respectively. These values are greater than the results from the bulk chemical analysis of 0.478 and 0.456, respectively. This may reflect an error in the relative magnitudes of the theoretical cross-sections. More worrying is the fact that the ratios of the two values disagree. Thus it is necessary to look more closely at the results for both samples. In order to compare both sets of results for the Cl:C ratios, they were combined by adjusting the samples data to have 16 Cl atoms per molecule. This was done by multiplying the values in the standard and industrial

samples by 16/15.3 and 16/14.6, respectively. Figures 5.27(a) and (b) show the extrapolated Cl:C ratios for both samples at large and small probe diameters. The graphs suggest that there is an underlying increase of the ratio with thickness and this was obscured by the scatter of the data points in the earlier graphs. It was noted earlier that the technique used to extrapolate the data from small probe diameters might bias the extrapolated values to the low side. However, figure 5.27(b) shows that the spread of data for the small probe diameters makes it difficult to spot such a bias. Further discussion of these graphs is presented later in this section.

Both the standard and industrial samples showed a thickness dependence for the C:N ratios at large probe diameters. This dependence was not obvious at small probe diameters for either sample. As with the Cl:C ratios, the C:N ratios for both samples were combined and are presented in figures 5.28(a) and (b). Figure 5.28(a) shows a linear decrease in the C:N ratio with increasing thickness for large probe diameters. The C:N ratios in figure 5.28(b) show that there is a similar underlying decrease in the C:N ratios with increasing thickness and again this was obscured by the scatter in the earlier plots.

The N:Cl ratios, for the standard and industrial samples, were adjusted to have 16 chlorine atoms per molecule by multiplying them by 15.3/16 and 14.6/16, respectively. The combined results are presented in figures 5.29(a) & (b). As for the C:N ratios, the N:Cl ratios show a linear thickness dependence at large probe diameters and those for small probe diameters show the same underlying variation.

The extrapolated C:N and N:Cl ratios at small probe diameters both show a greater data spread compared to the results for large probe diameters. As with the Cl:C ratios at small probe diameters, biasing, if any, from the extrapolation technique is difficult to spot due to the large data spread.

The combined results for the extrapolated Cl:C, C:N and N:Cl ratios show a convincing thickness dependence, particularly at large probe diameters. The

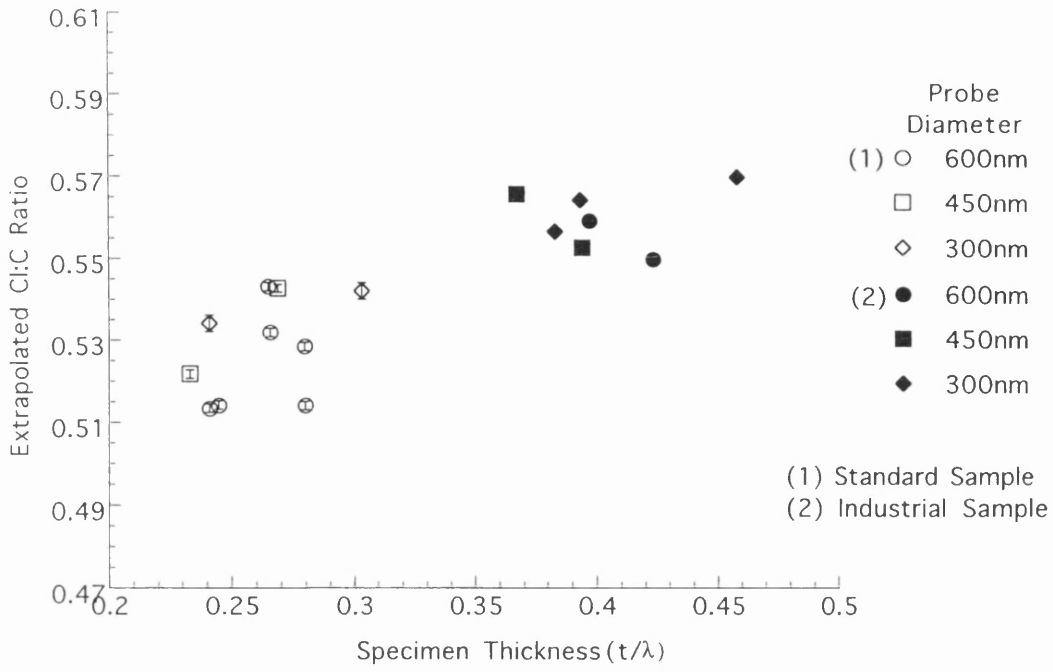

Figure 5.27(a) : Extrapolated Cl:C ratios from the standard and industrial samples (adjusted to have 16 Cl atoms/molecule) for large probe diameters.

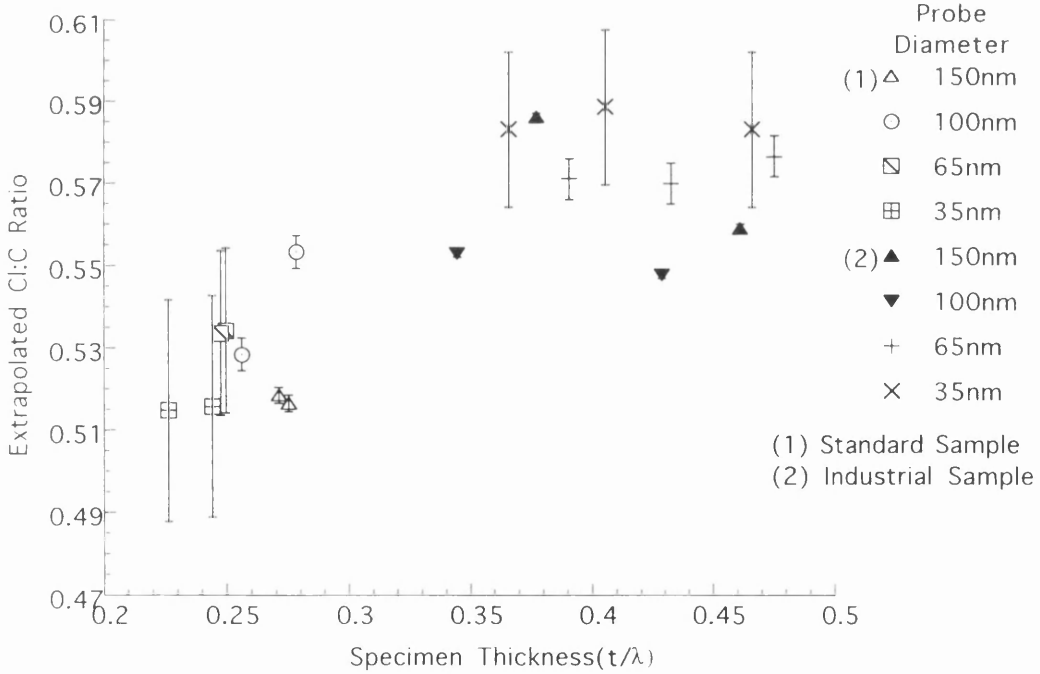

Figure 5.27(b) : Extrapolated Cl:C ratios from the standard and industrial samples(adjusted to have 16 Cl atoms/molecule) for small probe diameters.

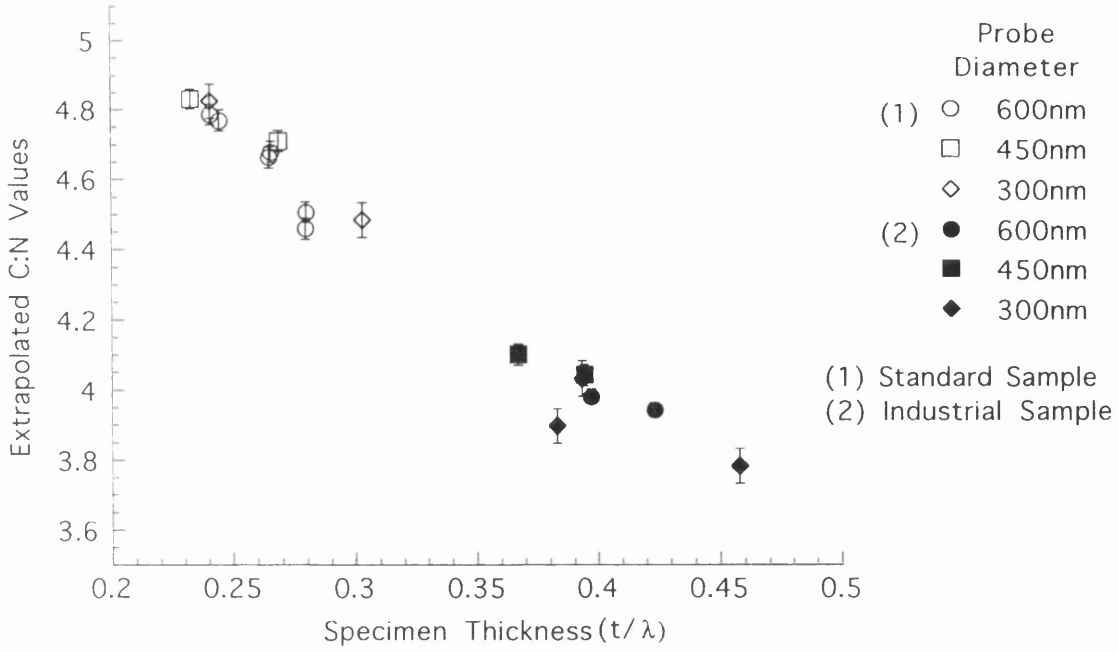

Figure 5.28(a) : Extrapolated C:N ratios from the standard and industrial samples (adjusted to have 16 Cl atoms/molecule) for large probe diameters.

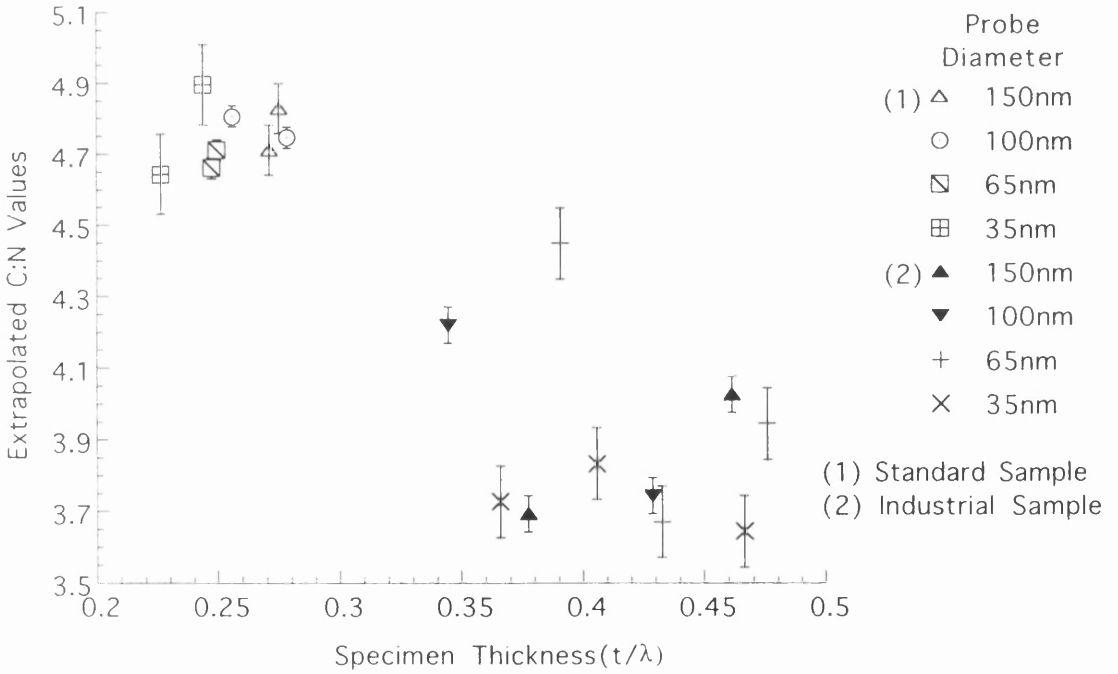

Figure 5.28(b) : Extrapolated C:N ratios from the standard and industrial samples (adjusted to have 16 Cl atoms/molecule) for small probe diameters.

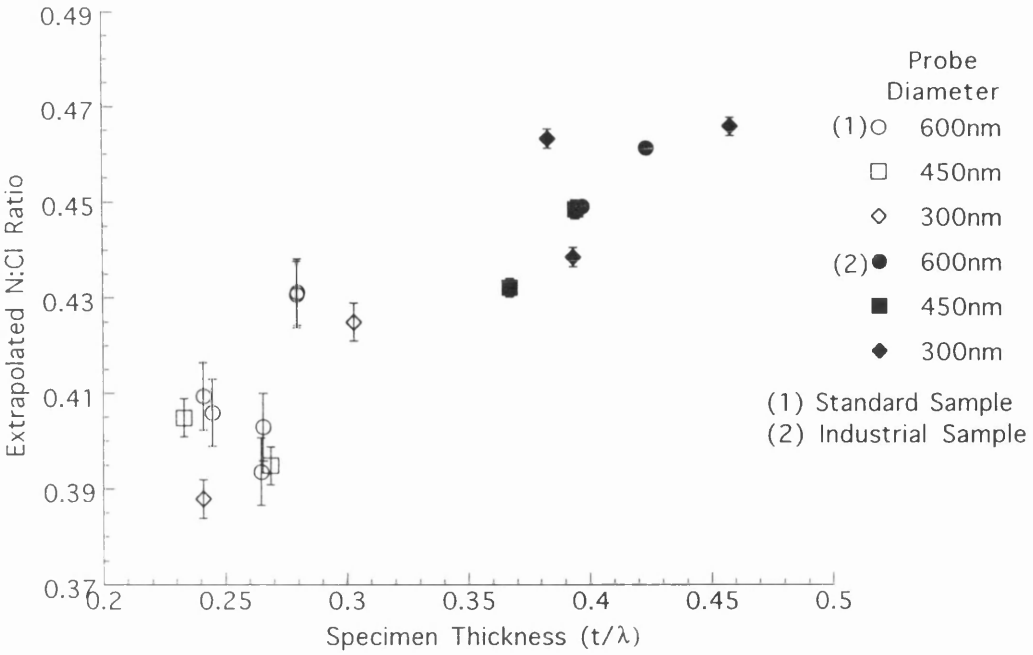

Figure 5.29(a) : Extrapolated N:Cl ratios for the standard and industrial samples (adjusted to have 16 Cl atoms/molecule) for large probe diameters.

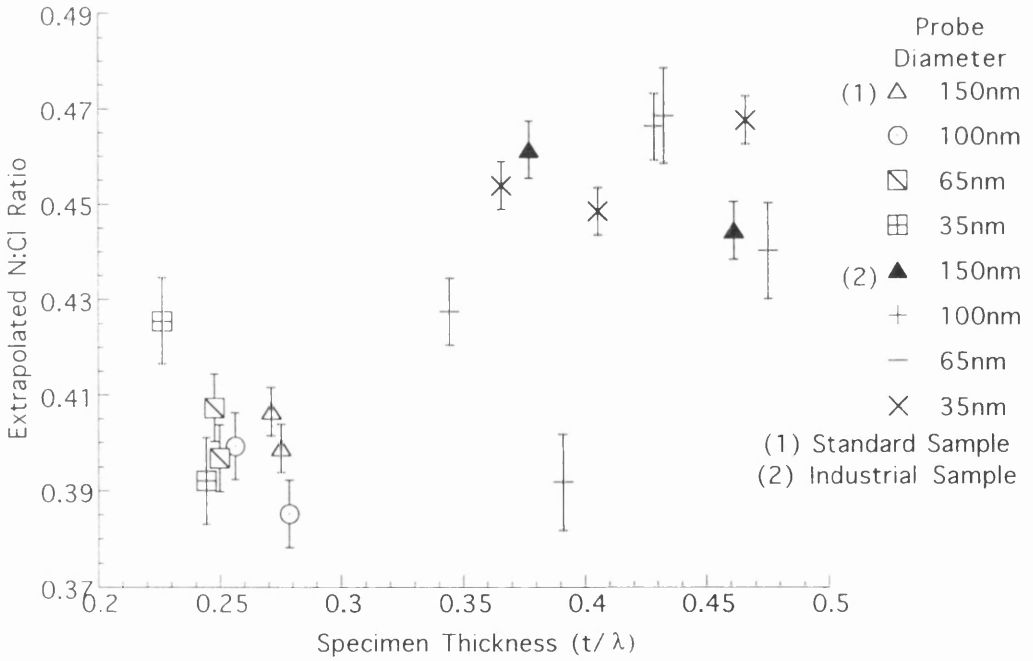

Figure 5.29(b) : Extrapolated N:Cl ratios from the standard and industrial samples (adjusted to have 16 Cl atoms/molecule) for small probe diameters.

thickness dependence may be a real effect of data acquisition or a result of data manipulation. Both these reasons are considered in the following discussion.

The thickness dependence may be a result of a process or processes which occur prior to, or during, acquisition of the spectra. The possible processes involved and their effect on the elemental ratios are discussed here.

Carbon contamination would have a greater effect at smaller thicknesses and lead to an increased Cl:C with thickness, as was observed. Carbon contamination is possible during irradiation, while spectra are being recorded. However, there was no observable increase in the carbon signal in any sequence of spectra. It is possible that a layer of carbon has been deposited on the surface of the specimens prior to data acquisition. It has been calculated, over the measured thickness range of 0.25 - 0.5t/λ, that a layer of carbon, 0.04t/λ thick, would be required to account for increase in the Cl:C ratio over this range. However, this is not consistent with the variation in the C:N ratio, over the same thickness range. The results show an increase in the Cl:C ratio of ~10%, whilst over the same thickness range, the C:N ratio falls by ~25%. It, therefore, seems unlikely that a layer of carbon on the surface of the material is the cause of the thickness variations. However, it cannot be excluded altogether, as several processes may be involved.

It may be possible that chlorine is lost prior to data acquisition, as a result of the experimental set-up procedure. This would also cause the Cl:C ratio to increase with thickness. However, the maximum dose incident on an area, prior to data acquisition, is ~0.01Ccm^{-2}. The data has shown that using a large probe diameter the material loses <2% of its chlorine content with ten times this dose. Therefore, it is unlikely that the specimens have lost chlorine as a result of the experimental set-up procedure. Furthermore, it would not explain the increase in the N:Cl ratio with thickness.

During irradiation it is known that C and N atoms are lost by diffusion. It is possible that in a given time more chlorine diffuses out of a thinner area. This

would result in an increase in the Cl:C ratio with thickness. If it is assumed that the N atom is smaller than the Cl atom, it is possible that the N atom has a greater diffusion length than the Cl atom. This would affect all three ratios. However, as mentioned earlier, there is no apparent dose rate dependence for the rate of loss of chlorine. Furthermore, the effect would also be observed at different diameters. The results show that the variation in the ratios with thickness, is similar for both large and small probe diameters. Therefore, this is not a plausible explanation for the variations but it cannot be ruled out without further experimental at different temperatures.

The above discussion has considered possible real effects of data acquisition which could result in a thickness dependence in the elemental ratios. As mentioned earlier, data processing methods may also be responsible for the thickness dependence. The problems associated with analysing the spectra and the effects they might have on the results are now considered. The main problems in analysing the CPC spectra are :

(**a**) separation of the ionisation edges :

- The C K-edge lies very close to the start of the background of the Cl L_1-edge. Figure 5.30 shows the Cl and C edges from two samples of different thickness, prior to deconvolution. The figure shows that for the thicker sample the Cl and C edge shapes are much flatter. This difference is more pronounced near the edge on-set. The data processing relies on the deconvolution routine getting back to the single scattering. The routine involves a number of steps which may introduce a bias which is thickness dependent. The routine also relies on the system being linear. However, nonlinearities in amplification and digitisation are known to exist. It may be that the background under the C K-edge is flatter in thicker samples which would result in the C being lower for thicker samples and thus explain the increase in the Cl:C ratio with thickness. However, this

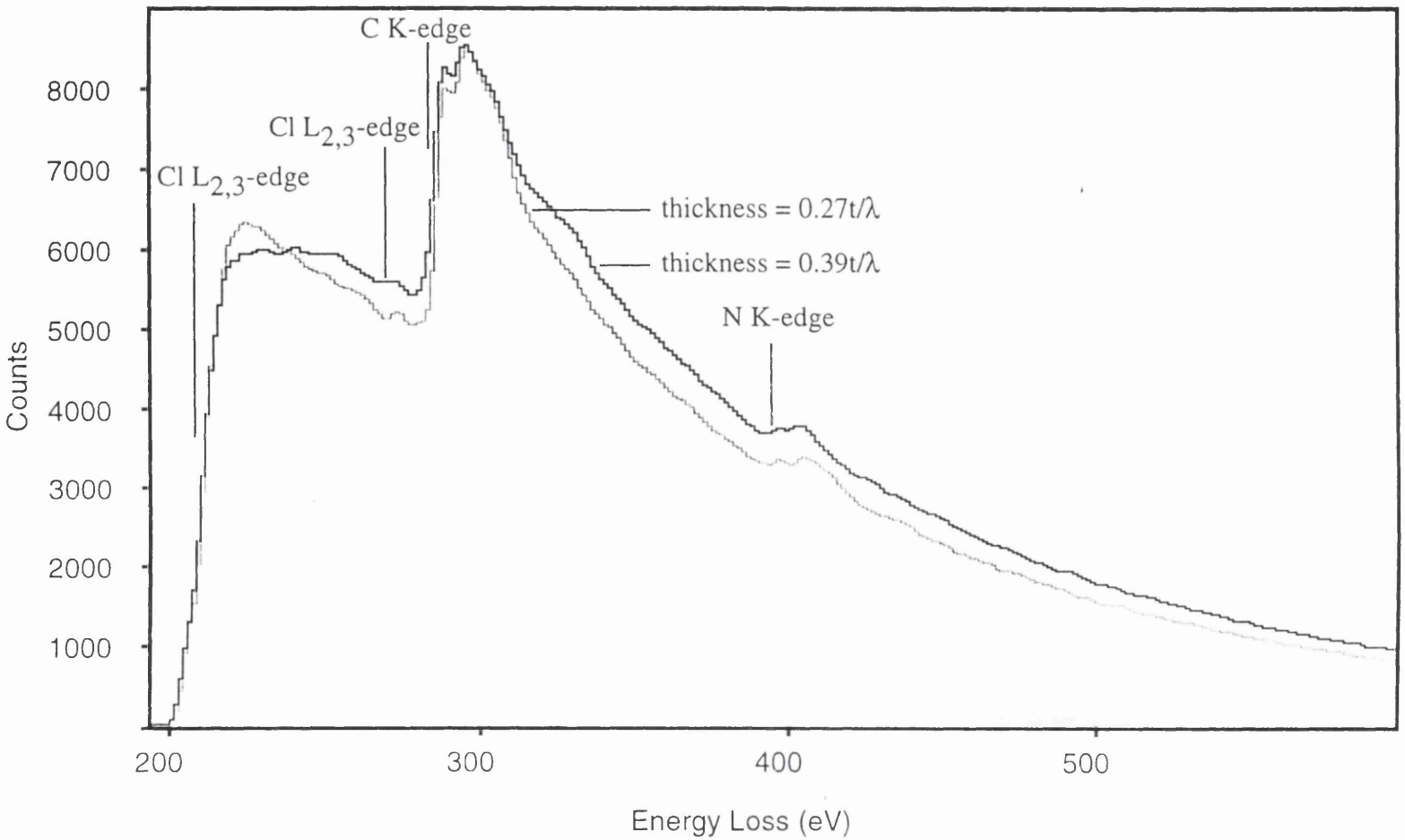

Figure 5.30 : CPC spectra, prior to deconvolution, from areas of different thickness.

mechanism alone cannot be used to explain the greater variation in the C:N ratio. Indeed, it does not explain the variation in the N:Cl ratio.

- The small N K-edge lies on the much larger C K-edge and so the greatest errors are expected in the determination of the size of this signal. At small thicknesses the signal to noise ratio will be low which may result in the nitrogen signal being underestimated. Thus as the thickness increases it would be expected that the C:N would decrease, while the N:Cl ratio would increase. This matches the experimental observations and so the error associated with determining the N signal may be a possible explanation.

(**b**) extrapolation of ratios

- large chlorine losses were observed, particularly at small probe diameters. It would also be expected that thinner samples would lose chlorine more quickly. A smaller volume means that more chlorine diffuses out of the surface, whilst a larger volume is more able to trap the chlorine. Rapid chlorine losses from thinner samples might result in the extrapolated N:Cl ratio being lower for thinner samples. However, at large probe diameters, the loss of chlorine is slow for both samples. Systematic extrapolation errors related to sample thickness would not occur for large probe diameters, therefore, this does not explain the thickness dependence of the N:Cl ratios.
- large nitrogen losses during acquisition may have an effect on the extrapolation of data. However, at large probe diameters the nitrogen loss is small and there were no observed extrapolation errors related to specimen thickness.

The above discussions have considered the thickness dependence of the Cl:C, C:N and N:Cl ratios. Whilst a combination of several mechanisms may be acting to give the observed thickness dependence, it seems more likely that this is a consequence of ionisation separation errors. The most likely being the errors introduced by the deconvolution routine and low N signal to noise ratios at lower thicknesses. The Cl:C increases by ~10% over the thickness range of 0.25 -

$0.5t/\lambda$. Over the same thickness range the N:C drops by ~25% and the N:Cl increases by ~15%. The thickness dependence for each of the ratios are therefore self-consistent. The fact that there is little evidence of a probe diameter dependence, suggests that the problems of analysis are not a result of the processes involved during data acquisition. This also demonstrates the validity of using this technique to analyse areas with small probe diameters down to ~35nm.

These results represent the best analysis of the experimental data and the associated limitations of the technique. The application of this technique to the analysis of single pigment particles is considered in the next section.

5.16 PEELS analysis of CPC pigment particles

A specimen of industrially produced CPC pigment particles was produced using the spraying technique described in chapter 1. The specimen was prepared without using the dispersing agent to avoid introducing additional carbon. The experimental technique, described in section 5.5, was used to acquire spectra from the pigment particles of the industrially produced sample. Figures 5.31(a) - (c) show the Cl:C, C:N and N:Cl ratios, respectively from a selection of particles analysed. From figure 5.31(a) it can be seen that the initial Cl:C ratio and the initial loss of chlorine is different for each particle. It is also appears as if the Cl:C ratio approaches a saturation level more quickly for several of the particles. This is also true for the C:N and N:Cl ratios shown in figures 5.31(b) & (c).

The ratios were extrapolated to zero dose using the technique described in section 5.10. The extrapolated Cl:C, C:N and N:Cl ratios, together with the calculated mean, standard deviation and standard error, are presented in tables 5.10 - 5.12. The ratios were also plotted as a function of thickness and are presented in figures 5.32(a) - (c). The range of thicknesses in these graphs is similar to the range of thicknesses of the combined epitaxial data shown in figure

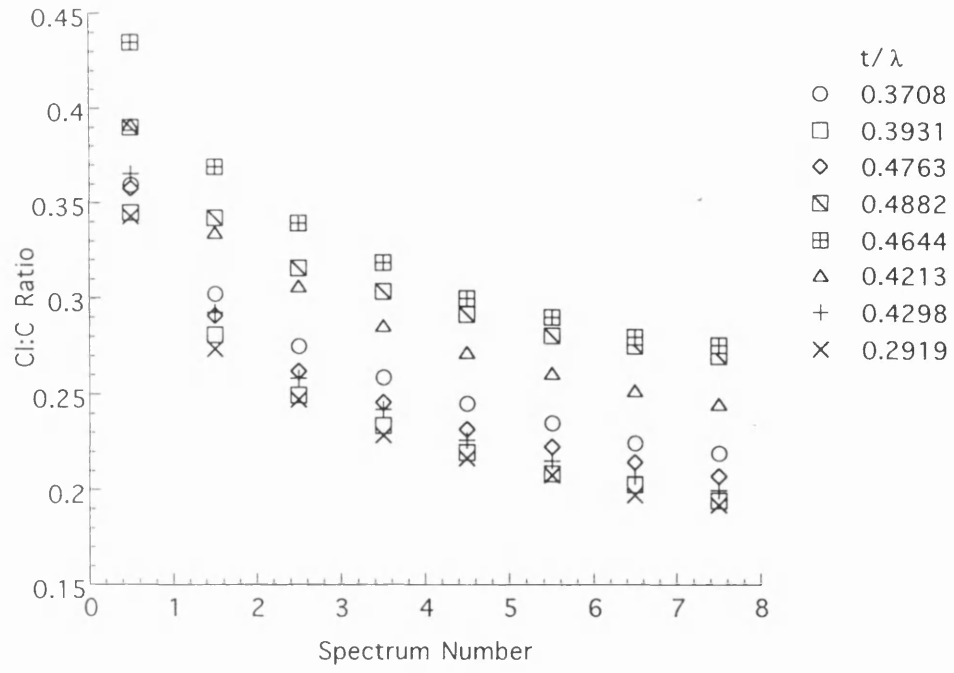

Figure 5.31(a) : Cl:C ratios for various pigment particles.

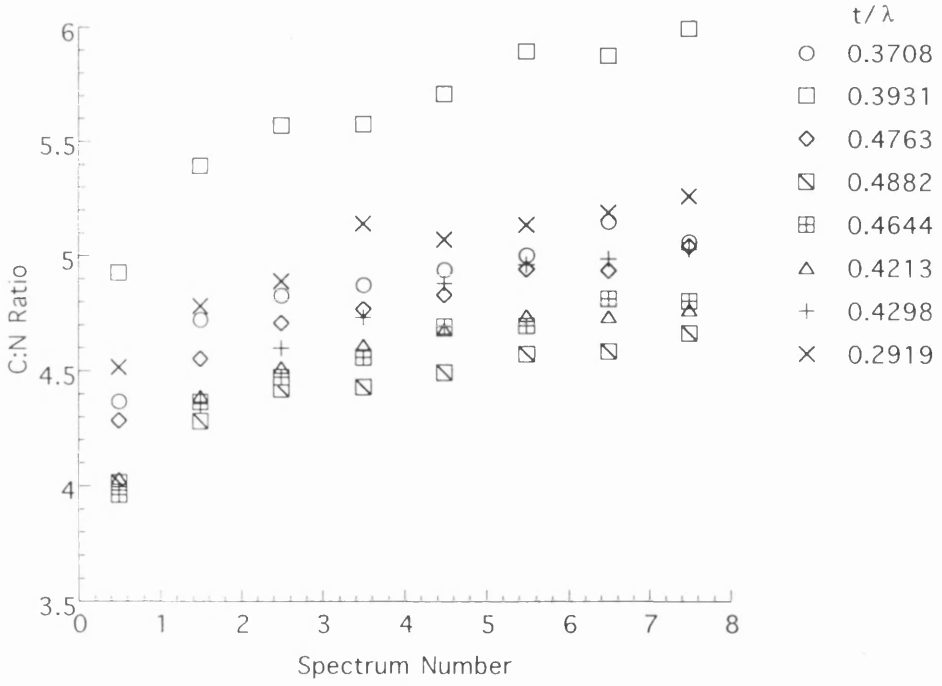

Figure 5.31(b) : C:N ratios for various pigment particles.

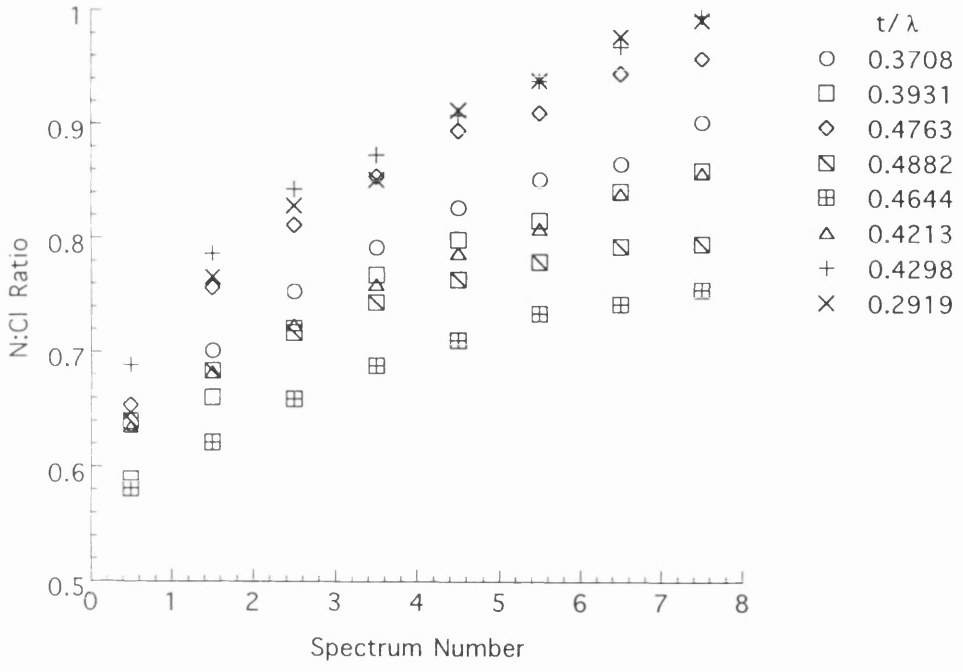

Figure 5.31(c) : N:Cl ratios for various pigment particles.

Table 5.10 : Extrapolated Cl:C ratios for various pigment particles.

Particle thickness (t/λ)	Extrpltd Cl:C ratio (α)	Error ($\delta\alpha$)
0.3708	0.401	0.013
0.3931	0.390	0.013
0.4763	0.407	0.016
0.4882	0.422	0.010
0.4664	0.489	0.021
0.4213	0.441	0.021
0.4298	0.417	0.015
0.2919	0.405	0.027

Table 5.11 : Extrapolated C:N ratios for various pigment particles.

Particle thickness (t/λ)	Extrpltd C:N ratio (α)	Error ($\delta\alpha$)
0.3708	4.087	0.100
0.3931	4.619	0.082
0.4763	4.118	0.075
0.4882	3.808	0.085
0.4664	3.666	0.100
0.4213	3.816	0.082
0.4298	3.726	0.076
0.2919	4.291	0.091

Table 5.12 : Extrapolated N:Cl ratios for various pigment particles.

Particle thickness (t/λ)	Extrpltd N:Clratio (α)	Error ($\delta\alpha$)
0.3708	0.601	0.010
0.3931	0.550	0.013
0.4763	0.591	0.011
0.4882	0.610	0.007
0.4664	0.558	0.010
0.4213	0.608	0.015
0.4298	0.623	0.015
0.2919	0.570	0.017

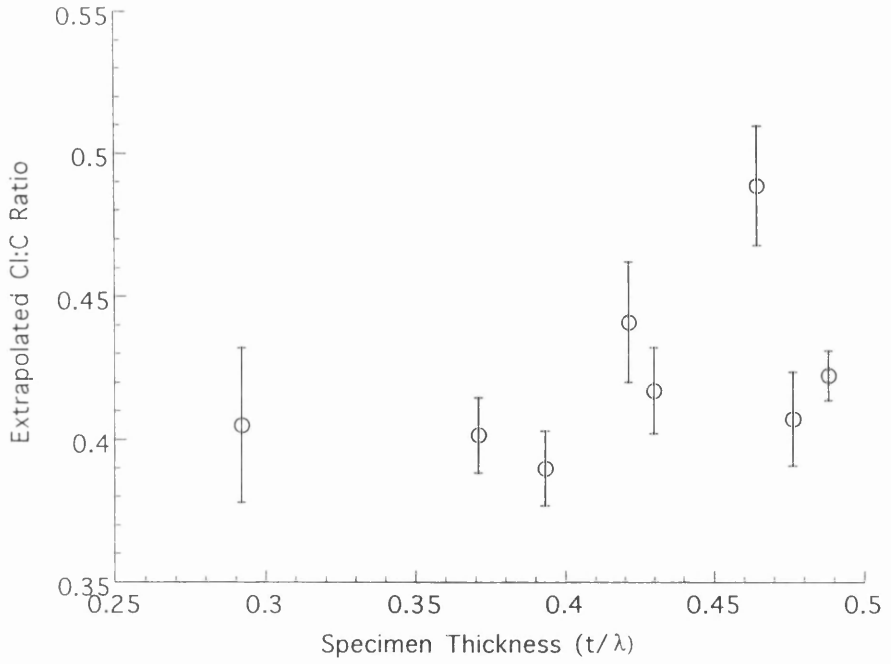

Figure 5.32(a) : Extrapolated Cl:C ratios for various pigment particles.

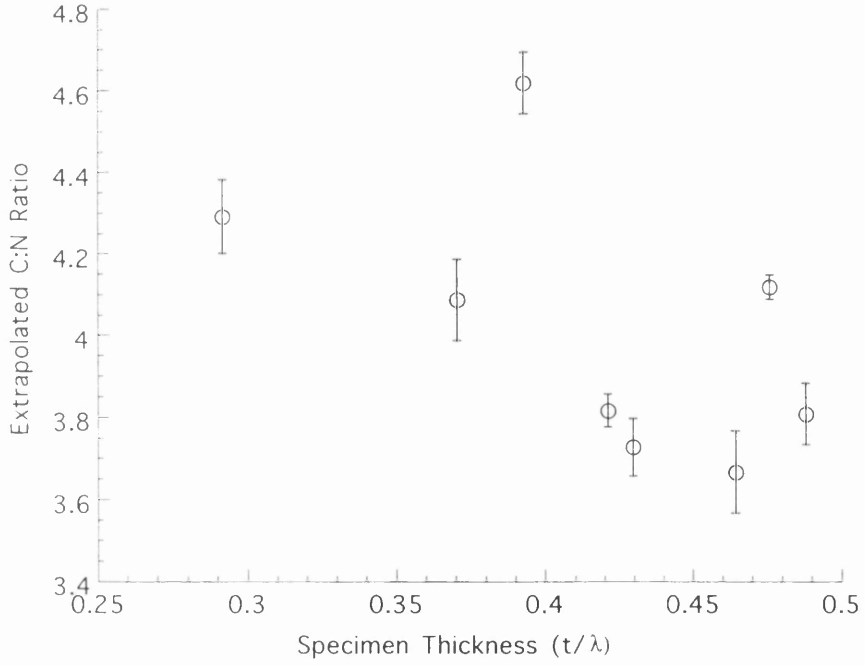

Figure 5.32(b) : Extrapolated C:N ratios for various pigment particles.

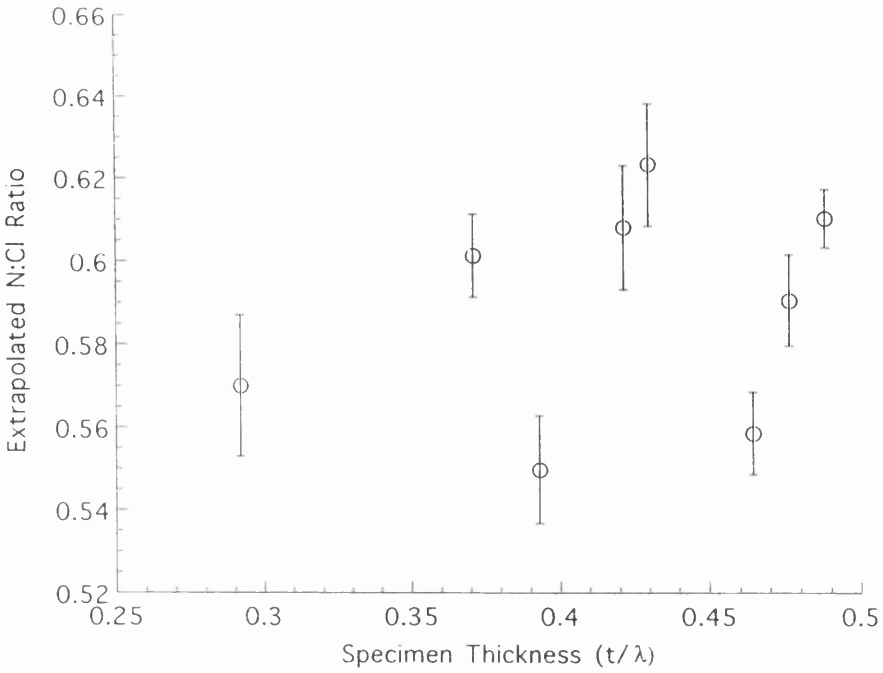

Figure 5.32(c) : Extrapolated N:Cl ratios for various pigment particles.

5.32(a). The Cl:C ratio appears to show no real thickness dependence as was the conclusion at the end of the previous section. However, the mean Cl:C ratio is 0.421 ± 0.011 compared to the value of 0.517 ± 0.003 which was obtained for the epitaxial film of the same material. The extrapolated C:N ratios shown in figure 5.32(b) show a thickness dependence which is similar to the trend shown in figures 5.28(a) & (b) for the epitaxial material. The values for the C:N ratios are similar to those found for the epitaxial material. A best fitting straight line to all of the extrapolated C:N ratios for the epitaxial material, was calculated. This line, together with the extrapolated C:N ratios for the pigment particles, are shown in figure 5.33. It can be seen that the C:N ratios for the pigment particles follow a similar trend to the epitaxial results. The extrapolated N:Cl ratios shown in figure 5.32(c) appear to show a thickness dependence which is similar to the trend shown by the epitaxial material. However, the actual values lie around 0.6, while those measured from the epitaxial films of the same material lie around 0.49.

The results for the extrapolated C:N ratios for the pigment particles are similar to those observed for the epitaxial material. This suggests that the differences in the Cl:C and N:Cl values result from the measurement of the Cl. The mean extrapolated Cl:C ratios being 0.421 ±0.011 for the particles and 0.517 ±0.003 for the epitaxial film. This is a difference of ~18%. The reason for the difference in the ratios from the same material could be a result of one or all of the following mechanisms :

- chlorine loss resulting from the experimental set-up procedure
- a more rapid chlorine loss during acquisition
- a difference in the chemical composition

In the following discussion, the justification and validity of these effects is discussed. The Cl:C ratios for the pigment particles and one data set from the epitaxial material, obtained using a 35nm probe diameter, are plotted together in

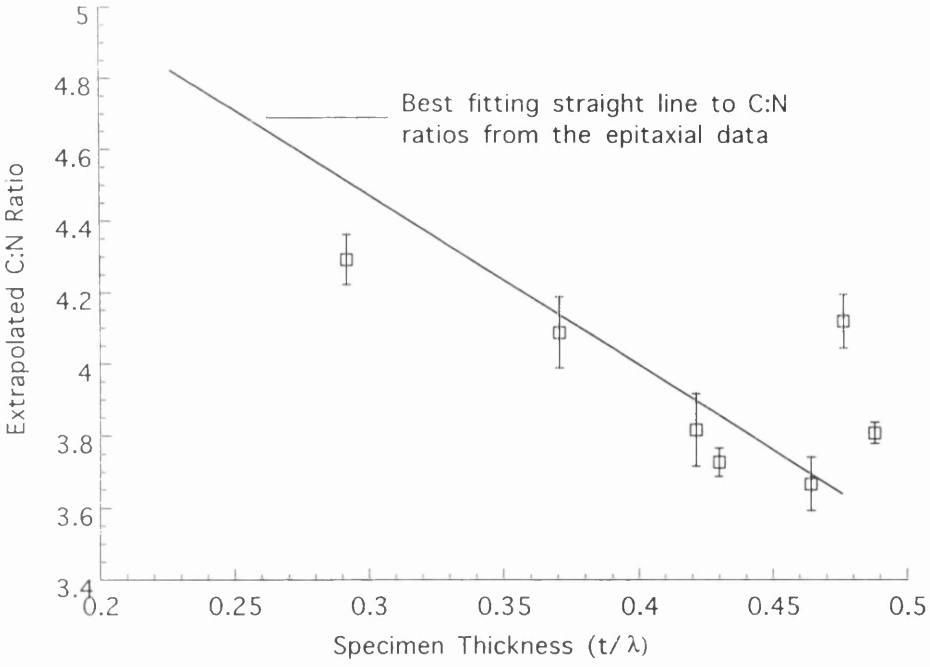

Figure 5.33 : Extrapolated C:N ratios for various pigment particles and fit to C:N ratios from epitaxial films.

figure 5.34. It is assumed that the loss is only dependent on the dose and no other mechanisms are involved for these two specimens. Therefore, if a pigment particle has lost chlorine prior to data acquisition, then its initial rate of loss should match the rate of loss from the epitaxial material at the same initial value. For example, points **a** and **b** on figure 5.34 have approximately the same value. If the assumption is true, then the rate of loss of chlorine, immediately after these two points, should be the same. It is clear that this is not the case. Therefore, this model cannot be used to explain the difference in the extrapolated ratios.

Another argument, again based on an initial loss of chlorine prior to data acquisition, may be put forward to explain the difference in chlorine content between the two specimens. This argument is based on the mechanism for chlorine loss described in section 5.15. During the experimental set-up procedure, chlorine may be lost from a pigment particle by diffusion. When the beam is blanked the process of diffusion may continue. The particles have a greater surface area to volume ratio and therefore more chlorine can escape completely from the pigment particles than from the epitaxial material. If this happens then less chlorine will diffuse back into the areas irradiated on the pigment particles. This may result in a drop in the chlorine level prior to data acquisition. However, as discussed in section 5.15, the dose incident on the specimen during experimental set-up is very small (a maximum of ~0.01Ccm$^{-2)}$. It is unlikely that this dose level could result in the pigment particles losing ~18% more chlorine than the epitaxial material during experimental set-up procedure.

If the initial loss of chlorine from the pigment particles is very rapid this would lead to large errors in the extrapolation of the data to zero dose, giving a value lower than expected. This is possible if there is a large loss of chlorine from the large surface area of the pigment than from the equivalent thickness of epitaxial material. In addition, Smith et al (1986) have demonstrated that radiation damage occurs more readily at faults in the CPC material. The pigment particles have a greater number of faults than the epitaxial material, therefore, a greater

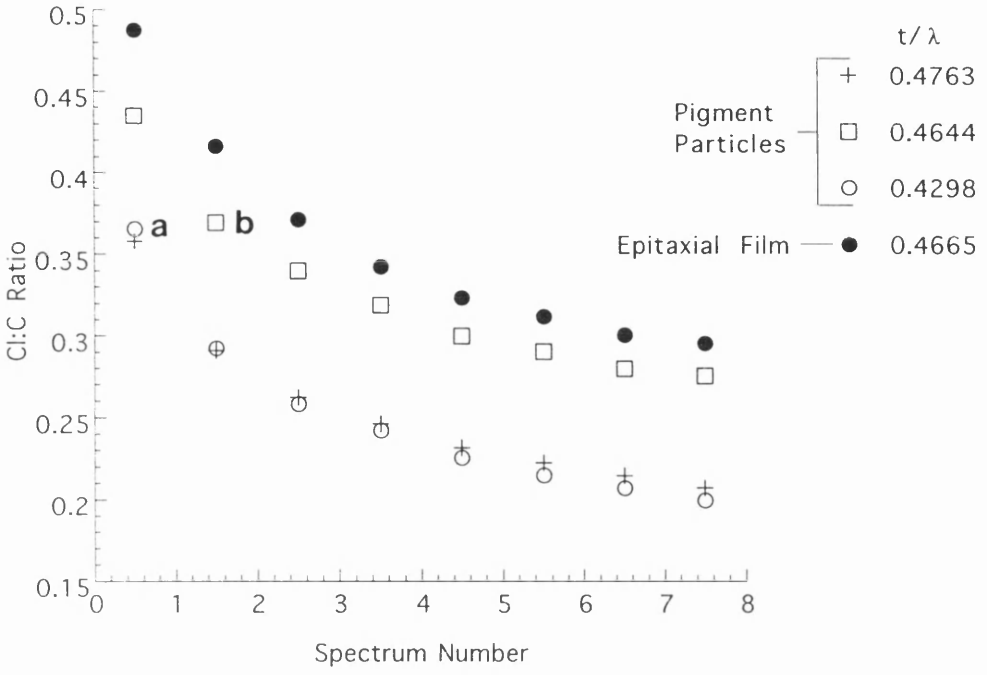

Figure 5.34 : Cl:C ratios from various pigment particles and from an area, ~35nm in diameter, of epitaxial film.

loss of chlorine would be expected from the particles. The variation in the epitaxial data at small probe diameters may be as a result of some areas being close to or on faulted material and others are not. Over large areas the effect of faults would be averaged out and thus there is less scattering of the data at large probe diameters.

The final possible reason suggested for the different extrapolated Cl:C and N:Cl ratios, was that the specimens had a different chemical composition. The pigment particles are known to have an average of 14.6 Cl atoms/molecule. The particles may contain a range of Cl atoms/molecule. It may be possible that the evaporation and epitaxial film growth process selects those with a high Cl content. This is only speculative and further experimental work is required to ascertain this. EDX analysis of the Cl to Cu ratio for large areas of epitaxial material and large numbers of pigment particles could be used to determine if this is the case.

From the discussion above, the most likely explanation for the difference in the Cl:C and N:Cl ratios is a more rapid chlorine loss from the pigment particles. This is a result of the highly faulted nature of the particles and the larger surface area to volume ratio of the pigment particles which allow chlorine to diffuse out more readily. A summary of the PEELS work performed in this project is discussed in the following section.

5.17 Summary of PEELS analysis of CPC material

Initial studies of CPC material were carried out using epitaxial films in order to determine the accuracy and limitations of the technique. The first problem which had to be overcome was the problem of extrapolation of the elemental ratios to zero dose. In an attempt to do this a special beam blanking unit was developed which reduced the time spent on an area to be analysed. This

minimised chlorine loss prior to acquisition and reduced the errors in the extrapolation.

The second problem was the analysis of the spectra, in particular, the separation of the ionisation edges. The spread of results in the extrapolated ratios and the thickness dependence of these ratios were reduced using empirical cross-sections to process the spectra.

Two samples of epitaxial films of CPC material were analysed. The first was a standard sample prepared in the laboratory to be surfactant free and almost fully chlorinated (15.3 Cl atoms/molecule). The second was an industrially prepared sample which contained surfactant and was highly chlorinated (14.6 Cl atoms/molecule). The results for both samples were compared by adjusting the data such that the samples contained 16 Cl atoms/molecule. These results showed that the Cl:C, C:N and N:Cl ratios had a thickness dependence which were a result of the data analysis. The first being multiple scattering effects which made it difficult to separate the edges and the small N signal at low thicknesses.

The foregoing technique was also used to analyse the pigment particles from the industrially produced sample. The extrapolated C:N ratios were similar to those obtained from the analysis of the epitaxial films, including an apparent thickness dependence. However, the extrapolated Cl:C and N:Cl ratios were markedly different from those obtained from the epitaxial films. This was most probably a consequence of very rapid initial chlorine loss from the pigment particles.

The adjusted Cl:C ratios (figures 5.27(a) & (b)) for both the standard and industrial samples, at both large and small probe diameters, were combined. Not taking account of the thickness dependence, the absolute Cl:C ratio which can be obtained is 0.547 ± 0.023, with a 95% confidence level over the thickness range 0.25-0.5t/λ. This is equivalent to approximately ±0.7Cl atoms/molecule. It is clear that this value could be improved if the t/λ variation was eliminated or could be accounted for in the analysis. This would allow any

particle to particle variations within a single pigment sample to be determined. Further details of how the accuracy of these results could be improved are given in chapter 6. The use of small probe diameters, such as are required for analysis of the pigment particles, was also practical for the epitaxial films. However, in order to analyse actual pigment particles, further modifications to the experimental technique are required to reduce the chlorine loss prior to data acquisition. This could be done by using a cooling stage, if available. EDX work carried out by McColgan et al (1990), have shown that cooling highly chlorinated CPC material reduces the chlorine loss by 1/3 compared to that at room temperature.

Chapter 6

SUMMARY AND CONCLUSIONS

6.1 Summary of project

As mentioned at the beginning of this project the colouring properties of CPC pigments are strongly dependent on the physical characteristics and chemical composition of the pigment particles. Investigations of the pigments was carried out using transmission electron microscopy which provided the high spatial resolution required. There were two aims for the project. Firstly, samples of highly chlorinated CPC pigments, produced using nominally identical conditions, were investigated in an attempt to determine how variations in their colouring properties arise. Samples of the same pigment, produced using different processes, were also investigated to determine how variations in their colouring properties arise. The second aim of the project was to use various techniques to investigate the physical characteristics and chemical composition of pigment particles.

The 1200EX CTEM was used to produce low magnification images of the particles. These images provided information about the size, shape and dispersibity of the pigment particles. High magnification images provided information about the internal structure of the pigment particles. A diffraction

technique, developed in the CTEM, allowed diffraction patterns to be recorded at ~50nm steps across small aggregates of CPC material. This provided information about how these aggregates were formed.

Techniques, available in the VGHB5 STEM, were also used to investigate the pigment particles. A technique based on the differential phase contrast (DPC) imaging mode was used to record simultaneous topographic and lattice images of the pigment particles. These images provide information regarding the surface and internal structure of the pigment particles. The technique was used to investigate further, the formation of large numbers of small aggregates present in the samples. The PEELS technique was used to study highly chlorinated CPC pigments in an attempt to measure the chemical composition of single pigment particles. Conclusions regarding this work are discussed in the following section.

6.2 Conclusions

It was found that pigments, produced using nominally the same process but with differing performance, exhibited different particle sizes and particle size distributions. The smaller particle size in one of the paint pigment samples could explain its poor dispersibility and consequently poor performance. Similarly, the wide particle size distribution in one of the plastic pigment samples may also explain its poor dispersibility and performance. Investigations of four samples of the same pigments produced using different manufacturing processes revealed that the sample with the best performance consisted of particles with rounded edges, thus reducing the possible area of contact between the particles. This makes it easier to disperse the particles and improves the colour strength. Lattice images showed no obvious difference in the crystallinity of each sample. The large number of particles with dislocations at the lattice fringes indicated that they were far from being perfectly crystalline. The low magnification images also

revealed that the samples were not single pigment particles with dimensions ~50nm but consisted mainly of small aggregates with dimensions of the order of several pigment particles.

Diffraction studies of the highly chlorinated CPC pigments revealed that the pigments were aligned on the carbon film of the grids, in predominantly two orientations; with either the [110] or [102] zone axis perpendicular to the film. Whilst this suggests that the particles exhibit preferred crystalline facets, it is not clear along which planes these lie. The particles contain a high density of twins, with a {110} twinning plane. These twins may exist in any one particle either on several {110} or just one. Many twin orientations would be expected from random defect formation, whilst a single twin variant may be a direct consequence of the β to α phase transformation. Insufficient evidence was available to determine which of these forms was the most likely. An investigation of the small aggregates using diffraction suggested that these were not a reaggregation of single particles but pieces of CPC material which had not been broken down by the pigmentation process.

The modified DPC imaging technique allowed topographic and lattice images of the same area to be recorded simultaneously. The technique was able to reveal both topographic features and lattice fringes in almost all directions except those parallel to the direction of differentiation. The edges of the particles were shown to have terraces and whilst many appeared to have flat surfaces, some were irregular. The images appeared to confirm the above suggestion, that the small aggregates were pieces of material not broken down by the pigmentation process. The topographic images showed areas of what appeared to be overlaying particles. The lattice images showed the lattice fringes to be continuous across these areas, suggesting that this is not a reaggregation of particles but a single lump of material.

Using EELS it was possible to determine the chlorine to carbon ratio with an accuracy of ~±0.7Cl atoms/molecule, from areas down to ~35nm in diameter, in epitaxial CPC material. There were two major problems in obtaining an

accurate analysis of the chemical composition. The first being radiation damage, which resulted in large errors when extrapolating the elemental ratios to zero dose. The second was the separation of the ionisation edges in the CPC spectra, which was thought to be the cause of an apparent thickness dependence in the elemental ratios. A specifically designed beam blanking unit reduced the amount of radiation damage prior to data acquisition and allowed spectra to be recorded from a previously unirradiated area. However, the rate of chlorine loss from areas <65nm in diameter resulted in large errors in the extrapolation technique. The use of empirical cross-sections helped to reduce both the thickness dependence and the data spread for the extrapolated ratios. The technique was applied to the analysis of single pigment particles. However, the initial rate of chlorine loss from the particles appeared to be greater than that for an area ~35nm in epitaxial material. For this reason it was not possible to extrapolate the elemental ratios to zero dose for the pigment particles. However, with further improvements to the technique this may be possible. These improvements and other suggestions for further work are discussed in the following section.

6.3 Suggestions for future work

In this section suggestions for future experiments and improvements to the experimental techniques used in this study are discussed. The results of this study suggested two possible reasons for twinning in the CPC pigments. Diffraction studies of the CPC material, at different stages of the manufacturing process, may help to determine how twinning arises. This would include analysis of the unhalogenated CPC and the intermediate material prior to pigmentation. These investigations may also provide more information about the faceting of the particles.

For the PEELS analysis, a number of approaches to improve the analysis can be tried. It is known that cooling the specimen to liquid nitrogen temperatures reduces the rate of chlorine loss by a factor of ~3 (McColgan et al, 199x). Thus the extrapolation error would be significantly reduced for a given dose to the specimen. This would help to reduce the scattering in the data. Unfortunately, this was not possible with the HB5. However, most instruments equipped with cooling stages and PEELS spectrometers do not have a suitable beam blanking system. A second step could be to acquire data over a much larger thickness range on the same material to confirm the thickness dependence inferred from the results in this thesis.

Other data analysis procedures exist. One approach would be to try multivariant statistical analysis on the series. This may help to improve the accuracy of extrapolations of the elemental ratios to zero dose. The technique has been used successfully on EDX spectra (e.g. Titchmarsh & Durnbill, 1996). Only if satisfactory progress is made here will it be worthwhile attempting to understand the behaviour of individual pigment particles.

REFERENCES

Agar, A. W. (1960) J. Appl. Phys. 11, 185.

Andrews, K. W., Dyson D. J., Keown S. R. (1971) In : "Interpretation of Electron Diffraction Patterns", Adam Hilger Ltd., London.

Bahr, G., Johnson, F.R. and Zeitler, E. (1965) Laboratory Investigations 14, 1115.

Batson, P.E. (1988) Proc. EUREM88, Ed. Goodhew, P.J. and Dickinson, H.G. (London: IOP) Conf. Ser. No. 93, Vol 2, 137.

Bentley, J., Lehman, G.L. and Sklad, P.S. (1982) In : Electron Microscopy, Proc. 10th Int. Cong., Hamburg, Vol. 1, 585.

Brockes, A. (1964) Optik, 21, 550.

Carr, W. (1978) J.O.C.C.A., 61, 397.

Chapman, J.N., Batson, P.E., Waddell, E.M. and Ferrier, R.P. (1978) Ultramicroscopy 3, 203.

Chapman, J.N., McFayden, I.R. and McVitie, S. (1990) IEE Transactions on Magnetics, Vol. 26, No. 5, 1506.

Chapman, (1995), Private Comunication.

Clark, W.R.K. (1979) Ph. D. Thesis, University of Glasgow.

Clark, W.R.K., Chapman, J.N., MacLeod, A.M. and Ferrier, R.P, (1980) Ultramicroscopy, 5, 195.

Colliex, C., Craven, A. J. and Wilson, C. J. (1977) Ultramicroscopy, 6, 71.

Cowley, J.M. and Moodie, A.F. (1957) Acta Cryst., 10, 609.

Cowley J. M. (1969) Applied Physics Letters 15, No. 2, 58

Cowley, J.M. (1976) Ultramicroscopy 2, 3.

Cowley, J. M. and Au, A. Y. (1978) Scanning Electron Microscopy I, SEM Inc., AMF O'Hare, Chicago, 53.

Cowley, J.M. and Spence, J.C.H., (1979) Ultramicroscopy 3, 433.

Craven, A.J. and Buggy, T.W. (1981) J. Microscopy 136, 27.

Craven, A.J. and Buggy, T.W. (1981) Ultramicroscopy 7, 27.

Craven, A.J. (1989) Inst. Phys. Conf. Ser., No. 98, Chpt. 2, 49.

Crewe , A. V. and Wall, J. (1970) Journal of Molecular Biology, 48, 375.

Crewe, A. V. (1971) in "Electron Microscopy and Material Science", Ed. Valdre, U., 162.

Dekkers, N.H. and De Lang, H. (1974) Optik, Vol. 41, No. 4, 452.

Dekkers, N.H. and De Lang, H. (1977) Philips Technical Review, Vol. 37, No. 1.

Drummond, M.J. (1985) Ph. D. Thesis, University of Glasgow.

Egerton, R.F. (1978) Ultramicroscopy 3, 243.

Egerton, R.F., (1979) Ultramicroscopy 4, 169.

Egerton, R.F. (1980) J. Microscopy, Vol. 118, Pt. 4, 389.

Egerton, R.F. (1986) Electron Energy_loss Spectroscopy in the Electron Microscope, Plenum, New York.

Egerton, R.F. and Cheng, S.C. (1987) Ultramicroscopy 21, 231.

Egerton, R.F. (1989), Ultramicroscopy 28, 215.

Frank, J. (1973) Optik, 38, 519.

Fryer, J.R. (1977) In : Proc EMAG 77 Ed. Misell, D., IOP Conf. Ser.36., p.423.

Fryer, J.R. (1980) J. Microsc., Vol. 119, Pt. 3, 1.

Fryer, J.R., McKay, R.B., Matther, R.R. and Sing, K.S.W. (1981) J. Chem. Tech. Biotechnol. 31, 371.

Fryer, J.R. (1984), Ultramicroscopy, 14, 227.

Glaeser, R.M. (1971) Journal of Ultrastructure Research, 36, 466.

Hawkes, P.W. (1978) J. Optics (Paris), 9, 235.

Hirsch, P. B., Howie, A., Nicholson, R.B., Pashley, D.W. and Whelan, M. J. (1965) in "Electron Microscopy of Thin Crystals, Butterworth & Co., London.

Hom, D. and Honigman, B. (1974) Polymorphic des Kupferphthalocyanine, XII Fatipec Congress.

Honigmann, B. (1966) J. Paint Technology, Vol. 38, N0. 493, 77.

Humphreys, C.J. (19810 Ultramicroscopy 7, 7.

Inman, E.R., (1967) Royal Institute of Chemistry Lecture Series No. 1.

Isaacson, M. and Johnson, D. (1975) Ultramicroscopy 1, 33.

Isaacson, M. (1977) In : Principles and Techniques of Electron Microscopy, Vol. 7, 1.

Kobayashi, T., Kurata, H. and Uyeda, N. (1982) Proceedings of the 10th International Congress on Electron Microscopy, Hamburg 2, 461.

Kobayashi, T., Fujiyoshi, Y. and Uyeda, N. (1982) Acta Cryst., A38, 356.

Krivanek, O.L., Ahn, C.C. and Keeney, R.B. (1987), Ultramicroscopy 22, 103.

Leapman, R.D., Rez, P. and Mayers, D.F. (1978) Proc. 9th Int. Cong. Electron Microsc., Ed. Sturgess, J.M., Vol 1, 526.

Leapman, R.D. and Swyt, C.R. (1981) In : Analytical Electron Microscopy, Ed. Geiss, R.H., San Francisco Press, San Francisco, 164.

Lewis, P.A. (1982) Pigment Handbook, Vol. 1, Interscience.

McColgan, P. (1990) Ph. D. Thesis, University of Glasgow.

McColgan, P., Chapman, J.N. and Nicholson, A.P. (1990) J. Microsc 160, Pt. 3, 315.

McColgan, P. and Chapman, J.N. (1990) Inst. Phys. Conf. Ser. No. 93, Vol. 1, Chpt. 3, 185.

Mackay, R.B. (1988) J.O.C.C.A., 71, 7.

Merkle, K. and Herbst, W. (1968) IX Fatipec-Congr. 2, 65.

Morrison, G.R., Chapman, J.N.and Craven, A.J. (1979) In : Proc IOP Conf. Ser.52., p.257.

Morrison, G. R. (1981) Ph.D. Thesis, University of Glasgow.

Moser, F.H. and Thomas, A.L. (1983) The Phthalocyanines (CRC, Boca Raton).

Murata, Y., Fryer, J.R., Baird, T. and Murata, H. (1977) Acta Cryst. A33, 198.

Murata, Y. (1978) In : Electron Microscopy 1978 (Proc. 9th Intern. Cong. on Electron microscopy, Toronto, 1978) ed. Sturgess, J.H., Vol. 3, p.49.

Phillips, R. (1960), Selected area diffraction in the electron microscope, Brit. J. Appl. Phys. 11, 504

Reicke, W. D. (1961), The exactness of agreement between selected and diffractinf areas in Le Poole's selected area diffraction technique, Optik 18, 278.

Reimer, L. (1960) Zeitschrift Naturforschung A15, 405.

Reimer, L. (1975) In : Physical Aspects of Electron Microscopy and Microbeam Analysis, Eds Siegel, B.M. and Beaman, D.R., Wiley, New York.

Reimer, L. (1984) In : Transmission Electron Microscopy, Springer Verlag.

Rose, H. (1977) Ultramicroscopy 2, 251.

Scherzer, O. (1949) J. Appl. Phys. 20, 20.

Siegal, B.M. (1972) Zeitschrift Natursforsch, A27, 325.

Smith, F.M. and Easton, J.D. (1966), J. oil Col. Chem. Assoc. 49, 614.

Smith, D.J., Fryer, J.R. and Camps, R.A. (1986) Ultramicroscopy, 19, 279.

Spence, J.C.H. and Cowley, J.M. (1978) Optik 50, No. 2, 129.

Steele, J.D., Titchmarsh, J.M., Chapman, J.N. and Paterson, J.H. (1985) Ultramicroscopy 17, 273.

Titchmarsh, J.M. and Durnbill (1996) J. Microsc. 184, 195.

Uyeda, N., Kobayashi, T., Ohara, M. and Harada, Y. (1972) Proc, of the 5th European Congr. on Electron Microscopy, The Institute of Physics, London, 566.

Uyeda, N., Kobayashi, T., Ishizuka and Fujiyoshi, Y. (1981) JEOL News Electron Optics Instrumentation, Vol. 19E, No.1., 2.